Intraseasonal variability in the southwestern and central tropical Atlantic Ocean

Dissertation
zur Erlangung des Doktorgrades
der Mathematisch-Naturwissenschaftlichen Fakultät
der Christian-Albrechts-Universität
zu Kiel

vorgelegt von

Karina von Schuckmann

IFM-GEOMAR
Leibniz-Institut für Meereswissenschaften
an der Universität Kiel

Kiel, September 2006

Referent/in:	Priv.-Doz. Dr. P. Brandt
Korreferent/in:	Prof. Dr. C. Böning
Tag der mündlichen Prüfung:	06.11.2006
Zum Druck genehmigt:	Kiel, den 06.11.2006

Der Dekan Prof. Dr. J. Grotemeyer

Abstract

Various kinds of intraseasonal variability (ISV) exist in the oceans which have recently been observed in many locations surrounding the tropical Atlantic Ocean. Their forcing mechanisms can involve different dynamic processes, i.e. intraseasonal wind fluctuations, internal ocean processes or remote forcing. In this study, current measurements from mooring sites close to the western boundary in the southern hemisphere and at the equator in the central basin are analyzed which reveal signals at intraseasonal periods. Basinwide altimeter measurements as well as results from two numerical model simulations with varying surface wind forcing are applied in order to clarify the dynamic processes essential for the observed intraseasonal signals. It is shown that in the tropical Atlantic two key processes lead to the generation of fluctuative energy at intraseasonal periods: barotropic and baroclinic instability.

Two individual maxima of eddy kinetic energy (EKE) can be separated analyzing the current measurements at 11°S close to the South American coast. One of these maxima is evident in the near surface layer. Together with altimetry measurements and the model simulations it could be shown that this signal is linked to disturbances propagating westward as baroclinic Rossby waves with phase speeds of 0.1-0.2 m/s and wavelengths of 400-1000 km along 11°S. The models are then used to diagnose the energetics in the tropical South Atlantic which reveals that - beside the enhanced signal close to the western boundary - EKE shows maximum values in the domain of the central South Equatorial Current (cSEC). EKE is generated mostly by baroclinic instability and the influence of barotropic instability is small. Cyclonic eddy-like features develop at the southern rim of the cSEC which seem to propagate southwestward to the North Brazil Undercurrent (NBUC), where the variability clearly increases.

The second EKE maximum is located at intermediate depths between 200 and 800 m depth which is accompanied by weak mean southward flow. Energy transfer terms derived from the model output shows that the NBUC becomes unstable at about 4°-5°S. A recirculation cell is indicated which is accompanied by enhanced EKE generated by barotropic instability. Part of this resulting EKE is converted into the mean field by stabilizing effects of baroclinic instability, possibly resulting in the weak southward recirculating flow observed in the current measurements. South of 9°S fluctuative energy is generated by both, barotropic and baroclinic instability. Effects of strong changes in stratification and reduced current shear account for the fact that EKE at intermediate depths is confined to that depth layer as observed in the mooring array data at 11°S.

In addition, the distribution of energy sources favoring the growth of near-surface tropical instabilities in the entire tropical Atlantic Ocean is of particular interest. Analyzing the model output it could be shown that predominantly in boreal summer barotropic as well as baroclinic instabilities generate EKE in a band $\pm$ 5° latitude. Barotropic instability occurs in the horizontal shear between the North Equatorial Countercurrent (NECC) and the northern South Equatorial Current (nSEC) as well as between the Equatorial Undercurrent (EUC) and the nSEC. Baroclinic instability grows in the domain of the cSEC and the nSEC. A principle oscillation pattern (POP) analysis along the equator reveals that two patterns of ISV at 20-40 d periods exist which propagate westward. The dominant one is generated near the equator and the second one is generated between 3°-5°N, that is in the domain of the tropical instabilities. The amplitude of the second POP pattern indicates that the oscillation could be associated with an equatorially trapped Yanai-type. A similar ISV signal is also evident in the measurements of the equatorial mooring at 23°W.

Zusammenfassung

In den Ozeanen existieren zahlreiche intrasaisonale Variabilitäten (ISV), die im tropischen Atlantischen Ozean beobachtet wurden. Die Antriebsmechanismen können unterschiedlichen dynamischen Prozessen unterliegen, wie intrasaisonalen Windfluktuationen, internen Prozessen des Ozeans oder fernwirkenden Kräften. Im Rahmen dieser Arbeit werden Strömungsmessungen aus Verankerungen am westlichen Rand auf der Südhemisphäre und am Äquator im zentralen Becken untersucht, in denen ISV ist. Zusätzlich werden Altimetermessungen und Simulationen von numerischen Modellen mit unterschiedlichem Windantrieb verwendet, um die dynamischen Prozesse zu identifizieren, welche die beobachteten intrasaisonalen Signale hervorrufen. Zwei Kernprozesse erzeugen fluktuative Energien auf intrasaisonalen Zeitskalen: barotrope und barokline Instabilität.

Die Strömungsmessungen bei 11°S nahe der südamerikanischen Küste zeigen, dass zwei unabhängige Maxima Wirbel-kinetischer-Energie (EKE) existieren, von denen das eine in Oberflächennähe zu finden ist. Die Altimetermessungen und Modellsimulationen zeigen, dass dieses Signal im Zusammenhang mit Anomalien steht, die mit Phasengeschwindigkeiten von 0.1-0.2 m/s und Wellenlängen von 400-1000 km als barokline Rossby-Wellen entlang 11°S nach Westen propagieren. Die Erzeugung der EKE im tropischen Südatlantik wird in den Modellsimulationen untersucht. Dabei zeigt sich, dass die EKE maximale Werte im Bereich des zentralen Südäquatorialen Stromes (cSEC) aufweist. Die EKE wird hauptsächlich durch barokline Instabilitäten erzeugt, während der Einfluss barotroper Instabilität gering ist. Zyklonal rotierende Bewegungen entstehen am südlichen Rand des cSEC, die südwestlich in Richtung des Nordbrasil Unterstroms (NBUC) propagieren und erhöhen dort die Variabilität.

Das andere EKE-Maximum ist zusammen mit einer schwachen südwärtigen mittleren Strömung in der Tiefe des Zwischenwassers zwischen 200 und 800 m Tiefe zu beobachten. Die Energietransferterme aus den Modellergebnissen zeigen, dass der NBUC bei 4°-5°S instabil wird. Es existiert eine Rezirkulationszelle, in der EKE durch barotrope Instabilität erzeugt wird. Ein Teil dieser EKE wird in mittlere Energie durch stabilisierende Effekte barokliner Instabilität umgewandelt, was möglicherweise die Ursache für die schwache südwärtige Strömung ist, die beobachtet werden konnte. Südlich von 9°S wird fluktuative Energie durch barotrope und barokline Instabilität erzeugt. Starke Änderungen der Schichtung und verringerte Strömungsscherung sind dafür verantwortlich, dass die EKE in den Beobachtungen bei 11°S auf den Bereich des Zwischenwassers beschränkt ist.

Desweiteren wird die Verteilung der Instabilitätsprozesse im oberflächennahen tropischen Atlantik untersucht. Die Modellergebnisse zeigen, dass vor allem im borealen Sommer barotrope, aber auch barokline Instabilitäten EKE in einem Band von ± 5° geographischer Breite erzeugen. Barotrope Instabilität entsteht in der horizontalen Scherung zwischen dem Nordäquatorialen Gegenstrom (NECC) und dem nördlichen Südäquatorialstrom (nSEC), sowie zwischen dem äquatorialen Unterstrom (EUC) und dem nSEC. Barokline Instabilität entsteht im Bereich des cSEC und des nSEC. Mit Hilfe einer POP (principle oscillation pattern) Analyse entlang des Äquators ergibt sich, dass zwei ISV-Signale im Periodenbreich von 20-40 d existieren, die nach Westen propagieren. Das dominante oszillierende Signal wird in der Nähe des Äquators und das zweite wird nördlich des Äquators bei 3°-5°N erzeugt, also im Bereich der tropischen Instabilitäten. Die Amplitude der zweiten POP deutet darauf hin, dass diese Oszillation mit einem Yanai-Typ erklärt werden kann. Ein ähnliches Signal erscheint ebenfalls in der äquatorialen Verankerung bei 23°W.

Contents

1. Introduction

1.1. Motivation and structure

Oceanic meridional heat flux is a critical element of the earth's climate system as it contributes to balancing the global energy budget. Generally, meridional heat transport is directed from the tropics to the polar regions, but in the Atlantic Ocean the oceanic heat transport is northward in both hemispheres (Figure 1.1). This anomalous heat transport is related to the role that the Atlantic ocean basin plays in the meridional overturning circulation (MOC). Within the MOC, the Deep Western Boundary Current (DWBC) in the Atlantic ocean carries dense and cold water masses formed in the North Atlantic southward across the equator into the South Atlantic. These water masses then circulate and upwell within the Antarctic Circumpolar Current (ACC), the Indian and Pacific Oceans, before they are carried back into the South Atlantic Ocean. In the subtropical and tropical Atlantic, the return flow of the MOC (also referred to as the upper limb) is evident which compensates the southward flow of cold water masses in the DWBC by a northward flow of warm water masses crossing the equator within the North Brazil Undercurrent (NBUC)/North Brazil Current (NBC) and finally feeding the North Atlantic Current regime (Gordon, 1986; Broecker et al., 1990, Figure 1.2), influencing the climate of Europe. The pathways of the MOC return flow in the tropical Atlantic are important since relatively cool water masses of southern hemisphere origin interact with the circulation regime in the warm water sphere of the Atlantic and thus with the overlying atmosphere. Consequently, the path that the MOC return flow takes affects the moisture and heat exchange between ocean and atmosphere and water mass characteristics as transported into the North Atlantic are strongly influenced by the circulation branches of the MOC in the warm water sphere and, hence, influence climate signals in the Atlantic.

In the tropics, the pathways of the upper MOC limb interact with the prevailing circulation regime. Besides the wind-driven mean circulation, shallow subtropical cells (STCs) exist in the tropical Atlantic which act as a mechanism for transferring mass, heat salt and tracers between the subtropics and the tropics (e.g. Schott et al., 2004). Through their effect on SST, the STCs have been proposed as the oceanic component of coupled modes of air-sea variability that influence atmospheric climate on multiple timescales, from intraseasonal to multidecadal. Thus, it is important to enhance the understanding of the variability of both, the northward meridional heat transport and the shallow cells and their influence on the atmosphere in order to improve the predictability of climate variability. In this study the focus will be on intraseasonal variability (ISV) in the tropical Atlantic Ocean which influences the superposing mean current regimes, and, hence, may influence climate variability on various time scales.

Previous investigations in the tropical Atlantic indicate that a variety of ISV in the period range of 10-150 d exists which influences the mean circulation regime. It has been

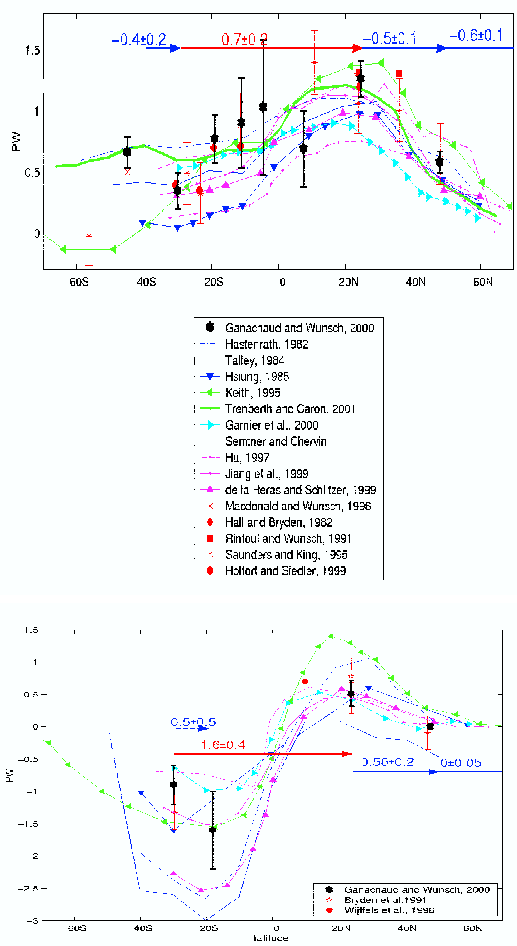

Figure 1.1.: *Estimates of horizontal oceanic heat transports and divergences (numbers above the arrows, positive/red for ocean heat gain, negative/blue for ocean heat loss) between selected latitudes using hydrography and climatologies in the Atlantic (upper panel) and in the Indian and Pacific oceans (summed, lower panel). From Ganachaud and Wunsch (2003).*

shown that intraseasonal features constitute an important component of the upper limb return flow of the MOC by contributing to the northward transport of southern Atlantic water into the northern subtropics due to a formation of anticyclones in the NBC domain just north of the equator (e.g. Goni and Johns, 2001). Besides this important ISV pattern, other signals are evident in the tropical Atlantic, which are presumed to play a role in the coupled ocean-atmosphere system and which are the focus of this thesis. Upper ocean tropical instabilities exist which are associated with tropical instability waves (TIWs) with typical periods ranging from 20 to 40 d (Weisberg and Weingartner, 1988). The TIWs cause variability in SST (Legeckis, 1977), cloud cover (Deser et al., 1993), wind (Chelton et al., 2001) and contribute to the equatorial heat budget (Hansen and Paul, 1984). Another important characteristic is the existence of equatorially trapped waves, which are important mechanisms for the adjustment of tropical oceans (França et al., 2003), influencing SST variability at the equator and affecting short-term climate variability as well.

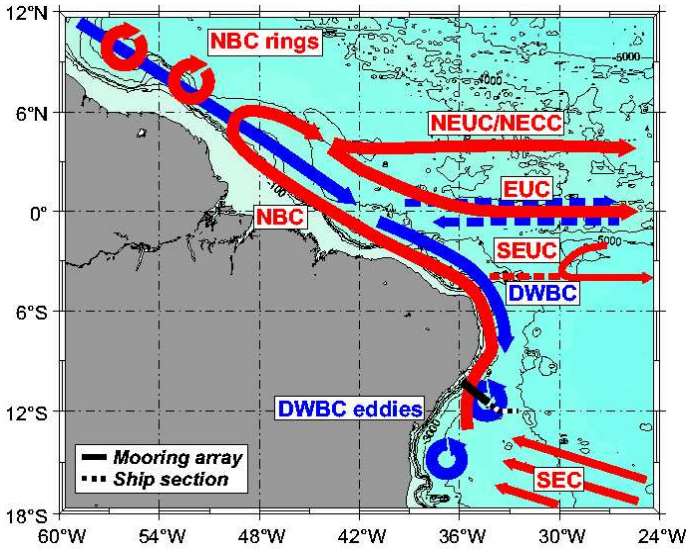

Figure 1.2.: *Circulation in the western tropical Atlantic. Schematic representation of mean currents and eddy generation at the western boundary of the tropical Atlantic with warm water pathways in red and North Atlantic Deep Water pathways in blue. Black bar and dotted black line at 11° S indicate positions of the measurement program. Current branches indicated are the South Equatorial Current (SEC), the North Brazil Current (NBC), the South Equatorial Undercurrent (SEUC), the Equatorial Undercurrent (EUC), the North Equatorial Undercurrent (NEUC) merged with the north equatorial counter current (NECC) and the Deep Western Boundary Current (DWBC) with altering zonal flows marked at the Equator. Modified after Dengler et al. (2004).*

These and other processes provide a variety of fluctuation patterns superimposed on the upper-limb and subtropical-tropical pathways. Basinwide observational records of hydrography and sea level changes exist which enable us to analyse these pathways, but presently only at the surface. Thus, numerical model experiments are needed in order to investigate the respective roles of these pathways, describe variability patterns of the mean flow, understand the controlling dynamics, and quantify the water mass characteristics that occur. As discussed above, ocean mesoscale variability affects the mean state of the tropical climate. Compared to a non-eddy resolving ocean model, resolving oceanic mesoscale variability leads to a simulation of oceanic features closer to what is observed in the measurements (Seo et al., 2006). This also means that investigations of ISV are needed to improve the understanding of the coupled Atlantic ocean-atmosphere system.

In this study, the distribution of ISV in the tropical Atlantic ocean is investigated, especially in the southern hemisphere, where the meridional heat transport is - anomalous to the other oceans - directed equatorward (Figure 1.1). More than four year long time series (from March 2000 to August 2004) of current speed and transport fluctuations within the upper limb of the MOC from a mooring array at 11°S are analyzed. In addition, basinwide year-long measurements of sea surface elevation derived from satellite altimetry and results from two differently forced numerical model simulations are investigated. One model simulation is forced with a monthly mean climatological ECMWF wind field and for the second simulation a daily ECMWF forcing is used. The target of this analysis is

to provide estimates of intraseasonal changes in the near surface layer of the NBUC and the central and western Atlantic ocean, as well as at intermediate depths close to the western boundary and to relate these to its forcing mechanisms. Thus, the main aim of this investigation is to understand intraseasonal changes of the upper MOC limb and of the mean circulation pathways in the western and central tropical Atlantic Ocean. One major aspect is to detect sources of high fluctuative energy in that domain and to discuss physical interpretations of the velocity and transport fluctuations, which requires comparisons of the observational and model data.

The thesis is organized as follows. In the next section a brief overview on the present status of science will be given, which describes the known features of the mean circulation field and its seasonal and subseasonal changes in the tropical Atlantic. In chapter 2 several data sources involving measurements as well as numerical model simulations are introduced which are the basis for this study. In chapter 3 local patterns of ISV along 11°S in the upper 1000 m will be described using velocity measurements from the mooring array, altimeter measurements and results from both numerical model simulations. In chapter 4 fluctuation patterns in the intermediate depth layer close to the western boundary are discussed in more detail and the distribution of eddy kinetic energy and energy transfer terms are investigated. The pathway of intermediate water masses along the western boundary is analyzed and its spreading after crossing the equator is discussed. In chapter 5 patterns of ISV in the near surface layer are analyzed and their forcing mechanisms are explored. In chapter 6 the findings of this thesis are summarized and discussed.

1.2. The western tropical Atlantic: Mean flow and temporal variability

In the western tropical Atlantic strong western boundary currents contribute to the inter-hemispheric transport of water mass properties. The current system is characterized by the interaction of the wind driven zonal current system, the MOC and the STCs. In this section the pathways and superposed variability features of this complex flow pattern will be summarized from literature results for the upper 1000 m, i.e. from the tropical surface water layer down to intermediate depths.

1.2.1. Mean circulation in the upper layer

The wind driven oceanic gyres are generated by the large-scale wind field, which, in the tropics, is dominated by the Southeast and Northeast Trade winds. In terms of mass conservation, these interior gyres are closed at their western end by western boundary currents. The western boundary currents are important in transporting the excess heat the earth receives in the tropics towards the poles. The role of the western boundary current in the tropical Atlantic Ocean, which participates in the interhemispheric exchange of water mass properties, is also related to the MOC. As mentioned above, the transport of heat in the Atlantic Ocean is not directed poleward in the southern hemisphere, but heat moves northward in both hemispheres due to the impact of the MOC (Figure 1.1). In general, the MOC describes a meridional flow field which is a mix of both wind-driven and thermohaline

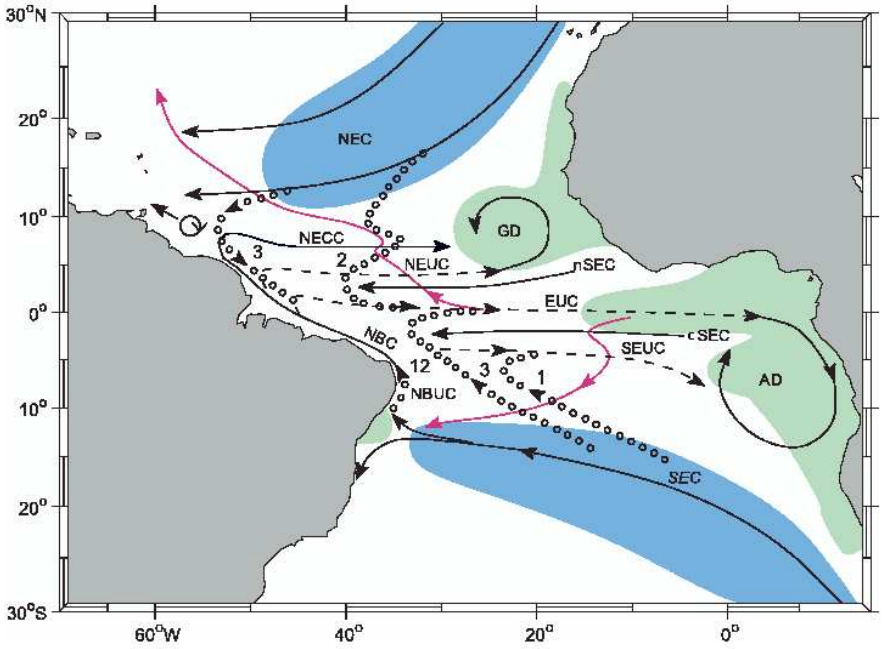

Figure 1.3.: *Schematic representation of the Atlantic STC circulation with subsduction (blue) and upwelling (green) zones that participate in the STC. SEC, NEC = North and South Equatorial Current; NEUC, SEUC = North and South Equatorial Undercurrent; NBC, NBUC = North Brazil Current and Undercurrent; GD,AD = Guinea and Angola domes. Interior equatorward thermocline pathways dotted, transport estimates marked for interior and western boundary pathways; surface poleward pathways for the central basin marked by thin, magenta line. After Schott et al. (2004).*

flow (Csanady, 2001; Rahmstorf, 2006). In the tropical Atlantic Ocean, pathways of the MOC consist of a southward transport of cold water masses from the north in the DWBC which are compensated by warm waters flowing northward in the upper limb of the MOC (Figure 1.2).

The South Equatorial Current (SEC) is the major southern pathway as part of the upper limb, by which water of South Atlantic origin is imported into the tropical Atlantic Ocean (Reid, 1989). The SEC regime covers a broad region between 6°N and 25°S of westward flow driven by the trade winds (Stramma and Schott, 1999). The SEC regime is classified into several branches, i.e. the southern band of the SEC at the northern rim of the southern hemisphere subtropical gyre south of 10°S, the central SEC (cSEC) between about 4°-6°S and the northern SEC (nSEC) between about 4°-6°N (Figure 1.3). From the south, the SEC reaches the western boundary at 12°-20°S in the near surface layer and a weak part turns southward into the Brazil Current (BC), whereas the larger fraction feeds into the northward flowing NBUC. Further north, the cSEC merges with the NBUC and forms the surface-intensified NBC and then crosses the equator northwestward (Schott et al., 1998, Figure 1.3). Being wind driven, the SEC responds quickly to variations in the wind field. The SEC is strongest during boreal summer and weakest during boreal winter (Molinari,

1982). Further north, the seasonal cycle of the cSEC and the NBC is shown to be weak (Schott et al., 1998).

The vertical structure of the northward NBUC along the Brazilian coast between 5°S and 10°S is that of an undercurrent with the current core of 80 cms^{-1} at about 200 m depth and small near surface currents (Schott and Böning, 1991; da Silveira et al., 1994; Stramma et al., 1995). After passing Cape São Roque at 5°S, the cSEC joins the NBUC, causing its vertical structure to change from an undercurrent to a surface-intensified current, namely the North Brazil Current (NBC). The NBC enters the northern hemisphere and retroflects into the zonal equatorial current system. Just north of the equator, the NBC feeds into the Equatorial Undercurrent (EUC). At about 5°N the NBC retroflects into the North Equatorial Countercurrent (NECC) (Figure 1.3). The latter retroflection is characterized by a large seasonal cycle which is related to changes in the wind stress curl in the northwestern tropical Atlantic (Garzoli and Katz, 1993; Johns et al., 1998). The NBC feeds the NECC when the NECC is present in July to January (Johns et al., 1990; Didden and Schott, 1992). In boreal spring to summer the NECC is weak or even eastward (Richardson and Reverdin, 1987). During the time of strong surface current retroflection at about 5°N, water mass transport along the western boundary is established by NBC rings, which pinch off in the retroflection region (Johns et al., 2003; Garraffo et al., 2003), whereas in boreal spring a major part of the NBC seems to continue along the boundary in the Guyana Current (Johns et al., 1998).

In the interior tropical Atlantic several branches of the mean circulation system are evident (Figure 1.3). Between the northern rim of the subtropical gyre in the southern hemisphere and the cSEC the South Equatorial Undercurrent (SEUC) exists which reaches the surface layer east of 35°W as an eastward flow during northern spring (Stramma and Schott, 1999). The core of the SEUC lies between 3° and 4°S at 150-600 m depths and its supply is through recirculation out of the SEC rather than via NBUC retroflection (Schott et al., 2005). In the source region west of 35°W the SEUC seems to be fed by oxygen-poor water from the near-equatorial SEC flow (Schott et al., 1998), whereas east of 35°W oxygen-rich water from the south is transported by the SEUC (Tsuchiya, 1986). Its northern hemisphere counterpart, i.e. the North Equatorial Undercurrent (NEUC), is located between 3° and 4°N at 90-350 m depths. The NEUC seems to receive its water from the nSEC as well as from the westward North Equatorial Current (NEC), but partial supply originates from the northern part of the NBC retroflection, as water masses show southern properties at some observation points (Schott et al., 1998, 2005).

As introduced above, the eastward flowing EUC is fed by the NBC retroflection just north of the equator (Figure 1.3). The EUC crosses the entire Atlantic while reducing in strength (Stramma and Schott, 1999). Hydrographic measurements show that the depth of the EUC core coincides with the depth of the equatorial thermocline (Metcalf and Stalcup, 1967; Schott et al., 1998). The driving mechanism of the EUC is related to an eastward pressure gradient caused by the easterly windstress at the equator. A seasonal cycle is found in depth variations of maximum eastward flow since the EUC in spring is nearer to the surface than in fall in the western Atlantic (Richardson and Reverdin, 1987; Schott and Böning, 1991). The EUC looses its water to the overlying layer by equatorial upwelling and to the SEC branch north and south of the equator (Stramma and Schott, 1999). First

suggested by Metcalf and Stalcup (1967) and later investigated by, for example, Schott et al. (1995), Hazeleger et al. (2003) and Zhang et al. (2003), the EUC is primarily fed by waters from southern hemisphere origin in the NBUC. In other words, the subtropical South Atlantic is the main source for the EUC. Less than a tenth of the transport in the EUC has northern hemisphere origin from the subduction region along the NEC (e.g. Hazeleger et al., 2003).

The pathways feeding the equatorial upwelling regions are related to the STCs. About 70% of the tropical Atlantic upwelling into the surface layer is associated with these shallow cells (Zhang et al., 2003). As mentioned above, the STCs describe the subtropical-tropical pathways and water masses from the subduction zones within the subtropical gyres are transported into the equatorial thermocline via the shallow cells (e.g. Schott et al., 2004). The water upwells at the equator and then returns to the subduction regions to close the cell. In contrast to the Pacific ocean, where the STC structure has been quite well established with observations and numerical modeling, the structure of the STCs in the Atlantic ocean is still controversial since it is complicated by the superimposed upper limb of the MOC. The Atlantic STCs exist in both hemispheres, but their pathways proceed not symmetric about the equator due to the influence of the MOC (see below). In the northern hemisphere, subduction processes in the subtropics occur whithin the NEC current regime (Figure 1.3). Results from a numerical model showed that pathways from the subtropics to the tropics exist in the interior Atlantic as well as along the western boundary and that it is impossible to distinguish between both possible STC pathways in the northern hemisphere (Malanotte-Rizzoli et al., 2000). The results of a study by Zhang et al. (2003) suggest that only about 2 Sv of water subducted in the northern hemisphere reaches the tropics through the interior pathway, whereas in the south Atlantic 4 Sv of equatorward thermocline flow follows the route in the interior. The western boundary contributes about 3 Sv in the northern hemisphere, and about 6 Sv from the southern subduction regime. The indistinct exchange window mostly in the west is mainly maintained by the influence of the Atlantic Intertropical Convergence Zone (ITCZ), which exists between the equator and about 10°N. The ITCZ produces a potential vorticity barrier due to wind-induced upwelling and the interior stratification and thus, the water mass flows around this barrier layer on its way to the equatorial thermocline, i.e. the EUC.

In contrast, the water masses in the southern hemisphere STC flow more directly toward the equator. Subduction occurs in the SEC regime south of 10°S (see Figure 1.3). The subducted water masses are then carried within the SEC toward the western boundary and continue to flow equatorward whithin the NBUC/NBC. Besides this western boundary route, an interior exchange window exists across 6°S between the western boundary and 10°W (Zhang et al., 2003). But the EUC is mainly fed by the retroflection of the NBC just north of the equator (e.g. Malanotte-Rizzoli et al., 2000; Schott et al., 2004). The core of the EUC is relatively cold and fresh. Equatorial upwelling occurs and the cell is closed by poleward Ekman flow in the ocean interior (e.g. Snowden and Molinari, 2003).

The major effect of the MOC on the STCs is mirrored in the fact that the STCs are asymmetric about the equator. A study using a numerical model forced without the influence of the MOC revealed that in this case the STCs appear to be symmetric about the equator (Fratantoni et al., 2000). The STC in the northern hemisphere is weak since the

MOC essentially prevents the subsurface branch of the North Atlantic STC from reaching the equator. In the southern hemisphere, the major contribution to both, the equatorward subsurface flow from the subduction region and the upper limb of the MOC is concentrated in the NBUC/NBC and this complexity makes it difficult to distinguish between the different contributions. Another model study showed that approximately one-third of the EUC water that upwells takes part in the STC and two thirds of the EUC water that upwells takes part in the MOC (Hazeleger and de Vries, 2003). In addition, it could be shown that upwelling at the equator is strongly affected by high-frequency variations (Hazeleger et al., 2003) which again underscores the need to enhance the understanding of ISV in the tropical Atlantic.

1.2.2. Mean circulation at intermediate depths: The spreading of AAIW

A modeling study by Fratantoni et al. (2000) presents evidence that a major part of the MOC return northward flow occurs in the intermediate layer below the thermocline. The pathways of the upper limb at intermediate depths are concentrated in the western tropical Atlantic and Antarctic Intermediate Water (AAIW) masses are carried in the lower part of the NBUC (or IWBC, see below) toward the equator (Suga and Talley, 1995). AAIW is characterized by a salinity minimum and an oxygen maximum. Following Stramma et al. (1995), AAIW is bounded between $\sigma_\Theta = 27.1$ kgm^{-3} and $\sigma_1 = 32.15$ kgm^{-3}. The AAIW in the South Atlantic originates from a surface region of the circumpolar layer, especially in the northern Drake Passage and the Falkland Current (FC) loop (Talley, 1996). The confluence zone near the western boundary at about 38°S is known to be important for the exchange of waters between the ACC and the subtropical gyre (Figure 1.4, Zapiola Eddy, for example). Additionally, fresh intermediate water is injected into the subtropical gyre and mixed with older recirculated intermediate water (Talley, 1996; Boebel et al., 1999a). AAIW is transported eastward at the southern flank of the subtropical gyre and fractions of intermediate water masses from the Indian Ocean are contributed to the South Atlantic AAIW at its easternmost position via the Agulhas Current (Suga and Talley, 1995; Stramma and England, 1999). From the southeastern Atlantic AAIW flows northwestward within the southern branch of the SEC system which bifurcates close to the western boundary north of 20°-30°W (Santos Bifurcation, Figure 1.4). Two thirds of the AAIW flow south along the western boundary and recirculate as mentioned above and the remaining one third continues along the western boundary (Schmid et al., 2003, Figure 1.4).

On its way to the north, the NBUC shallows at about 5°S and continues as the NBC towards the equator with maximal vertical extension to 500 m depth. Schott et al. (1998) show that a second core of northwestward velocity exists at about 800 m depth, marking the AAIW layer core and the Intermediate Western Boundary Current (IWBC). An analysis of float trajectories at 800 m depth by Richardson and Schmitz (1993) showed that the IWBC continues parallel to the Brazilian shelf, crosses the equator and enters the Caribbean through the Grenada Passage. Interesting to note in this context is that the float trajectories are marked with anticyclonic movements. Results from a numerical model simulation indicated that the IWBC becomes unstable while crossing the equator and breaks up into eddies (Jochum and Malanotte-Rizzoli, 2003b). Direct velocity observations confirm this pathway of AAIW (Wilson and Johns, 1997). Investigations of subsurface

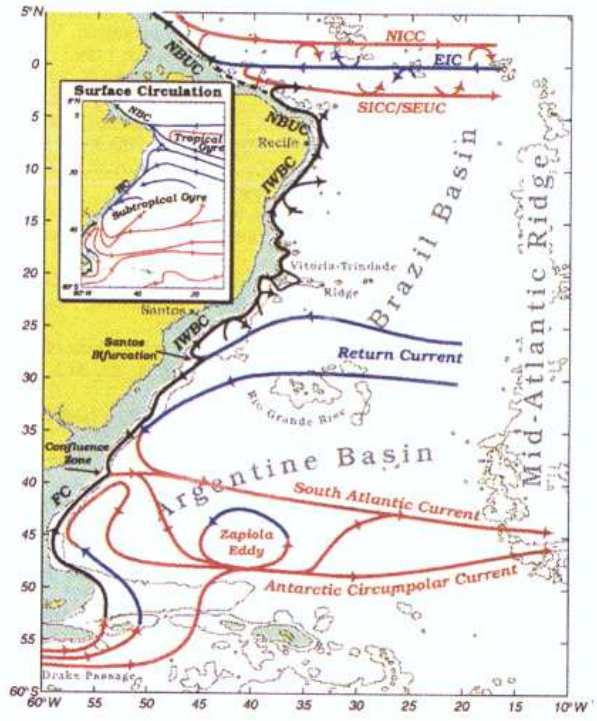

Figure 1.4.: *Schematic diagram of mean flow patterns at intermediate depths in the South Atlantic. Contour lines indicate 3000 m and 1000 m depths and the coastline. Red lines indicate eastward and blue westward velocity. Abbreviations: Falkland Current (FC); Northern Intermediate Counter Current (NICC); Equatorial Intermediate Current (EIC); Southern Intermediate Counter Current (SICC); South Equatorial Under Current (SEUC); Intermediate Western Boundary Current (IWBC); North Brazil Under Current (NBUC). A small schematic diagram by Peterson and Stramma (1991) is added showing the near-surface flow with the Brazil Current (BC), the North Brazil Current (NBC) and the tropical and subtropical gyres. After Boebel et al. (1999a).*

intensified NBC rings also imply that AAIW exists directly north of the equator in the vicinity of the western boundary (Johns et al., 2003).

However, the question how AAIW crosses or spreads along the equator is still under consideration. Based on several meridional velocity shipboard sections across the equator strong zonal currents are found which have been identified as the westward Equatorial Intermediate Current (EIC) centered at the equator and eastward southern and northern Intermediate Countercurrents at 2° latitude on both sides of the equator, respectively (Schott et al., 1998, 2003; Brandt et al., 2006, signified in Figure 1.4). Data from a collection of acoustic floats near 800 m support the result that the zonal equatorial intermediate currents are robust features of the Atlantic equatorial circulation (Ollitrault et al., 2006). On the other hand, the mean EIC is, however, presently not consistently simulated by numerical models and a dynamical explanation for the observed intermediate currents has not yet been provided. Based on an analysis of a numerical model output the authors argue that these observed mean currents could be interpreted as seasonal

planetary waves instead. However, fraction of intermediate water masses of south Atlantic origin reach the equatorial band, upwell in the vicinity of the equator into thermocline waters and modify the water mass properties of the near surface layer (Boebel et al., 1999a).

1.2.3. Temporal variability in the Atlantic: Seasonal and subseasonal time scales

Seasonal variability

The intensity of the wind regime in the Atlantic is characterized by large seasonal variations caused by the impact of land masses on the air pressure distribution. In the tropics, this effect is mainly noticeable in the Intertropical Convergence Zone (ITCZ) where the Northeast Trade winds meet the Southeast Trade winds near the equator. The position of the ITCZ varies between the equator and about 10°N, reaching its northernmost position in boreal summer and moving to a position just north of the equator in boreal winter (e.g. Stramma and England, 1999). Air-sea interactions exist and climate conditions are regionally influenced since the ITCZ is always being drawn toward the area of warmest surface temperatures. For the case that, for example, the ITCZ moves northward, precipitation is increased in the Sahel region and drought is evident in northeastern Brazil (Hastenrath and Greischar, 1993). The seasonal changes of the wind field lead to variations of the circulation in the tropical Atlantic. One of the clearest example of this variability is the occurrence of the NECC in boreal summer and fall and weakening in winter, which is connected to strong seasonal changes in the NBC retroflection (e.g. Stramma and England, 1999). An analysis of altimeter measurements has shown that the variability of the sea surface height (SSH) field along the equator is dominated by the seasonal cycle (França et al., 2003). The seasonal variability of the SSH gradient along the equator is correlated with the variability of the zonal wind (Katz, 1995) and the propagation of equatorial waves is an important mechanism to adjust the SSH gradient to variability in the zonal wind field (Schouten et al., 2005). Another analysis using in situ measurements and results from a numerical model simulation has shown that the seasonality of the equatorial flow above about 200 m appears to be influenced by directly wind forced Rossby beams (Brandt and Eden, 2005). In the deep ocean, semi-annual fluctuations are mainly forced by the equatorial zonal wind stress variability and the wind energy is transmitted towards the deep layers by vertically propagating equatorial waves (Thierry et al., 2004). The results of Brandt and Eden (2005) have shown that current maxima of the zonal velocities at intermediate depths in boreal summer are induced by Rossby beams generated by the reflection of Kelvin beams.

Intraseasonal Variability

Ring generation One of the strongest signals of ISV is evident along the western boundary in the northern tropical Atlantic. Rings are shed in the region where the NBC retroflects into the tropical zonal current system. After separating from the retroflection region, the rings travel northwestward along the Brazilian coast (Johns et al., 1990; Didden and Schott, 1993; Johns et al., 2003; Garraffo et al., 2003). The NBC rings are large anticyclones (warm core rings) and typically more than 5 rings are generated each year and may account for more than 1/3 of the total interhemispheric exchange in the Atlantic MOC (Goni and Johns, 2001). The rings translate with azimuthal speeds up to 1 m/s northwestward to

the Caribbean Sea and either decompose in the vicinity of the Lesser Antilles or become deflected northward east of the Lesser Antilles, from which the transport of the deep parts of the rings is inhibited by the regional bathymetry (Fratantoni and Richardson, 2006). According to the theory of Nof and Pichevin (1996), the ring generation and their north-westward drift is forced by the influence of the planetary and topographic β-effect in the retroflection zone. A study using numerical model results indicated that barotropic instability processes within the NECC generate radiating Rossby waves which reflect at the Brazilian coast and create about 6-7 rings per year (Jochum and Malanotte-Rizzoli, 2003a). Observations and models indicate that three types of NBC rings exist, i.e. two subsurface intensified ring types which differ in vertical extension and one subsurface intensified ring (Johns et al., 2003). The mechanisms which are accountable for the formation of the subsurface intensified rings are still under considerations. One explanation could be a pinch-off of deep eddies in the retroflection zone of the NBC into the EUC, but which does not explain why those rings contain portions of intermediate water masses (Johns et al., 2003). Another hypothesis derived from model results leads back to instability processes of an intermediate depth current that breaks up into eddies as it changes sign of potential vorticity while crossing the equator (Jochum and Malanotte-Rizzoli, 2003a).

In the deep ocean a generation of ring variability is also evident in the tropical Atlantic. In the domain of the DWBC at about 8°S the DWBC breaks up into eddies and the cold North Atlantic Deep Water (NADW) mass from the north is transported via migrating eddies rather than by a continuous flow (Dengler et al., 2004, Figure 1.2). The variance in the NADW layer at 1500-3000 m depths peak at about 60 days and differences of this ISV between the years exist (Schott et al., 2005). Model results indicate that baroclinic and barotropic instabilities are responsible for the ring generation in the DWBC domain (Dengler et al., 2004).

Madden-Julian oscillation The Madden-Julian oscillation (MJO) is the dominant mode of ISV in the tropical troposphere. The oscillation in the period range of 30-50 days is the result of large-scale circulation cells in the tropical domain that move eastward. Accompanied anomalies in zonal winds and the velocity potential in the upper troposphere propagate around the whole globe (Madden and Julian, 1971). The MJO is characterized by large regions of enhanced tropical rainfall, which appears first in the central Indian Ocean and propagates eastward over the western and central tropical Pacific. Further east, the signal vanishes in the eastern Pacific but reappears in the tropical Atlantic Ocean. The time scales of the MJO are long enough to interact with the upper ocean and the MJO has been found to be linked to SST variations, especially in the Indian and Pacific Oceans (Jones et al., 1998; Hendon et al., 1998). Actually, it could be shown for the Pacific Ocean that subseasonal fluctuations in the wind speed caused by the MJO play a prominent role in affecting the evolution of the El Niño/Southern Oscillation cycle (McPhaden et al., 2006). The influence of MJO is also in the tropical Atlantic Ocean evident. Strong intraseasonal wind oscillations between about 10°S and 10°N exert changes in sea surface temperature (SST) through latent heat loss from the ocean and thus may play an important role in affecting climate variability in this region (Foltz and McPhaden, 2004). Equatorial Kelvin wave propagation is evident in the Atlantic with an about two months periodicity. The source of the equatorial Kelvin wave seems to be the zonal wind stress at the equatorial western Atlantic associated to an atmospheric oscillation, i.e. the MJO (Katz, 1997).

TIWs In the Pacific as well as in the Atlantic Ocean tropical Instability Waves (TIWs) have been observed by the meandering of the sharp fronts of the equatorial cold tongue of 23°C water along and just south of the equator (Legeckis, 1977; Legeckis and Reverdin, 1987) and they are robust and commonly observed features of the eastern ocean basin. The TIWs appear as near-surface waves with a period of around one month and a zonal wavelength of 1000 km and westward phase speeds of 0.2-0.5ms^{-1}, whereas their group velocity is directed eastward or westward (e.g. Polito et al., 2001). They are formed between 5°S and 5°N in the eastern and central basin (e.g. Philander and Pacanowski, 1986). The TIWs have a stronger surface expression in the Northern Hemisphere than in the Southern Hemisphere (Foltz and Carton, 2004).

TIWs play an important role in the heat and momentum balance of the surface regions in the tropical oceans. Weisberg and Weingartner (1988) have shown for the tropical Atlantic Ocean that the waves influence the southward heat transport during the period when the NECC is most rapidly gaining heat which indicates that the TIWs act to balance the heat stored in the tropical zonal current. Furthermore, Menkes et al. (2002) investigate the effect of TIWs on equatorial Atlantic plankton and nutrient distribution suggesting remarkable meridional undulations which influence the redistribution of the physical and biological tracers in that domain. The TIWs also project variability onto the atmosphere since it seems that these instabilities have a large impact on the ITCZ (Caltabiano et al., 2005).

Packets of these waves are excited after the Southeast Trade winds intensify in boreal spring, when the zonal currents in the equatorial band accelerate, equatorial upwelling intensifies and the TIWs act to reduce the enhanced shears of the mean zonal currents. The instabilities cause large perturbations of the SST front of the cold tongue as mentioned above. Especially in the tropical Atlantic, different results exist concerning the generation mechanisms of the TIWs. On the one hand the instability waves are believed to be generated mostly by the horizontal shear of the zonal ocean currents, more precisely between the nSEC and the NECC (e.g. Kelly et al., 1995) or the nSEC and the EUC (Jochum et al., 2004). Barotropic instability than prevails and effects of baroclinic instabilities appear to be negligible (e.g. Weisberg and Weingartner, 1988; Philander et al., 1986; Kelly et al., 1995). On the other hand McCreary and Yu (1992), for example, show in a numerical simulation that mainly baroclinic instability accounts for the generation of TIWs. Grodsky et al. (2005) suggested by analyzing observational data from an equatorial mooring at 23°W that the TIWs are maintained by both barotropic and baroclinic conversions and that both instability processes are of comparable size. They argue that baroclinic instability mechanisms are not negligible in that region because salinity fluctuations favor the growth of this process. One can see that controversy exists over the relative importance of barotropic and baroclinic processes and there is no simple explanation for the observed strong year-to-year variability in the appearance of TIW in the tropical Atlantic.

2. Data used in this study

This study predominantly concentrates on the southwestern tropical Atlantic with focus on the western boundary current regime in the upper layer. Direct current measurements observed in a mooring array in this area are used and the analysis is extended disposing basinwide measurements from altimetry and results from two numerical model simulations. In addition, several sections derived from shipboard measurements are used to compare the model results with measurements. Finally, variability patterns for the northern hemisphere are also discussed and comparable basinwide data sources as well as observations from a mooring array close to the western boundary near the equator are analyzed.

2.1. Direct current and hydrographic measurements

2.1.1. Mooring array at 11°S

During the German program CLIVAR (Climate Variability and Predictability), a mooring array was initially deployed in March 2000 at the Brazilian shelf break following the gradient of bathymetry to about 240 km offshore near 11°S. The moorings were deployed during R/V Meteor cruise M47/1 and finally retrieved in August 2004 during cruise M62/2 (Figure 2.1). The aim was to investigate the deep western boundary current regime in this region as part of the global circulation and to analyse the equatorward return flow of the MOC in the upper layer. The array consists of five moorings K1-K5, and several exchanges were required to service the moorings. More precisely, in November 2002, moorings K2 and K4 were prematurely exchanged during R/V Sonne cruise S151 since near-surface floatation was lost, possibly caused by mechanical failure. Then, in February 2002, the first scheduled exchange was done during R/V Ron Brown cruise, and K1-K4 were redeployed. The offshore mooring K5 was deployed only from March 2000 to February 2002 with instruments below 1500 m depth. During cruise S170 (May 2003), moorings K1-K4 were exchanged again. The moorings in the boundary current regime were equipped with upward looking ADCPs (Acoustic Doppler Current Profilers) for near surface measurements. More precisely, during May 2003 to August 2004, 75-kHz Longranger ADCPs were used at station K1 and K2 and a 150-kHz narrowband ADCP during the other deployment periods and at K1-K3. At deeper levels, direct current measurements were recorded by RCMs (Aanderaa rotor current meters) and by ACMs (acoustic current meters). In Table A.1 (appendix) mooring positions as well as temperature profiling instrumentation is given but for a detailed listing of instrument depths, record length, instrument failure, etc. the reader is referred to Schott et al. (2005) (their Table 1). Publications which use data from this mooring array at 11°S are listed in Schott et al. (2002), Dengler et al. (2004) and Schott et al. (2005).

Data processing was performed at IFM-Geomar Kiel. Current records derived from ADCP measurements were interpolated to fixed depths by evaluating the instrument depths from surface backscatter (Visbeck and Fischer, 1995). All time series of the mooring array were

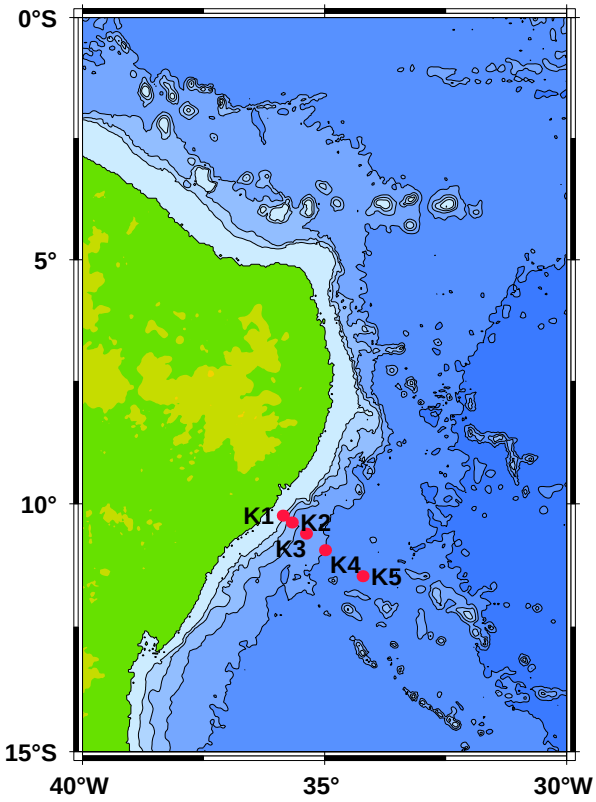

Figure 2.1.: *Location of a mooring array near 11° S (red dots). The array consists of five stations, K1-K5. K1-K4 were deployed from March 2000 to August 2004, and station K5 from March 2000 to February 2002 only.*

40-hours low-pass filtered and subsampled every 12 hours. Information due to the accuracy of the current measurements can be evaluated from a combination of instrument error and random error σ. The instrument bias accounts 0.5 to 1 cms^{-1} for ADCPs. Different parameters can influence the instrumental bias, e.g. temperature, mean current velocity and signal to noise ratio. The random error is defined as

$$\sigma = \frac{2.4 \cdot 10^5}{FD\sqrt{N}} \tag{2.1}$$

(RD Instruments, 1989), whereas F is the ADCP frequency, D the vertical resolution and N denotes the number of pings per two hours. Thus, with F = 150 kHz (75 kHz), D = 8 m and N = 340, the random error constitutes σ = 1.1 cms^{-1} (2.1 cms^{-1}) for both ADCPs. The specified measurement error is referred to the 2-hourly mean. During the different deployment periods, several types of RCMs have been used, i.e. RCM 5, RCM 6, RCM 7 and RCM 8. Those instruments still use the traditional concept of rotor and vane, which encounters problems in measuring low current speeds accurately. The error in measurement accounts for $\pm$ 0.01 ms^{-1} or $\pm$ 2% of velocity and the absolute error in directional reference amounts $\pm$ 7.5° at small background flow and $\pm$ 5° at high velocity (according to the manufactors information, Aanderaa, 1981, 1993).

2.1.2. Mooring at 23°W

Directly at the equator at 23°W, a mooring was deployed between 2001 to 2006. It was one part of the Pilot Research Moored Array in the Tropical Atlantic (PIRATA) project which is an international program, contributed by France, Brazil and USA. The measurements maintain a network of surface and near-surface measurements regarding the thermal structure, air-sea fluxes of momentum, heat and fresh water in the tropical Atlantic on a variety of frequency scales that are relevant to regional climate variability (Servain et al., 1998). For more details on the PIRATA project the reader is referred to www.brest.ird.fr/pirata/piratafr.html.

Three deployment periods exist between 2001 to 2006, with a break in 2003. The 23°W mooring was first deployed from R/V L'Atalante in December 2001 and recovered one year later in December 2002 from R/V Le Suroit. Current measurements were obtained by an upward looking ADCP located at 130 m depth, yielding a total depth range covered from 12 m to 130 m depths. The second deployment was in February 2004 from R/V L'Atalante, which was recovered in May 2005 from R/V Le Suroit. During this deployment period two ADCPs were used, from which one was an upward looking ADCP at 50 m depth and the second was a downward looking ADCP located at 60 m depth. Thus, profiles exist between 12 m and 700 m with a gap of 30 m between two ADCPs at about 120 m depending on the rather small vertical mooring excursion (Brandt et al., 2006). The next mooring was deployed immediately after recovering with a similar mooring design and then finally retrieved in June 2006 from R/V Meteor. All upward looking ADCPs worked at 300 kHz frequency and the downward looking ones measured at 75 kHz frequency. The profiles in the near-surface layer are limited to depths below 12 m because of surface reflection effects (Giarolla et al., 2005). The profiles have a vertical resolution of 4 m and a time step of 1 hour. For the purpose of this study the time series are subsampled to 12 h resolution.

2.1.3. Shipboard measurements

In this study, several mean sections will be used which provide current as well as hydrographic information of the tropical Atlantic, respectively. For direct current measurements, shipboard ADCPs and lADCPs (lowered ADCPs) have been used. The shipboard ADCP covers the range between about 30 m and some intermediate depths, depending on instrument type used. Possible versions of shipboard ADCPs might be a 150 kHz RD Instrument with a depth range limited to about 250 m, ocean surveyor (OS) 75 kHz RDI with a 700 m depth range (Fischer et al., 2003), or OS 38 kHz ranging up to 1200 m depth. The error of velocities is estimated to be better than 2-4 cms^{-1}. The lADCP was developed from the 150 kHz narrowband ADCP of RD Instruments. Data processing has been done during the individual cruise, where an average velocity profile was evaluated by solving an inverse problem as described by Visbeck (2002). The accuracy of the velocity measured by the lADCP is assumed to be better than 5 cms^{-1}.

The time series of current velocities derived from the vessel-mounted ADCPs and from the lADCPs are linearly interpolated onto the same horizontal grid. Tidal corrections were not considered since they are assumed to be negligible (Schott et al., 2005). Then, shipboard ADCP data and lADCP data were merged while the shipboard ADCP was weighted five times higher than the lADCP measurements due to higher accuracy and better horizontal

resolution. Upward of 30 m, the mean currents were linearly interpolated toward mean surface current field derived from a drifter climatology (Lumpkin and Garraffo, 2005). Finally, the mean sections were gridded using Gaussian weights with horizontal and vertical cutoff scales of 0.05° and 30 m and of 0.15° and 50 m, respectively.

The sections of hydrographic parameters such as temperature and salinity have been measured by Neil Brown and Seabird CTD (conductivity temperature depth) systems. The accuracy of those measurements is determined by taking additional water probes at several depths to induce e.g. salinity and to use thermometers measuring temperature in order to obtain results which are measured by instruments different from those of the CTD systems. The use of statistics allows to estimate the accuracy of the measurements which typically range from 0.002°-0.003°C for temperature and 0.0020-0.0025 for salinity. Finally, the data are gridded using Gaussian weights as described above.

Section	Ship	Extension	Time	Parameter
28°W	Seaward Johnson	5°S-0°N	Jan 2000	U,V,T,S
	Meteor	5°S-2.5°N	May 2002	U,V,T,S
	Sonne	5°S-2.5°N	May 2003	U,V,T,S
	Ron Brown	6°S-10°N	Aug 2003	U,V,T,S
	Meteor	5°S-2°N	Aug 2004	U,V,T,S
23°W	Polarstern	20°S-20°N	Jun 2005	T,S
26°W	see 28°W			
	Thalassa (23°W)	5°S-5°N	Aug 1999	U,V,T,S
	Seaward Johnson (25.5°W)	5°S-4°N	Jan 2000	U,V,T,S
	Seaward Johnson (23°W)	5°S-4°N	Jan 2000	U,V,T,S
	Meteor (23°W)	5°S-4°N	Apr 2000	U,V,T,S
	Meteor (24°W)	0°N-5°N	Oct 2002	U,V,T,S
	Polarstern (23°W)	20°S-20°N	Jun 2005	U,V,T,S
11°S	Meteor	35°W54'-32°W00'	Mar 2000	U,V,T,S
	Sonne	35°W54'-32°W00'	Nov 2000	U,V,T,S
	Meteor	35°W54'-32°W00'	May 2002	U,V,T,S
	Sonne	35°W54'-32°W00'	May 2003	U,V,T,S
	Meteor	35°W54'-32°W00'	Aug 2004	U,V,T,S

Table 2.1.: *Description of shipboard measurements and the composition of the mean sections used in this study*

In this study several mean sections are used, i.e. 26°W (Brandt et al., 2006), 28°W, 23°W, 11°S and 4.5°S. The cruises during which individual sections were measured and their horizontal extensions are listed in Table 2.1. Data processing and gridding have been applied as described above for all cruises, except for the 4.5°S section. The salinity and temperature distribution along this section are obtained from the WOCE Hydrographic profile data (Diggs et al., 2002). The data processing has been done under WOCE standard implementations. Data quality checks exist which compare one time surveys to other WOCE and to historical data.

2.1.4. WOCE Global Hydrographic Climatology

In order to describe the mean state of the ocean, the WOCE (World Ocean Circulation Experiment) Global Hydrographic Climatology (WGHC) (Gouretski and Koltermann, 2004) is used. The precision of single variables in the parameter field is given and its changes are statistically significant. Thus, the climatology represents a reference data set of the ocean and its variability. The first climatology of the world ocean was evaluated by Levitus (1982) and those data have been widely used by the oceanographic community. Then, three improved versions of the 1982 climatology have been developed, that is the World Ocean Atlas 1994 (WOA94, Levitus and Boyer, 1994a; Levitus et al., 1994; Levitus and Boyer, 1994b), World Ocean Database 1998 (WOD98) (Levitus et al., 1998) and the World Ocean Atlas 2001 (WOA01) (Conkright et al., 2002), from which the latter appeared in 2001. The climatology presented here (WGHC) was produced by a group of the German Federal Maritime and Hydrographic Agency (Bundesamt für Seeschiffahrt und Hydrographie (BSH)) who after 1999 continued the activities done at the Special Analysis Center of the WOCE Hydrpgraphic program (WHP) (mentioned in section 2.1.3).

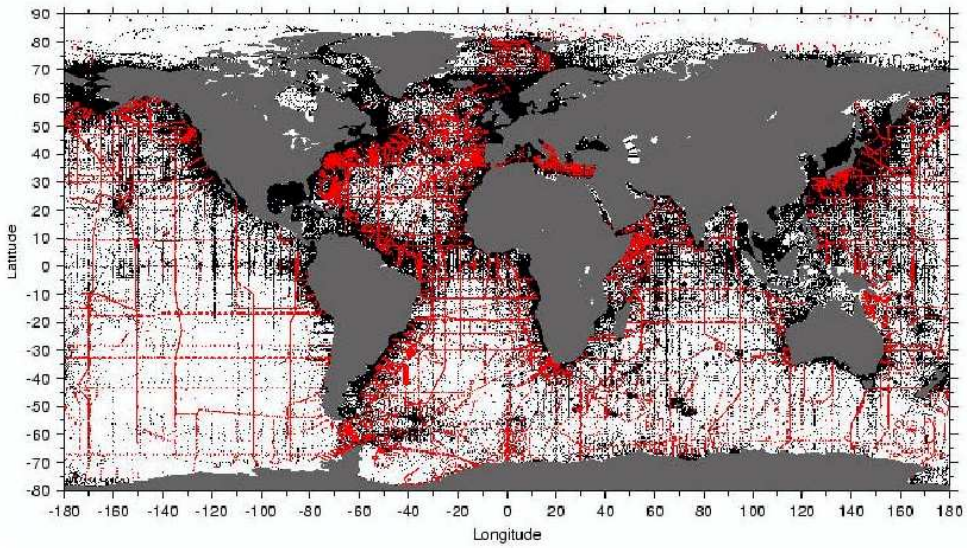

Figure 2.2.: *Gouretski and Koltermann (2004), historical (black) and reference (red) profiles from the combined data set.*

The data basis is composed of several data sets, but the WOD98 database was used as a main data source for the production of the WGHC data field since the WOA01 was not available when compilating the WGHC. Also hydrographic observations of the WOCE WHP were used, which were made during 1990 to 1998. In addition, a substantial number of profiles have been obtained from several institutes in Germany, Russia, France and USA. An overview of the data density used for evaluating the WGHC is shown in Figure 2.2 (Gouretski and Koltermann, 2004, their Figure).

The quality evaluation of the WGHC dataset involves the different quality checks done by the basic datafields. In addition, the data were further validated by using the method developed by Gouretski and Jancke (1999). However, several error sources exist, e.g.

random errors, systematic errors, offsets and biases. For further information the reader is referred to the documentation of the WGHC dataset (Gouretski and Koltermann, 2004). Objective analysis (e.g. Bretherton et al., 1976) is used in order to compute the climatological hydrographic field on a regular grid. The data are distributed onto a 0.5° resolved grid and 45 depth levels.

2.1.5. A drifter-derived climatology of near-surface currents

During the Surface Velocity Program (SVP) observations have been collected by standardized satellite-tracked surface drifting buoys (Niiler, 2001). The drifter observations are centered at a depth of 15 m and were made in the period October 1990 to February 2004. The database consits of 728 drifter of which 86% was collected by drifters deployed within the tropical Atlantic. Lumpkin and Garraffo (2005) used this database to evaluate a drifter-derived climatology of the world's near-surface currents. Pseudo-Eulerian current estimates are derived from the Lagrangian observations. Therefore, the measurements are grouped in spatial bins and within each bin, treated as a time series composed of a time-mean value, annual and semiannual harmonics and residuals, using inverse techniques

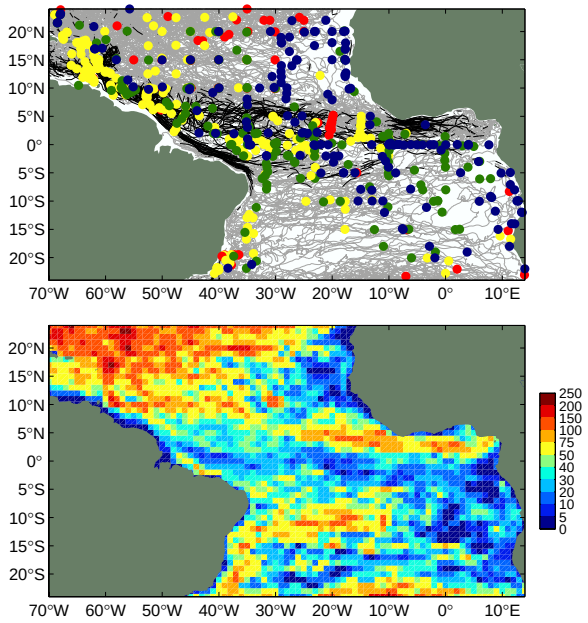

Figure 2.3.: *Lumpkin and Garzoli (2005), Top: Trajectories of drifters moving at speeds < 50 cm/s (light gray) and faster (black). Deployment locations are indicated by colored bullets: 1990 to 1997 (red), 1998 to 1999 (yellow), 2000 to 2001 (green) and 2002 to February 2004 (blue). Some recent deployments overlay older ones. Bottom: Density of observations (drifter days per square degree)*

(Lumpkin, 2003). Thus, seasonal biasing of the means is avoided where the seasonal cycle is strong (e.g. NECC domain, equatorial band). The pseudo-Eulerian currents are mapped at a spatial resolution of 1°x1°. The methodology was tested using drifters in a 1/12° simulation of the tropical Atlantic ocean which demonstrates that the dataset successfully resolves the mean currents and its seasonal variations throughout most of the tropical Atlantic (Lumpkin and Garzoli, 2005).

2.2. Altimeter measurements

The mapped sea level anomalies (MSLA) used in this study were produced by SSALTO (Segment Sol multimissions d'Altimétrie, d'Orbitographie et de localization précise, Ssalto multimission ground segment) / DUACS (Data Unification and Altimeter Combination System) as part of the Environment and Climate European Enact project and distributed by AVISO (Archiving, Validation and Interpretation of Satellite Oceanographic data), with support from CNES (Centre National d'études Spatiales, French space agency). Among the available products one can distinguish between two temporal classes. Two near real time (NRT) products which are available within one week and one month after the date of measurement and also delayed time (DT) products. These are reprocessed products which are updated nearly every six months. In this study the DT products are used because the DT-MSLA products are more precise than respective NRT-MSLA products (AVISO, 2004). The time interval of the merged product is 7 days on a 1/3° Mercator grid, starting in October 1992. For the named grid, the resolution for latitude and longitude is identical and varies with the cosine of latitude (e.g. from 37 km at the equator to 18.5 km at 60°N/S).

The merged products were obtained from TOPEX/Poseidon (T/P), ERS-1 and -2, Jason-1 and ENVISAT altimeter missions. The Altimeter data have many sources of error. They need to be corrected for instrumental errors, environmental perturbations (wet tropospheric and ionospheric effects), the ocean wave influence (sea state bias), the tide influence (ocean tide, earth tide and pole tide) and inverse barometer effect. All these corrections are computed for each altimeter measurement by various methods and model fields of auxiliary data. The ERS altimeter corrections were updated to make T/P and ERS corrections homogeneous. For more details on corrections see Traon and Ogor (1999).

Merging multisatellite data sets requires homogeneous and intercalibrated sea surface hight (SSH) data sets. The latter are obtained by performing a global crossover adjustment of ERS orbit, using more precise T/P data as a reference (Traon and Ogor, 1999). Then consistent sea level anomalies (SLA) data from different satellites are extracted by using repeat-track analysis (Ducet and Traon, 2000). They are relative to a 5-year-mean (January 1993 to January 1998). Then the SLA time series are filtered, using a linear Lanczos low-pass filter in order to reduce measurement noise. The MSLA are obtained using the mapping method detailed in Ducet and Traon (2000). The method is a global suboptimal space/time objective analysis that takes into account along-track correlated errors. The data error includes white noise measurement and long wavelength errors (LWE) due to residual orbit errors which are not negligible in low-energy regions (Traon et al., 1998). The maps are then computed, taking LWE into account and using realistic correlation scales of the ocean circulation (see Ducet and Traon, 2000).

The intercalibrated and homogeneous gridded data sets have an excellent global compatibility, the root mean square of their differences being less than 3 cm in low ocean variability regions. In high-variability areas the differences are mainly explained by the mapping errors (Ducet and Traon, 2000). A comparison with WOCE surface drifters revealed that the combined product captures the spatial structure of the observed variability (Ducet and Traon, 2000). However, the combined SLA maps provide more homogeneous and reduced mapping errors than either individual data set and a more realistic sea level than maps of T/P data alone.

2.3. FLAME model simulations

The model simulations used in this study are part of the FLAME-hierarchy (Family of Linked Atlantic Ocean Model Experiments). The FLAME model used here is an eddy resolving resolution version (1/12°) and encompasses the Atlantic Ocean from 70°N to 18°S. The model is based on a configuration of the Modular Ocean Model (MOM) (Pacanowski, 1995), from which a parallelized code version of MOM (Redler et al., 1998) is refined by C. Eden (SPFLAME).

Primitive equations build the physical basis of the model (Müller and Willebrandt, 1989) and the equations are discretized on an Arkawa-B grid (Arkawa and Lamb, 1977). The model uses an isotropic grid, i.e. the resolution for latitude and longitude is identical and varies with the cosine of latitude. 45 depth levels are used, with spacings of 10 m in the uppermost levels. Vertical spacing increases to 250 m at 2500 m depth and remains constant up to a maximal depth of 5500 m. The topography is taken from the ETOPO5 (1988) dataset. Open boundary conditions are implemented at 18°S and at 70°N. The model's spin up phase lasted for 10 model years. The spin up started from a state of rest and a combination of the datasets of Levitus and Boyer (1994b) and Boyer and Levitus (1997), and it is forced by the ECMWF climatology which will be described below. The variable surface forcing is then realized by adding the monthly net heat flux and wind stress anomalies to the ECMWF-based climatology data.

The model simulations FLAME 1 and FLAME 2: Both model configurations used in this study are based on the general model features of the 1/12° FLAME model as described above. They only differ in their surface forcing. The surface forcing in the climatological state of the ocean model contains monthly mean fields which originate from a 6-hourly analysis at the ECMWF of the years 1986 to 1988 (Barnier et al., 1995). Those monthly mean fields are averaged to obtain a climatological year of surface forcing and then they are linearly interpolated onto the model time. This model simulation with climatological forcing is named FLAME 1 hereinafter for the purpose of this study. The thermal and wind forcing of the second model simulation used here is based on daily fields of high resolution ECMWF data for the years 2001 to 2004 (Eden and Jung, 2006) and is named FLAME 2 hereinafter. Thus, interannual variations can be simulated which allows a direct comparison of the large amount of observational data collected during this time period.

For both surface forcing fields mentioned above, the surface boundary condition for heat

is formulated by Haney (1971) and includes a relaxation to climatological sea surface temperature (SST). The relaxation itself is directly derived from a linearized form of the bulk formula for the surface heat flux (Barnier et al., 1995). The freshwater flux into the ocean is realized as a restoring to climatological surface salinities after Levitus and Boyer (1994b) and Boyer and Levitus (1997) at a constant timescale of 15 days in the surface grid boxes for both model simulations FLAME 1 and FLAME 2. The reason not to use a boundary condition similar to the heat flux formulation are large uncertainties in the available precipitation and river runoff datasets.

3. General description of intraseasonal variability at 11°S

Based on mooring data at 11°S, satellite altimeter data as well as simulations from a numerical 1/12° Atlantic model, the local intraseasonal variability (ISV) close to the western boundary and its connection to the interior is analyzed. First, basic features of variability in the mooring array data will be described with a focus on intraseasonal time scales. Then, the spectral characteristics are presented from several data sources which allow for the identification of different dynamic regimes. Subsequent comparisons of differently forced model simulations deliver first insights into possible forcing mechanisms on the domain of investigation.

3.1. Combined current records of the mooring array at 11°S

The current measurements of the mooring array at 11°S close to the western boundary are used to analyze intraseasonal variability of the western boundary current regime. More than four years of current measurements are available, precisely from March 2000 to August 2004. Due to monitoring problems such as corrosion of connectors or damages by the fishery, some extensive gaps exist in the records. However, in this section the original records are analyzed in order to discuss ISV. The detailed configuration of the mooring array is described in section 2.1.1.

To determine the mean background current regime at 11°S an average section is calculated from the available original current records. The current vectors are rotated clockwise by an angle of 36° parallel to the coast. The arithmetic mean of alongshore velocity is derived at every instrument depth and finally interpolated onto a regular 5 km by 20 m grid using Gaussian weights (Figure 3.1). The instrument depths at mooring K1-K4 are marked in Figure 3.1. A domain of mean northeastward velocity exists for which maximum values are measured at about 250 m depth at K2 and K1. The northeastward velocities are associated with the NBUC, which is part of the interhemispheric exchange as the upper limb of the MOC. The measurements at K3 in the upper 500 m are located at the eastern flank of the NBUC. K4 is positioned outside the equatorward boundary current. Farther offshore a weak mean southward flow exists at about 500-1500 m depth which is only covered by mooring K4. At 1500-3500 m depth a poleward current core exists which captures the southward transport of deep water from the north, namely the DWBC. The average current core of the DWBC is located at mooring K3. The mooring K5 offshore has only got a two-year-long measurement and the observations are confined to deeper layers below 1500 m while only little flow exists at K5.

To analyze ISV in the near surface layer measurements at 100 m depth will be discussed and corresponding current anomalies are shown in Figure 3.2 at different mooring positions

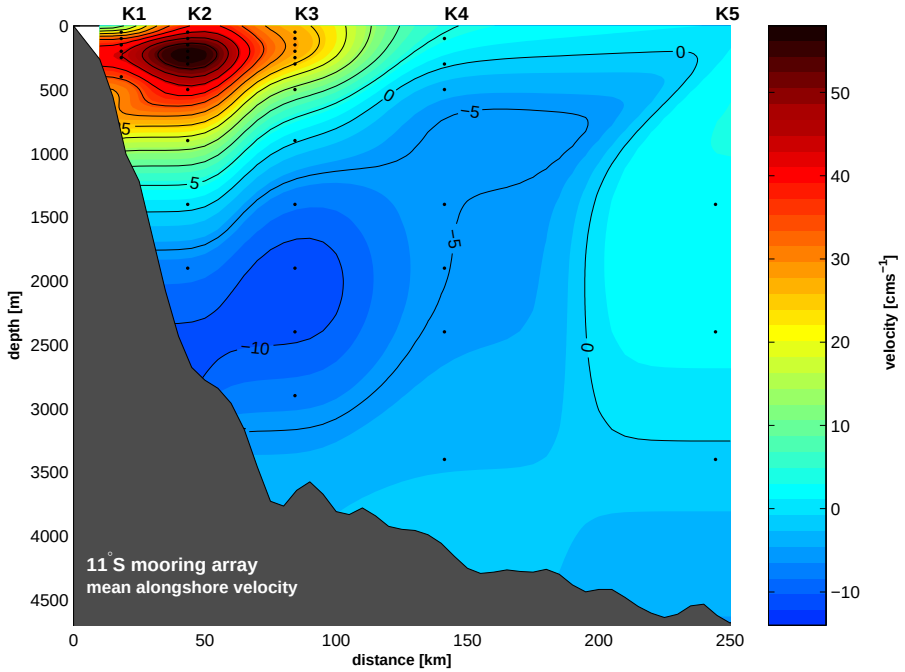

Figure 3.1.: *Mean section along 11°S derived from the original mooring array alongshore (36 deg true) records at positions K1-K4 from March 2000 to August 2004. Mooring positions are marked in Figure 2.1 (section 2.1.1). Topography is obtained from DVS data of different cruises.*

K1 to K4 for the years 2000 to 2004. The time series are 40-hour low-pass filtered to eliminate tidal effects and the current vectors are again rotated clockwise by an angle of 36° parallel to the coast. The mean velocities as shown in Figure 3.1 are subtracted, respectively. However, the anomalies at the nearshore position K1 show mainly high-frequency variability. Velocity changes sign two to three times a month and the fluctuations exceed 50 cm/s amplitude. Besides these dominant high-frequency fluctuations, variability exists with periods of 2-3 months (e.g. boreal spring to summer 2002). The dominant signal at K2 is characterized by fluctuations with periods of about 2-3 months similar to K1. The amplitudes of the high-frequency (< one month) signal diminish at K2 which consequently means that these fluctuations are confined to the near boundary region. Further offshore two to three monthly fluctuations are again the dominant signal but those amplitudes scale down with increasing distance from the NBUC current core.

The spectral distributions of the current records at 100 m depth at mooring position K1 to K4 are shown in Figure 3.3. As mentioned before gaps exist during the deployment period for several reasons (Figure 3.2). Consequently, sections of the time series without interruption are used for spectral analysis. The power spectral density is calculated for each complete part of the combined current meter records with comparable window length and then the average power spectral density is composed in order to determine reliable spectral distributions at each mooring position. For the spectral average the short measurement periods in the years 2000 and 2001 at K2 are neglected for the power spectral density estimates. Finally, the power spectral density of the cross-shore and alongshore component are summed. In addition, the 95% significance level is shaded for the single spectra at

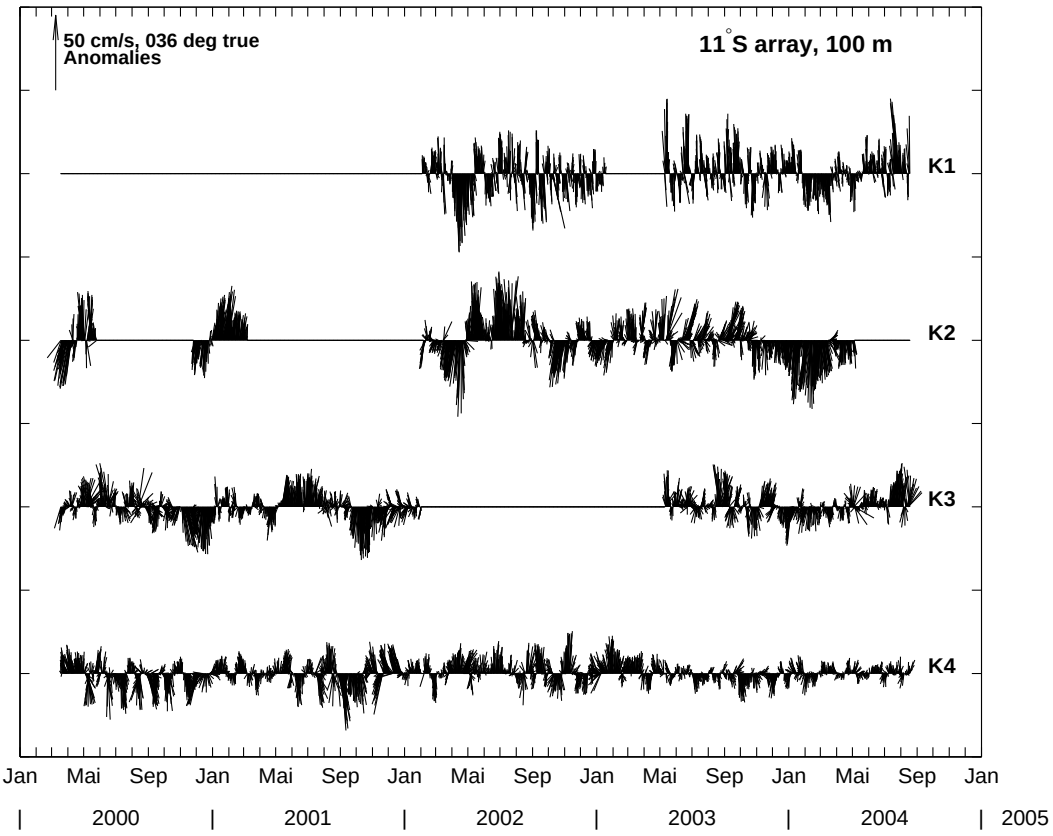

Figure 3.2.: *Combined vector time series of 40-hour low-passed current anomalies at 100 m depth from March 2000 to August 2004. Records at K1 to K3 are taken by upward looking ADCPs, at K4 by acoustic current meter. Mooring positions are marked in Figure 2.1 (section 2.1.1). Data gaps are due to lost instrumentation. The time series are rotated 36° parallel to the coast.*

position K1-K4. In the lowest panel of Figure 3.3 the spectral distributions are plotted together in order to discuss differences and similarities at the four mooring positions in more detail.

Most variance exists in the spectral distribution in the core of the NBUC (K2) in the low frequency range and at the nearshore position K1 in the high frequency range. The spectra at K3 and K4 show smaller energy amplitudes. As mentioned before, weekly to biweekly variability dominates mainly the velocities at the nearshore positions K1 and K2. This part of the spectra shows sharp bounded peaks indicating that only a limited number of frequency components contribute to the signal (e.g. tidal effects would produce line spectra). Amongst others, Wunsch and Gill (1976) pointed out some unexpected peaks in nearshore sea level records from the tropical Pacific, which seem to have a similar appearance on roughly the same periods. They show that the oscillations are due to oceanic resonance of wind variability.

In contrast, a rapidly decaying autocorrelated function implies a broad spectral distribution and a large number of frequency components in the original waveform (Emery

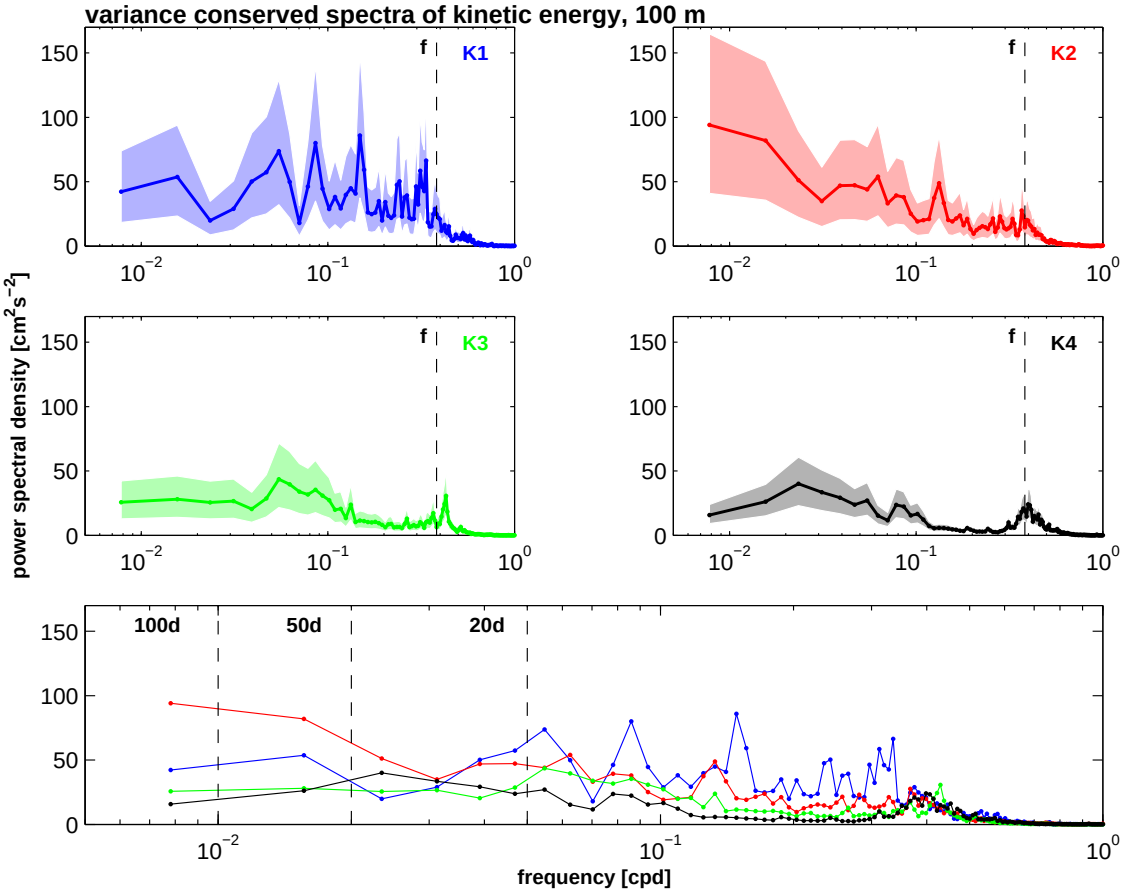

Figure 3.3.: *Power spectral density for combined time series at 100 m depth of stations K1 to K4 from March 2000 to August 2004 (Figure 3.2). The 95% confidence interval is shaded in corresponding colors. The lower panel shows the power spectra together.*

and Thomson, 2001), which means the broader the spectral peak the more frequency components contribute to the signal in the spectra. The spectral distributions at K3 and K4 are broad spectra at which the highest variances are present at periods of 40-60 d and at 2.48-2.54 d. The inertial period at 11°S corresponds to $1/f = 2.6$ d and is marked with a dashed line in the single spectral distributions of Figure 3.3. Besides the spectrum at K3, all spectral distributions peak at inertial frequency f. Consequently, inertial oscillations exist and are an important part of turbulent kinetic energy. K3 peaks at about 2.3 d period which is somewhat smaller than the intertial period, but it is not clear why the low frequency peak does not match the inertial frequency. K3 is positioned in the eastern flank of the NBUC and local effects may drive a modulation on the inertial oscillations.

The distribution of power spectral density with periods of 50-100 d is found to be strongest in the core of the NBUC (K2) and at the nearshore position K1. At K3 and K4 the values remain at a low level. This means that inside the NBUC 50-100 d variability is dominant at 100 m depth. In this context the enhancement of the discussion with the help of the shaded 95% significance interval becomes important. Particularly at K2 a broad significance interval is present at 50-100 d periods and it is important that for any

implication a simultaneous discussion of the time series is essential. As already discussed the anomalies at K2 show fluctuations on monthly to bimonthly periods (Figure 3.2). Compared to the offshore positions the amplitudes of the fluctuations are higher which is consequently evident in the spectral distribution of Figure 3.3. On the other hand the 95% significance interval in the low frequency range clearly proves the existence of corresponding high variance and documents the sharp bounded spectral lines with periods of 5-20 d.

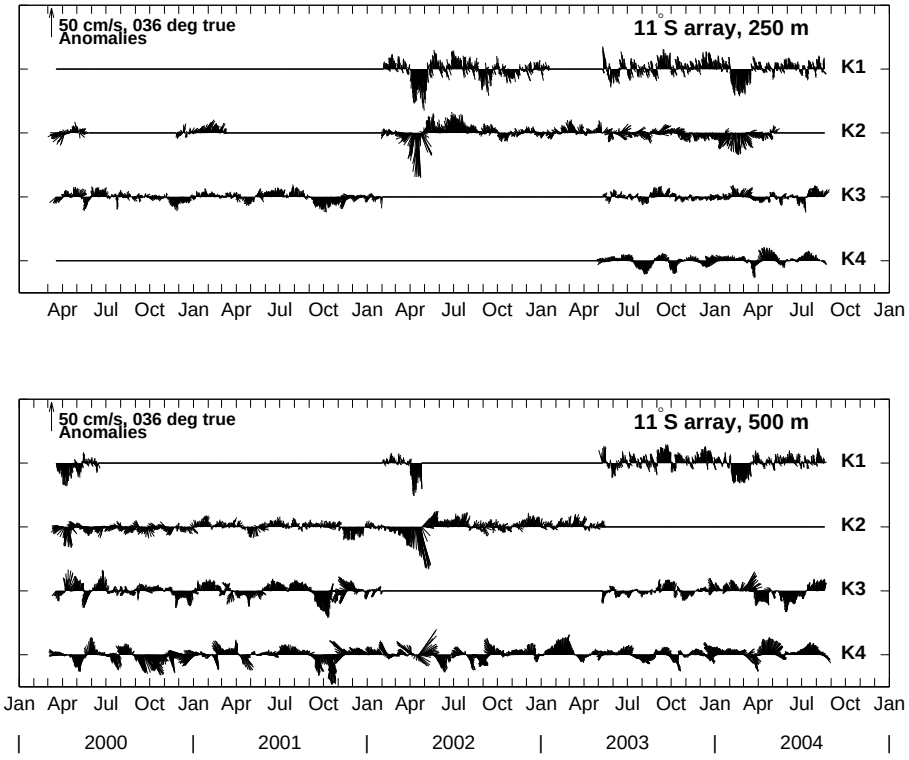

Figure 3.4.: *Combined vector time series of 40-hour low-passed current anomalies at 250 m and 500 m depth from March 2000 to August 2004. Records are taken by FSI-ACM (Falmouth Scientific Instruments - Acoustic Current Meter) or Aandera RCM (Rotor Current Meter). Mooring positions are marked in Figure 2.1 (section 2.1.1). Data gaps are due to lost instrumentation or intermitted deployment.*

To characterize the observed signals on intraseasonal timescales with rising depths, combined vector time series of 40-hour low-passed current anomalies at 250 m and 500 m depth are shown in Figure 3.4. Mean velocities are again subtracted, but show that the time series at 500 m depth measure the lower edge of the NBUC at K1 to K3 and at K4 a mean southward flow exist at 300-900 m depth offshore from the NBUC (Schott et al., 2005, and Figure 3.5). At 250 m the amplitudes of the anomalies are largest at the nearshore positions K1 and K2. Strong anomalies exist in spring 2002 and 2004 with amplitudes up to 50 cms^{-1} which are clearly bounded to the nearshore positions. At K3 and K4 the anomalies are low and fluctuate on higher frequencies than those at K1 and K2. The anomalies at 500 m depth show similar characteristics but with higher amplitudes at the offshore position. Two to three monthly periods dominate the variability at K3 and K4. Furthermore the amplitudes of the anomalies at the nearshore positions diminish with depth, especially

at K1. As seen in the anomalies at 100 m depth (Figure 3.2) weekly to biweekly current reversals are the dominant mode of variability in the western flank of the NBUC. At 250 m and 500 m depth those fluctuation patterns exist as well but they are superimposed by monthly to bimonthly variability. The amplitudes of the anomalies at the offshore position become stronger with increasing depth, especially at K4 where the anomalies at 100 m show two to three monthly fluctuations but at 500 m depth this signal is strongest.

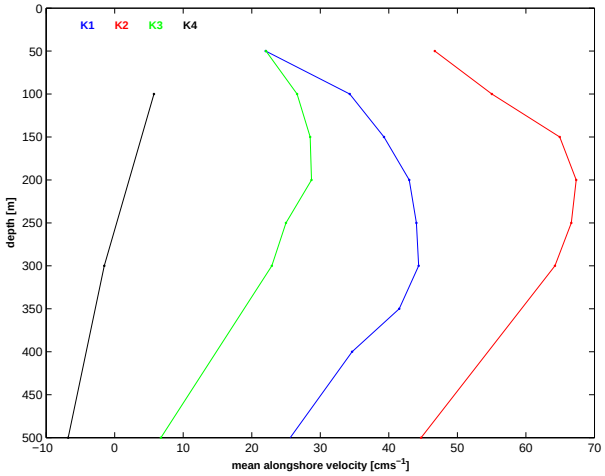

Figure 3.5.: *Mean alongshore velocities distributed with depth at mooring positions K1 to K4 for the upper 500 m. These mean values are subtracted from each corresponding time series to obtain anomaly time series (Figures 3.2 and 3.4).*

In addition to the mean section in Figure 3.1 mean values of alongshore velocities at K1 to K4 for the upper 500 m are shown in Figure 3.5. These values have been subtracted from the time series, respectively, in order to discuss fluctuation patterns of anomalies (Figures 3.2 and 3.4). Obviously the measurements at K1-K3 bracket the NBUC whereas the velocities at K2 are strongest. K1 is located in the onshore flank and K3 in the offshore flank of the NBUC, from which the mean alongshore velocities are stronger at position K1 (Figure 3.5). The mean values at K4 are negative which shows that K4 lies outside the NBUC. Furthermore the NBUC becomes maximal at 200-250 m depth at all three mooring positions K1-K3.

The variance conserved power spectral density of kinetic energy at mooring positions K1 to K4 at 250 and 500 m depth has been calculated based on the anomalies presented in Figure 3.4 and calculated similar to the spectral distributions at 100 m depth (Figure 3.6). For the sake of clarity the corresponding 95% significance intervals are not shaded. The sharp peak at 20 d, as it was found at 100 m depth (Figure 3.3), can be seen at 250 m and 500 m depth at the nearshore positions K1 and K2 (Figure 3.4). The power spectral density values of the peaks decrease with increasing depth which means that those signals are confined to the near surface layer. Furthermore the prominent variance signal near inertial frequency diminishes with depth.

As already suggested from the qualitative discussion of the anomalies (Figure 3.4) fluctuations with periods of 50-100 d are more dominant at 250 m and 500 m depth,

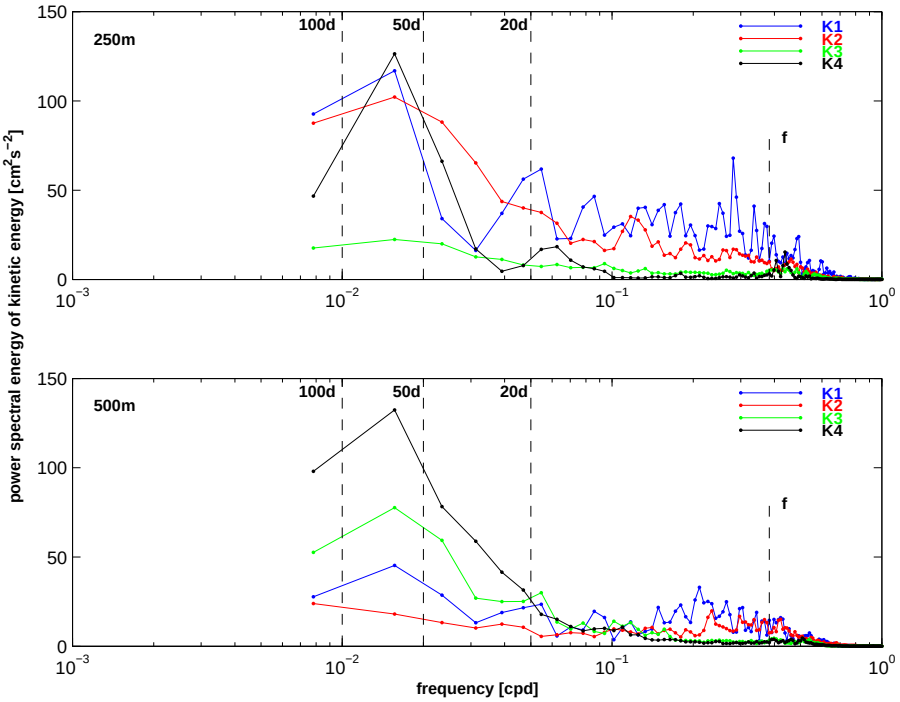

Figure 3.6.: *Variance conserving spectra of kinetic energy at 250 m and 500 m depth for combined time series of stations K1 to K4 from March 2000 to August 2004 (Figure 3.4).*

especially further offshore. Although a broad 95% significance interval exists for the spectral distribution at K4 at 250 m (not shown) the peak with periods of 50-100 d contains most of the variance in the entire spectrum. This shape reoccurs at 500 m depth and the significance interval minimizes (not shown) since more than four years of measurements are available at K4. This means that the two to three monthly fluctuations at K4 increase with increasing depth. A similar development with increasing depth is present at K3. The nearshore positions are characterized by a different behavior. The variance becomes maximal at 50-100 d periods and the mean alongshore velocity shows maximal values at 200-250 m depth (Figure 3.5). The variance values diminish at those depths where the mean background velocities decrease, namely at 100 m and 500 m depth. The result shows that two modes of variability exist with periods of 50-100 d. One is confined to the area of the NBUC and becomes maximal in the core of the NBUC at 250 m depth. The second one is dominant outside the NBUC and the variance increases with increasing depth.

The latter result can be supported by the distribution of eddy kinetic energy (EKE) (Figure 3.7). The EKE is computed as

$$EKE = \frac{1}{2}(u'^2 + v'^2)$$

where $u' = u - \overline{u}$ and $v' = v - \overline{v}$ are the deviations from the time averaged zonal and meridional velocities, $\overline{u}$ and $\overline{v}$, respectively. The time averaged velocities are calculated at each instrument depth. Then the EKE is derived and finally gridded via objective mapping. However, in the upper 1000 m two modes of variability exist as suggested by the spectral distributions in the upper 500 m (Figures 3.3 and 3.6). One is confined to

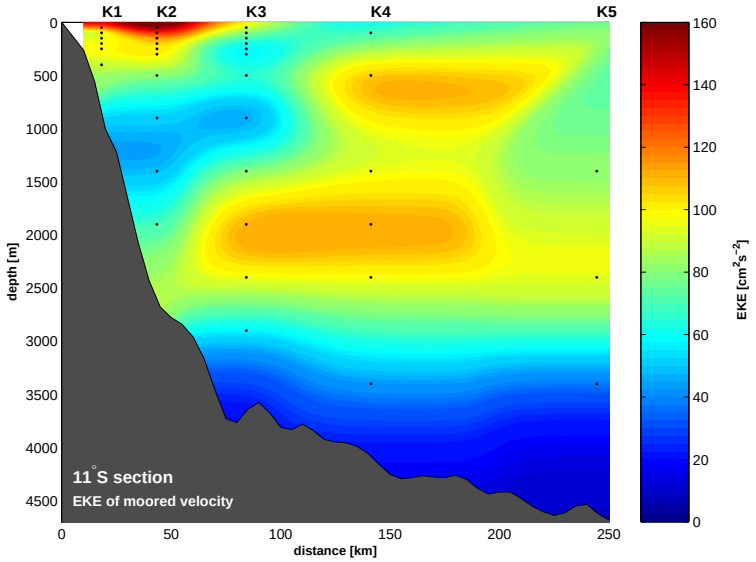

Figure 3.7.: *Eddy kinetic energy (EKE) of moored velocity at 11°S (e.g. Figure 3.2). Instrument depths are marked with a black dot, respectively. The 11°S topography is derived from shipboard measurements of different cruises (M. Dengler, pers. comn.).*

the area bracketed by the NBUC from which highest values of EKE are found in the core of the NBUC (K2). The second area of high EKE lies at approximately 500 m depth and further offshore at mooring position K4 which is orientated clearly outside the NBUC domain. Obviously only one instrument at K4 at 500 m depth reveals peaking EKE and consequently making this result less robust. However, one has to keep in mind that this result is based on one of the longest time series (more than four years of measurements, see Figure 3.2). Furthermore a comparison of the observations to model results will support the existence of a localized EKE maximum (see section 3.4).

In addition, a maximum in the EKE distribution exists at 1500-2500 m depth and is attributed to mesoscale variability in the DWBC regime. Dengler et al. (2004) showed from mooring array data at 11°S, direct water mass observations and results from a numerical ocean circulation model (similar to the one used in the following sections) that the Atlantic DWBC breaks up at 8°S and the North Atlantic Deep Water (NADW) migrates southward via mesoscale eddies along the western boundary. In this study, an analysis of the eddy-resolving general circulation model shows that baroclinic and barotropic instabilities are responsible for the DWBC eddy generation. At this point it is not clear whether the 50-100 d signal observed in the upper 500 m is triggered by the eddy variability in the NADW layer. For the variability in the NBUC domain Schott et al. (2005) also showed that a dominant fluctuation with a period of about two month exists. In order to establish a discussion of a possible connection to the variability in the DWBC layer they correlated the NBUC transport time series with all other current time series of the 11°S array. They showed that the NBUC variability is restricted to the upper layer and is uncorrelated to the variance in the NADW regime. Additionally in Schott et al. (2005), an empirical orthogonal function (EOF) analysis has been determined from the alongshore current components. The pattern of the first EOF is restricted to the domain of the NBUC. Furthermore different analyses have shown that the variability in the intermediate depth

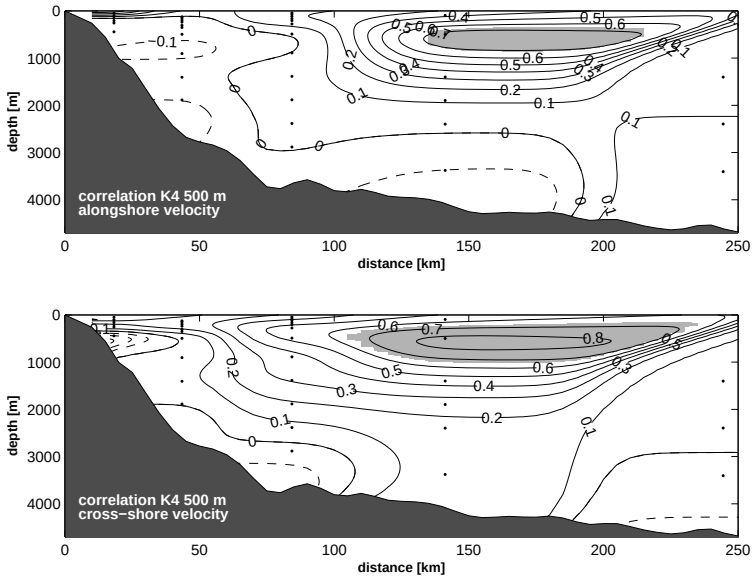

Figure 3.8.: *Correlation of alongshore and cross-shore time series at K4 at 500 m depth with all alongshore and cross-shore current component records of the array (dots), whose gaps are filled via EOF interpolation (see text for more detail). The area within the 95% significance level is shaded gray.*

layer offshore is not affected by high fluctuations in the DWBC layer (M. Dengler, personal communication). A comparison of numerical model results will underline this discussion (see section 3.4).

Although earlier investigations have shown that the variance in the NBUC domain is isolated from the mesoscale fluctuations at 1500-2500 m depth, the question remains whether the high variability outside the NBUC domain at 500 m depth (Figure 3.7) is affected by the deep rings. As already mentioned, only the long time series in 500 m at K4 shows large EKE with values comparable to those in the DWBC regime (Figure 3.7). Thus, the 500 m alongshore and cross-shore time series at K4 are used to correlate with all other available alongshore and cross-shore time series of the mooring array (Figure 3.8). The calculations are based on the combined moored current records with gaps filled via EOF interpolation. A description of the interpolation method can be found in the publication of Schott et al. (2005) and in section 3.2. The number of degrees of freedom (DOF) are determined with the method suggested by Bretherton et al. (1999) in order to obtain the 95% significance level of the correlation coefficients (shaded gray). It is important to mention that the calculation of Figure 3.8 includes a subsequent interpolation of the correlation values onto a 5 km by 20 m grid using Gaussian weights. Therefore, areas of highly unrealistic correlations are evident where no data exist (i.e. at K5 in the upper 1000 m).

The correlation shows that the variance of the alongshore and cross-shore time series at K4 are isolated and are therefore neither linked to the variability in the DWBC layer nor to the NBUC domain. This indicates that the observed modes of variability (Figure 3.7) are not affected by the deep rings. However, Figure 3.8 also leaves space for

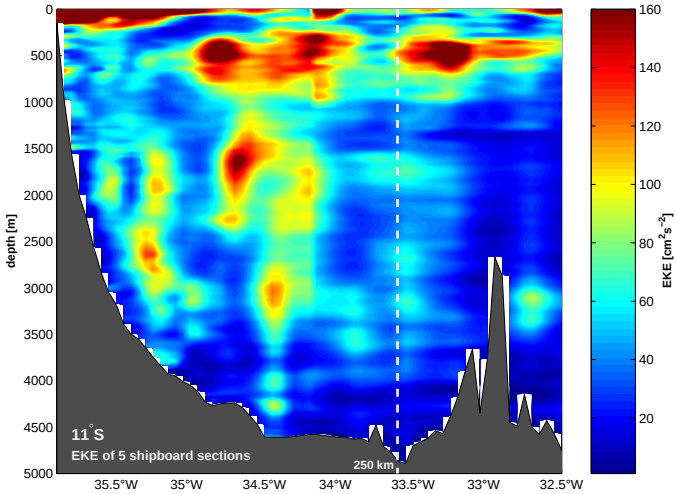

Figure 3.9.: *Eddy kinetic energy (EKE) calculated from five repeated shipboard current-profiling sections along 11° S (see section 2.1.3). The distance 250 km off the coast is marked (white dashed line). The 11° S topography is derived from ship measurements of different cruises (M. Dengler, pers. comn.).*

scepticism since the fluctuations measured from current meters at K4 at 500 m depth are completely isolated. Correlation values exceeding the 95% significance level are restricted directly to the measurements at 500 m depth offshore which indicates that the dynamics recorded at this depth offshore are completely different from the measurements of the surrounding records. Thus, it is interesting to see whether comparable signals are evident in different data sources. In Figure 3.9 the EKE is evaluated using five repeated shipboard current-profiling sections along 11°S. Until 250 km distance off the coast, signals of high EKE are evident in the near surface layer close to the western boundary, at depths of about 400-700 km offshore and partly in the domain of the DWBC regime. Further offshore, the signals in the near surface layer as well as at depths of the DWBC diminish and only at intermediate depths values of EKE remain high. Although the latter result is derived from only few measurements, the distribution of EKE along the section is comparable to the EKE distribution evaluated from the mooring array data. As will be shown later, the numerical model results will support the EKE estimates (section 3.4).

Summarizing briefly, the analysis of combined current records at 11°S near the western boundary shows that prominent maxima of EKE exist. One is confined to the NBUC domain. Spectral analysis of the combined current records showed that maximal EKE values are associated with 50-100 d period fluctuations. Several investigations have shown that these fluctuations are not affected by variability in deeper layers (Schott et al., 2005). The second EKE maximum is located outside the NBUC at intermediate depths. It is important to note that these fluctuations are only measured at K4 at 500 m depth. However, the spectral distributions at K4 at 500 m show that the EKE maximum is due to 50-100 d fluctuations. A correlation analysis shows that the variability at 500 m at K4 is neither influenced by the ISV in the NBUC domain nor by the fluctuations in deeper layers.

In the following sections further investigations will be done to detect the shape of the

observed signals. Transport calculations derived from the mooring array data will be discussed. In addition, altimeter data and results from a numerical ocean model will be used to detect the origin of the variability.

3.2. Transport calculations

The anomalies in Figure 3.2 and 3.4 show that temporal gaps are present in the 11°S mooring array records which make transport calculations difficult. Several methods are possible to fill the gaps. Here the method presented by Schott et al. (2005) is used which allows to compare the results obtained here with earlier estimates. First, temporal gaps are filled with zeros and EOFs are calculated from the combined current records. The time series show no obvious trends and the statistics do not change which means that calculating EOFs from the incomplete records seems to be justified (Schott et al., 2005). The first four EOFs are used to fill the record gaps which explain 83% of the total variance. The first EOF pattern represents most of the NBUC variability. As the spectral analysis in section 3.1 has shown that the 5-20 d variability is mostly confined to the shelf region and consequently variability shorter than one week is not interesting for NBUC transport fluctuations, the interpolated time series are low-passed with a 10-day filter.

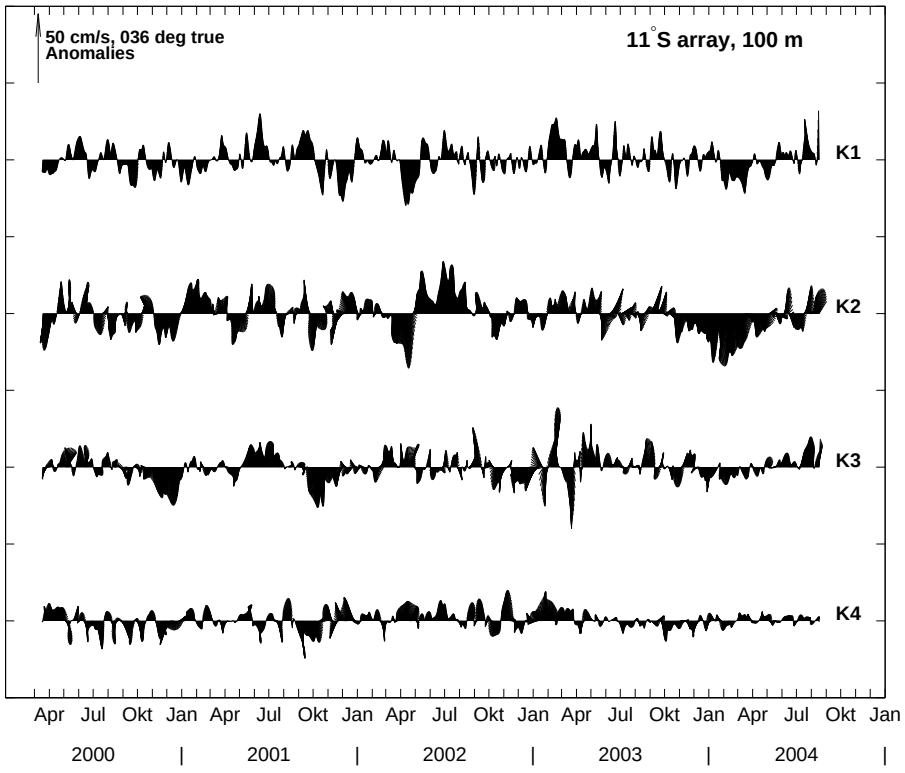

Figure 3.10.: *Combined vector time series of 40-hour low-passed current anomalies at 100 m depth from March 2000 to August 2004. Records at K1 to K3 are measured by upward looking ADCPs, at K4 by acoustic current meter. Mooring positions are marked in Figure (2.1, section 2.1.1). Data gaps are filled via EOF calculations (see Schott et al., 2005).*

The current anomalies at 100 m depth whose temporal gaps are filled via EOF analysis are shown in current vector plots in Figure 3.10. The zonal and meridional current vectors are again rotated parallel to the coast (36° true). The mean alongshore currents range from 5-60 cm/s for the different mooring positions which are similar to the mean values derived from the incomplete current records (section 3.1). Again, K2 is located in the core of the NBUC with maximal mean current. K1 and K3 measure in the eastern and western flank of the NBUC. K4 lies outside the NBUC. Variance reaches values from about 50 cm^2s^{-2} up to 150 cm^2s^{-2} which are generally lower than derived from the gappy and unfiltered current records. Additionally, EKE becomes again strongest at K2 but the values are lower than those calculated from the current records in Figure 3.2.

The current vector plots in Figure 3.10 show that variability with periods shorter than three weeks persits at the nearshore position K1. Highest anomalies are present at K2, predominantly with biweekly to three monthly periods. The offshore positions K3 and K4 are characterized by monthly to three monthly fluctuations. ISV differs in strength on interannual timescales. Nevertheless, prominent features of ISV are evident and the anomaly patterns seem to be similar compared to those in Figure 3.2. But the current vector plots also show that the anomaly fluctuations are smoothed and consequently the amplitudes are generally lower than those in Figure 3.2, probably due to the 10-day low-pass filtering. In addition, as already mentioned the variances and EKE show lower amplitudes compared to those of the incomplete records. The use of only the first four EOFs might explain as well the lack of low-frequency variability.

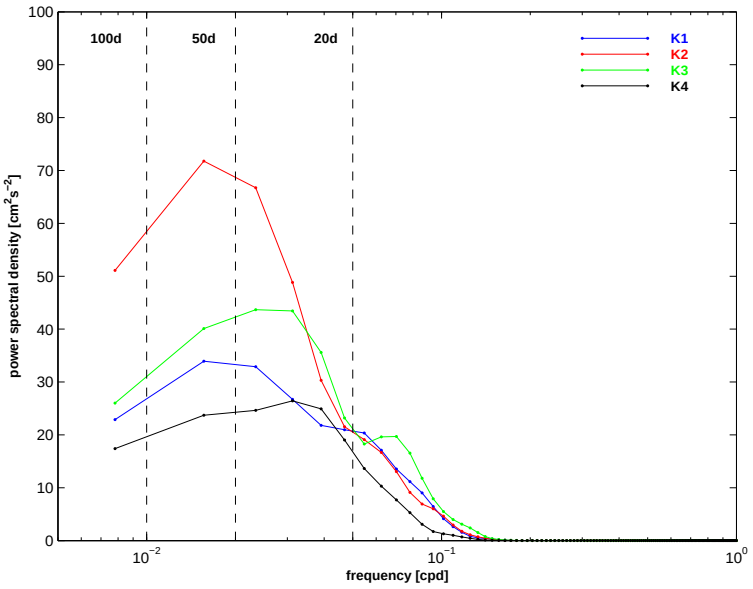

Figure 3.11.: *Variance conserving spectra of kinetic energy from near the surface (100 m depth) for combined time series of stations K1 to K4 from March 2000 to August 2004 (Figure 3.10).*

The power spectral density of the interpolated records at 100 m depth (Figure 3.10) for the years 2000 to 2004 is shown in Figure 3.11. For clarity the 95% significance intervals are not shaded. But the width of the intervals are of the order similar to the

one shown in Figure 3.3 for mooring position K4 since at K4 at 100 m depth a complete time series exists. The power spectral density is derived using the same NFFT (Fast Fourier Transformation) and window length as in Figure 3.3. Most of the variance is distributed between the periods of 50-100 d. The maximum is present at K2 where the mean NBUC is strongest at 100 m depth. At the eastern and western flank of the NBUC the variance decreases. These energy distributions are similar to those derived from the original records. Farther offshore the high power spectral density exists between periods of 20-50 d rather than between 50-100 d which is comparable to the results of Figure 3.3.

The spectral distributions derived from the interpolated current records at 250 m and 500 m depth reveal similar results compared to the power spectral density in Figure 3.6 of the previous section despite the fact that the variability is smoothed and the variance values are generally lower (not shown). Consequently the analysis has shown that the dominant mode of variablity remains in the interpolated dataset. Furthermore tests have been done in which additional gaps were introduced and reconstructed original time series closely resemble the original record (Schott et al., 2005). Thus, data processing from velocity records including an EOF interpolation works reasonably well and the transport estimates from those time series will include the prominent intraseasonal features observed in the mooring array at 11°S.

Figure 3.12 shows the mean moored alongshore velocity obtained from the interpolated current records. The alongshore velocity time series are mapped onto a 5 km by 20 m

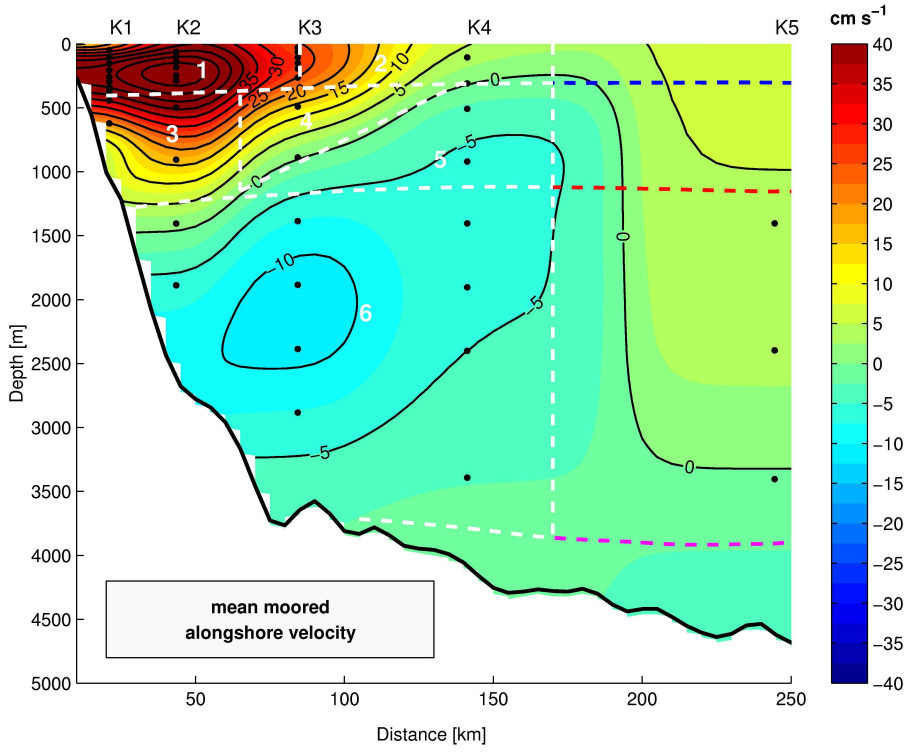

Figure 3.12.: *Section of mean alongshore velocity retrieved from moored records along 11°S (locations marked by dots) and boxes 1-6 (heavy dashed) used for calculating transport time series (after Schott et al., 2005).*

grid using Gaussian weights for every time step. Then the arithmetic mean is calculated. For the transport calculations six boxes as defined by Schott et al. (2005) are used and marked with dashed lines in Figure 3.12. Boxes 1 to 4 capture the NBUC transport, from which boxes 1 and 2 are centered in the upper NBUC, box 4 captures the offshore deep part of the NBUC and finally box 3 is located at intermediate depths close to the western boundary. The other two boxes are situated in the deeper layers and southward flow, i.e. the AAIW (box 5) and the NADW layer (box 6). The boxes are horizontally separated by the isopycnal surfaces σ_Θ =26.8 kgm^{-3} for the upper layer boxes 1 and 2, σ_Θ =32.15 kgm^{-3} for the boxes 3 and 5 and box 6 is bounded by the isopycnal σ_Θ =45.90 kgm^{-3} (Figure 3.12, dashed lines). In addition, box 4 is vertically bounded by an isotach of zero NBUC velocity. A note on transport errors has been done using numerical model results and the reader is referred to section 3.4 for more information.

At the beginning of this chapter, a section of mean moored alongshore velocity is shown which differs from the mean section presented in Schott et al. (2005) (Figure 3.1). This is due to the fact that in Figure 3.12 the arithmetic mean is calculated from the time series where gaps have been filled via EOF interpolation method as described above and in Schott et al. (2005). In Figure 3.1, mean values are evaluated from the incomplete time series. The gridding method using Gaussian weights is exactly the same in both sections. Only small differences are evident, e.g. enhanced mean velocities in the NBUC domain.

3.2.1. NBUC variability

The analysis of the combined current records in the previous section has shown that 50-100 d variability exists in the NBUC domain. The intraseasonal variance shows maximal values when the mean northward NBUC velocity becomes maximal and the variance decreases with increasing distance from the undercurrent core (e.g. K2 at 250 m depth, Figure 3.6). This indicates that a mode of ISV exists with periods of 50-100 d which is confined to the NBUC domain. For the purpose of discussing this result the NBUC transport anomalies (box 1-4) are shown in Figure 3.13 (a). The total NBUC transport at 11°S accounts for 25.7 Sv and is about equal to its transport at 5°S. Thus, the SEC bifurcation is located south of 11°S and the NBUC is fully established at 11°S (Schott et al., 2005). The NBUC transport anomaly time series shows strong fluctuations with amplitudes of about ± 15 Sv. Mostly fluctuations with bimonthly periods are dominant within the NBUC. The standard deviation from the mean is very high and accounts for roughly 20% in magnitude of the NBUC mean transport. From the anomalies it is not evident whether a seasonally modulation of ISV exists. The summed annual and semiannual harmonics show weak amplitudes and hardly exceed ± 5 Sv. Maximal northward NBUC flow derived from the annual plus semiannual harmonics occurs in boreal summer. A weaker maximum in winter is due to the influence of the semiannual cycle. Consequently the combined annual and semiannual cycle result in maximal northward NBUC transport in boreal summer and minimum in October to November (see also Schott et al., 2005, their Figure 12).

In addition, the variance conserving power spectral density in Figure 3.13 (b) is calculated from the transport time series in (a). The 95% significance interval is shaded blue. The discussion of the anomaly time series has already shown that a dominant mode of

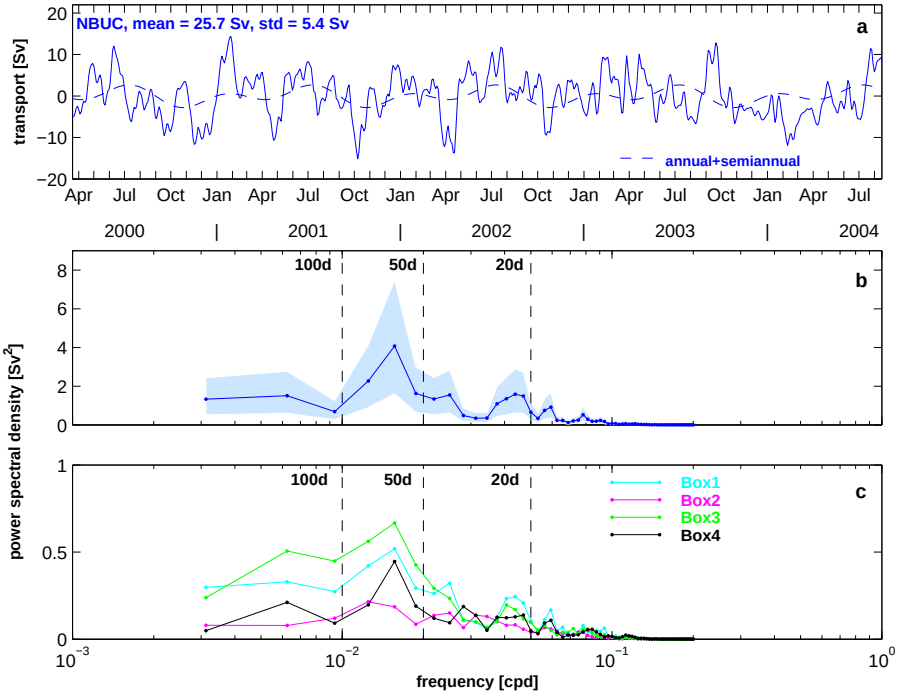

Figure 3.13.: *(a) NBUC transport anomalies at 11°S and the superposition of annual and semiannual harmonic (dashed line). (b) Variance conserving power spectral density for the NBUC transport in (a). The 95% significance level is shaded. (c) Variance conserving power spectral density for the transport time series of boxes 1-4 from March 2000 to August 2004 (see Figure 3.12).*

bimonthly variability exists which is confirmed by the power spectral density distribution in (b). Although a broad significance interval exists it is clearly shown that the dominant mode of ISV is present at periods of 50-100 d compared to the variances attributed to the rest of the frequencies in the spectrum. Figure 3.13 (c) shows the spectral distributions of the different transport boxes 1 to 4 for the entire deployment period which are disposed in Figure 3.12. Thus, it is possible to show which part of the NBUC domain influences the intraseasonal NBUC variability. For the sake of clarity the significance intervals are not shown. They are on a similar order of magnitude as in (b) since the same NFFT padding is used. As expected, the highest power spectral density values are achieved within box 1 and box 3 which capture the main currents related to the northward NBUC (Figure 3.12). The variance decreases towards the east (box 2 and box 4 transports), especially in box 2 which is located in the upper layer. Thus, the 50-100 d variability is clearly confined to the NBUC domain because the variance decreases with increasing distance from the current core.

Summarizing briefly, the analysis in the previous section has shown that a dominant mode of 50-100 d ISV exists in the domain of the NBUC. With the help of transport calculations this result could be manifested and additionally prove that the ISV is confined to the core of the NBUC. In the following sections basinwide datasets such as sea level anomaly from altimetry and results from a numerical model will help to describe the shape of the NBUC ISV.

3.2.2. Variability at intermediate depths outside the NBUC

The results obtained from the combined current records also show that a second mode of 50-100 d variability exists which is located outside the NBUC in the layer of the AAIW. Hence, the transport anomaly time series calculated from combined current records whithin box 5 which encompasses the southward flow in the AAIW layer offshore of the deep NBUC is plotted in Figure 3.14 (a). The box 5 transport anomaly time series shows strong fluctuations, ranging from about −9 Sv to 6 Sv. Longer period fluctuations of about 3 months exist as well as monthly to bimonthly periods which are characterized by lower amplitudes. Three monthly fluctuations show high amplitudes and a strong oscillating character (e.g. summer 2000, autumn 2003). Additionally the standard deviation of the box 5 transport is greater compared to the mean transport. This means that high variability dominates rather than a steady mean southward flow in the AAIW layer. The power spectral density derived from transport anomalies of box 5 (Figure 3.14 (a)) are shown in 3.14 (b). As expected, most of the variance is distributed at 50-100 d periods and

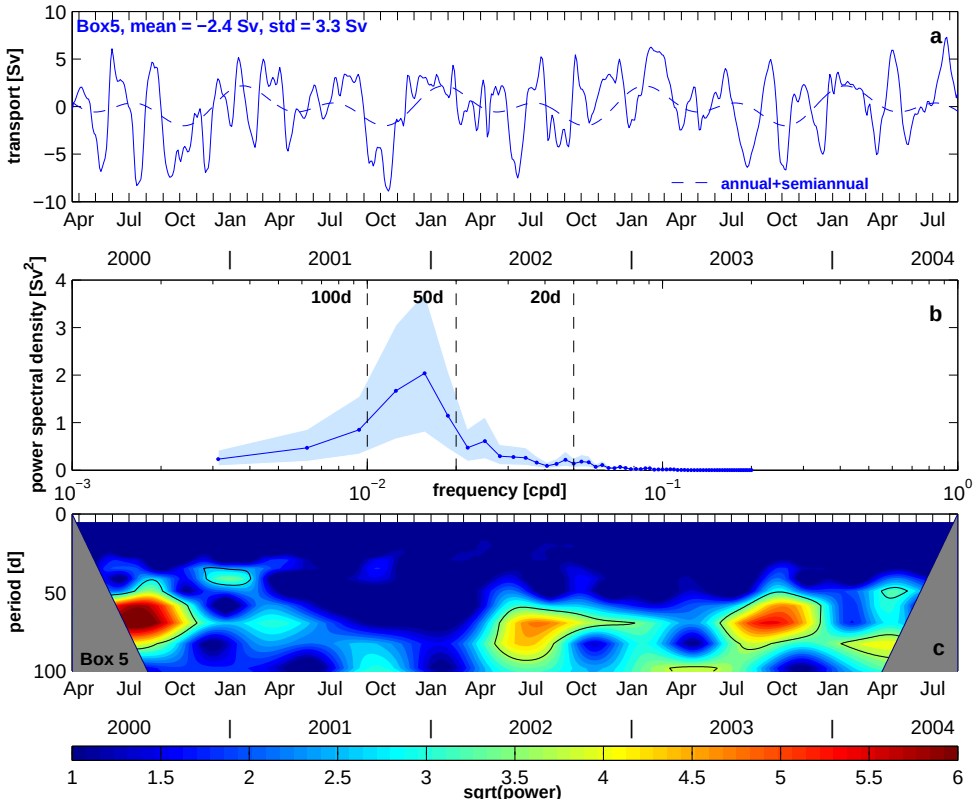

Figure 3.14.: *(a) Transport anomalies at 11°S of box 5 in the AAIW layer (see Figure 3.12) and the superposition of annual and semiannual harmonic (dashed line). (b) Variance conserving power spectral density for the box 5 transport in (a). The 95% significance level is shaded. (c) Square root (sqrt) of wavelet energy of the box 5 transport time series in (a). The 95% significance level is marked with a black line and the cone of influence is shaded gray.*

this result proves the qualitative suggestion. In this context it is important to note that the analysis of the combined current records in section 3.1 hints to an isolated mode of variability outside the NBUC in the AAIW layer which is captured by box 5. Other observations than presented in this section will indicate in the following that ISV in the box 5 transport time series underlies other dynamics than those in the NBUC or DWBC domain.

The superposition of the annual and semiannual harmonic reveals maximal southward transport in boreal autumn (Sept. to Oct.). The oscillating ISV events reoccurred from year to year (except 2001) and could be connected to the semiannual cycle (Figure 3.14, (a)). The distribution of transport anomalies of box 5 in the period-time domain will visualize the strong seasonal modulation of 50-100 d variability in the AAIW layer. Therefore a wavelet analysis is used (Figure 3.14 (c)). The wavelet transform determines both the dominant modes of variability and how these modes vary in time by decomposing a time series into time-frequency space. For the purpose of this analysis the so called Morlet wavelet is used, which consits of a plane wave modified by a Gaussian envelope (Lau and Weng, 1995). This wavelet is complex valued and has the advantage that it is able to detect both time-dependent amplitude and phase for different frequencies exhibited in the time series. In Figure 3.14 the cone of influence (COI) is shaded gray. Because one is dealing with finite-length time series, errors will occur at the beginning and end of the wavelet power spectrum. The COI is the region of the wavelet spectrum in which edge effects become important. Assuming a chi-square distribution (ξ_2^2) the 95% confidence level is determined by multiplying the background spectrum by the 95th percentile value for ξ_2^2 (Torrence and Compo, 1998). Before starting the time-frequency analysis the time series are normalized by their variance. The wavelet analysis in Figure 3.14 (c) shows that the variance is significantly (95%) high in boreal summer at periods of 50-100 d, except in the year 2001. Consequently, three events of strong ISV can be detected in the AAIW layer. Furthermore the wavelet energies show that the events are stronger in the year 2000 compared to the years 2002 and 2004 and thus differences in strength between the years exist. Although not significant, in 2001 50-100 d ISV is clearly evident.

As already mentioned the transport derived from current records within box 5 shows mean southward flow of about -2 Sv in the AAIW layer. A mean section derived from 9 individual shipboard velocity sections at 5°S at the western boundary shows that there is substantial southward flow offshore from the NBUC in the AAIW layer (Schott et al., 2005). This suggests the existence of an offshore band of intermediate water recirculation in the latitude range of 5°-11°S. Also the results of Schmid et al. (2003) using Langrangian measurements indicate that a mean southward flow exists in the layer between 500 m and 1200 m in the latitude band of 5°-12 °S at the western boundary. Boebel et al. (1999a) showed that a Langrangian drifter experienced a southward drift in the same region. In both cases the southward deflection of the floats is associated with an eddy. During the period of eddy-like drifting the float never came close enough to the western boundary to become entrained in the NBUC.

3.3. Intraseasonal variability in sea level records

The analysis of the moored velocity measurements at 11°S at the western boundary in section 3.1 and 3.2 detects ISV in the NBUC domain and in the southward offshore flow at intermediate depths. To investigate the origin and forcing mechanisms of the NBUC variability, basinwide satellite measurements can be used. In contrast to the variability in the AAIW layer, one would expect that the upper layer NBUC ISV is mirrored in sea surface elevation. Thus, a merged and adjacent mapped mean sea level anomaly (MSLA) dataset from satellite altimetry (SSALTO/DUACS, see section 2.2 for more details) is an appropriate dataset to investigate ISV observed at the western boundary. In this section the ISV signal in MSLA data will be described locally at 11°S at the western boundary and after that the signal will be investigated along the entire east-west extend of the 11°S section.

3.3.1. Comparisons and observations

The dominant mode of variability at 11°S in the NBUC domain ranges from 50 d to 100 d periods. Now it is interesting to investigate whether a similar signal exists in the altimeter measurements. The gradient derived from the MSLA dataset is evaluated which is related to the geostrophic velocity. Assuming that the large-scale oceanic flows are nearly geostrophic and in hydrostatic balance, the surface geostrophic velocity can be obtained directly from the gradients of the ocean topography, denoted by η

$$v = \frac{g}{f}\frac{\partial \eta}{\partial x}, \quad u = -\frac{g}{f}\frac{\partial \eta}{\partial y}$$

(e.g. Fu and Chelton, 2001), where u and v are the zonal and meridional velocity components, g is the earth's gravity acceleration and f is the coriolis parameter. Near the equator the geostrophic approximation is sensitive to small sea-level variations (Picaut and Busalacchi, 2001), so the calculation of the altimetry-derived surface currents excludes the equatorial band. Picaut et al. (1989) has shown from TOGA-TOA dynamic heights and current meter measurements that altimetry-derived geostrophy can be extended to the equator, but only for periods greater than a month. But, nevertheless, the MSLA gradient for the area 35.3°W-33.7°W, 11°S is plotted in Figure 3.15 (a) together with the NBUC transport time series evaluated from the moored combined current records at 11°S (section 3.2). The MSLA gradient is calculated at every time step using six subsequent grid points in longitude. The coefficients of a first order polynomial that fits these data are derived and then the inclination is evaluated. Obviously bimonthly and longer fluctuations exist in both parameters of different measurement sources. Patterns exist which appear simultaneously (e.g. winter 2000 and 2001). But the interrelationship between the NBUC transport and MSLA gradient timeseries is low since the correlation coefficient only amounts to 0.17 which is below the 95% significance level (= 0.21). In Figure 3.15 (b) the coherence of the time series in (a) is calculated and the corresponding 95% significance level is marked. Although little correlation between both parameters exists the coherence of NBUC transport anomaly and MSLA gradient shows that fluctuations are significantly correlated in the period range of 60-70 d. Thus, the calculated coherence implies that 50-100 d ISV of the NBUC is associated with fluctuations in the altimeter measurements. MSLA can thus be used to extend the study of ISV from the western boundary into the

interior tropical Atlantic.

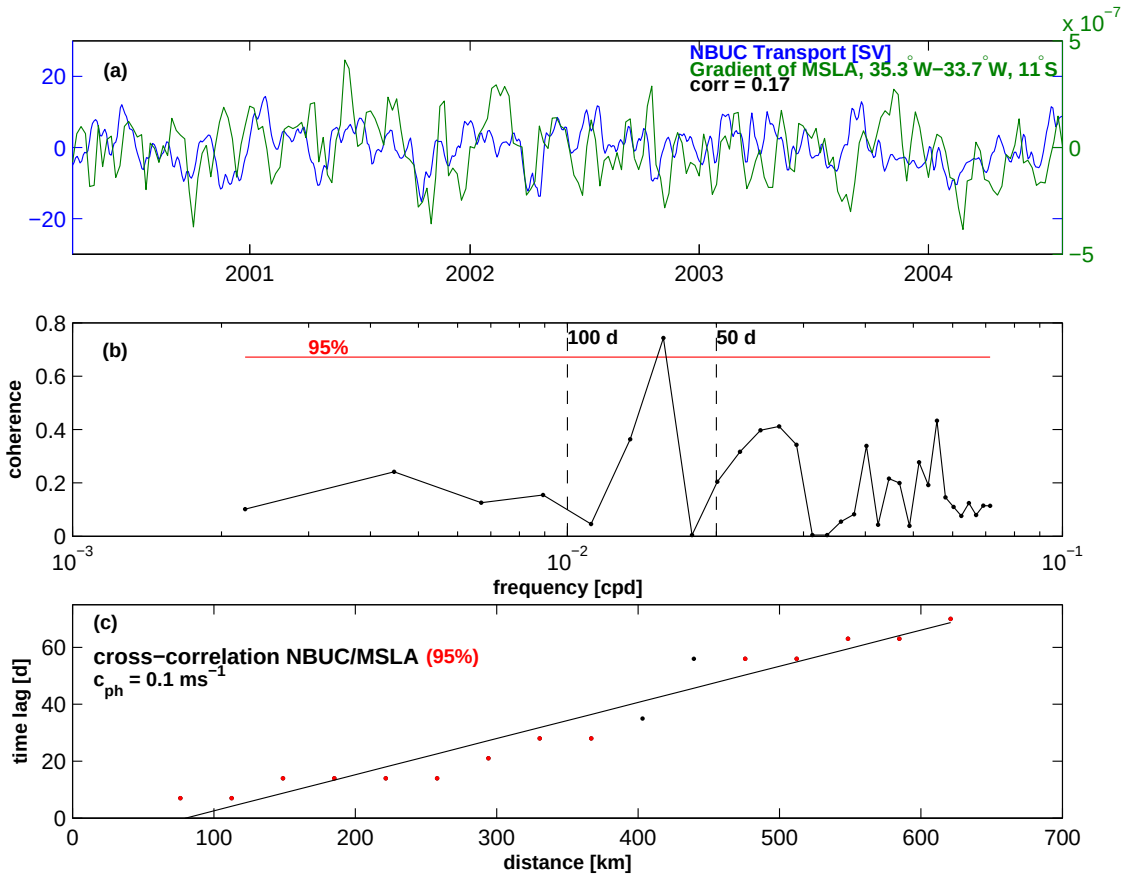

Figure 3.15.: *(a) Gradient of MSLA (35.3° W-33.7° W, 11° S, green) together with NBUC transport anomalies derived from mooring array data (section 3.2, blue). (b) Coherence between time series in (a). The 95% significance level is marked with a red line. (c) Time lags of maximal coefficients from a cross correlation of NBUC transport anomalies and MSLA of subsequent grid points in longitude at 11° S distributed with distance. Red dots indicate those values which exceed the 95% significance level and a regression is added.*

The discussion of the mooring array data in section 3.1 and 3.2 had shown that the variance with 50-100 d periods decreases with increasing distance from the NBUC core which corresponds to an isolation of the fluctuation pattern in the NBUC domain. Thus, the bimonthly fluctuation pattern in the MSLA dataset should only be present at the western boundary and the variability at the western boundary should not be connected to fluctuation patterns in the MSLA data of the interior tropical Atlantic. But a reverse situation is present. As seen in the following MSLA time series at the western boundary are connected to those further offshore along the 11°S section. In Figure 3.15 (c) time lags of maximal cross-correlation coefficients of the NBUC transport time series and MSLA time series of consecutive grid points are shown for the western basin. The time domain used spans the years 2000 (March) to 2004 (August). Those correlation coefficients are colored red when they exceed the 95% significance level which accredit ongoing discussion.

Additionally a regression is calculated from the different time lags. Obviously the time lag increases with increasing distance from the western boundary which probably hints to a propagation mechanism. The inclination of the regression graphs yields a phase velocity of $c_{ph} = 0.1$ ms^{-1}. Thus, against all expectations, the variability offshore appears to be connected to the variability at the western boundary. Evidence exists which suggests a propagating mechanism from the east with a phase velocity of 0.1 ms^{-1}. In this context it is important to note that altimeter measurements in the periphery of the continent could be affected by land reflections of satellite radar returns (Brooks et al., 1990). If this effect appears to be important or not will be mentioned in the following paragraph.

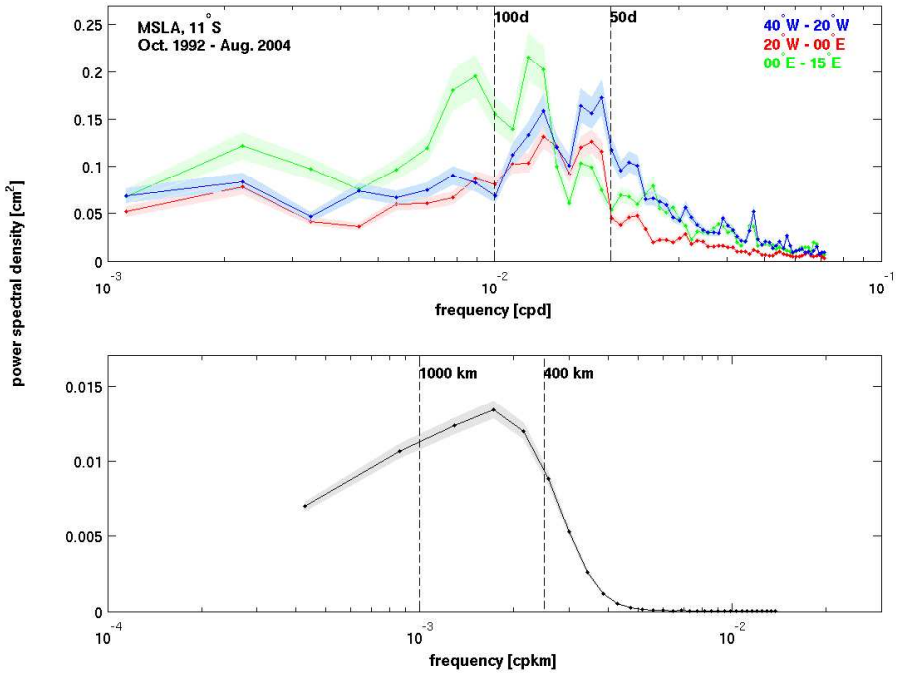

Figure 3.16.: *Mean variance conserved power spectral densities along 11°S section, which is separated in a western (40°W-20°W, blue), middle (20°W-0°E, red) and eastern (0°E-15°E, green) part for the time domain of October 1992 to August 2004 (upper panel). The lower panel shows the wavelength-spectrum along the section. The 95% significance interval is shaded in corresponding color.*

In order to investigate dominant period and wavelength scales at 11°S mean power spectral densities are calculated along the section in time and space. (Figure 3.16). For the spectra in the upper panel the section is separated in a western (40°W-20°W, blue), middle (20°W-0°E, red) and eastern (0°E-15°E, green) section so that possible longitudinal differences of the signal can be detected. Then the power spectral density is calculated from the MSLA between October 1992 and August 2004 at every longitude grid point and finally a mean power spectral density is extracted for every basin. Additionally, the 95% significance levels are shaded. Several spectra are available for calculating the mean power spectral density and consequently the significance interval is narrow and the variance distribution seems to be reliable. The interesting feature is that most of the variance is distributed between 50-100 d periods which is similar to the results of the observations at the boundary (e.g. Figure 3.13). Differences exist between the parts and because the main

variance in the western and middle section lies at 50-100 d periods whereas in the eastern section the variance additionally peaks at periods greater than 100 d. Furthermore the influence of the annual and semiannual cycle is maximal in the eastern section. Interesting to note is that the energy between 50-100 d periods is distributed in two peaks at about 80 d and 60 d. The variance at the latter period decreases with increasing distance from the coast. Summarized, the spectral distributions in Figure 3.16 show that 50-100 d ISV exists in the interior and that the shape of the spectrum in the western section is only resembled by the spectrum in the middle section but with lower variance. On the one hand this means that the signal with 50-100 d periods is concentrated onto the western part of the 11°S section. On the other hand this indicates that effects due to land reflections of satellite radar returns are negligable with respect to the process under study.

For calculating the wavelength spectrum the section is not separated into different basins so that minimum resolvable wavelength can be obtained. The power spectral density distributed with wavelength is calculated every time step along 11°S and finally the mean power spectral density is shown in Figure 3.16 (lower panel). The shaded 95% significance interval is narrow and consequently underlines the result that wavelengths between 400-1000 km are dominant along the 11°S section.

In the next step the MSLA will be discussed in a time-longitude plot. The mean spectral distributions in space and time of MSLA along 11°S have shown that the dominant mode of variability shows periods of 50-100 d and wavelengths of 400-1000 km. Thus, a band-pass filter in space (100-1500 km) and time (10-150 d) is applied and the filtered MSLA is shown in the longitude time domain along 11°S in Figure 3.17. The years 2000 (March) to 2004 (August) are chosen so that the time axes is adapted to the deployment period of the mooring array (section 3.1). Obviously westward propagating features exist in Figure 3.17. The most prominent signals seem to be characterized with 50-100d periods and wavelengths between 400-1000 km (see also Figure 3.16) which result in phase velocities of 0.1-0.2 ms^{-1}. A phase velocity of 0.1 ms^{-1} is already evaluated by comparing ISV of the NBUC to those of the MSLAs (Figure 3.15, (c)) which consequently underlines the relationship between the results derived from the NBUC transport time series and the MSLA.

It is important to note that the propagating features are mostly confined to the western part of the basin. This is already shown by the discussion of the spectral distributions in Figure 3.16 (upper panel). Several studies found as well an amplification of westward propagating signals from east to west in the time-longitude plot (e.g. Fu and Chelton, 2001, amongst others), which could be connected to influences of major bottom topography such as the Mid Atlantic Ridge (Chelton and Schlax, 1996). Modeling results obtained by Gerdes and Wübber (1991) found that (meridional) topography-induced coupling between a barotropic and a baroclinic Rossby wave can generate a larger amplitude baroclinic Rossby wave to the west of the topography, whereas Chelton et al. (1998b) concluded that these geographical variations are due to increased stratification which results from westward intensification of the subtropical gyre. Thus, several possibilities are suggested which could result in a westward amplification of the propagating feature in Figure 3.17. Ongoing analysis in the following sections will concentrate on sources and forcing mechanisms of those signals which probably lead to enhanced discussions on the westward intensification of the signal in Figure 3.17.

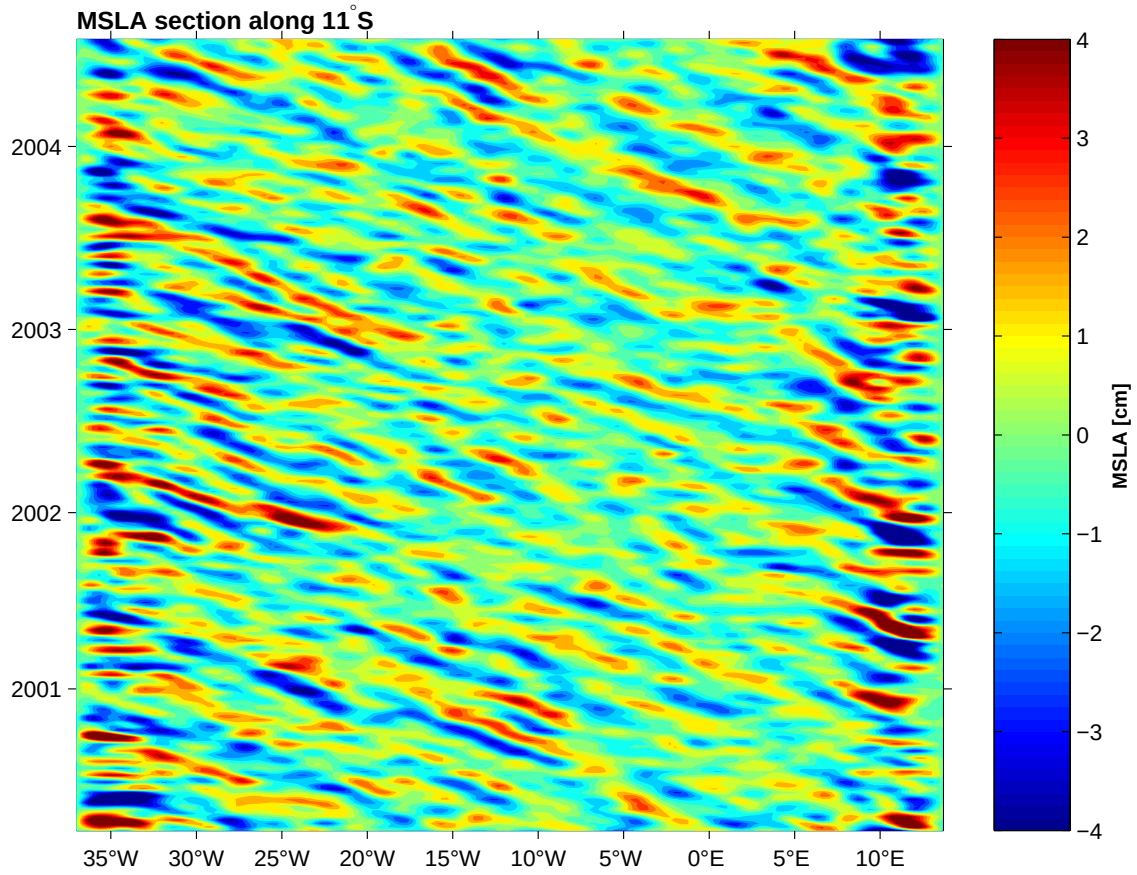

Figure 3.17.: *Time-longitude plot of SSALTO/DUACS MSLA along 11°S, bandpass filtered in time (10-150 d) and space (100-1500 km) during March 2000 to August 2004.*

The fluctuations accumulate in the vicinity of the northward western boundary current. This is probably due to a reflection of the westward propagating signal from the interior because when the signal reaches the western boundary the variability intensifies (Figure 3.17). But enhanced variability is restricted to the NBUC domain. Furthermore strong variability exists at the eastern boundary, but as already indicated in Figure 3.16 the variability is mostly due to periods between 80-150 d. The patterns at the eastern boundary do not propagate westward through the entire basin and the variability in the western basin appears not to be influenced by the variability in the east.

The ISV of MSLA in the western basin of the 11°S section are not clearly seasonally modulated but the propagating features favorably reach the western boundary in boreal winter to spring of the following year (e.g. winter/spring 2001/2002). Furthermore Figure 3.17 shows that an interannual modulation of amplitude and strengths exists. The amplitudes reach values up to ± 5 cms^{-1} in 2002 and 2003, whereas in 2000 and 2004 the signals are weaker. The moored velocities also show interannual differences from which the variance is minimal in the year 2004 (Figure 3.2). Thus, temporal modulations of ISV exist in the altimeter measurements which are comparable to those of the mooring array.

Briefly summarized, the comparison of altimeter measurements to current observations derived from a mooring array near the western boundary at 11°S has shown that 50-100 d variability in the altimeter measurements is related to similar ISV in the moored records. The prosecution of the prominent signal at the western boundary into the interior tropical Atlantic has shown that westward propagating fluctuations exist characterized by periods of 50-100 d, wavelengths of 400-1000 km and westward phase velocities of 0.1-0.2 ms^{-1}. Evidence exists that the propagating fluctuations are concentrated at the western part of the 11°S section. In the vicinity of the NBUC the fluctuations of MSLA accumulate. An analysis in the following section will describe the shape of the signal observed at 11°S section in more detail and physical mechanisms will be discussed which trigger ISV at the upper-layer western boundary current regime.

3.3.2. Shape of the observed signal and the role of planetary Rossby waves

As the next step it is interesting to analyze the physical background of the observed signal. For example a study by Kuragano and Kamachi (2000) classified spatial and temporal scales of sea-level variability for different latitude bands by using Topex/Poseidon (T/P) data. At mid and low latitudes they show the presence of Rossby waves, regarding propagating disturbances of which the effect of the earth's curvature is the primary restoring mechanism and which phase speed is given by

$$c_{nx} = \frac{-\beta}{k^2 + l^2 + R_n^{-2}} \quad , \tag{3.1}$$

whereas R_n is referred to as the Rossby Radius of deformation for mode n, l, k denoting meridional wave numbers, respectively and β describes the meridional gradient of the Coriolis parameter (e.g. Pedlosky, 1987). All Rossby waves move with westward phase velocity but the energy translation varies for different types of planetary waves, e.g. westward for long and eastward for short Rossby waves. Their shape is characterized by sea surface height variations of around 10 cm, phase velocities of approximately 10 cms^{-1} and wavelengths of hundreds to thousands of kilometers. Several modes exist which have been determined by solving an eigenvalue problem that depends only on the local stratification. Mode zero is due to a vertically uniform ocean. This barotropic mode is too fast to be resolved in Altimeter measurements. All other modes are dependent on stratification. The prominent first baroclinic mode is surface intensified and propagates much more slowly (Chelton and Schlax, 1996). Generally the vertical structure of baroclinic waves becomes more complicated as the mode number increases, while the phase speed decreases. Rossby waves play an important role for the dispersion of ocean-climatic signals and for the adjustment of the ocean to changing forcing (e.g. wind stress variability).

A two dimensional spectral analysis in both time and space is calculated from the MSLA along 11°S in order to investigate the shape of the signal. First of all a Fourier decomposition in space is calculated for every time step to obtain the time-dependent Fourier coefficients for corresponding wave numbers k. Then a spectrum is derived from the sum of both Fourier-coefficients for corresponding frequencies ω (see Storch and Zwiers, 1999). Thus, the variance of MSLA along 11°S is distributed into a frequency-wavenumber (hereinafter ω/k) domain in Figure 3.18. The dispersion relation for mode 1 baroclinic Rossby waves is given for different Rossby radii of deformation for different longitudes in

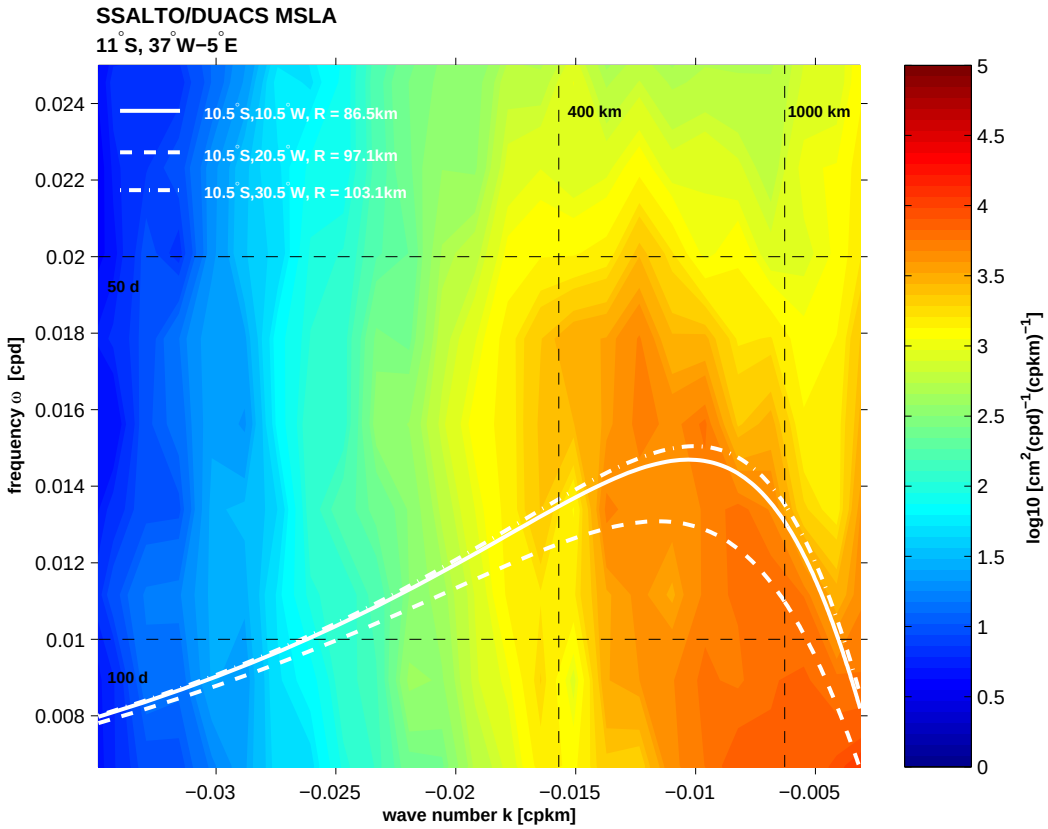

Figure 3.18.: *Space-time variance conserved spectral energy of SSALTO/DUACS MSLA along 11° S, 37° W-5° E. The dispersion relation of baroclinic Rossby waves is given for different baroclinic Rossby radii of deformation (white lines) at different longitudes derived from the global Atlas of the First-Baroclinic Rossby Radius of Deformation by Chelton et al. (1998a).*

the 10°-11°S band which are derived from the global Atlas of the first-baroclinic Rossby Radius of Deformation by Chelton et al. (1998a).

The variance distribution in the ω/k domain in Figure 3.18 shows that the area of high variance masks the curve progression of the dispersion relations for mode-1 baroclinic Rossby waves. More precisely, high energy exists in that part of the dispersion relation which is defined for long and short Rossby waves with periods of around 50-100 d and about 400-1000 km wavelength. Additionally high variance is present in the transition from long to short Rossby waves which means that the Rossby waves are characterized by a minimum of their zonal group velocity and that besides the eastward (short) and westward (long) group velocity a meridional energy transfer exists. Similarly, but for the Indian Ocean, Brandt et al. (2003) also found strong and coherent fluctuations in a mooring array in the central Somali basin that are characterized by southwestward phase propagation and northward energy propagation. The propagation was due to first baroclinic mode Rossby waves. However, the distribution of MSLA variance in the ω/k domain shows that along the 11°S section short and long Rossby waves exist and zonal as well as meridional energy propagation occurs.

Indeed the domain of maximal variance matches the curve progression of the dispersion relation but Figure 3.18 also shows that some of the resulting phase velocities ($c_p h = \frac{\omega}{k}$) lie above the dispersion relation which means that those phase speeds are faster than the theoretical ones, especially for short Rossby waves. Several studies obtained similar discrepancies between theory and observation of baroclinic Rossby waves (e.g. White, 1977; Meyers, 1979; Bernstein and White, 1981). Kessler (1990) presents evidence that the observed westward phase speeds are systematically higher than the predicted ones at latitudes polewards of about 7°N while at lower latitudes the observed phase speeds are slower than predicted by the standard theory for first-baroclinic Rossby waves. A collection of westward phase speed estimates in published analyses presented in Fu and Chelton (2001) (their Figure 9) shows that the observed discrepancies are not yet validated globally, especially on the southern hemisphere. Several studies proposed an explanation for the fast observed phase speeds. But only Killworth et al. (1997) suggested the most promising solution to date: They had shown that the background ocean is not in a state of rest as assumed in linear theory and consequently breaks down. More precisely changes in the potential vorticity gradient induced by the precense of east-west baroclinic mean flow can alter free Rossby wave modes, e.g. speed up phase velocities. On the other hand, LaCasce and Pedlosky (2004) and Isachsen et al. (2005) have shown that one consequence of baroclinic wave instability is that observed phase speed appears to be about two times the baroclinic long wave speed.

In addition, high variance exists in the ω/k domain which is located beneath the dispersion relation for baroclinic mode-1 Rossby waves. This means that the observed phase velocities are slower than the theoretical ones, especially near that part of the theoretical dispersion relation which linear theory defines as long Rossby waves. Thus, fluctuations exist which migrate slower than planetary waves, e.g. eddies (Nof, 1981). In the following chapter those mechanisms will be investigated in order to describe causes and effects of ISV in the interior tropical Atlantic onto the western boundary current regime.

To summarize, the distribution of MSLA variance in the ω/k domain shows that along the 11°S section short and long Rossby waves exist with 50-100 d periods and wavelengths of 400-1000 km and a zonal as well as meridional energy propagation occurs. Phase velocities occur which are higher than the theoretical values. This can be explained by changes in the potential vorticity gradient (Killworth et al., 1997). It is induced by the precense of east-west baroclinic mean flow which can alter free Rossby wave modes, e.g. speed up phase velocities. In addition, phase speeds of long Rossby waves are present which are slower than the theoretical values. Thus, besides modulation of ISV through long and short Rossby waves, other mechanisms e.g. mesoscale eddy activity may be important to explain the ISV at 11°S.

3.4. Southern tropical Atlantic ISV in a 1/12° FLAME model

Velocity and sea surface height (SSH) data derived from two differently forced runs of a 1/12° FLAME model are used for ongoing analysis and discussion. The first run is forced with monthly mean climatological NCEP/NCAR Reanalysis windfields, which are linearly interpolated from month to month (climatological run, hereinafter

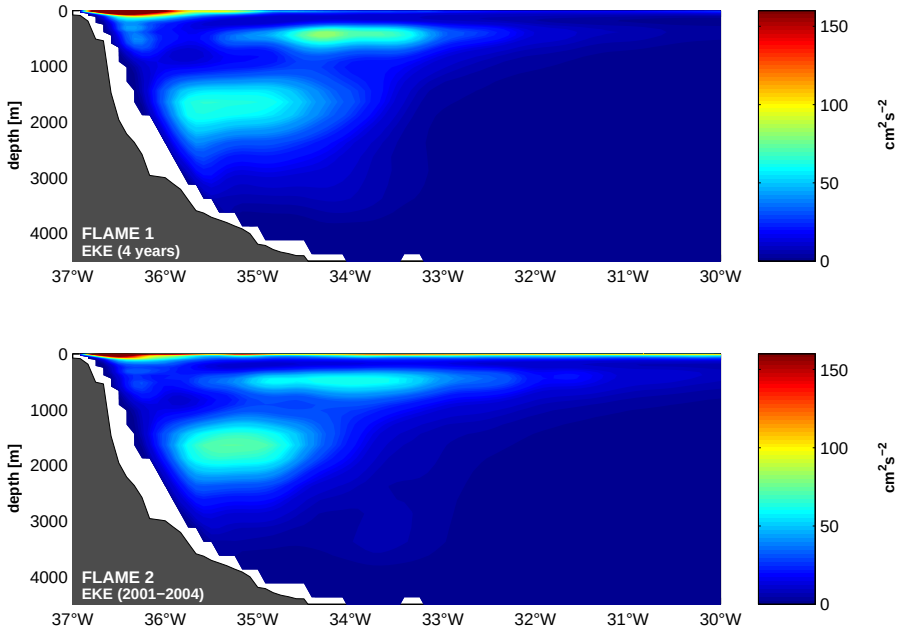

Figure 3.19.: *Eddy kinetic energy (EKE) derived from four years of FLAME 1 model data (upper panel) and for the years 2001 to 2004 of FLAME 2 records (lower panel) distributed with depth along 11°S. The 11°S topography is derived from ship measurements of different cruises (M. Dengler, pers. comn.).*

called FLAME 1). The second run is forced with daily ECMWF wind field (hereinafter called FLAME 2). For more details on the model design the reader is referred to section 2.3.

The analysis of model data may help to analyze mechanisms on space scales, whereas observations are often limited to bordered areas (e.g. mooring arrays), short timescales (ship sections) or single parameters (satellite observations). Here model runs with different wind forcing are used in order to understand the role of physical forcing mechanisms of oceanic variability. In the first instance it is important to see whether the model results yield ISV similar to observed ISV in the southern tropical Atlantic. At first the EKE is calculated from both model simulations (Figure 3.19) and compared to the observations (Figure 3.7). Four years of FLAME 1 data are used for calculating the EKE along 11°S in the upper panel whereas the EKE shown in the lower panel is obtained from FLAME 2 velocities of the years 2001 to 2004.

The modelled EKE distribution with depth reveals prominent features in both model results. In the upper layer the strongest signal of EKE exists near the western boundary in the NBUC domain. The signal is mostly confined to the upper 500 m but deep reaching patterns up to 1000 m exist in the domain of the NBUC current core since those patterns are weak. In the DWBC layer an area of strong EKE is present. As previously discussed in section 3.1 those variability patterns are already investigated by Dengler et al. (2004). They were identified as eddies transporting water masses southward in the DWBC layer, rather than by a continuous flow as previously thought. Additionally, Figure 3.19 shows that a domain of high EKE exists in the AAIW layer farther offshore. The EKE values are as strong as in the DWBC layer and the variability is confined to 500-1000 m depth.

Neither the variability in the near surface layer nor in the DWBC layer is connected to this dominant pattern (Figure 3.8).

Comparing the EKE along 11°S of different model simulations reveals interesting results. The signal in the near surface layer of FLAME 1 is clearly confined to the NBUC domain. No additional amount of high EKE is evident in the near surface layer for the FLAME 1 results (Figure 3.19, upper panel). In contrast the EKE derived from FLAME 2 velocities reveals both a dominant EKE signal in the NBUC layer and high EKE in the near surface layer further offshore (lower panel). The signal in the NBUC domain is comparable in strength and extent. But the fact that upper layer high EKE further offshore is only dominant in FLAME 2 indicates that wind forcing plays a fundamental role in triggering variability at 11°S since FLAME 2 is forced with daily winds. Furthermore the signal in the AAIW layer farther offshore is stronger in FLAME 1 which underlines the assumption that this pattern is isolated from the variability in the upper layer and in the DWBC layer.

The comparison of the model EKE distribution to the EKE derived from the mooring array data at 11°S shows good agreements. The dominant EKE pattern in the upper layer is confined to the NBUC domain in the observations (Figure 3.7) as well as in both results of FLAME (Figure 3.19). The EKE maximum in the AAIW layer offshore is interesting to discuss because only the current meter at 500 m depth at mooring K4 shows strong variability (Figure 3.7). But the model results clearly confirm this signal with an intensity comparable to the EKE maximum at the DWBC. This confirms that the pattern is present in the observations and negates possible dubiety since only one instrument of the entire mooring array shows strong variability in the AAIW layer farther offshore. It should be pointed out that the definition of EKE in this context includes all the fluctuations relative to a long term mean: the inertial and internal wave response, the mesoscale eddy field, Rossby waves, the seasonal signal and interannual fluctuations. No attempt was made here to separate the relevant time scales.

Concluding, two patterns of high variability exist along 11°S in the model and are comparable to the observations. Next the fluctuations in the NBUC domain will be discussed in both model runs and subsequently compared to the results of the mooring array. Secondly, the variability in the AAIW layer outside the NBUC will be investigated in more detail. It is possible to extend the analysis in the intermediate depth layer with the use of model results since no more measurements are available in the AAIW layer offshore.

3.4.1. Intraseasonal variability in the upper layer of the 11°S section

The distribution of EKE at the western boundary shows that strong variability exists in the NBUC domain (Figure 3.7 and 3.19). The discussion of mooring array data in section 3.1 revealed that those patterns are due to NBUC fluctuations with 50-100 d periods which are strongest in the core of the NBUC (e.g. Figure 3.6). Schott et al. (2005) show that the bimonthly signal is not influenced by fluctuations of the DWBC layer. Furthermore a NBUC transport time series was obtained from the mooring array data which consequently contains 50-100 d fluctuations (Figure 3.13). A comparison of altimeter MSLA measurements with the NBUC time series shows that it is possible to trace the 50-100 d signal further offshore (Figure 3.15). The signals can be explained by Rossby waves with westward phase velocity

of c_{ph} = 0.1-0.2 ms^{-1} and wavelengths of about 400-1000 km (Figure 3.18). In the following, meridional velocities are used from the model output at 11°S near the western boundary in order to estimate NBUC transport time series similar to the transports derived from the mooring array data. Furthermore, the sea surface height (SSH) from the model output will be investigated and compared to the results of the altimeter measurements.

NBUC transport calculations

In Figure 3.20 four year means of FLAME 1 and FLAME 2 meridional velocity near the western boundary at 11°S is shown, respectively. Additionally, box boundaries are marked which are used for transport calculations (white dashed lines). Horizontal lines are due to isopycnal (σ_0 =26.8 kgm^{-3} and σ_1 =32.15 kgm^{-3}) depths which are calculated from the corresponding model results for consistency. Vertical boundaries are chosen under dynamical aspects. For example box 2 is extended farther east compared to the observations (Figure 3.12) so that boxes 1 to 4 encompass the complete NBUC domain. Box 5 detects the mean southward transport in the AAIW layer outside the NBUC (Figure 3.14) but will be discussed in the following section. Positions of the mooring array are

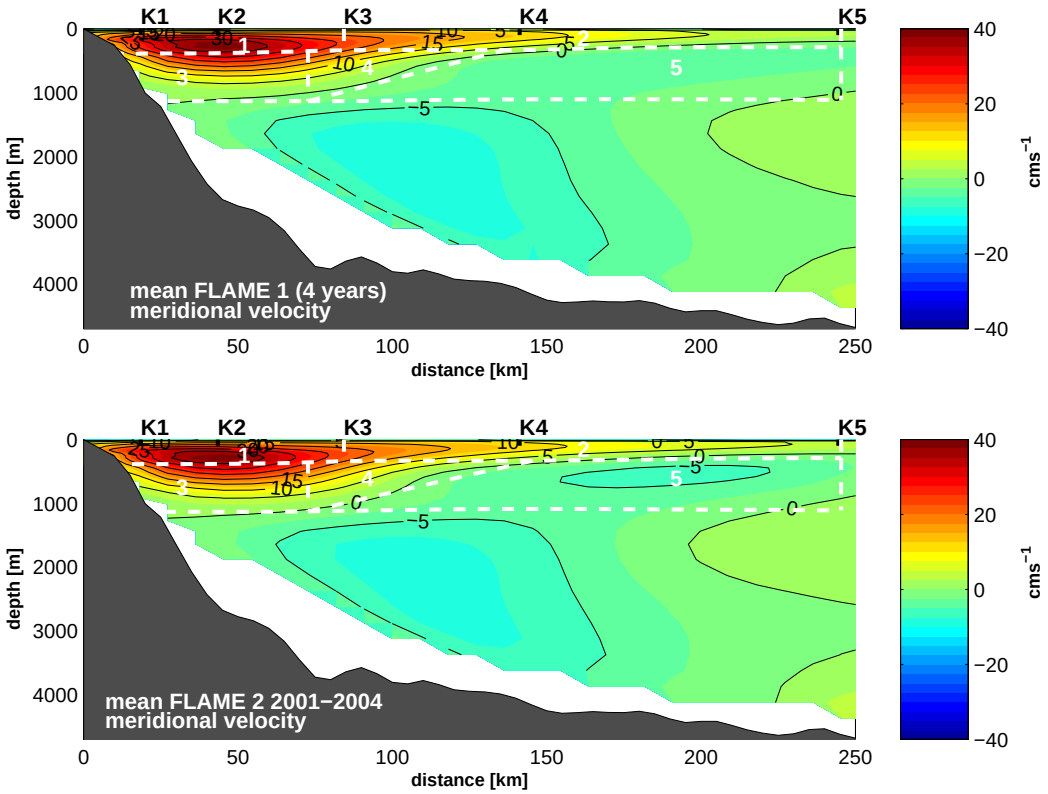

Figure 3.20.: *Four year mean alongshore current distribution from 1/12° FLAME model (FLAME 1 upper panel and FLAME 2 lower panel) along 11° S. Distance positions of the mooring array are marked for comparison. Marked are box boundaries of boxes 1-5 (dashed white) used for calculating transport time series, whereas the boundary from upper (boxes 1-2) to lower NBUC (boxes 3-4) is due to* σ_0 *=26.8* kgm^{-3} *isopycnal and lower NBUC is bounded by* σ_1 *=32.15* kgm^{-3} *(derived from model T/S field). Box 5 is located between both isopycnals offshore in the AAIW layer.*

marked for a better comparison to the observations, which are projected onto the zonal section chosen in the model output.

Several mean current cores exist in Figure 3.20. In the upper 1000 m mean northward velocity is evident at the western boundary, i.e. the NBUC. Further offshore weak mean southward flow exists in the layer of the AAIW. At 1500-3500 m a deep southward flow is present at the western boundary, namely the DWBC. Comparing the mean meridional velocity of FLAME 1 to FLAME 2 shows that only little differences exist. The NBUC and the DWBC appear to be similar in both model results, but the mean southward flow in the AAIW layer further offshore is stronger in FLAME 2.

The comparison of the mean section from the mooring data (Figure 3.12) to the model results (Figure 3.20) shows that the mean current regime is simulated reliable in the FLAME model, namely the mean NBUC reaches values up to 40 cms^{-1} in the observations as well as in the model. Also, the model mean DWBC is as intense as the observations. Only the eastern flank of the NBUC is extended further east in the model results. Additionally, the mean southward flow in the AAIW layer shows a stronger signal in both model results compared to the observations which is probably due to the fact that only one current meter covers the intermediate layer offshore. However, in general both models reflect the mean background current fields near the western boundary at 11°S and they are comparable to the mooring array measurements.

As the next step the NBUC transport is calculated from the model results. Box boundaries are defined in Figure 3.20 and boxes 1-4 are used for transport calculations since they encompass the NBUC. The NBUC transport anomalies for FLAME 1 (blue), FLAME 2 (red) and the mooring observations (green) are shown in Figure 3.21 (a). The NBUC transport time series in (a) are mainly influenced by the annual and semiannual cycle. The FLAME 1 transport shows maximal amplitude in boreal summer and decreases in boreal winter. Also the NBUC transport of the FLAME 2 simulation peaks during that time. In contrast to, the influence of the annual cycle on the NBUC time series derived from the measurements is low (Figure 3.21, (b)). Although small, superimposed on the seasonal cycle, ISV is evident in both model simulations.

The comparison of both model NBUC transport anomalies shows that NBUC FLAME 1 is in phase with NBUC FLAME 2 to a large extent. High-frequency fluctuations are also evident in the results of FLAME 2. On the one hand this is due to the fact that the FLAME 1 run is forced with a mean monthly windfield and the ocean's response with periods greater than two months to direct wind forcing can be simulated with FLAME 1. On the other hand the comparison indicates that the high-frequency variability is clearly due to wind forcing. Figure 3.21 (b) shows the mean seasonal cycle which is derived from the NBUC transport in (a), respectively. As already mentioned in the discussion of the anomalies in (a) the mean seasonal cycle has its maximum in June to July and minimizes in November to December. Furthermore the amplitudes of the mean seasonal cycle are higher in FLAME 1. Thus, the adding of wind variability attenuates the influence of the mean seasonal cycle. The arithmetic mean and the standard deviation (STD) for the model NBUC transport time series are given in Figure 3.21 (a), from which the second STD value is calculated from the transports without the mean seasonal cycle in (b), respectively. The

mean NBUC of FLAME 1 is comparable to FLAME 2, but surprisingly the STD of the climatological run is higher than the STD of FLAME 2. One would expect a contrary situation because more variance is anticipated in the FLAME 2 result since more variance is used for forcing the model. But the second STD values (no mean seasonal cycle) show that a reverse situation occurs and the STD in FLAME 2 is higher than the STD in FLAME 1 NBUC transports. The STD values differ in both model results since the mean wind field which forces the model runs is different in FLAME 1 and FLAME 2 (see section data for more details). The variance of the model results becomes comparable if the mean seasonal cycle is removed from the time series.

In Figure 3.21 the NBUC transport time series calculated from the mooring array

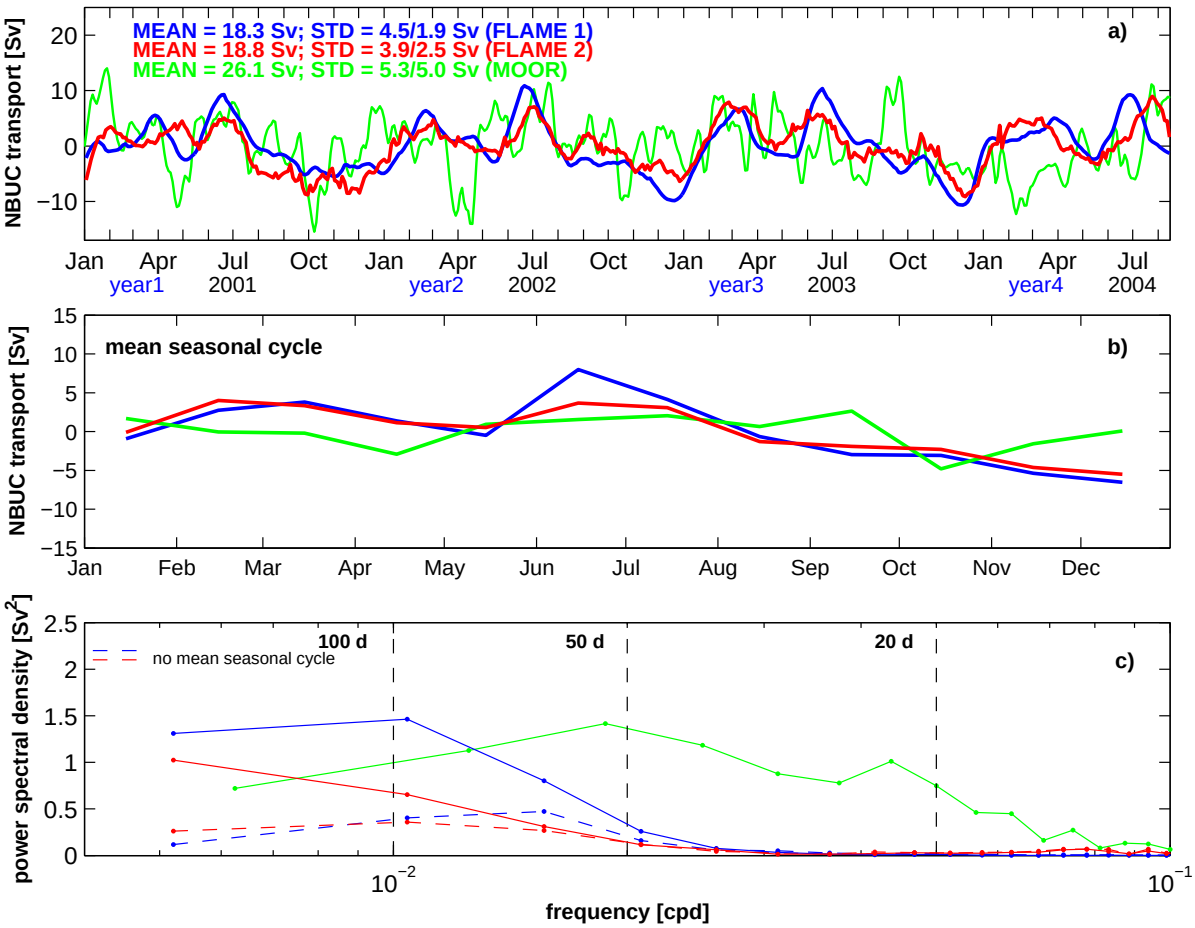

Figure 3.21.: *NBUC transport anomalies (boxes 1-4, Figure 3.20) from the FLAME 1 (blue) and FLAME 2 (red) model results and derived from the mooring array data (section 3.2, green). The arithmetic mean and the standard deviation (STD) are given in corresponding colors. The second STD value is calculated from the transport time series after subtracting the mean seasonal cycle in (b). (b) Mean seasonal cycle of different NBUC transports in corresponding colors (see (a)). (c) Variance conserved power spectral densities of different NBUC transport time series in corresponding colors. Additionally the power spectral density is calculated from the model time series with the mean seasonal cycle removed (dashed lines).*

data is added in order to compare the model results to the observations (green lines). A qualitative discussion of the moored NBUC transport is already given in section 3.2 so that here the discussion will be reduced on similarities and differences of the observations and the model results. The mean seasonal cycle of the observations in Figure 3.21 (b) shows small amplitudes. In contrast to this the mean seasonal cycle of the FLAME 1 result shows higher amplitudes. Only FLAME 2 reveals a comparable curve progression to the observations because mean seasonal cycle amplitudes are reduced and as seen before the mean wind forcing is different to the FLAME 1 forcing. The mean NBUC and the STD of the observations are considerably higher than those values obtained from the model results. Furthermore the anomalies in Figure 3.21 (a) show that fluctuations with one month period and smaller exist in the observations as well as in FLAME 2, but the amplitudes of these fluctuations are comparably small in FLAME 2. This together with the large difference of STD suggests that fluctuations with monthly and smaller periods are smoothened since those fluctuations are traced back to wind forcing. A daily wind forcing accounts for the variability in the FLAME 2 results and consequently possible wind forced mechanisms could be resolved. Thus, it is not clear why intraseasonal variability exists in the observations with 10-30 d periods which can be not resolved with the model results.

In Figure 3.21 (c) the power spectral densities are shown for the different transport time series. Additionally, those spectral distributions are given which are derived from the time series without the mean seasonal cycle in (b) (dashed lines). The spectral distribution in the NBUC domain is already described in detail when the mooring observations are deiscussed (section 3.1 and 3.2). The dominant mode of variability is characterized with 50-100 d periods but also high variance exists between 10-30 d periods. At this point it is interesting to know whether prominent features of ISV in the observations are also evident in the model results. The spectral distributions of FLAME 1 and FLAME 2 show that high variance occurs as well between the 50-100 d period, from which the power spectral density in this period range is higher in FLAME 1. The same situation appears when the annual cycle is removed. As expected the power spectral density shows lower values but the main signal of the spectrum is distributed between the 50-100 d period and the power spectral density is again higher in FLAME 1. Additionally, the shape of both spectra (FLAME 1 and 2) seems to be similar. Thus, although variance is added in the FLAME 2 model run with daily wind forcing the variance of the NBUC transport in the 50-100 d period range is lower than the variance derived from the climatological run in the same period range. This indicates that internal ocean mechanisms trigger the 50-100 d ISV in the NBUC, rather than wind forcing. As already shown in Figure 3.21 (a) the fluctuations with 30-50 d periods are only evident in FLAME 2 but the variance is clearly higher in the observations. The increased power spectral density values with periods smaller than 20 d in FLAME 2 suggest a direct wind forcing. But the spectral distributions in this period range clearly underline that those fluctuations are not captured by the model results.

To discuss possible errors while calculating the transport time series with the mooring array data the same mapping procedure is repeated with the model results. For calculating the transport time series from the model results in Figure 3.21 (a) every available grid point is used whereas the mooring array delivers less data resolution in the section (instrument depths are marked in Figure 3.22). For transport calculations the mooring array data are mapped on a 5 km by 20 m grid using Gaussian weights (see section 3.2

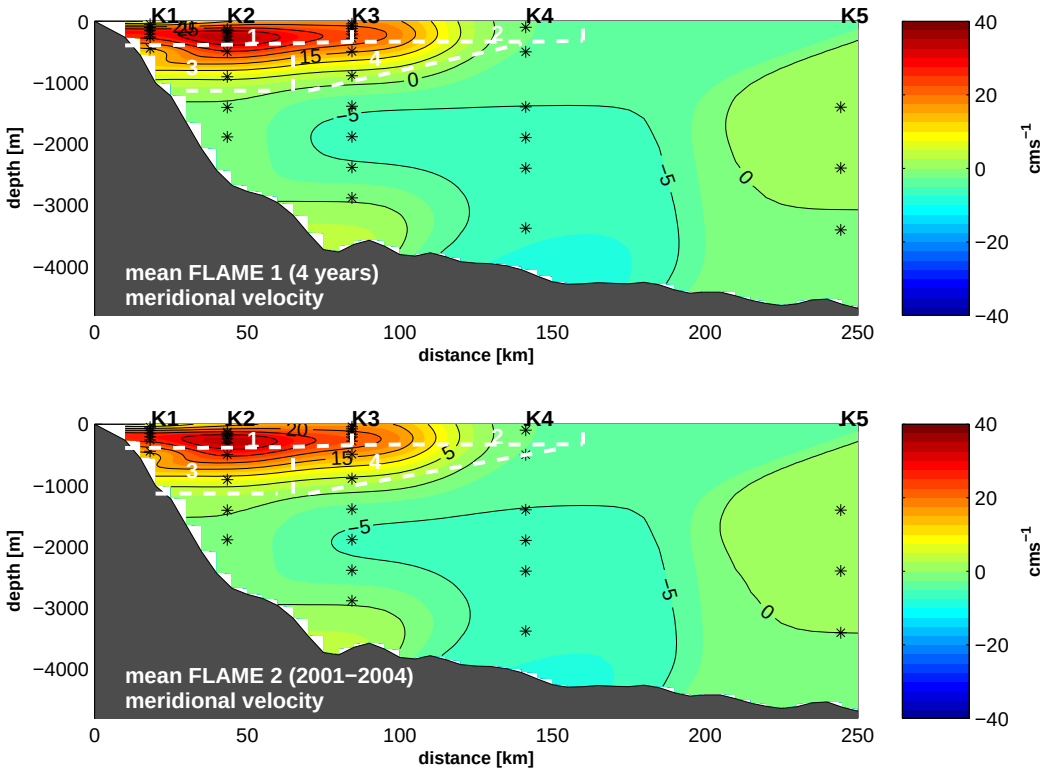

Figure 3.22.: *Same as Figure 3.20, but only grid points are used which correspond to instrument depths of the mooring array.*

and Schott et al., 2005, for a detailed description on the mapping procedure). Thus, the model meridional velocities are used at every instrument depth and finally interpolated on a 5 km by 20 m grid as used for the mooring data. The mean mapped velocities are shown in Figure 3.22 for the FLAME 1 (upper panel) and FLAME 2 (lower panel) model results. Additionally the distance positions of the mooring array and the box boundaries for NBUC transport calculations are marked for comparison. The mean mapped velocities show that the NBUC is established as already given in the full resolution mean of Figure 3.20. Maximal mean velocities of 40 cms^{-1} are evident in the core of the NBUC which is already shown in Figure 3.20. The comparison of the observations in Figure 3.12 and the model results in Figure 3.20 shows that the NBUC in the model results is extended further east. The mean velocities in Figure 3.22 suggests that this is due to missing measurements in the near surface layer further offshore since the eastern flank is located similar to the observations. Large differences occur in the area of the DWBC but will not be discussed here.

Figure 3.23 shows different transport time series calculated from meridional model velocities on different grid resolutions, namely the model resolution or real transport (blue, see Figure 3.20) and the mooring resolution (green) for FLAME 1 (upper panel) and FLAME 2 (lower panel). The real transport is calculated from the gridded velocities of the model results and the mooring resolution transport is derived from those velocities which are distributed on the instrument depths of the mooring array. The comparison of the different sampling resolutions shows that good agreement is evident. In the climatology run,

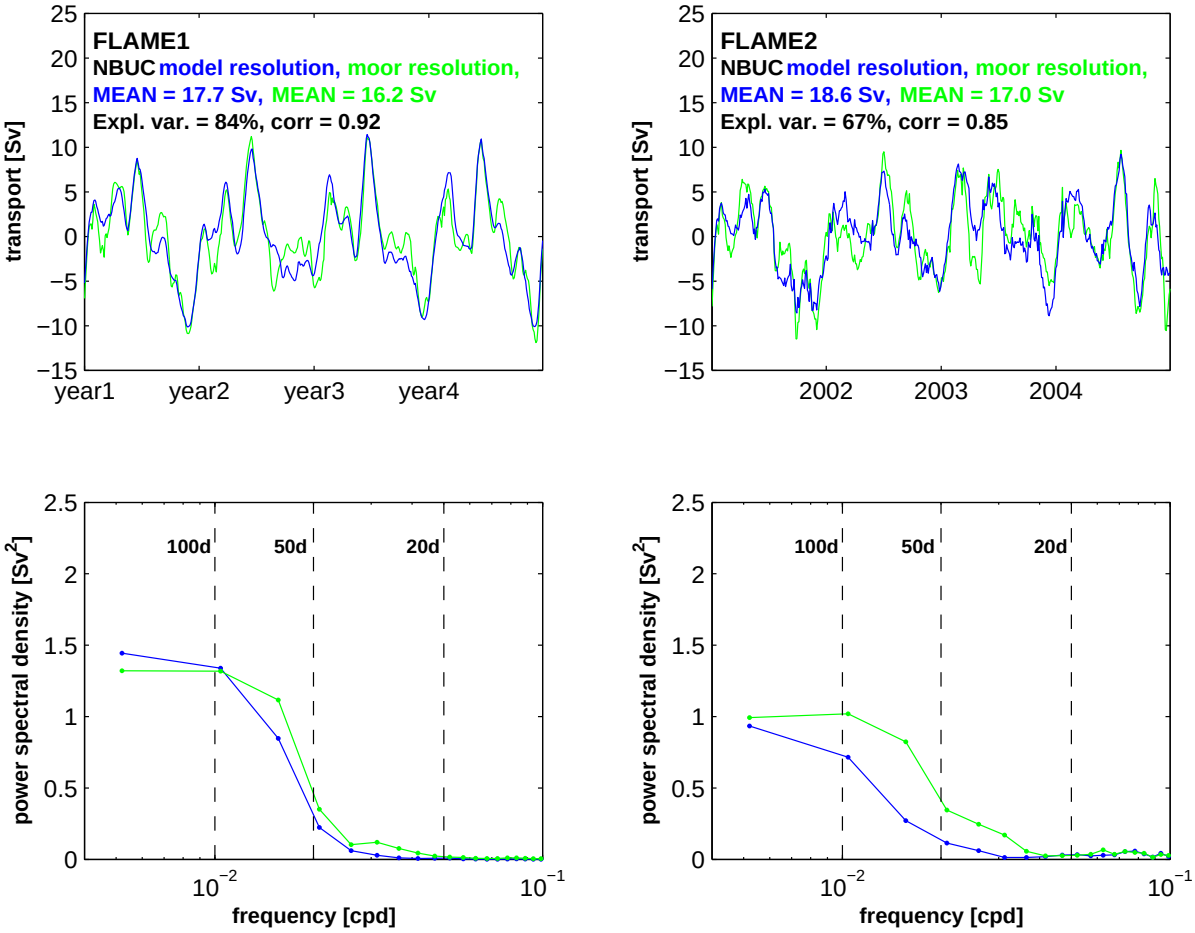

Figure 3.23.: *NBUC transport time series calculated from FLAME 1 (left) and FLAME 2 (right) meridional velocities with different resolutions, namely model resolution (blue) and moor resolution (green). The latter corresponds to the distribution of instrument depths at the 11°S mooring array (marked in Figure 3.22). In addition, corresponding variance conserved power spectral densities are evaluated, respectively (lower panels).*

the correlation between both resolutions is very high (0.92). 84% of the model resolution can be explained by the coarser grid and the mean NBUC transport is only 0.5 Sv lower in the mooring resolution. It is important to mention in this context, that mean NBUC transports shown in Figure 3.23 may differ to those calculated in Figure 3.21. This can be explained by the fact that in Figure 3.23 the complete time series available from the model simulation is used (2001 to 2004) and in Figure 3.21 the time axis of the model results is adapted to the measurements (2001 to August 2004). In FLAME 2, correlation decreases, but remains comparably high (0.85). 67% of the model resolution can be explained by the mooring resolution. The difference of the mean NBUC accounts for 1.6 Sv in FLAME 2.

In addition, the comparison of the time series with different resolutions also reveals that fluctuations on intraseasonal time scales are somewhat enhanced in the mooring resolution. This difference is evident in both model simulations but is amplified in the FLAME 2 results. Thus, the corresponding spectra of those time series in the upper panels of Figure

3.23 are evaluated, respectively (lower panels). The spectra are evaluated in the same manner as in Figure 3.21. In the FLAME 1 result, only small differences exists. In the FLAME 2 model simulation the comparison of the spectral distribution clearly reflects the discrepancies as described above. In the period range from 50-100 d energy is generally higher in the moor resolution compared to the real model resolution. Indeed, this effect diminishes with increasing frequency, but amplified variance in the coarser moor resolution also exists between periods of 20-50 d.

In Figure 3.21, the comparison of the model simulation to the mooring array data reveals that variance on intraseasonal time scales in the NBUC transport is higher in the observations compared to the model results. Evaluating transport errors using the model simulation with respect to the coarse data coverage of the mooring array yields that variance on intraseasonal time scales is amplified as well in the time series derived from the mooring resolution. Thus, the discrepancy which is obvious in Figure 3.21 can be partly explained by the effect of the coarse data coverage and errors due to interpolation methods. But on the other hand, enhanced variance content in the observations compared to the model results can be not completely explained by this effect since the EKE grieved from the mooring measurements are higher compared to corresponding model results (Figure 3.7 and 3.19).

In the next step the model results are analyzed to find out whether ISV in the NBUC domain is influenced by the variability further offshore and in deeper layers. A correlation

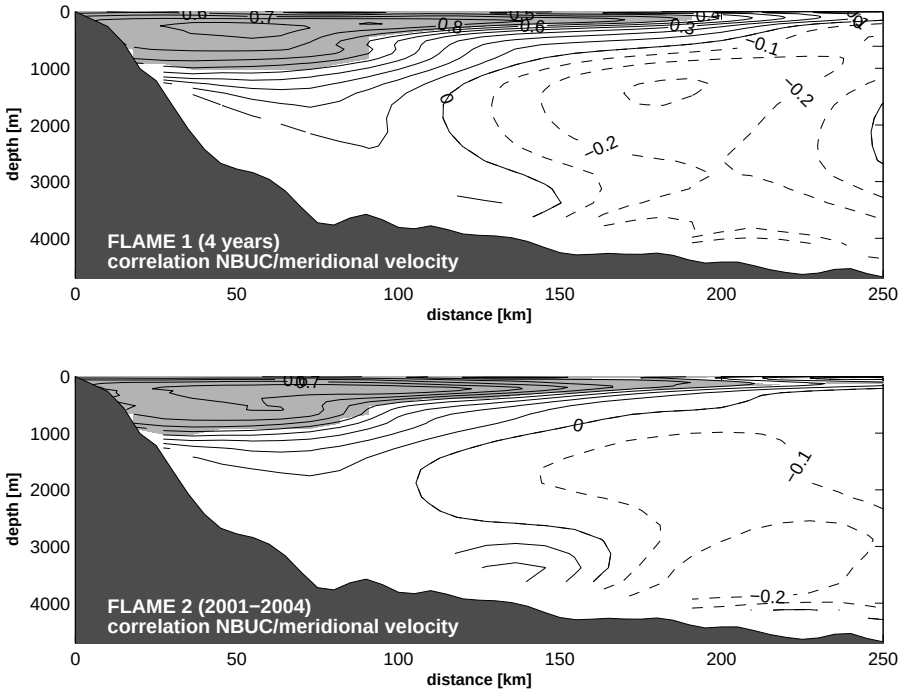

Figure 3.24.: *Correlation of 4-year NBUC transport time series with all available meridional velocities along the 11°S section for FLAME 1 (upper panel). Correlations above the 95% significance level are shaded gray. Lower panel: same for the FLAME 2 simulation in the years 2001 to 2004.*

of the NBUC transport time series of the mooring array observations with all available time series has shown that the variability in the NBUC domain is neither influenced by the DWBC rings nor by fluctuations in the AAIW layer further offshore (Schott et al., 2005). Analogous to this analysis, correlations of NBUC time series with meridional velocity at every grid point are shown in Figure 3.24 for FLAME 1 (upper panel) and FLAME 2 (lower panel). Values above the 95% significance level are shaded gray. The variability of the NBUC transport is confined to the upper 1000 m near the western boundary and further offshore the gray shaded domain converges to the near surface layer with increasing distance from the coast. The mean sections in Figure 3.20 show that this domain brackets the NBUC in both model simulations. Thus, as already shown in the mooring array data ISV in the NBUC transport time series discussed in the model simulations is not influenced by the fluctuations in the AAIW layer further offshore of the DWBC variability (Dengler et al., 2004).

Summarizing briefly, transport estimates from the model simulations FLAME 1 and FLAME 2 reveal interesting results. A spectral analysis of the NBUC transport time series shows that maximum variance is evident in the period range of 50-100 d which is comparable to the results obtained from the mooring array data. Surprisingly, the spectral distributionsof both model simulations is similar. The power spectral density in the FLAME 1 result is even higher. Thus, first evidence exists that ISV in the NBUC domain is generated due to ocean internal mechanisms, rather than wind forcing. In addition, high-frequency fluctuations exist in the observations whose variance is hardly captured by the model.

Analysis of sea surface height

The analysis of mapped sea surface anomalies from altimeter satellite measurements in section 3.3 has shown that it is possible to prosecute the intraseasonal fluctuations in the NBUC domain at the western boundary into the interior tropical Atlantic along the 11°S section. Evidence exists that long and short Rossby waves propagate with westward phase velocity of around 0.1-0.2 m/s with 50-100 d periods and wavelengths of 400-1000 km. Seasonal as well as interannual modulations characterize the westward propagating feature. The comparison of observed NBUC variabilities at 11°S to those from the model simulations is in good agreement. Consequently, it is interesting to analyze whether the model simulations reveal similarities to the altimeter observations. Thus, in this section sea surface height (SSH) obtained from the FLAME 1 and FLAME 2 model run will be analyzed and compared to the results from the satellite observations.

In order to get an overview on the variance distribution along 11°S mean power spectral densities are derived for SSH of FLAME 1 and FLAME 2 in space and time. Figure 3.25 shows mean power spectral densities calculated from four years of FLAME 1 (a) and FLAME 2 (b) SSH along the 11°S section. The section is separated in three parts, namely a western (40°W-20°W, blue), middle (20°W-0°E, red) and eastern (0°E-15°E, green) section. The spectra are calculated at every available model grid point along 11°S and are subsequently averaged in corresponding samples. Additionally the 95% significance interval is shaded in corresponding colors, respectively. Both model results show that the dominant signal of variance in the western and middle section is distributed at periods of 50-100 d which is clearly proved with the 95% significance interval. Furthermore, it is evident

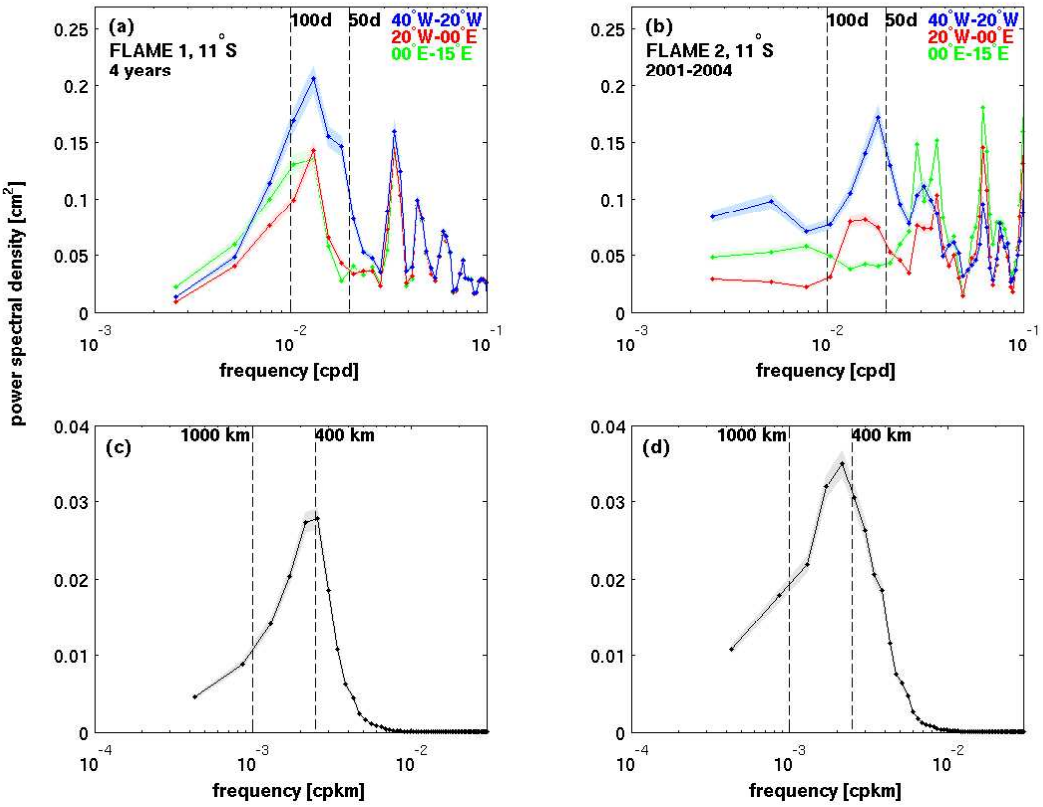

Figure 3.25.: *(a) Mean power spectral densities from 4 years of FLAME 1 SSH, separated in western basin (40° W-20° W, blue), middle (20° W-0° E, red) and eastern (0° E-15° E, green) basin along 11° S section. (b) Same for FLAME 2, 2001 to 2004 mean. (c) Wavelength spectrum from 4 years of FLAME 1 SSH along 11° S section. (d) Same for FLAME 2, 2001 to 2004. The 95% significance level is shaded in corresponding colors, respectively.*

that the 50-100 d signal increases with increasing distance from the western boundary. Especially in the result with daily wind forcing the 2 to 3 monthly fluctuations minimize in the periphery of the eastern boundary. Figure 3.25 (c) and (d) show the wavelength spectra along 11°S from FLAME 1 and FLAME 2 SSH, respectively. Prominent signals exist at wavelengths of 400-1000 km.

Both model results show distinctive agreements with the analysis of the altimeter measurements along 11°S (Figure 3.16). Thus, the model results underline that dominant signals exist with 50-100 d periods and wavelengths of 400-1000 km. It is interesting to note that only little differences exist between the mean spectra of FLAME 1 and FLAME 2 which implies that other dynamics than wind forcing trigger the 50-100 d variability in the western part of the 11°S section. In contrast, the mean spectra at the eastern boundary show a clear influence of wind variability forcing. This may denote that fluctuations near the eastern boundary are differently forced than ISV in the western section.

In the next step the time-longitude plots of sea level anomalies (SLA) along 11°S are shown in Figure 3.26 for FLAME 1 (upper panel) and FLAME 2 (lower panel). A band-pass

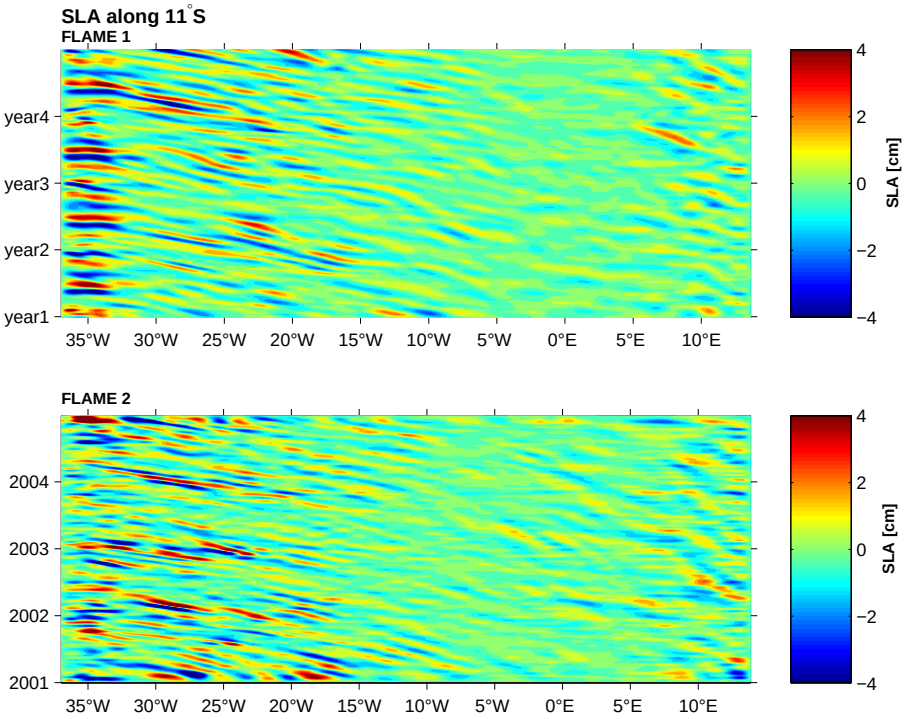

Figure 3.26.: *Time-longitude plot of sea level anomalies (SLA) along 11°S for FLAME 1 (upper panel) and FLAME 2 (lower panel). A band-pass filter in time (10-150 d) and space (100-1500 km) is applied.*

filter in both time (10-150 d) and space (100-1500 km) is applied. Both panels show that westward propagating disturbances exist which are confined to the western part of the 11°S section. Especially in the climatological run the signal accumulates when the propagating feature reaches the western boundary. The signals are not clearly seasonally modulated but evidence exists that the signals mingle with the northward western boundary current favorably in boreal winter.

Altough FLAME 1 is forced with monthly climatological ECMWF winds an interannual modulation exists in the propagating features (Figure 3.26, upper panel). The analysis of the NBUC transport time series in both model simulations already suggests that the wind field does not play a role in the forcing of 50-100 d variability in the NBUC domain (Figure 3.21). The analysis of SSH data shows that a westward propagating disturbance exists in the western part of the 11°S section with periods of 50-100 d and wavelengths of 400-1000 km. Those features are forced via ocean internal mechanisms rather than wind forcing.

To discuss the distribution of variance in space and time a two-dimensional spectral analysis in the frequency-wave number (hereinafter ω/k) domain is calculated from the FLAME 1 results (Figure 3.27) and from the FLAME 2 SSH (lower panel) along 11°S section between 37°W and 5°E. A more detailed description of the applied method was given earlier in section 3.3.2. The dispersion relation for first-mode baroclinic Rossby waves is added for reference using radii of deformation derived from a global atlas (Chelton et al., 1998a). As already suggested in Figure 3.25 the main signal is distributed between 50-100

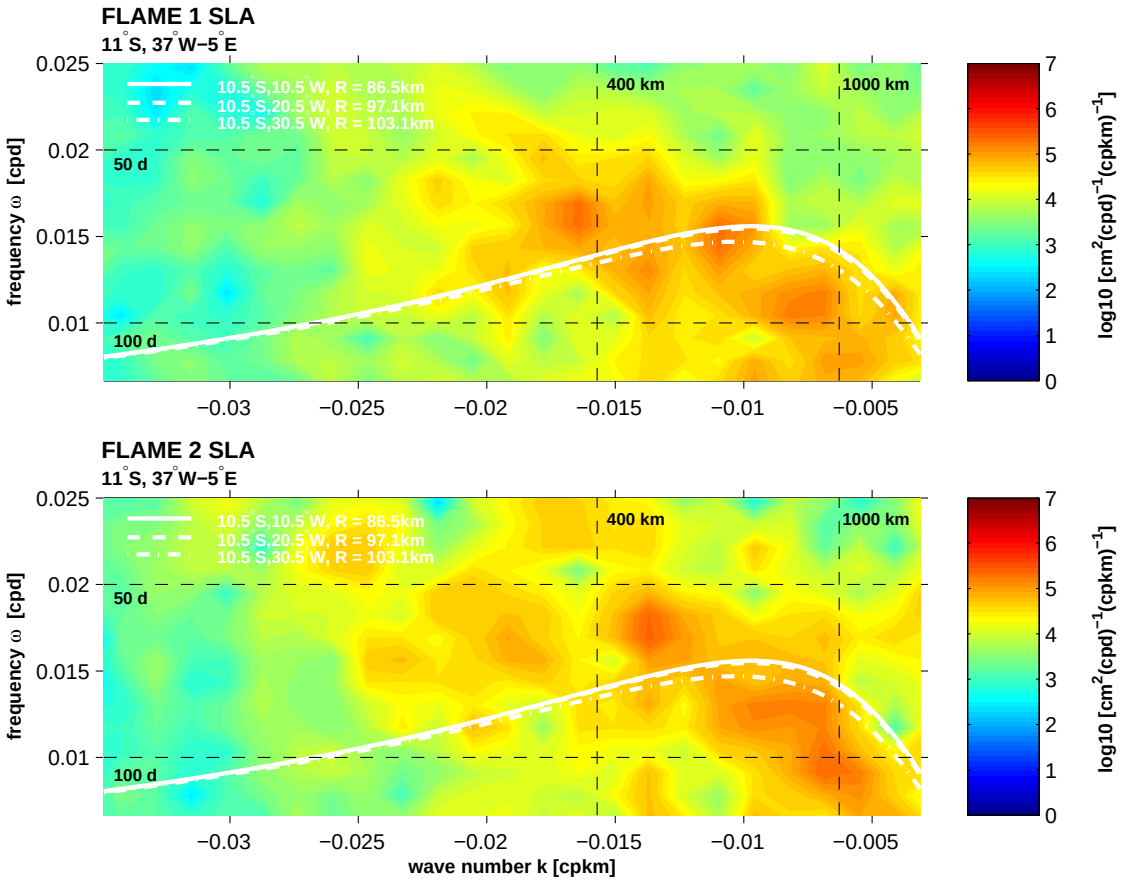

Figure 3.27.: *Space-time variance conserved spectral energy of FLAME 1 (upper panel) and FLAME 2 (lower panel) SLA along 11°S, 37°W-5°E. The dispersion relation of baroclinic Rossby waves is given for different baroclinic Rossby radii of deformation (white lines) derived from the global Atlas of the First-Baroclinic Rossby Radius of Deformation by Chelton et al. (1998a).*

d periods and wavelengths of 400-1000 km in both model results and the domain of high variance in FLAME 1 scarcely differs from that in FLAME 2. The theoretical dispersion relation for first-mode baroclinic Rossby waves shows that parts of the area of high variance mask the curve progression. Thus, evidence exists that a signal of long as well as short Rossby waves is present in the SSH data of both model simulations along the 11°S section. Furthermore high variance is present in that part of the dispersion relation which reflects the transition of long to short Rossby waves. Such waves are characterized by a meridional group velocity.

Figure 3.27 shows that a domain of high variance lies above the dispersion relation for first-mode baroclinic Rossby waves and a domain which is distributed beneath the curve progression. The latter is most likely distributed in that part of the dispersion relation which is defined for long Rossby waves and may be due to higher modes of baroclinic Rossby waves or other movements, e.g. eddy dynamics. The domain which is distributed above the theoretical dispersion relation accounts for Rossby waves which are faster than in theory. Those patterns are already discussed in section 3.3.2 in more detail. The

corresponding analysis which is applied on MSLA of satellite altimetry (Figure 3.18) is comparable to the model results. The discussion of Figure 3.18 has shown that the signal of high variance in the area of short Rossby waves decreases with increasing distance from the western boundary. This is not clearly evident in the model results (not shown).

However, as already shown in the altimeter measurements the distribution of model SSH variance in the ω/k domain has shown that long and short Rossby waves exist along 11°S with 50 to 100 d period and wavelengths of 400-1000 km. Evidence exists that disturbances are present whose westward phase speeds are slower than those for first mode baroclinic Rossby waves which might be due to higher baroclinic modes or eddy dynamics. These signals are annually modulated and the analysis of SSH implies that these westward propagating features are forced by ocean internal mechanisms rather than by wind forcing.

3.4.2. Intraseasonal variability in the intermediate water layer further offshore

The distribution of EKE along the 11°S section also reveals an area of high EKE values outside the NBUC and in the AAIW layer (Figure 3.7) which is simulated by both model results (Figure 3.19). A transport time series is estimated from the mooring data at intermediate depths further offshore (box 5, Figure 3.12) which shows that the dominant signal lies again in the period range of 50 to 100 d (Figure 3.13, (b)). Annual modulations of the ISV in this layer exist with maximal amplitudes in boreal summer and a weak signal in 2001. In the following similar transport calculations will be done using both model results.

The mean section of meridional velocity in Figure 3.20 shows the box boundaries of box 5 which captures a mean southward flow at intermediate depths outside the NBUC and corresponds to the area of high EKE (Figure 3.19). In Figure 3.28 the different model transport time series of box 5 are shown together with the appropriate transport derived from the mooring array. The arithmetic mean of box 5 transport time series calculated from the climatological run amounts to -4.3 Sv. Superimposed on the mean southward transport fluctuations with periods of 2-3 months exist. Their amplitudes do not exceed $\pm$5 Sv. The standard deviation amounts to 2.3 Sv. The mean seasonal cycle of the FLAME 1 transport (Figure 3.28, (b), blue line) shows that no mean seasonal cycle exists since the amplitudes does not exceed 2 Sv. The FLAME 2 transport of Figure 3.28 (red line) is characterized by a mean southward transport of -4.8 Sv and a standard deviation of 3.1 Sv. The transport anomalies show fluctuations with 2-3 month periods which to some extend oscillate and recur in the different years. These signals are centered in boreal summer (e.g. 2001 and 2002) and the amplitudes of the fluctuations range from -10 Sv to 5 Sv.

The mean southward transport derived from the FLAME 1 model simulation is almost as large as the mean value of FLAME 2. Calculating the standard deviations show that in FLAME 2 it is somewhat higher than in FLAME 1, even if the mean seasonal cycle is subtracted from the transport time series (Figure 3.28 (a), second STD values, respectively). The fluctuations which exist in the anomaly time series of both model results are to some extend out-of-phase, e.g. in summer 2001 the time series are 90° phase delayed. The mean seasonal cycle in Figure 3.28, (b) shows that the amplitudes of the FLAME 2 results are somewhat higher.

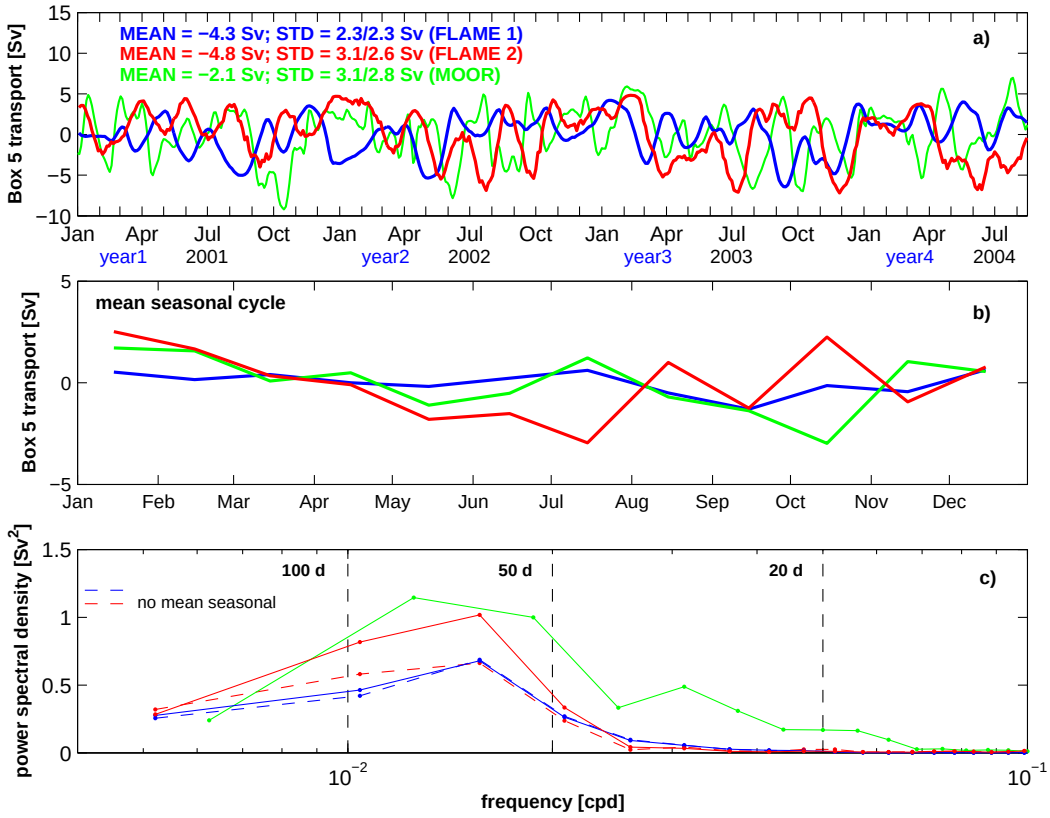

Figure 3.28.: *Box 5 transport anomalies (Figure 3.20) from the FLAME 1 (blue) and FLAME 2 (red) model results and derived from the mooring array data (section 3.2, green). The arithmetic mean and the standard deviation (STD) are given in corresponding colors. The second STD value is calculated from the transport time series after subtracting the mean seasonal cycle in (b). (b) Mean seasonal cycle of different box 5 transports in corresponding colors (see (a)). (c) Variance conserved power spectral densities of different box 5 transport time series in corresponding colors. Additionally, the power spectral density is calculated from the model time series without mean seasonal cycles (dashed lines).*

The mean southward transport within box 5 accounts for half as much in the mooring observations compared to the model simulations (Figure 3.28, (a)). In contrast, the standard deviation derived from the model transport time series is comparable to the observations after subtracting the mean seasonal cycle. The only difference is that the moor STD is marginally higher than the model results. The variance conserved spectra in Figure 3.28, (c) are calculated from the transport time series in (a). As expected, they show that the dominant signal is found within 50-100 d periods in all three transport time series. Furthermore, the spectral distributions show that the shape of the FLAME 1 result appears to be similar to the FLAME 2 model simulation. In the case of removed seasonal cycle the spectra are identical (Figure 3.28, (c), dashed lines). Thus, evidence exists which shows that ocean internal mechanisms trigger ISV in the 50-100 d period range, rather than wind forcing. Additionally, the spectra reveal that variances with periods less than 50 d are higher in the observations. This means that also at intermediate depths mechanisms exist which could not be reproduced by the model simulations.

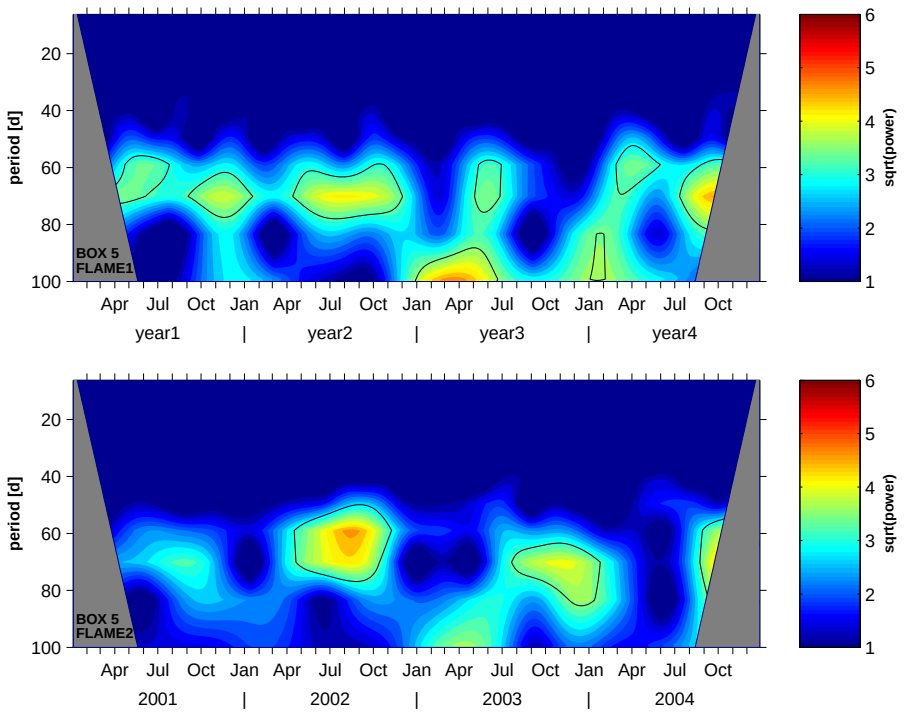

Figure 3.29.: *Upper panel: Wavelet analysis of FLAME 1 box 5 transport. The 95% significance level is marked with a black line and the COI is shaded gray. Lower panel: same for FLAME 2.*

The transport observations in Figure 3.14, (c) show that a distinctive feature within the transport variability at intermediate depths further offshoe exists, that is to say a precise seasonal as well as an interannual modulation of the 50-100 d fluctuations. Also the transport anomalies in Figure 3.28, (a) show that an iterative signal in the FLAME 2 result exists. Consequently, a wavelet analysis is applied in order to present peaking variance depending on time. Figure 3.29 shows the wavelet analysis of FLAME 1 (upper panel) and FLAME 2 (lower panel) box 5 transport. A description of the wavelet analysis application is described in section 3.2 in more detail. The 95% confidence level is marked with a black line and the COI is shaded gray.

The results of Figure 3.29, upper panel show that a band of high energy is present at 60-80 d periods over the entire time domain. Significant signals exist in boreal summer which are stronger compared to those in the rest of the year (e.g. year 2). Furthermore, it is evident that the intensity of the signal differs from year to year in the FLAME 1 result. The transport estimations of the FLAME 2 model simulation reveals interesting results (Figure 3.29, lower panel). Again, a band of significant high energy exists in the period range of 60-80 d. But the signal is clearly seasonally modulated and becomes maximal in boreal summer. Additionally only little energy is present in 2001 since the intensity of the signal differs from year to year. This result is in distinctive agreement with the observations in Figure 3.14, (c).

To summarize, the transport time series at intermediate depths outside the NBUC which are derived from the model simulations show comparable patterns to the mooring obser-

vations. ISV with 50-100 d exists which is seasonally as well as interannually modulated with maximal amplitudes in boreal summer and little energy in 2001. The comparison of the model simulations reveals evidence that ocean internal forcing influences the ISV of the mean southward transport at intermediate depths, rather than wind forcing. Additionally, it could be shown that variances at intermediate depths with periods < 50 d are not present in the model results.

3.5. Summary

The analysis of the mooring array measurements at 11°S near the western boundary has shown that ISV with periods of 50-100 d is evident locally along the section. The variability patterns are restricted to different layers, more precisely three isolated maxima of high EKE exist. The first maximum is confined to variability in the NBUC domain. Especially in the core of the NBUC the signal of ISV becomes maximal. The second maximum is located at intermediate depths outside the NBUC and the third is confined to the DWBC layer. The latter is due to the breakup of the DWBC into eddies near 8°S (Dengler et al., 2004).

The analysis of the model results FLAME 1 and FLAME 2 along the 11°S section simulate the observed distribution of high EKE in the NBUC domain, in the DWBC domain as well as at intermediate depths outside the NBUC. Further investigations show that these patterns are connected to fluctuations at periods of 50-100 d. But one difference exists, that is the variance is somewhat smaller in the model results compared to the observations, especially in the period range of < 50 d. This can partly be explained by interpolation errors.

For the analysis of variability pattern in the NBUC domain another dataset is used, i.e. basinwide measurements of the sea surface elevation from altimetry. Similar to the mooring array data, 50-100 d period ISV is evident at 11°S in the MSLA measurements. The analysis of the MSLA data also reveals that this ISV is connected to westward propagating disturbances from the interior with phase speeds of 0.1-0.2 m/s and wavelengths of 400-1000 km along the section. The propagating features are confined to the western part of the section and they are interannually modulated. In addition, phase speeds are evident which are different from linear theory. High variance in the ω/k domain is as well present in the transition region from short to long Rossby waves. Thus, evidence exists for zonal phase propagation and meridional energy transfer.

Sea surface height simulations from the FLAME 1 and FLAME 2 output show good agreement with the altimeter measurements. Westward propagating features are evident in both model results, also characterized by 50-100 d periods and about 400-1000 km wavelengths along the 11°S section. Although FLAME 1 is forced by monthly climatological ECMWF winds an interannual modulation exists in the propagating features, but also in the FLAME 2 result. Consequently it is not the wind forcing alone which is responsible for the ISV along the section. Thus, first evidence exists that ocean internal mechanisms account for the generation of ISV in the NBUC domain at 11°S.

To investigate the variability pattern at intermediate depths outside the NBUC transport, estimates from the mooring array data are analyzed. The 50-100 d fluctuations are

interannually modulated with maxima in boreal summer and a weak signal in 2001. The results from FLAME 1 and FLAME 2 show surprisingly good agreement, especially in FLAME 2 due to the interannual modulation. In addition, a comparison of both model simulations shows again that ocean internal mechanisms affect the ISV development at intermediate depths further offshore.

Besides the discussion of ISV along 11°S, one of the main results of this section is that basinwide datasets, such as the altimeter measurements and as the model simulations FLAME 1 and FLAME 2, mirror the local fluctuation patterns in the mooring array data at 11°S close to the western boundary. Thus, the aim of ongoing analysis is to investigate generating mechanisms of these ISV patterns and their connection to the southern tropical Atlantic in order to bring these results into a global context.

4. Intraseasonal variability in the intermediate layer offshore from the NBUC

The analyses of the mooring array data at 11°S near the western boundary as well as data from two model simulations show that high EKE exists in the intermediate layer offshore the NBUC, whose generation mechanisms are isolated from those in the DWBC and in the core of the NBUC. The comparison of the two model simulations reveals that internal instability mechanisms account for the generation of EKE in the intermediate layer further offshore. The mean transport in the area of interest is directed southward. The standard deviation of the transport time series exceeds the mean transport in the mooring observation and accounts for roughly 85% of the total mean in both model runs. Thus, the observed mean southward flow is accompanied by high variability which is already implied by the existence of high EKE in this area. Similar results can be found in Schmid et al. (2003) and Boebel et al. (1999a). Both studies used Lagrangian measurements which indicate that a mean southward flow exists in the layer between 500 m and 1200 m in the latitude band of 5°-12°S at the western boundary. In both results the southward deflection is associated with an eddy. During the period of eddy-like drifting the float never came close enough to the western boundary to become entrained in the NBUC. Also Schott et al. (2005) discuss

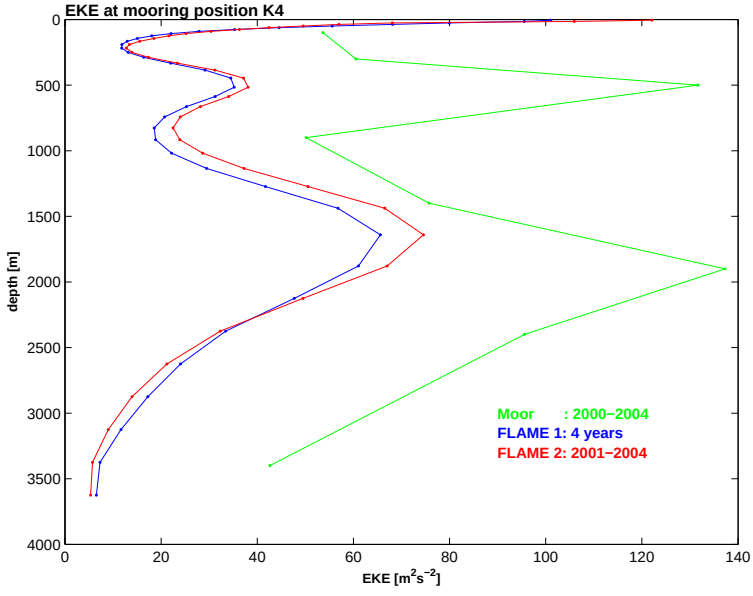

Figure 4.1.: *Eddy kinetic energy (EKE) of mooring measurements (2000-2004, green), FLAME 1 (4 years, blue) and FLAME 2 (2001-2004, red) at mooring position K4. The sampling interval of the mooring array data is adjusted to those of the model results.*

the possibility that the NBUC retroflects just north of the northeastern tip of Brazil. Not only at 11°S a southward offshore flow is evident, but also across the 5°S section as derived from a 1/12° MICOM model simulation (Schott et al., 2005, see Bleck et al. (1992) for more details on the model). In addition, an analysis of steric heights for the 800 dbar level implies a narrow cell off Brazil with southward offshore flow which is supplied by a recirculation of the NBUC, rather than by the SEC (Reid, 1989). An analysis of Suga and Talley (1995) has shown that AAIW enters the equatorial region at 4.5°S in the western boundary current, except for a long tongue that reaches at 4°S the western boundary, suggesting possible inflow from the interior. But Arhan et al. (1998) indicate that AAIW is confined to the western boundary in that region since no AAIW crosses the section in the interior. Thus, evidence exists that the long tongue east at 4°S observed by Suga and Talley (1995) hints to a recirculation pattern rather than inflow of AAIW from the interior in this latitude band.

Furthermore it is interesting to note that the EKE maximum is sharply located in a depth layer of 400-600 m which is shown in Figure 4.1. Here, the EKE derived from 4 years of mooring array data and both model simulations FLAME 1 and FLAME 2 is given at mooring position K4 which is in the center of the signal. The mooring time series are adapted to the 3 day sampling interval of the model results. The EKE show local minima at 300 and 800 m depth which can be seen in the mooring data as well as in both model runs. In addition, the comparison of the EKE in Figure 4.1 shows that the variance of the observations is generally higher as in the model simulations discussed in section 3.4. In this chapter the region of high EKE at 400-600 m depth outside the NBUC will be discussed in more detail. For this purpose mooring array data, shipboard measurements, WOCE climatology and model results will be investigated in order to discuss the origin and forcing of the signal. Finally a comparison of the results in a different numerical model shows that those fluctuations are not restricted to the FLAME simulations.

4.1. Origin of the signal

During the different deployments to service the mooring array at 11°S several shipboard measurements along the section have been made. A CTD is used to measure profiles of salinity, temperature and depth as well as a lowered ADCP (lADCP) which reveals current information (see also section 2.1.1). Altogether data from five cruises during the years 2000-2004 are used to calculate a mean salinity section along 11°S in Figure 4.2. Additionally, mean potential densities are derived from the temperature and salinity CTD measurements in order to separate and discuss different water masses (Figure 4.2, (a)).

In the near surface layer high saline water exists (Subtropical Underwater (STUC)) which is formed in the tropics and subtropics and spreads equatorward and poleward as a subsurface salinity maximum (Tomczak and Godfrey, 1994). Beneath, the South Atlantic Central Water (SACW) is centered between the isopycnals $\sigma_\Theta = 24.5$ kg/m^{-3} and $\sigma_\Theta = 27.1$ kg/m^{-3} (Figure 4.2, (a)). The SACW shows uniform properties throughout its range and its T/S relationship is described by a straight line (Schott et al., 2005, their Figure 3). In the layer of around 400-1000 m AAIW exists which is bounded between $\sigma_\Theta = 27.1$ kg/m^{-3} and $\sigma_\Theta = 32.15$ kg/m^{-3}. The North Atlantic deep water (NADW) along the boundary is marked by a salinity maximum as well as by oxygen and other tracer maxima (e.g. Rhein and Send, 1995) and can be separated by isopycnal surfaces into three layers,

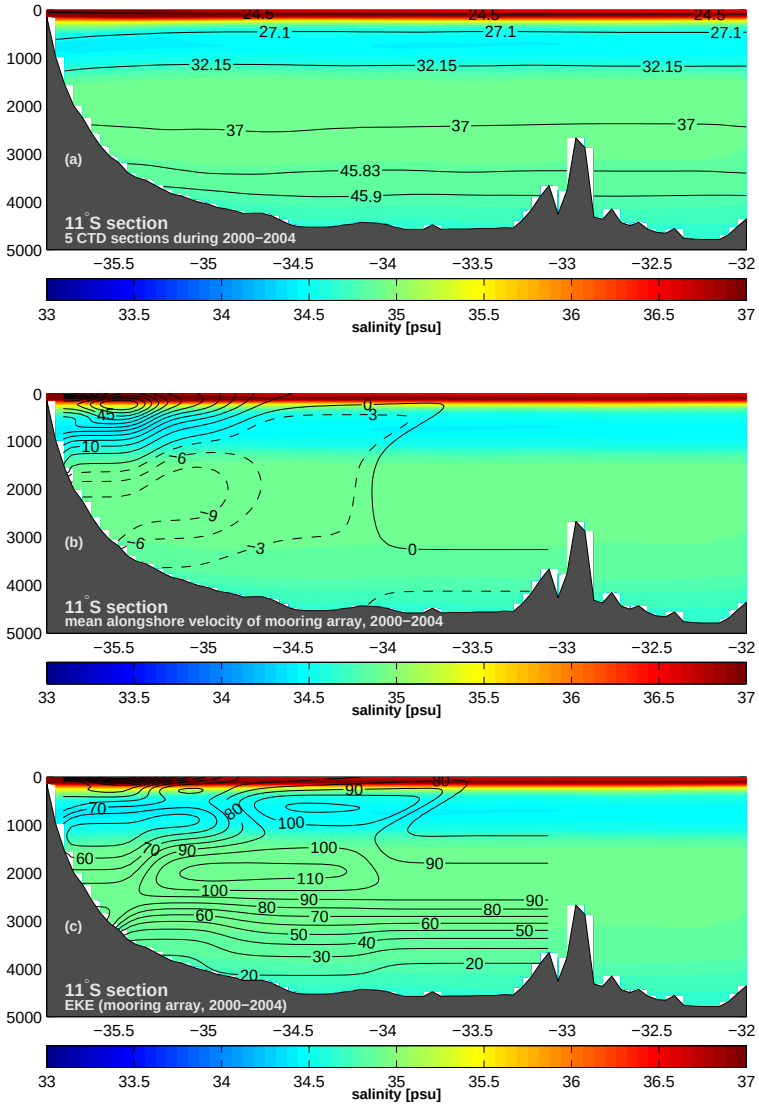

Figure 4.2.: *Mean salinity distribution along 11° S section derived from 5 CTD sections during 2000-2004 and (a) contours of mean density surfaces derived from CTD temperature, salinity and pressure [kgm^{-3}], (b) contours of mean alongshore velocity [ms^{-1}] of the mooring array in 2000-2004, (c) eddy kinetic energy (EKE) [m^{2}s^{-2}] calculated from the mooring array velocities during 2000-2004.*

namely $\sigma_\Theta = 32.15$ kg/m^{-3} and $\sigma_\Theta = 37$ kg/m^{-3} for the upper NADW (uNADW), $\sigma_\Theta = 37$ kg/m^{-3} and $\sigma_\Theta = 45.83$ kg/m^{-3} for the middle NADW (mNADW) and $\sigma_\Theta = 45.83$ kg/m^{-3} and $\sigma_\Theta = 45.9$ kg/m^{-3} for the lower NADW (lNADW) (e.g. Schott et al., 2005). Below the lNADW the northward spreading Antarctic Bottom Water (AABW) exists which originates in the Weddel Sea and in the Antarctic Circumpolar Current (ACC). This water mass is not observed anymore north of 4.5°S (Siedler et al., 1996).

Figure 4.2, (b) shows the mean alongshore velocity of the mooring array, masking the upper and lower limb of the MOC at 11°S. The NBUC spans the upper 1500 m and water masses of STUC, SACW and AAIW are transported northward whithin the boundary

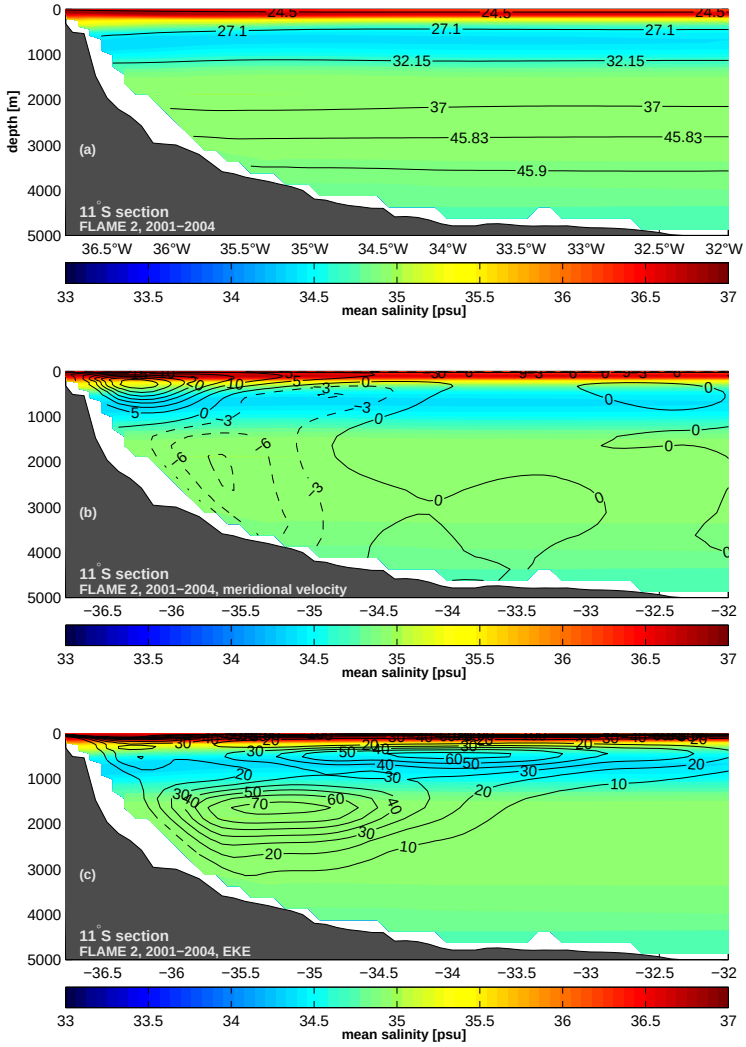

Figure 4.3.: *Mean salinity distribution along 11° S section derived from FLAME 2 salinity snapshots during 2001-2004 and (a) contours of mean density surfaces derived from FLAME 2 temperature, salinity and pressure [kgm^{-3}], (b) contours of mean alongshore velocity [ms^{-1}] of FLAME 2 in 2001-2004, (c) eddy kinetic energy (EKE) [m^{2}s^{-2}] calculated from FLAME 2 velocities during 2001-2004.*

undercurrent. The mean isopycnal surfaces are tilted downward in the periphery of strong northeastward velocities due to the NBUC (Figure 4.2, (a)). Outside the NBUC mean southward flow exists which is bounded to the depth of the AAIW layer. At 1500-3500 m depth the DWBC transports NADW southward. The core of the DWBC is located at depths of upper and middle NADW.

The EKE derived from the mooring velocities (2000-2004) is contoured in Figure 4.2, (c). Especially the EKE maximum at intermediate depths outside the NBUC is a matter of interest in this context. The comparison of salinity distribution and EKE along the 11°S section shows that a signal of high EKE is located in the layer of the AAIW and the maximum is centered near the $\sigma_\Theta = 27.1$ kg/m^{-3} isopycnal depth (compare (a)).

The mean alongshore velocity of the section is directed southward in this area. Further investigations will be done in order to discuss the contiguity between the observed mean southward transport and the signal of high EKE in the layer of the AAIW.

A mean salinity section along 11°S derived from the FLAME 2 model simulations is shown in Figure 4.3. The average is calculated from four years of model data (2001-2004) and mean isopycnal surfaces of the model output are contoured in Figure 4.3, (a) and the depths levels of those surfaces are comparable to these derived from the CTD casts (Figure 4.2, (a)). The hydrographic structure of the model result is comparable to the observations in Figure 4.2. A salinity maximum marks the STUW in the upper layer. Beneath, the salinity minimum of AAIW and the saline upper water mass fresher SACW exists. The salinity of the NADW is lower than in the observations. Below $\sigma_\Theta = 45.9$ kgm^{-3} a signal of old AABW exists.

Similar to the observations the mean meridional velocity distribution of the FLAME 2 model simulation shows that the NBUC spans the area of the upper layer water mass, central and intermediate water layers, whereas the core of the DWBC is as well centered between the isopycnal surfaces $\sigma_\Theta = 32.15$ kgm^{-3} and $\sigma_\Theta = 45.83$ kgm^{-3} (Figure 4.3, (a), (b)). The mean southward velocity at intermediate depths outside the NBUC masks as well the layer of AAIW. The maximum of EKE in this layer is located in the upper part of the intermediate layer near the 27.1 kgm^{-3} isopycnal depth (Figure 4.3, (c)). However, the model simulation shows comparable results to those derived from the observations. With the model results it is possible to extend the domain of the analysis, where missing measurements would terminate further investigations otherwise.

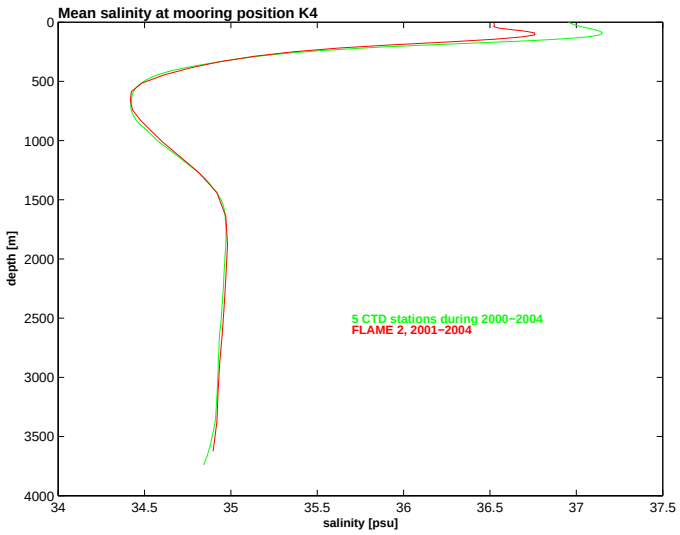

Figure 4.4.: *Mean salinity distribution with depth at mooring position K4 derived from FLAME 2 salinity snapshots during 2001-2004 (red line) and from 5 CTD stations during 2000-2004 (green line)*

The distribution of EKE with depth at mooring position K4 shows that the signal in the AAIW layer is sharply bounded to depths of 400-600 m (Figure 4.1). The distribution

of mean salinity with depth derived from 5 CTD stations (green line) and four years of FLAME 2 results (red line) is plotted as well at the mooring position K4 in Figure 4.4. Beside the salinity maximum of STUC in the upper layer a second extremum exists. In 400-600 m the salinity reaches its minimal value due to the existence of AAIW in that depths layer. Obviously the minimal salinity values of 34-34.5 psu are terminated to that sharply bounded depth layer. Comparing this result to the EKE distribution in Figure 4.1 shows that a possible connection exists between the signal of high EKE and the sharply bounded development of a salinity minimum at 400-600 m depth outside the NBUC. This possible relationship which is shown in the observations as well as in the model simulation motivates to investigate the appearance of the fluctuations in that depth level further offshore and to discuss the origin of the water mass within these fluctuation patterns.

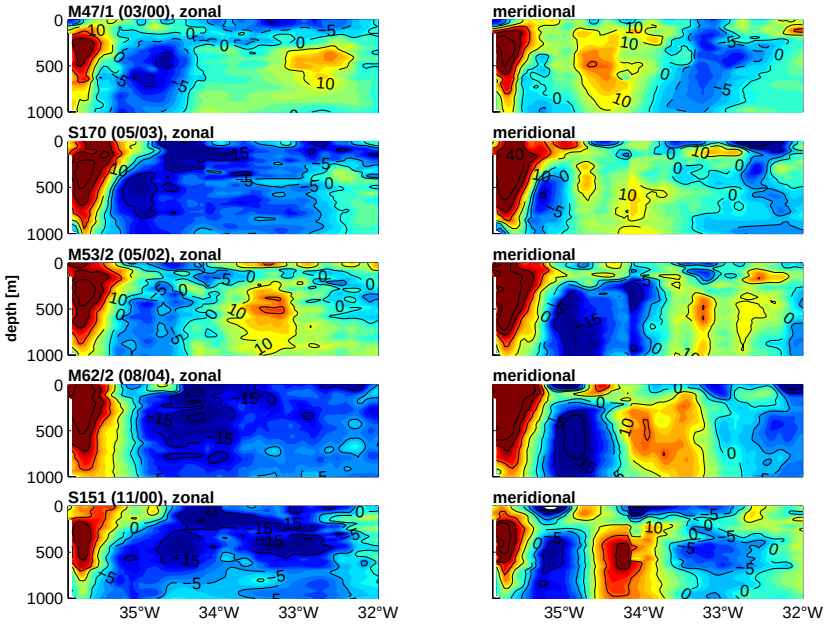

Figure 4.5.: *Zonal (right panels) and meridional (left panels) current distributions from the individual current velocity profiling surveys by ADCP/lADCP [cms^{-1}] of five sections along 11° S*

In Figure 4.5 the upper 1000 m of five individual shipboard sections of zonal and meridional velocity are shown. The NBUC is deep reaching, to about 1000 m and well developed, indicating that the bifurcation of the southern SEC is located well south of this section (Schott et al., 2005). Except in March 2000, southwestward flow exists outside the NBUC suggesting an offshore recirculation branch in the σ_Θ = 26.8 - 32.15 kgm^{-3} density range as already indicated in the mooring array data (e.g. Figure 4.2, (b)). Beside the southward current core a northward recirculation with similar strengths exists immediately offshore from the southward current core, compensated partially by some northward currents (e.g. S151, November 2000). The core of the southward velocity is centered at a depth of about 500 m, while the northward flow immediately offshore from the southward flow is located at about the same depth. The maximum velocity of both cores is about the same strength, reaching values up to 20 cms^{-1}. Especially in August (M62/2) and November (S151) these patterns are obvious in the meridional velocity sections. The zonal

velocities remain generally westward outside the NBUC, except in March (M47/1) and May (M53/2) an eastward velocity core exists offshore with maximal velocities up to 10 cms^{-1}.

The pattern of the north/south directed velocities is partly extended up to 32.5°W. This is mostly obvious in the meridional sections but also evident in the zonal measurements. The signal of high EKE in the mooring array data is located in a similar intermediate depth range outside the NBUC and appears in the easternmost measurement position (e.g. Figure 4.2, (c)). The EKE sections in both model results show that high values are achieved at intermediate depths outside the NBUC and extend to 32°W offshore, which is similar to that area of altering velocities in the CTD sections (Figure 4.3, (c), Figure 3.19 and 4.5).

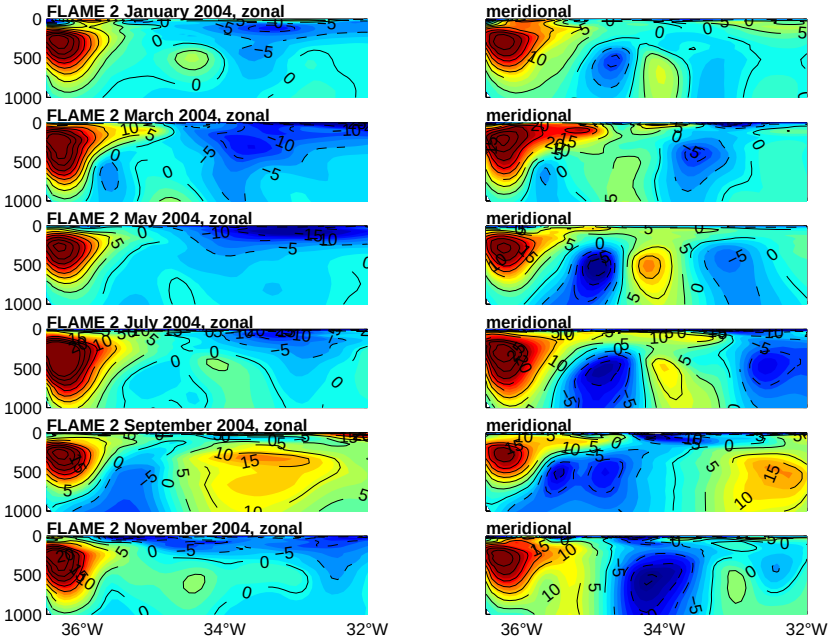

Figure 4.6.: *Zonal (right panels) and meridional (left panels) current distributions from the individual FLAME 2 snapshots [cms^{-1}] along 11° S during 2004.*

Individual snapshots of FLAME 2 meridional and zonal velocities at 11°S are shown every two months of the year 2004 in Figure 4.6 for the upper 1000 m. As also seen in the observations, the NBUC is fully established as a deep reaching continuous northeastward flow attached to the western boundary. Beside the NBUC at intermediate depths similar flow patterns as in the observations are evident in the meridional velocity sections. A southward current core exists besides the NBUC whose velocities partly exceed 10 cms^{-1} and the core is centered at about 500 m depth. Again, immediately offshore of the southward flow a northward current core appears to compensate the southward flow. The maximum velocity of the offshore core is about 5 cms^{-1} lower than its inshore counterpart. The zonal velocities outside the NBUC are mostly directed westward except of some eastward signals, e.g. in September.

Thus, the investigations of individual velocity fields from the model output and those from the shipboard measurements reveal that a pronounced dipolar velocity structure exists which is centered at intermediate depths outside the NBUC. A signal of high EKE masks the area of these patterns. A picture consistent with these patterns which are accompanied by values of high EKE is that of eddies, rotating anticyclonally or cyclonally and translating meridionally at intermediate depths outside the NBUC. The evidence of a pronounced salinity minimum at the same depths as the EKE achieves its maximal values in the upper 1000 m and suggests that these eddies contain AAIW.

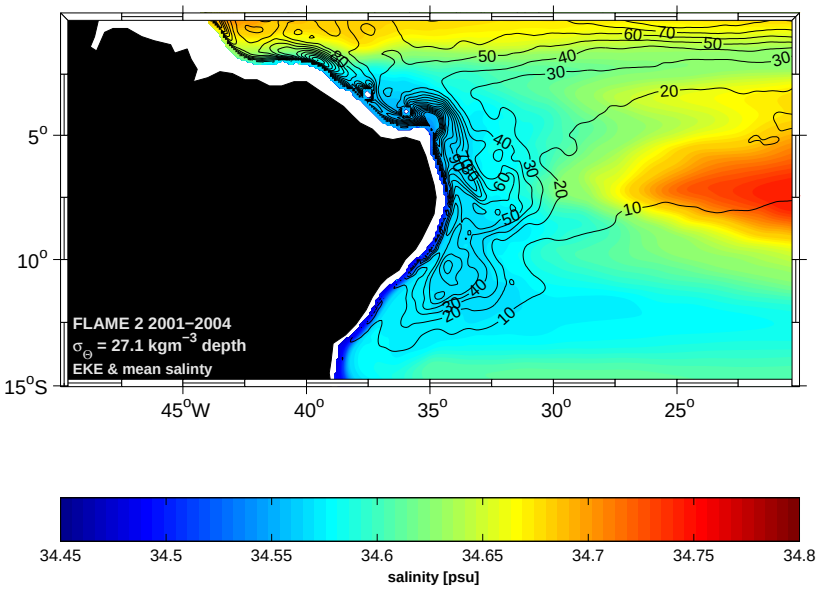

Figure 4.7.: *Distribution of mean salinity of 4 years of FLAME 2 results (2001-2004) on the* $\sigma_\Theta = 27.1$ *kgm*$^{-3}$ *density surface in the tropical southwest Atlantic. Eddy kinetic energy (EKE) which is calculated from four years of FLAME 2 velocities (2001-2004) is contoured.*

In the next step a four year mean salinity on isopycnal depths ($\sigma_\Theta = 27.1$ kgm^{-3}) is derived from FLAME 2 results in the tropical southwest Atlantic and shown in Figure 4.7. Additionally, the EKE calculated from the FLAME 2 velocity field on the same density surface is contoured. The lowest salinity values exist near the western boundary describing a direct path of AAIW from the south via the NBUC. Following the paths of the NBUC further to the north these values of salinity < 34.5 psu are only traceable until about 5°S. From that position on, salinity increases with decreasing distance from the equator. Near the equator the values exceed salinities of 34.65 psu. Thus, it is not clear whether AAIW, which is transported by the NBUC to the north and which is characterized by a pronounced salinity minimum, reaches the equator or not. A band of low salinities between 34.5-36.6 psu exists parallel to the coast which spans the domain of about 14°S to 4°S and up to 30°W offshore. Besides some areas of high EKE which can be directly connected to the NBUC this salinity band is accompanied by values of high EKE. A broad area of high EKE is centered at about 10-14°S, but the dominant signal of high EKE is concentrated in the area of 4-6°S in the periphery of the coast. These signals at around 5°S and the fact that the salinity minimum increases after this

latitude suggests that a recirculation pattern of the NBUC must exist at about 5°S which transports AAIW to the south further offshore. This recirculation cell is accompanied by eddy-like patterns further to the south. Besides the EKE maxima to the south a domain of high EKE exists between 4°S and the equator along the western boundary, indicating that a fraction of AAIW might cross the equator accompanied by high variability.

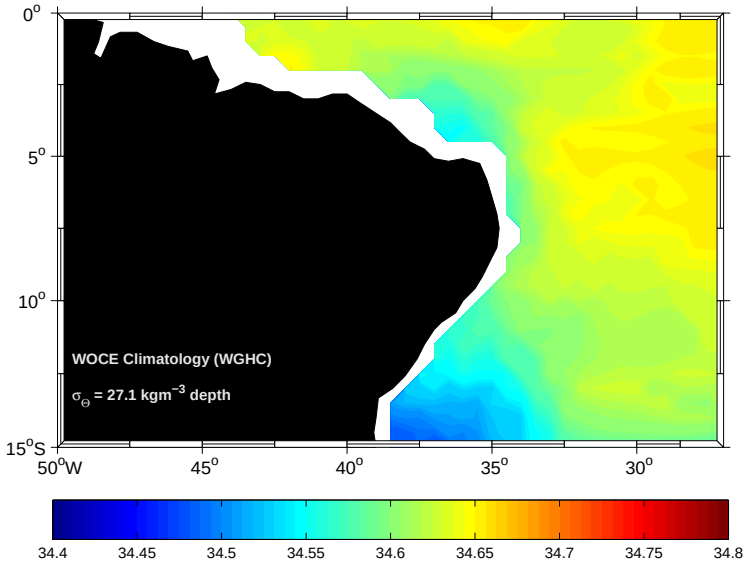

Figure 4.8.: *Distribution of mean salinity of the WOCE Global Hydrographic Climatology (WGHC) on the σ_Θ = 27.1 kgm^{-3} density surface in the tropical southwest Atlantic.*

To compare the results obtained from the model simulation to the observations a salinity distribution in the southwest tropical Atlantic derived from a climatology is examined (Figure 4.8). In order to show an independent dataset from the climatology which forces the model simulation the WOCE Global Hydrographic Climatology (WGHC) is used. For more details on this dataset the reader is referred to section 2.1.4. The data are interpolated onto depths of the σ_Θ = 27.1 kgm^{-3} density surface. As expected, a salinity minimum exists along the western boundary. It is interesting to note that similar to the model results these minimal values are confined to the domain of 4°S-15°S and till 33°W offshore. Beyond 5°S the salinity increases with decreasing distance to the equator alongshore. A possible recirculation pattern is indicated at around 4-5°S. But a differentiation between low salinities in the NBUC domain to those further offshore can not be resolved due to the sparse data coverage (0.5° spatial resolution).

Concluding, the analysis has shown that patterns of high EKE exist not only locally at 11°S, but also in a band parallel to the coast between 5°S-14°S. Additionally, the analysis indicates that a recirculation cell of the NBUC exists at around 5°S which transports AAIW to the south, accompanied by eddy-like variablity. The salinity distribution also shows that the continuous flow of a pronounced salinity minimum is terminated to the domain south of 5°S at the western boundary indicating that no direct transport of AAIW to the equator exists. But an area of high EKE is present north of 5°S at the western boundary suggesting

a possible migration of eddies which could transport AAIW to the equator, rather than a continuous flow at intermediate depths. Important to note is that the model analysis from the climatological run reveals similar results but which are not shown here for a matter of clarity.

4.2. Barotropic and baroclinic instabilities at 11°S

The available potential energy (APE) was defined by Lorenz (1955) as the difference between the total potential energy for a given sample state of the fluid and that state of the same fluid mass in the reference state, where the isentropic surfaces are horizontal. Following Oort et al. (1989) the mean available potential energy and the mean potential energy (MPE) of the fluctuations (EPE) can be written as

$$MPE = -\frac{g}{2}\frac{(\bar{\rho}-\tilde{\rho})^2}{\tilde{\rho}_z} \quad , \qquad EPE = -\frac{g}{2}\frac{\overline{\rho'\rho'}}{\tilde{\rho}_z} \quad ,$$

where g is the earth's gravity acceleration, ρ is the density of the water, overline indicates the arithmetic mean and bar denotes the deviation from the mean, respectively. The change of density is written as the difference between the local density $\rho(x, y, z, t)$ and a mean temporal density stratification $\tilde{\rho}(z)$. The mean kinetic energy (MKE) and the kinetic energy of the fluctuations are given as

$$MKE = \frac{1}{2}\rho_0(\bar{u}^2 + \bar{v}^2) \quad , \qquad EKE = \frac{1}{2}\rho_0(\overline{u'^2 + v'^2}) \quad ,$$

where u and v are the zonal and meridional velocity components and ρ_0 indicates the mean density field.

There are energy transfer terms describing the conversion between the mean energy fields MPE and MKE and its fluctuative counterparts EPE and EKE, respectively. The energy conversion terms are given as

$$T_1 = g(\overline{\rho-\rho_0})\bar{w} \quad \text{(exchange MPE and MKE)} \tag{4.1}$$

$$T_2 = -\frac{g}{\tilde{\rho}_z}(\overline{\mathbf{u}'\rho'}\cdot\nabla\bar{\rho}) \quad \text{(baroclinic instability)} \tag{4.2}$$

$$T_3 = g\overline{w'\rho'} \quad \text{(exchange EPE and EKE)} \tag{4.3}$$

$$T_4 = \rho_0(\overline{\mathbf{u}'\mathbf{u}'}\cdot\nabla\bar{\mathbf{u}}) \quad \text{(barotropic instability)} \tag{4.4}$$

Regarding nomenclature, variables printed in bold letters denote vectors, whereas others represent scalars. T_2 describes the exchange between MPE and EPE and is sometimes referred to as baroclinic instability. T_2 shows up if there is a vertical shear of the mean flow. T_4 describes the exchange between MKE and EKE caused by horizontal shear of the mean flow and is called barotropic instability.

To illustrate the relations between the different components in the Lorenz cycle (Lorenz, 1955), it is often useful to study the components in the context of an energy box diagram of the form shown in Figure 4.9. Important to note is that forcing, advection, pressure work, friction and diffusion are neglected in the energy cycle (indicated by external arrows in Figure 4.9). The arrows show the direction of the energy transfer between the mean energy fields and their fluctuative part, respectively. Important to note is that one has to regard

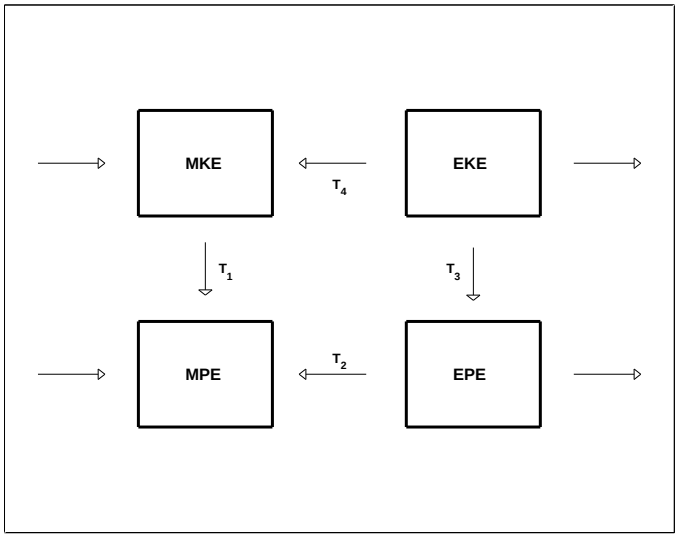

Figure 4.9.: *The energy cycle following Lorenz (1955). See text for more information.*

the sign of T_1 to T_4 for ongoing description of the box diagram in Figure 4.9. However, the box diagram shows that for the case of a positive value of T_4, energy is transfered from the fluctuative field into the mean current. For the case of a negative value of T_4 energy is transfered from the mean current into the perturbation and EKE is generated. Thus, the mean current will be destabilized. A positive value of the baroclinic instability term T_2 would produce an increase of MPE because energy is transformed from the perturbation into the mean state. On the other hand, a negative value of T_2 describes the conversion of energy from a mean state into the fluctuation and the instability of the current increases. Additionally, a discussion of the transfer term T_3 which describes the energy transition between the turbulent fields might help to understand ongoing mechanisms in the domain of interest. With the direction of the energy transfer (e.g. negative T_3 means energy transfer from EPE to EKE) it is possible to investigate whether barotropic or baroclinic instabilities might play a dominant role in generating fluctuation patterns. Finally, a negative value of T1 means that energy is transfered from MPE to MKE which is due to the mechanisms described in the beginning of this section.

In this section the energy transfer terms (e.g. barotropic and baroclinic instabilities) will be calculated from the mooring array data as well as from the model results along 11°S. The results will be discussed in a section along 11°S derived from a different numerical model. Besides these local investigations a basinwide discussion of the energy transfer and generation will be done for the tropical southwestern Atlantic using results of the FLAME model simulation.

4.2.1. Generation of eddy kinetic energy along 11°S

In this section the distribution of barotropic and baroclinic instability terms will be investigated along 11°S. For this purpose, data from the mooring array at 11°S will be used. Additionally, the corresponding quantities are evaluated from the FLAME model simulation as well in order to compare the model results to those obtained from the measurements.

Barotropic instability term T_4

The energy transfer term T_4 is calculated from the meridional and zonal velocity components of the mooring array data. They consist of variances and covariances, e.g. $\overline{u'u'}$ and $\overline{u'v'}$ and of the shear of the mean current orientated normal and parallel to the center of the mean current (equation 4.4). From the mooring, only a fraction of T_4 can be calculated, namely

$$T_4^* = \overline{u'^2}\frac{\partial \overline{u}}{\partial x} + \overline{u'v'}\frac{\partial \overline{v}}{\partial x} \quad ,$$

because the derivative in meridional direction can not be calculated from the available mooring array data. In Figure 4.10 the covariance, variance shear terms and the combined expressions describing the zonal barotropic instabilities are derived from the mooring array data. The variance and covariance are calculated at each measurement position and finally gridded on a regular 5 km by 20 m grid using Gaussian weights. The zonal changes of velocities are calculated after gridding the mean zonal and meridional velocities on the same regular grid.

Since only a fraction of the energy conversion can be calculated from the mooring array data it is difficult to discuss these distributions and possible results regarding instability mechanisms may not be robust. But the analysis is important to compare T_4^* to the corresponding model results. Thus, if good agreement is evident, the complete T_4 term can be evaluated from the model results on the basis that similar signals are apparent in the

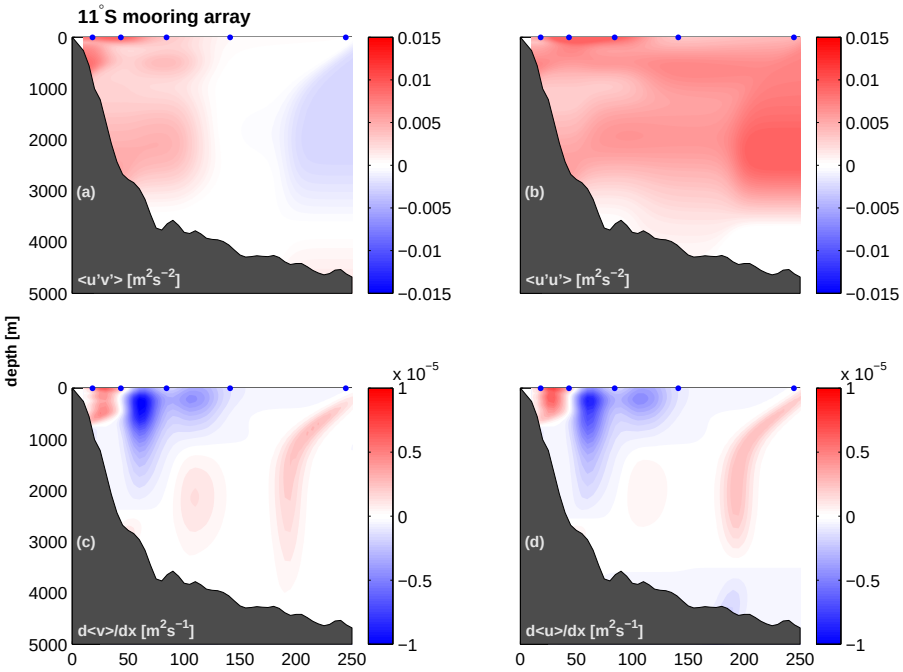

Figure 4.10.: *Distribution of (a) covariance $\overline{u'v'}$ and (b) variance $\overline{u'u'}$ in $[m^2s^{-2}]$, (c), (d) zonal changes of mean velocities $[m^2s^{-1}]$ calculated from the mooring array data along 11° S. Mooring positions are indicated with a blue marker, respectively.*

observations.

However, the covariance term $\overline{u'v'}$ (Figure 4.10, upper panels) reveals a bimodal structure with positive values near the western boundary and negative correlations further offshore. Several maxima of positive correlations in the western part of the section exist from which one is confined to the NBUC domain one at intermediate depths and the other in the DWBC domain. The variance of the zonal velocity reaches maximal values in the NBUC and DWBC domain, as well as in the AAIW layer outside the NBUC. Especially the band of maximal correlations at intermediate depths is extended till the eastern edge of the section.

The shear of the zonal and meridional velocity fields (Figure 4.10, (c) and (d)) reflect the prevailing mean current system as illustrated in Figure 3.12. With increasing distance from the coast the zonal shear remains negative. This domain of negative values is extended till intermediate depths. Small scale changes at the offshore mooring position are due to the mapping, particularly for the reason that no measurements are available in the upper 1000 m at mooring position K5. The changes of velocity at depths of 1000-3000 m remain small. The sign of the shear values changes at about 100 km distance from the coast from negative to positive values indicating an inflection point of velocity strengths, possibly due to the migrating eddies pointed out by Dengler et al. (2004).

To compare the observations to the model results, corresponding expressions such as the covariance and variance $\overline{u'v'}$ and $\overline{u'u'}$ and the shear terms are calculated from the model simulations (Figure 4.11). Here, the FLAME 1 results are investigated. The model

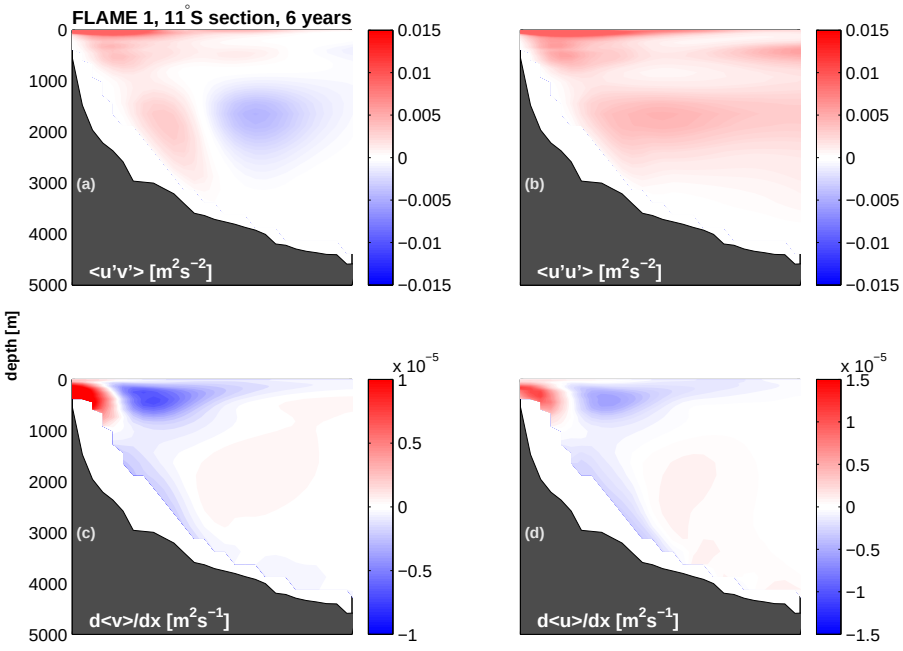

Figure 4.11.: *Distribution of (a) covariance $\overline{u'v'}$ and (b) variance $\overline{u'u'}$ in $[m^2s^{-2}]$, (c), (d) zonal changes of mean velocities $[m^2s^{-1}]$ calculated from the FLAME 1 model results along 11° S.*

data of FLAME 2 show similar results and are therefore not shown in this section. The variances and covariances are calculated at each grid point. The shear terms are derived by calculating centered differences on interior points and forward differences are used on the left and right edges. Means are derived from 6 years of model data.

The model calculations reveal similar results to those obtained from the mooring array data. The distribution of the covariances remains positive in the western part of the section and changes sign in deeper layers further offshore. The variance of the zonal velocities shows maxima in the near surface layer within the NBUC domain, in the DWBC domain and at intermediate depths outside the NBUC. Zonal shear of velocity changes sign in the area of maximal NBUC velocity (Figure 4.2, (b)) and remains negative outside the NBUC in the upper 1000 m, indicating a decrease of the mean velocity field. At around 1000-3000 m depth the zonal shear terms change sign, but the values tend towards zero.

Summarizing briefly, the comparison of the model simulation to the observations indicates that the distribution of T_4^* (consiting of covariance, variance and shear terms) shows distinctive agreement. Thus, the complete T_4 term can be evaluated from the model simulations on the basis that similar signals are apparent in the observations.

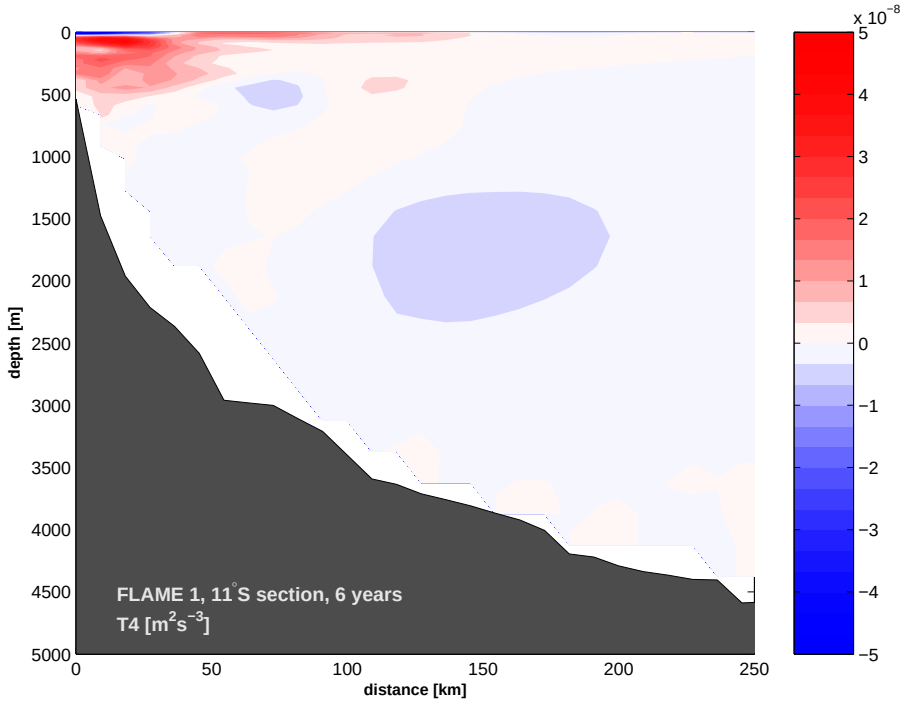

Figure 4.12.: *Distribution of the barotropic instability term T_4 (equation 4.4) $[m^2 s^{-3}]$ calculated from six years of FLAME 1 model simulation along 11° S. Negative sign denotes transfer into the fluctuations.*

The distribution of the complete barotropic instability term T_4 (equation 4.4) along 11°S is shown in Figure 4.12. T_4 is calculated from six years of FLAME 1 data. As expected, three areas of high values exist which hint to energy conversion between MPE and EPE. In the domain of the NBUC T_4 remains positive which means that energy is

transformed from the fluctuation into the mean current, except for one region, that is a domain of negative values in the near surface layer close to the western boundary. Outside the NBUC at intermediate depths an area of negative values exists. A negative sign of T_4 indicates that EPE is generated by barotropic instabilities. Close to that negative pattern a positive signal of T_4 is evident about 130 km offshore indicating that the mean current might be stabilized. But compared to these values obtained in the NBUC domain T_4 is weak in the AAIW layer and within the DWBC domain which means that the area of generating the fluctuations, which have been previously discussed, is centered further north or south, rather than locally at 11°S. In particular Dengler et al. (2004) already showed that the generation of fluctuative variability in the DWBC domain is centered further to the north due to the break up of the DWBC at 8°S. Thus, further investigations need to be done in order to describe the generation mechanisms of the fluctuation pattern at intermediate depths outside the NBUC. Either baroclinic instabilities generate fluctuative energies in that area or the EKE is generated further to the north or to the south.

Baroclinic instability term T_2

The energy transfer term T_2 contains covariances $\overline{u'\rho'}$ and $\overline{v'\rho'}$ as well as the ratio between horizontal and vertical changes of density. For the mooring array data, only the deviation in x-direction can be calculated, i.e.

$$T_2^* = -\frac{g}{\rho_0}\overline{u'\rho'}\frac{\partial\overline{\rho}/\partial x}{\partial\overline{\rho}/\partial z} \quad . \tag{4.5}$$

The calculation of the baroclinic term from the mooring array data is somewhat more complex. To estimate the potential density temperature and salinity are needed. During the deployment period of the mooring array only temperature records are available. These measurements exist at several depths and the area between K2 and K4 and from 300 to 2400 m depth is covered more or less by temperature measurements. Salinity information is only available from shipboard measurements along the 11°S section during 2000-2004. The average salinity section calculated from these CTD measurements is shown in Figure 4.2. The mean T/S relationship derived from CTD measurements during five surveys at mooring position K2, K3 and K4 is examined. Then, a salinity time series is derived at every instrument depths by estimating the salinity due to the mean T/S relationship. Thus, a time series of salinity as a function of temperature from the mooring array is examined. Together with the temperature records the potential density is calculated, whereas the surface is considered as the reference level. The covariance $\overline{u'\rho'}$ is then estimated at every instrument depth and then interpolated on a regular depth 50 m sampling interval. The mean potential densities are evaluated from five CTD casts at each mooring position, respectively. Then, the horizontal and vertical changes of mean density are computed using centered differences on interior points and forward differences on the left and right edges.

As already mentioned before, investigating a fraction of the total energy transfer term in the available observations, that is in this case T_2^*, establishes the possibility to compare the observations to the model results. Then, if good agreement is evident, the complete T_2 term can be evaluated from the model simulations. Investigating T_2^* alone would lead to results and suggestions which do not appear to be robust.

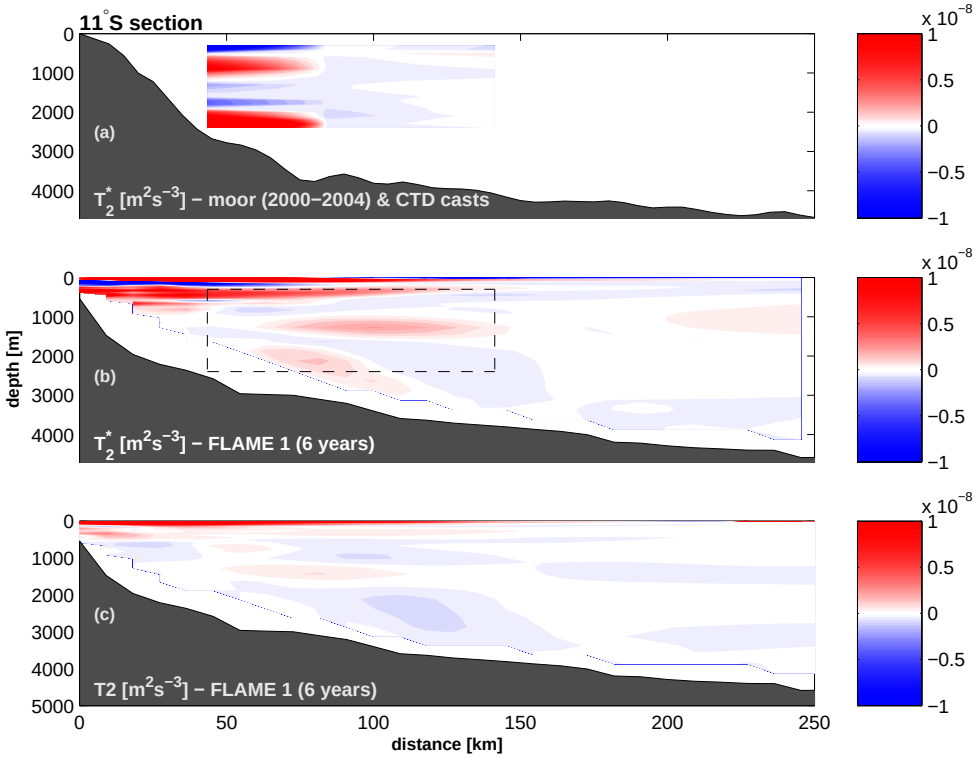

Figure 4.13.: *(a) Distribution of T_2^* $[m^2 s^{-3}]$ calculated from the mooring array data and several CTD casts at 11° S (see text for more details). (b) same as in (a), but derived from the FLAME 1 model simulation along the entire 11° S section. The area covered by the observations is marked with a dashed line. (c) Distribution of the baroclinic instability term T_2 (equation 4.2) evaluated from the FLAME 1 model simulation along 11° S. Negative sign denotes transfer into the fluctuations.*

But nevertheless, corresponding comparisons are shown in Figure 4.13. In (a), T_2^* is calculated from the observations as described above and (b) shows the similar distribution, but derived from the model simulation FLAME 1 (six years) and along the complete 11°S section. The area which is covered by observations is marked with a dashed line. Figure 4.13 (a) and (b) show that it is difficult to compare the distributions of T_2^* from the observations and the model results. T_2^* changes sign several times and remains negative further offshore. Near the boundary, T_2^* becomes positive in about 1000 and 2000 m, which is evident in the observations as well as in the model results. But the distribution of T_2^* along the section in (b) also indicates that T_2^* is sensitive to local changes which underlines the assumption that a discussion of T_2^* alone would lead to misinterpretations and thus the complete T_2 term is evaluated from the model results.

The lower panel of Figure 4.13 shows the distribution of T_2 (equation 4.2) along the 11°S section, which is calculated from six years of the FLAME 1 model simulation. The area masking the NBUC domain shows generally positive values until about 1000 m depth which is more or less the lower edge of the NBUC in the FLAME simulation (compare Figure 4.3, (b)). Thus, the NBUC domain is characterized by positive values of T_2 indicating that the NBUC is stable at 11°S. At intermediate depths an area of negative values exists indicating

a generation of EPE. Also in the domain of the DWBC the values of T_2 become negative according to DWBC eddy variability (Dengler et al., 2004). But the values of T_2 in both areas remain small which indicates that the main area of generating high fluctuative energies must be located somewhere else, rather than locally at 11°S.

Summary

The barotropic and baroclinic energy exchange terms along the 11°S section are discussed. As expected, three areas of dominant barotropic and baroclinic energy transfer terms exist which hint to energy conversion between the mean energy field and its turbulent counterpart, i.e. the NBUC and DWBC domain as well as in the AAIW layer outside the NBUC. In the NBUC domain however, the values remain generally positive, while small areas of negative values of T_2 and T_4 exist in the NBUC domain in the near surface layer close to the western boundary indicating that a conversion of the mean current into the fluctuation exists. A distribution of EKE along the section shows high values in this area, but for a discussion on the variability in the near surface layer the reader is referred to chapter 5.

In the domain of the DWBC negative values exist. But these values are small because of the fact that fluctuative energy is mostly generated further to the north (Dengler et al., 2004). In the domain of the AAIW layer further offshore the baroclinic as well as the barotropic terms become negative. Thus, evidence exists that EKE is generated at 11°S due to barotropic and baroclinic instabilities but these values are small as well. This indicates that EKE in the AAIW layer outside the NBUC is mostly generated further to the north or to the south, rather than locally at 11°S, which will be investigated in the following.

4.2.2. Generation of eddy kinetic energy in the southwestern tropical Atlantic

The previous investigations have shown that at 11°S in the AAIW layer outside the NBUC a signal of high EKE exists, as well as in the NBUC and DWBC domain. To extend this result, the vertical EKE distribution at all depths in a band 2° parallel to the coast and further to the north is shown in Figure 4.14. The results from the FLAME 2 model simulation are used here for the years 2001-2004 and the FLAME 1 results are neglected due to the fact that these distributions are comparable to the results shown in Figure 4.14.

Several peculiarities can be discussed in the EKE distribution. Three depth layers show enhanced EKE levels. In the near surface layer the EKE increases with decreasing distance to the equator and maximum values are achieved at 5°S. In the domain of the DWBC it is interesting to pursuit the results obtained from Dengler et al. (2004). Between 1500-2000 m depth high EKE exists south of 8°S latitude since the DWBC breaks up into eddies at this point. The EKE achieves maximal values at about 9°S and decreases further to the south. At 6°-7°S a domain of high EKE exists at 2500-3500 m depths, which is not further discussed here.

In the AAIW layer at about 500 m depth a domain of high EKE is evident. The analyses of the mooring array data as well as of the model simulations have shown that the area of high EKE in that layer is limited to 400-600 m depth (Figure 4.1). In Figure 4.14 this is evident in a latitude band of about 8.5°S to 11°S. Further to the north the signal is

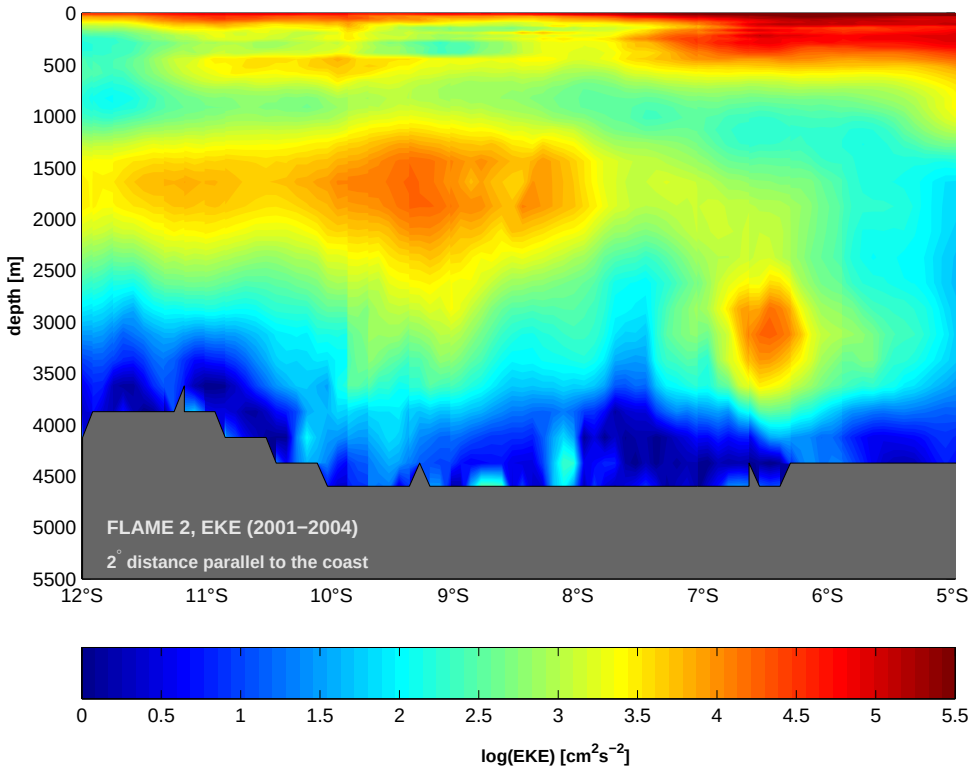

Figure 4.14.: *Distribution of EKE in a band 2° parallel to the coast between 12°S and 5°S. The EKE is calculated from 4 years of FLAME 2 results (2001-2004).*

extended from about 500 m up to the surface indicating that not only the AAIW layer but also the entire NBUC domain is joined in the mechanisms generating EKE close to the western boundary.

To analyze possible generation mechanisms of enhanced EKE found in the western south Atlantic, the barotropic instability term is examined in this area. A distribution of T_4 (equation 4.4) is shown in Figure 4.15 (upper panel) for the 500 m depth layer derived from six years of FLAME 1 results. The distribution displays an interesting aspect, i.e. generally negative values close to the western boundary, changing sign immediately beyond to positive values, which is followed by a domain of negative values further offshore. Beyond this point at about 2° distance from the coast the values drop to zero. The meridional pattern is bounded between about 12°S to 5°S. Besides some small areas of positive values in the domain close to the boundary, the values of T_4 are generally negative indicating a conversion from mean kinetic energy into EKE. In other words, the NBUC transfers energy into EKE and the western boundary current becomes unstable, especially at about 4°-5°S where the values become strongest (Figure 4.15 (upper panel)). In contrast to this the analysis of barotropic instabilities locally at 11°S has shown that the values of T_4 are generally positive in the NBUC domain, indicating that the NBUC is stable at 11°S (Figure 4.12). This shows that evaluating the instability term at the section is very sensible to local changes and it is important to investigate the surroundings since small-scale spatial variability in the terms exist and regional budgets are not robust (Beckmann et al., 1994).

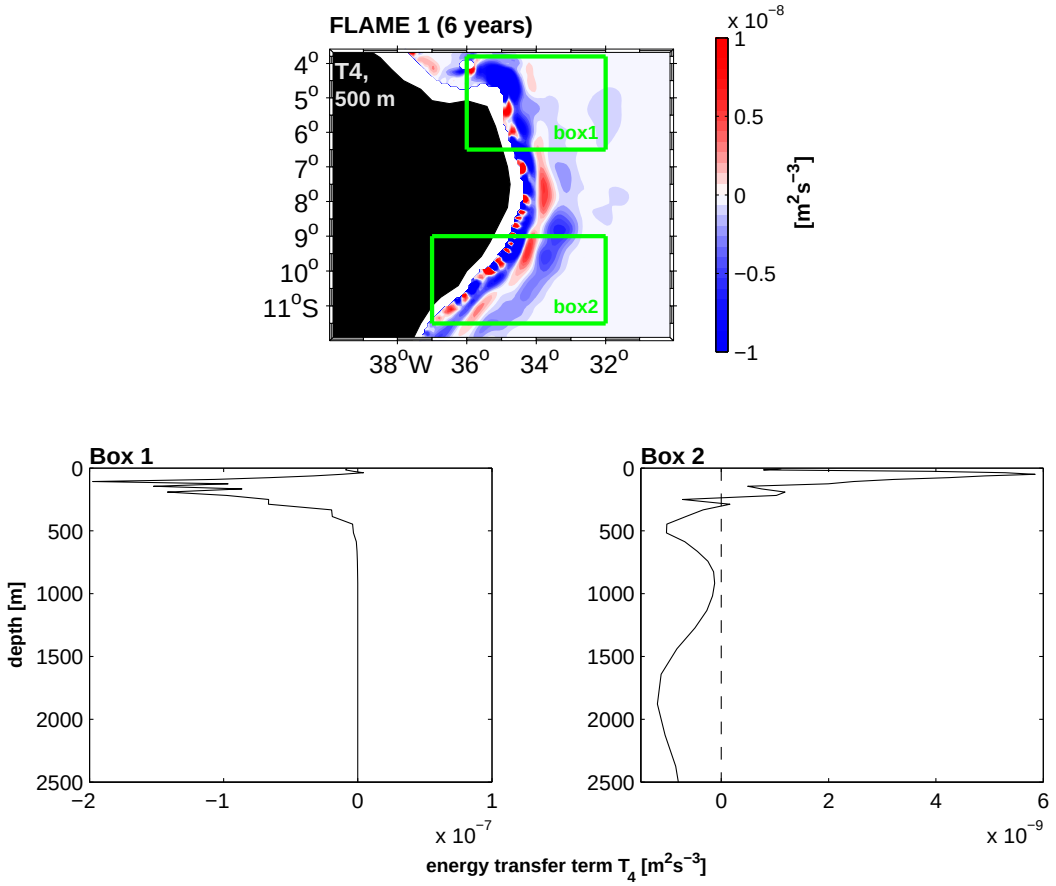

Figure 4.15.: *Distribution of the barotropic instability term T_4 $[m^2 s^{-3}]$ at 500 m depth in the south-western tropical Atlantic (upper panel). T_4 is calculated from six years of FLAME 1 model results. Lower panels: Vertical distribution of box 1 (left) and box 2 (right) mean T_4. Corresponding box boundaries are marked in the upper panel. Negative sign denotes transfer into the fluctuations.*

The area of positive T_4 shows that energy conversion from EKE into MKE exists which probably hints to a recirculating southwestward flow in the AAIW layer. The discussion of the mooring array data (e.g. section 4.1) and the analysis of RAFOS float trajectories (Boebel et al., 1999a; Schmid et al., 2003) coincide with this assumption. Furthermore, the EKE distribution with depth along the coast shows that high EKE between 400-600 m depth is bounded by 8.5°-11°S and 5°-7°S (Figure 4.14). The generation of these distributions can be explained with Figure 4.15 (upper panel). The offshore band of the T_4 meridional pattern is characterized with a negative sign, especially at 9°-10°S where these values become maximal. This shows that EKE is generated mainly at 9°-10°S due to barotropic instability. The mean current, e.g. the recirculation cell becomes destabilized because MKE is converted into EKE. This would explain different results from the previous analysis, that is high EKE values at intermediate depths outside the NBUC (e.g. Figure 4.2, (c)) and the band of high EKE between 9°-11°S (Figure 4.14). The latter result is associated with the fact that in Figure 4.15 (upper panel) the strongest negative values are achieved at about 9°-10°S outside the NBUC.

In addition, high values of T_4 at 500 m depth (Figure 4.15, upper panel) as well as of EKE in the upper 1000 m (Figure 4.14) are observed at 4-5°S, respectively. The negative sign of T_4 denotes that a conversion from the mean current into the fluctuations is evident. But this result is confined to the 500 m depth layer. Thus, an investigation of instability mechanisms with depth is needed. Therefore, the mean distributions of T_4 in two different boxes (marked in Figure 4.15, upper panel) are evaluated. These distributions are shown in the lower panels of Figure 4.15.

The distinctive signal is evident in the upper 500 m of the box 1 mean, peaking at about 200 m (Figure 4.15, lower left panel). The sign of T_4 remains negative in this depth layer and drops to zero energy conversion below about 500 m depth. The vertical distribution of EKE in this domain shows increased EKE as seen in Figure 4.14. Consequently, evidence exists that the NBUC becomes destabilized at about 4°-5°S and EKE is generated in this area due to barotropic instability. With calculating the mean values marked off by box 2 the situation changes for the upper 500 m (Figure 4.15, lower right panel). Values of T_4 are generally lower and T_4 changes sign. EKE obviously decreases in the NBUC domain further to the south (Figure 4.14). Although low, stabilizing mechanisms of the mean field due to barotropic instabilities exist south of 8°S which counteract the generation of EKE further north.

Below about 500 m depth two noticeable minima exist, that is sharply bounded peaks between 500-600 m and 1500-2000 m depth. T_4 drops to zero between both extrema but never becomes positive. This means that EKE is generated at intermediate depths and in the DWBC domain because of the influence of barotropic instability south of 9°S. The generation of EKE is confirmed by Figure 4.14, where EKE drops to zero north of about 8°S in the DWBC domain and is bounded to 400-600 m depths.

In the next step the energy transfer term due to baroclinic instability T_2 (equation 4.2) is examined in the southwestern tropical Atlantic. The distribution of T_2 at 500 m depth is evaluated from six years of FLAME 1 data and contoured in Figure 4.16 (upper panel). The distribution of T_2 appears to be more complex and less dominant compared to the barotropic instability term, because several areas of altering sign of T_2 exist and the T_2 values seem to be generally lower. As pointed out before, this shows that local budgets are not robust and it is important to incorporate the results along 11°S into a basinwide point of view. First, the domain of the NBUC close to the western boundary will be a matter of discussion. Between 9°-11°S T_2 is mostly negative indicating that the NBUC becomes destabilized in this area. This again does not coincide with the instability analysis locally along 11°S in section 4.2.1. Further to the north T_2 changes sign several times and it is not possible to examine whether a stabilizing or destabilizing mechanism prevails. Further offshore an area of positive values exists between 7°-11°S pointing to an energy conversion from the perturbation into the mean current. Thus, further evidence exists that a mean recirculation cell is formed outside the NBUC which transports AAIW to the south and which is generated by baroclinic as well as by barotropic instabilities.

The lower panels of Figure 4.16 show the vertical distribution of box 1 (left) and box 2 (right) mean T_2, respectively. Corresponding box boundaries are marked in the upper panel of Figure 4.16. Due to the fact that the definition of EPE in section 4.2 is in

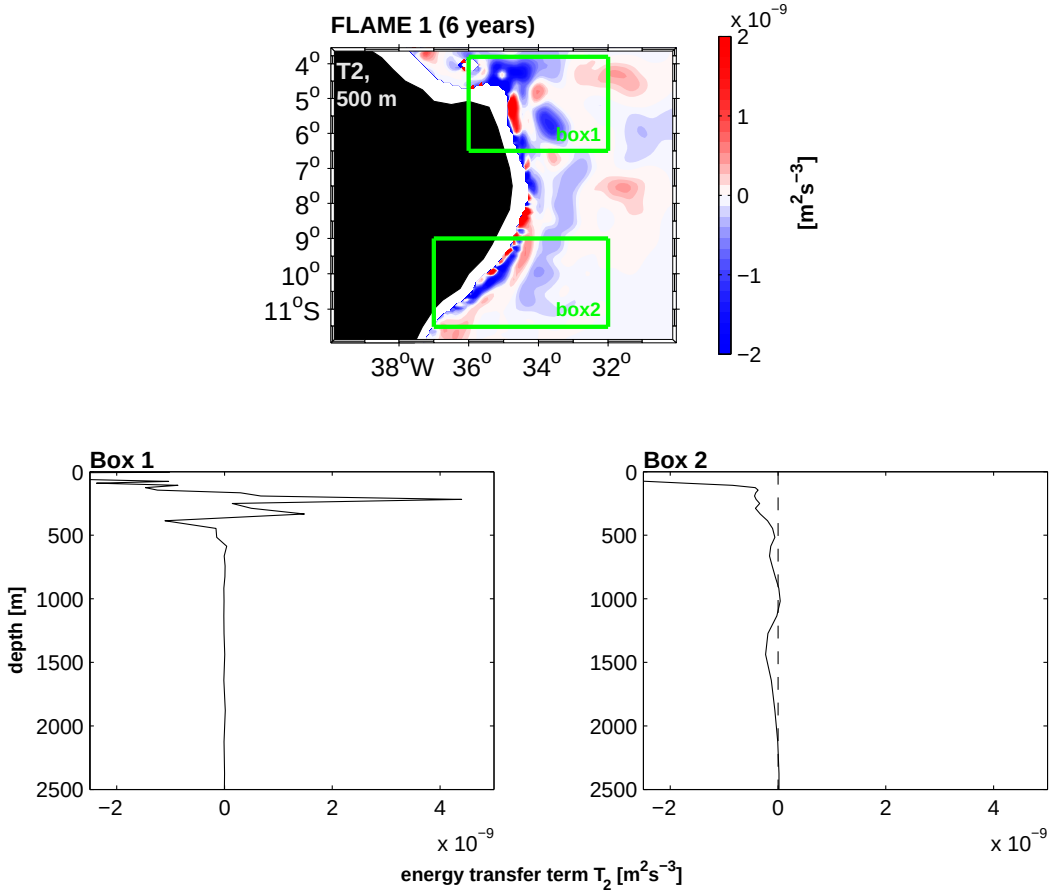

Figure 4.16.: *Distribution of the baroclinic instability term T_2 $[m^2 s^{-3}]$ at 500 m depth in the south-western tropical Atlantic (upper panel). T_2 is calculated from six years of FLAME 1 model results. Lower panels: Vertical distribution of box 1 (left) and box 2 (right) mean T_2. Corresponding box boundaries are marked in the upper panel. Negative sign denotes transfer into the fluctuations.*

principle only valid for infinitesimal small vertical excursions of the isopycnal, values of T_2 increase unrealistically in the near surface layer and are not shown at depths below 20 m.

Compared to the magnitude of T_4 in Figure 4.15 values of T_2 are generally lower. The highest values of T_2 result from the box 1 mean in the upper 500 m. Between about 100-400 m the values of T_2 are positive which points to an energy conversion from EPE into MPE (Figure 4.9). As seen in Figure 4.15, EKE is generated due to barotropic instability whereas baroclinic instability, although comparably small, acts to stabilize the mean current field in that depth range. Below 400 m, T_2 decreases and becomes negative between about 400-600 m depth (Figure 4.16, lower left panel). Negative sign denotes flux into the fluctuations. Thus, baroclinic as well as barotropic instability contribute to the generation of fluctuative energy at intermediate depths, from which the influence of the latter mechanism is considerably stronger. Further south values of T_2 decrease and remain negative (Figure 4.16, lower right panel). Local extrema exist, that is at intermediate depths and in the DWBC domain. But values are small. Interesting to note is that in both box means T_2 rapidly drops to zero below about 500 m depth. The reason why the

baroclinic instability drops to zero is due to the fact that the crossover from central water to intermediate water is evident in this depth layer. The distribution of mean salinity in Figure 4.4 shows that a strong salinity gradient exists at 500 m depth and salinity reaches its absolute minimum. Consequently, vertical changes of potential density must be strong in the transition from central to intermediate water masses. The term of T_2 includes the change of mean potential density with depth, i.e. the stratification. The term $\frac{\partial\overline{\rho}/\partial x}{\partial\overline{\rho}/\partial z}$ as well as $\frac{\partial\overline{\rho}/\partial y}{\partial\overline{\rho}/\partial z}$ decreases which is obviously the reason for the weak values of T_2 in that depth layer. Thus, the generation of EKE is interrupted at about 500 m since no energy flux into the fluctuations is evident. Below 500 m, values of T_2 increase but remain low. As shown in Figure 4.15 horizontal instability produces EKE at intermediate depths. Negative values of T_4 decrease below about 500 m depths due to the fact that current shear decreases (e.g. Figure 4.2, (b)). As seen before, baroclinic instability contributes as well to the generation of fluctuative energy in that depth layer and decreases below 500 m depth due to strong changes in stratification. Consequently, EKE is generated by barotropic and baroclinic instability at intermediate depths, which seems to be shielded from the mechanisms below.

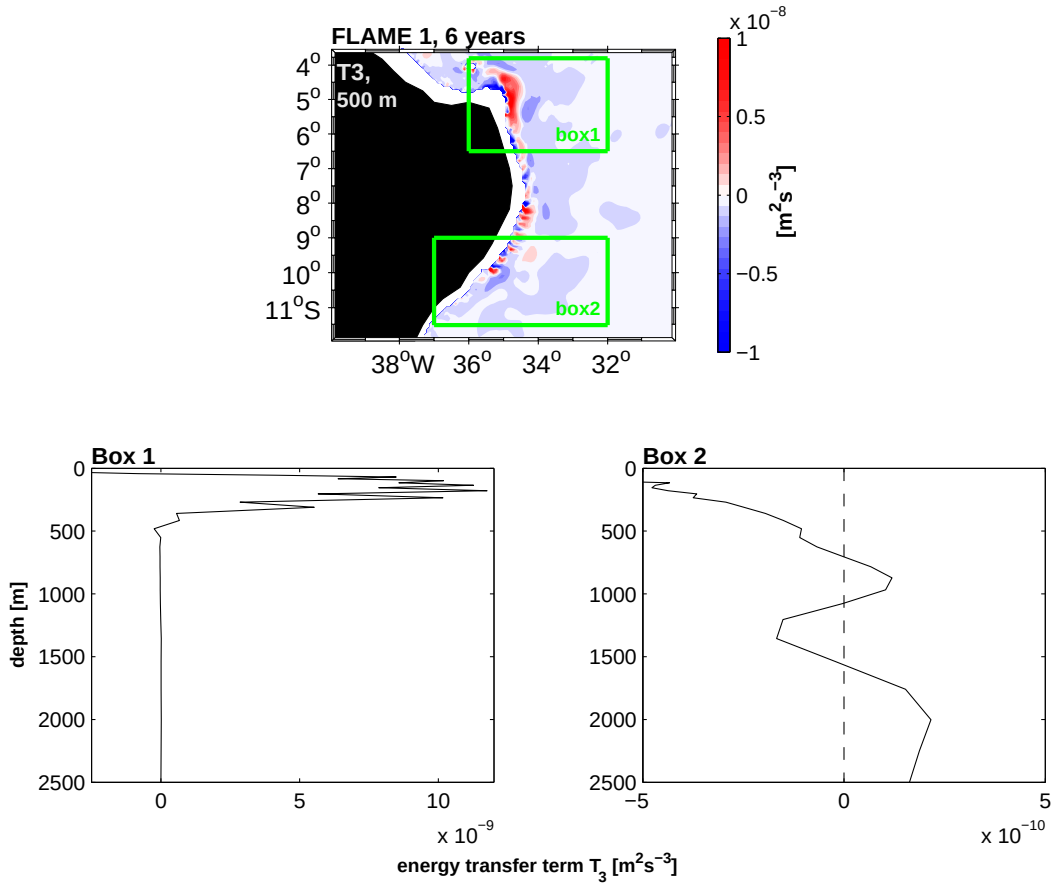

Figure 4.17.: *Distribution of the energy transfer term T_3 $[m^2s^{-3}]$ at 500 m depth in the southwestern tropical Atlantic (upper panel). T_3 is calculated from six years of FLAME 1 model results. Lower panels: Vertical distribution of box 1 (left) and box 2 (right) mean T_3. Corresponding box boundaries are marked in the upper panel. Negative sign denotes transfer from EPE into EKE.*

Another interesting expression describes the interaction between EKE and EPE. This energy conversion term T_3 is evaluated from the covariances between vertical velocity and density (equation 4.3). The distribution of T_3 in the southwestern tropical Atlantic at 500 m depth derived from six years of FLAME 1 results is shown in Figure 4.17 (upper panel). Especially in the area close to the western boundary the sign of T_3 alters strongly about zero. These small-scale spatial variabilities in the T_3 term result from upwelling and downwelling caused by flow over rough bottom topography since the transfer term involves the vertical velocity (Beckmann et al., 1994). However, the values of T_3 close to the western boundary are generally positive, indicating a transfer from EKE to EPE (Figure 4.9). This agrees well with the fact that EKE is produced in this area rather than EPE (Figure 4.15 and 4.16). Positive T_3 becomes strongest at about 4°-5°S. Again, this coincides with the distribution of T_4 whose minima exist at about 4°-5°S as well, indicating an increased generation of EKE in this area. Outside the NBUC domain values of T_3 remain negative and their strength decreases with increasing distance from the coast. Thus, evidence exists that a transfer of energy from EPE to EKE exists but is characterized with low values around zero. As shown before, outside the NBUC an energy conversion from the perturbation into the mean current exists and consequently the amount of perturbation energy decreases and thus the transfer between the perturbation energies must decrease.

In the lower panels of Figure 4.17 the vertical distributions of box 1 (left) and box 2 (right) mean T_3 are shown. As expected from the T_4 and T_2 distributions, the prominent peak of T_3 is to be found in the upper 500 m of the box 1 mean with maximal values at about 200 m depth and positive sign. The results of Figures 4.15 and 4.16 have shown that more EKE is generated than EPE is transferred into MPE. In this context, the vertical distribution of T_3 reveals that less EKE is converted into EPE than it is generated due to barotropic instability (Figure 4.17). This means that the residual EKE amount is advected or dissipated since this amount of energy is not converted within the Lorenz cycle. Below 500 m values of T_3 drop to zero in the box 1 mean.

Values of T_3 evaluated from the box 2 mean in Figure 4.17 (lower right panel) are generally lower compared to the distribution further north. In the upper 500 m T_3 is positive and energy is transferred from EPE into EKE. Since these values are comparable low, energy transfer must be accompanied by advection or dissipation of fluctuative energy. Below 500 m, T_3 drops to zero. This distribution of T_3 reflects the result obtained in Figures 4.15 and 4.16. Due to baroclinic instabilities, EPE is generated in the AAIW layer which is interrupted when changes in stratification become important. Then, as seen in Figure 4.17 (lower right panel), EPE is converted into EKE. In addition, EKE is generated by barotropic instability. Since negative values of T_4 are higher compared to negative values of T_2 at intermediate depths, energy must be advected or dissipated. At 1000-1500 m depth, T_3 becomes again negative indicating an energy conversion from EPE into EKE. The analysis of barotropic and baroclinic instabilities has shown that both account for the generation of high fluctuative energy in this depth range (Figure 4.15 and 4.16), from which T_4 is dominant. Thus, one would expect enhanced energy transfer from EKE into EPE since the generation of EKE acts to be stronger. But a reverse situation is evident. T_3 becomes negative which indicates a transfer from EPE into EKE. Thus, most of the fluctuative energy which is generated mostly by barotropic instability in this depth layer is not balanced within the Lorenz cycle and EKE is advected or dissipated as indicated by

arrows in Figure 4.9. The results obtained by Dengler et al. (2004) suggest that EKE is advected due to migrating eddies, rather than dissipated.

Summarizing briefly, horizontal maps of energy transfer terms at 500 m depth imply that the NBUC becomes unstable at about 4°-5°S and a recirculation cell of intermediate water masses is indicated as already suggested by several authors (e.g. Schott et al., 2005). The recirculation pattern at about 4°-5°S is accompanied by a signal of high EKE which is evident in the upper 500 m in that domain. It could be shown that barotropic instability generates this EKE signal. Although comparable small, effects of baroclinic instability act to stabilize the mean current field. In other words, in the upper 500 m of the NBUC domain at 3.5-6.5°S, energy is transferred from the mean current field into the fluctuations by horizontal shear instability and a recirculation cell is established. Part of this resulting EKE is converted into EPE and finally transferred into MPE, possibly resulting in slow southward recirculating flow. The residual EKE amount must be advected or dissipated from the recirculation cell since it is not converted within the Lorenz cycle.

South of 9°S values of energy transfer terms decrease and the sign of energy conversion changes. The NBUC becomes stabilized since EKE is transferred into the mean current field. Two local extrema exist, that is at intermediate depths and in the DWBC domain, where fluctuative energy is generated by both, barotropic as well as baroclinic instability. Effects of strong changes in stratification and reduced current shear account for the fact that EKE in the AAIW layer appears to be shielded from the mechanisms in the DWBC domain. Again, indications exist that fluctuative energy must be advected or dissipated.

In the introduction of this chapter several papers are introduced which also discuss a possible southward flowing recirculation cell outside the NBUC between about 5°-11°S (e.g. Schott et al., 2005), but which is confined to the AAIW layer. The question arises why the recirculation cell is restricted to intermediate depths since the NBUC spans the upper 1000 m. This can be explained as follows. As already suggested, T_4 is directed from the mean field into the perturbation for the upper 500 m. This effect becomes maximal at about 200 m depth (i.e. the core of the NBUC) and decreases rapidly with depth. Especially between 4°-8°S this vertical distribution is evident, but values further to the south decrease. Thus, the recirculation is established due to horizontal shear instabilities but the development of a mean southward recirculation flow is not possible in the upper 400 m. Below 400 m and between 5°-8°S, T_2 is small in magnitude and T_4 drops to zero. Thus, a mean southward flow of AAIW might be established. Further to the south (9°-12°S), negative T_2 and T_4 values decrease and the situation changes. The mean southward flow becomes unstable in the AAIW layer since effects due to shear instability dominate. The EKE at intermediate depths is shielded from the mechanisms in the DWBC domain since effects due to rapidly density changes dominate at about 500 m depth as described above.

4.3. Flow of AAIW from the south

As analyzed above, a recirculation cell of the NBUC is evident at about 4°-5°S and a southward flow of AAIW is developed outside the NBUC between about 5°-11°S. In addition, this flow is accompanied by high fluctuative energies since the recirculation flow

becomes unstable between about 9°-11°S and eddy-like patterns on intraseasonal time scales are dominant as investigated in the observations at 11°S. But the previous analysis is bounded to the area of about 5°-11°S. The fate of the southward flow still remains questionable and will be discussed in this section. Further to the south the role of eddies will be discussed and the signal of AAIW will be traced from about 5°S further to the north as those watermasses possibly cross the equator and spread on different pathways into the northern hemisphere.

4.3.1. The southward recirculation flow

Investigations on energy transfer terms indicate that between 9°-11°S the southward recirculation flow becomes unstable and EKE is generated (section 4.2.2). In addition, evidence exists that EKE is dissipated or advected, rather than converted into the mean field. To analyze whether EKE is advected or dissipated a sequence of snapshots in the year 2004 from the FLAME 2 simulation is shown in Figure 4.18. Contoured is the salinity on the 27.1 kgm^{-3} isopycnal surface and the arrows denote the current vector field in the same depth layer.

Starting on September 14th it is possible to pursuit a salinity minimum along the western boundary, indicating a northward flow within the NBUC of AAIW from the south. At around 5°S the salinity minimum as well as the velocities indicate that a recirculation of AAIW and a continuous southward flow of AAIW between 5°S and 10°S exists outside the NBUC. South of 10°S this flow becomes destabilized as suggested by the analysis of energy transfer terms in section 4.2.2. At the end of the month the flow breaks up and eddy-like variability exists at about 9°-12°S, which is already discussed locally at 11°S in the previous section. The domain of high fluctuations remains between about 9°-12°S and south of about 12°S southward flow as well as variability drops to zero. The strength of southward flow as well as the fluctuation patterns diminish as the time goes on (Figure 4.18). Thus, the recirculation pattern is bounded to about 5°-12°S and a migration of eddy-like variability further to the south is not evident along the western boundary. This suggestion is displayed by the salinity distribution. The recirculation is trackable, especially due to its salinity minimum compared to its surroundings. South of about 12°S a salinity minimum as observed further to the north is not evident. Consequently, EKE which is generated in the recirculation cell between 8°-11°S due to barotropic instability is dissipated rather than advected since migrating eddies further to the south are not evident along the western boundary and the southward flow collapses south of about 12°S.

Further to the north the situation appears to be different. The NBUC curves back upon itself so far as to pinch off eddies (e.g. Figure 4.18, 26/09/2004). These features then move northwestward and occasionally reach the equator. This scenario is also described in Figure 4.19, which shows a sequence of snapshots in the year 2003 (left panels) derived from FLAME 2 results. The salinity is contoured on the $\sigma_\Theta = 27.1$ kgm^{-3} isopycnal surface, respectively. In the beginning of August a recirculation of southward AAIW flow is established between 5°-10°S. Two weeks later eddies are detached at about 4°-5°S in that area where the NBUC becomes unstable and a recirculation is established. The eddies travel northwestward, carrying water of southern hemisphere origin which is traceable due

to its salinity minimum. The signals reach the equatorial band and becomes part of the interhemispheric water mass exchange.

To pursuit the northwestward migration of a salinity minimum a time-latitude plot of salinity on the $\sigma_\Theta = 27.1$ kgm^{-3} isopycnal surface is shown in the right panel of Figure 4.19. A path along the 2000 m isobath is chosen (marked in the snapshot of 26/10/2003) in order to trace back the salinity minimum along a path parallel to the coast. However, the time-latitude plot shows that a propagation of a salinity minimum towards the equator is evident. The strongest signals appear to be terminated between 2°-5°S but some signals reach the equator. The phase velocities of these features reach values of about 3-5 cm/s. No clear seasonal modulation is evident but the signals appear to be centered in boreal winter.

4.3.2. AAIW crossing the equator

The AAIW is the deepest component of the upper limb of the MOC and provides a substantial part in this interhemispheric exchange. It is important to understand the

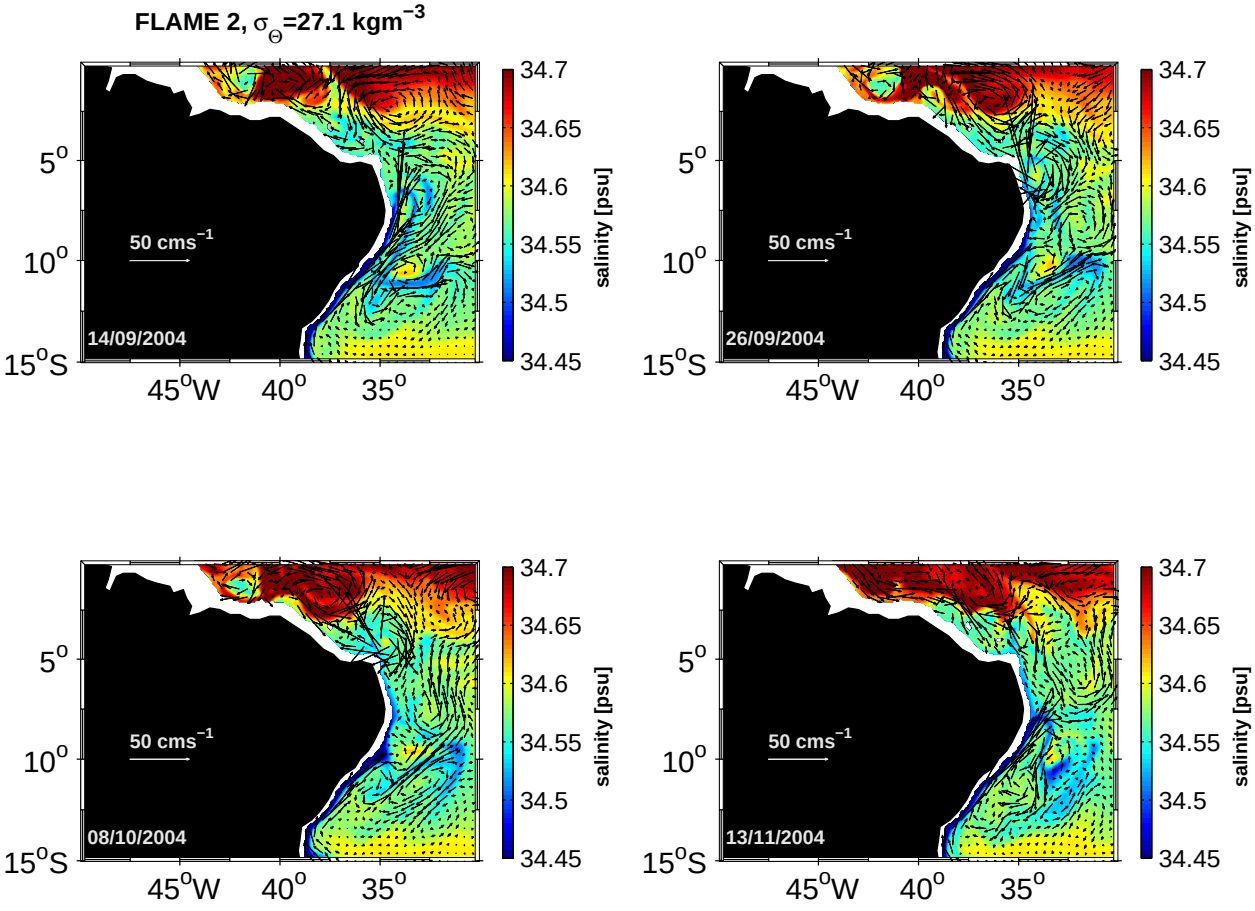

Figure 4.18.: *Individual snapshots in the year 2004 from FLAME 2 model results in the southwestern tropical Atlantic. The salinity at date is contoured and the velocity vectors are shown on the $\sigma_\Theta = 27.1$ kgm^{-3} isopycnal surface, respectively.*

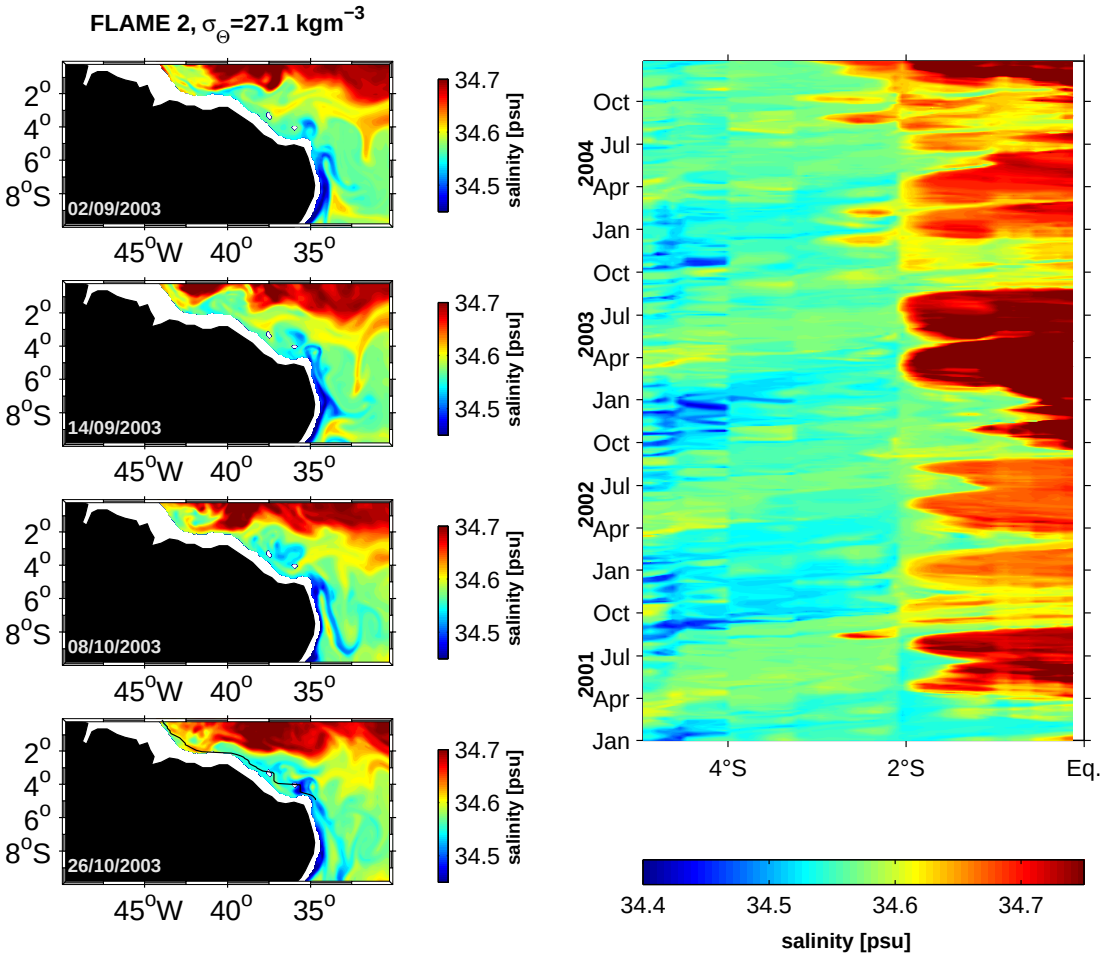

Figure 4.19.: *Right panels: Individual snapshots in the year 2003 from FLAME 2 model results in the southwestern tropical Atlantic. The salinity at date is contoured on the* $\sigma_\Theta = 27.1\ kgm^{-3}$ *isopycnal surface, respectively. Left panel: Time-latitude plot of FLAME 2 salinity along the 2000 m isobath (marked in 26/10/2003 snapshot) on the* $\sigma_\Theta = 27.1\ kgm^{-3}$ *isopycnal surface.*

pathways of AAIW since intermediate water is thought to warm and upwell in the vicinity of the equator into thermocline water and thus participates on the thermohaline circulation. As already mentioned in section 1, its formation area is centered in the southwestern region of the Argentine Basin (e.g. Boebel et al., 1999b) and then the AAIW spreads eastward in the South Atlantic Current (Stramma and Peterson, 1990). Three possible pathways are suggested which describe the progress of AAIW through a complex spreading pattern, i.e. continuation into the Indian Ocean, flow around the subtropical gyre of the South Atlantic and a northward transport as a western boundary current (Schmid et al., 2000). In this chapter the latter pathway is analyzed in more detail. The investigations have shown that the direct transport of AAIW from the south to the equator along the western boundary is intermitted due to the fact that a recirculation cell of AAIW exists between 4°-11°S. But evidence exists that eddies are shed from the retroflecting NBUC and these features then move along the South American coast, carrying AAIW northwestward and ocasionally

reach the equator. Thus, those features are accountable for transporting low saline and oxygen rich intermediate water masses to the equator.

Until now it is less clear how the AAIW crosses the equator. Thus, it is interesting to investigate whether the migrating eddies along the western boundary on the southern hemisphere cross the equator and to answer the question what happens if those features actually enter the northern hemisphere. Due to the results of some studies, two pathways of AAIW in the northern hemisphere are possible after crossing the equator, namely along the western boundary as part of the meridional transport of South Atlantic water from the equatorial to the subtropical Atlantic and a spreading along the equator as it supplies and ventilates thermocline waters in the vicinity of the equator. To investigate intermediate currents at the equator, e.g. Schott et al. (1998) show that strong zonal currents exist along the equator which could explain the equatorial tracer tongue. Jochum and Malanotte-Rizzoli (2003b) argue that seasonal Rossby-waves are evident and that the observed strong zonal currents could be the result of an alaising of the tropical wave field. Consequently, measurements as well as model studies have shown that AAIW spreads along the equator.

On the other hand less observations are evident which describe the spreading of AAIW along the western boundary of the northern hemisphere in the IWBC. Above the IWBC the NBC retroflects into the EUC just north of the equator while the near-surface part of the NBC continues to about 5°N and finally turns into the NECC (Schott and Böning, 1991). The meridional transport of South Atlantic water from the equatorial to subtropical North Atlantic is then established by NBC rings (see chapter 1 for more details). Three types of rings are proposed, i.e. two surface intensified rings which differ in vertical extension and subsurface intensified rings (Johns et al., 2003). It could be shown from the same authors that those rings carry South Atlantic water along the western boundary, especially mentioned in this context, AAIW of southern hemisphere origin. Thus, measurements have shown that AAIW also spreads along the western boundary into the North Atlantic.

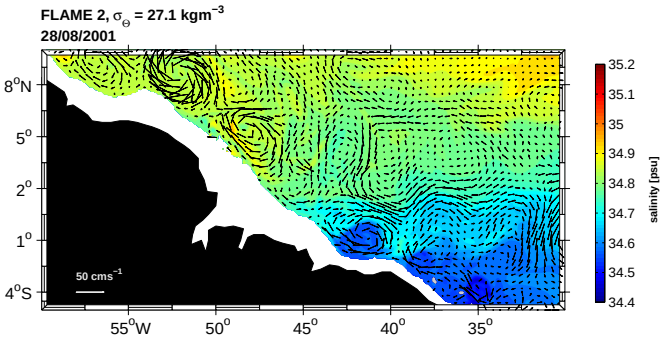

Figure 4.20.: *Snapshot (28/08/2001) of FLAME 2 salinity (contour) and velocity (arrows) on* $\sigma_\Theta = 27.1\ kgm^{-3}$ *isopycnal depths.*

One important question conserned with the dynamics that result to the formation of the deep rings whose maximal swirl velocity is present at depths of 600-800 m (Johns et al., 2003). One explanation could be a pinch off deep eddies in the retroflection zone of the NBC into the EUC. But this cannot explain why they usually have a thick layer of South

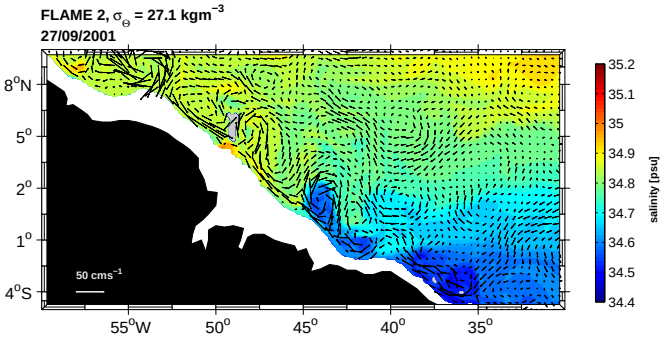

Figure 4.21.: *Same as Figure 4.20, but on 27/09/2001.*

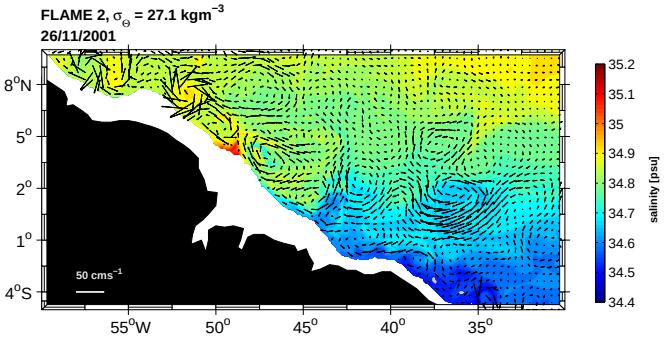

Figure 4.22.: *Same as Figure 4.20, but on 26/11/2001.*

Atlantic water extending down to intermediate depth levels as well as high swirl velocities in that layer. Another hypothesis derived from model results leads back to instability processes of an intermediate depth current that breaks up into eddies as it crosses the equator (Jochum and Malanotte-Rizzoli, 2003a). However, to shortly discuss the question how AAIW can be evident in the subsurface intensified rings, a sequence of snapshots from the FLAME 2 result is shown in Figure 4.20 to 4.22 in the year 2001 on $\sigma_\Theta = 27.1$ kgm^{-3} isopycnal depths. Contoured is the salinity and the arrows indicate the velocity vectors. In August an eddy-like pattern (clockwise rotation) is well developed close to the western boundary south of the equator which encloses a salinity minimum, propably due to AAIW (not shown). The pattern crosses the equator as time goes through (September, Figure 4.21) and AAIW spreads up to about 3°N. In November (Figure 4.22) the eddy-like pattern breaks down and most of the AAIW signal spreads eastward along the equator. The eddy pattern breaks down possibly due to the fact that the sign of relative vorticity must change while crossing the equator in order to conserve potential vorticity (Edwards and Pedlosky, 1998) and thus the eddy breaks up. But also evidence exists that a fracture of the AAIW pattern from the south spreads further to the north along the boundary since a salinity minimum becomes enclosed into ring-dynamics whose formation remains a matter of discussion.

To show that AAIW crossing the equator is not confined to the time domain of the snapshots in Figure 4.20 to 4.22 and is in fact evident in several years a time-latitude plot of FLAME 2 salinity on $\sigma_\Theta = 27.1$ kgm^{-3} isopycnal depths during 2001-2004 is shown in Figure 4.23 (right panel). A path parallel to the coast (roughly mirrors the 2000 m isobath)

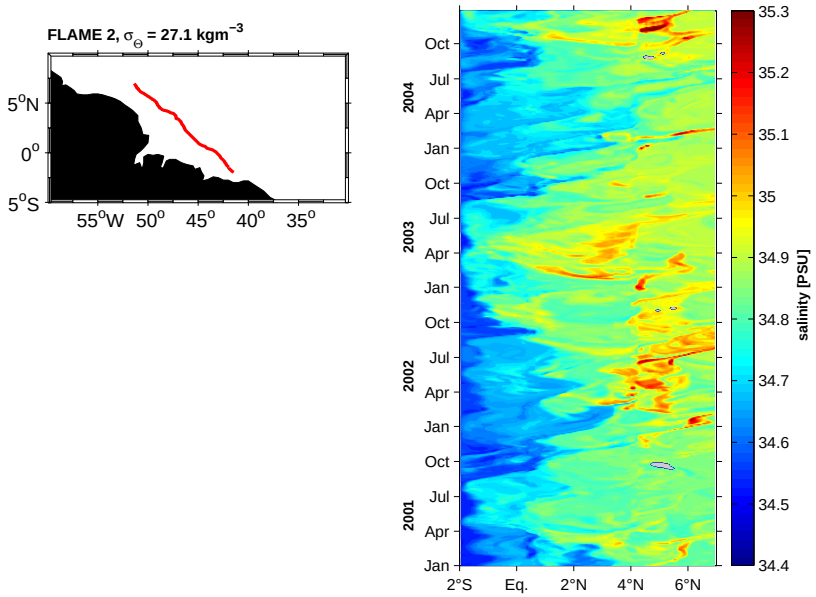

Figure 4.23.: *Right: Time-latitude plot of FLAME 2 salinity on $\sigma_\Theta = 27.1\ kgm^{-3}$ isopycnal depths during 2001-2004. A line parallel to the coast is chosen, which is marked in the left panel.*

between 2°-7°N is chosen and marked in Figure 4.23 (left panel).

The signal of low salinity (possibly due to AAIW) is evident south of the equator. The AAIW signal occasionally crosses the equator, preferably in late boreal summer. These signals propagate to the north and reach latitudes of about 4°N primarily in boreal spring. Only little evidence exists, that the salinity minimum propagates to areas north of about 4°N (e.g. April-July 2004). But generally, the signals appear to be trapped within the equatorial band and do not reach latitudes north of about 5°N. In addition, it is interesting to note that interannual differences are evident since the pattern which are characterized by a salinity minimum reach e.g. in 2001 latitudes of only about 3°N and in 2004 the watermass spreads till north of about 4°N.

Summarizing briefly, the analysis has shown that a signal of AAIW occasionally crosses the equator on the route along the western boundary and also reaches latitudes north of about 4°N. But most of the AAIW signal from the south spreads eastward whithin the equatorial band. This pathway of AAIW and the role of equatorial intermediate currents, e.g. just north of the equator in this context remains a matter of investigations. But also evidence exists that fractions of AAIW are enclosed in deep NBC rings (Johns et al., 2003) and thus transported further to the north along the western boundary. The formation of the deep rings is evident at about 5°N (e.g. Figure 4.20) and AAIW might be enclosed when the signals from the south occasionally reach these latitudes (Figure 4.22). The question which dynamics result to the formation of the deep rings remains unsolved. But the analysis implies how the AAIW signal of southern origin is enclosed within the deep NBC rings as observed by Johns et al. (2003).

5. Intraseasonal variability in the near surface layer of the tropical Atlantic

In this section, the distribution of ISV in the western and central tropical Atlantic Ocean (10°S-10°N) will be analyzed using data from altimetry and results from the FLAME model simulations. This investigation is separated into two parts. The first part concentrates in the southern hemisphere, where ISV is detected at 11°S close to the South American coast which is probably connected to the interior tropical Atlantic (chapter 3). In the second part, results obtained in the southern hemisphere are contrasted to the variability distribution in the northern hemisphere tropics. Basinwide EKE distributions as well as energy transfer terms are calculated in both hemispheres using model results and altimeter measurements in order to identify the area of main energy sources and, hence, describe the characteristics and origin of ISV in the western and central tropical Atlantic Ocean.

5.1. Distribution of intraseasonal variability in the southwestern tropical Atlantic

To specifically analyze the distribution of ISV in the southwestern tropical Atlantic the standard deviation of altimetry-derived MSLA for the years 2001 to 2004 is shown in Figure 5.1. Only four years of altimeter measurements are chosen in order to match the time domain of the model simulation. The MSLA time series are band-pass filtered 10-150 d in time and 100-1500 km in space. Thus, only variability on intraseasonal time scales is contained in the standard deviation. In the western basin of the tropical Atlantic a band of

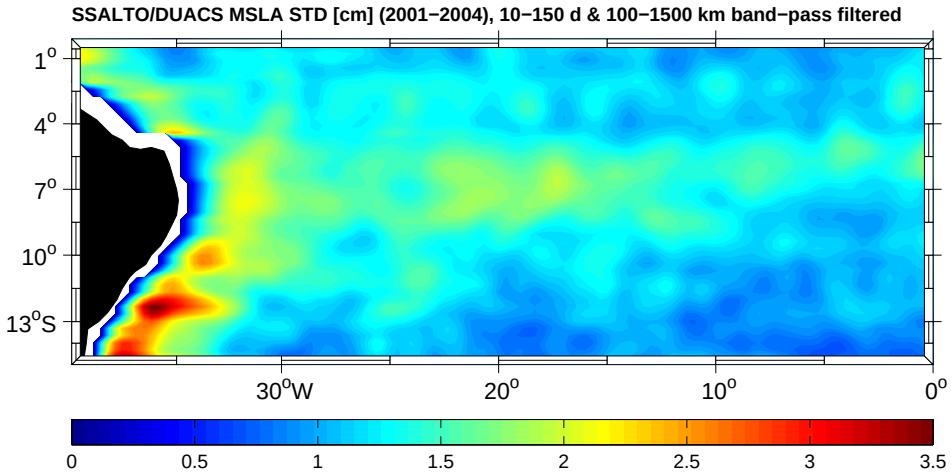

Figure 5.1.: *Distribution of standard deviation (STD) calculated from four years of altimetry-derived MSLA time series (2001 to 2004) for the southwestern tropical Atlantic. The MSLA time series are band-pass filtered 10-150 d in time and 100-1500 km in space.*

large standard deviations exists between about 5°-10°S which appears to be connected to fluctuations close to the western boundary, in particular further to the south. The standard deviation increases in the periphery of the western boundary and remains large south of 10°S. North of 5°S the standard deviation shows maximum values only near the equatorial region at the western boundary and thus probably exists due to equatorial dynamics. Fluctuations in the western basin do not seem to be connected to variability in the east since the standard deviation diminishes east of about 10°W. For this reason the domain east of 0°E is excluded here.

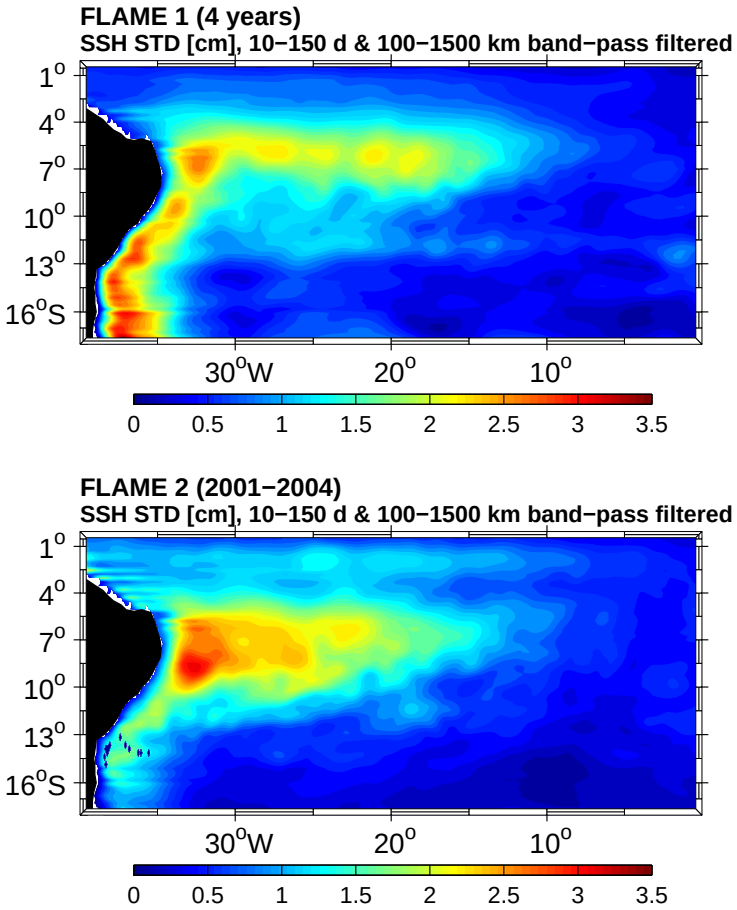

Figure 5.2.: *Distribution of standard deviation (STD) calculated from four years of FLAME 1 (upper panel) and FLAME 2 (2001 to 2004, lower panel) SSH for the southwestern tropical Atlantic. The SSH time series are band-pass filtered 10-150 d in time and 100-1500 km in space.*

Figure 5.2 shows the standard deviation calculated from four years of FLAME 1 (upper panel) and FLAME 2 (2001 to 2004, lower panel) SSH in the southern tropical Atlantic. Before evaluating the standard deviations, the time series are again band-pass filtered 10-150 d in time and 100-1500 km in space. The distributions of enhanced STD is comparable to the distribution derived from the satellite measurements. Close to the western boundary the standard deviation in the climatological model run is higher compared to the values of the FLAME 2 output. In addition, the band of large standard deviation

between 5°-10°S is distributed on a broader area in FLAME 2 than in FLAME 1. The question arises why these discrepancies occur between both model simulations. As already mentioned, the only difference between both model simulations is the wind field which forces the model. If instability mechanisms exist between 5°-10°S a free instability mode is able to develop more or less undisturbed on intraseasonal time scales in the climatological run. In the FLAME 2 simulation, high-frequency components of the wind field exist which might excite different modes as the instability mode develops. But nevertheless, the signal of high variability between 5°-10°S and along the western boundary is evident as suggested by the distribution of the standard deviation derived from the altimeter measurements.

Summarizing briefly, the leading intraseasonal variability pattern in the southern tropical Atlantic exists in a band between about 5°-10°S west of 10°W and is extended along the western boundary, in particular further to the south. Local investigations at 11°S in section 3.3 and 3.4 show that this ISV pattern is connected to westward propagating features with periods between 10-150 d and wavelengths of 100-1500 km. Seasonal as well as annual modulations of the intraseasonal signals are evident. A comparison of results from the altimeter observations to those obtained from the model simulations indicates that ocean internal mechanisms generate the ISV in the southern tropics, rather than wind forcing.

5.2. Evidence and generation of eddy kinetic energy in the southern tropical Atlantic

5.2.1. Distribution of eddy kinetic energy

The previous section has shown that high intraseasonal variability is apparent between 5°-10°S in the western tropical Atlantic in the southern hemisphere. In the next step it is important to investigate whether fluctuating energy is distributed in the same manner and the EKE derived from the altimeter data is evaluated. The geostrophic velocity gridded product

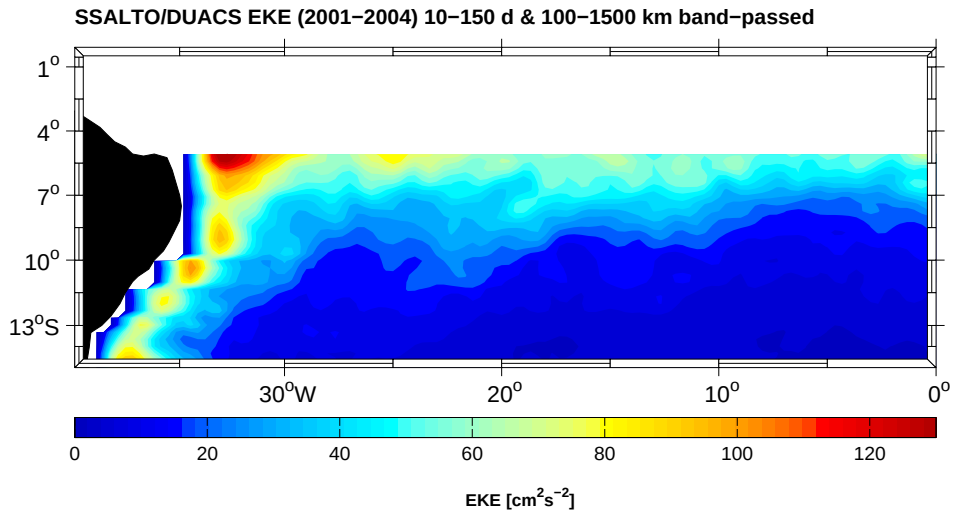

Figure 5.3.: *Eddy kinetic energy (EKE) evaluated from four years (August 2001 to December 2004) of SSALTO/DUACS MSLA from altimetry. The time series are band-pass filtered 10-150 d in time and 100-1500 km in space.*

is taken from AVISO (see section 2.2 for more details) which are evaluated as described section 3.3. Over long wavelengths, the errors in geostrophic velocity caused by geoid errors are on the order of 5 to 10 cms^{-1}, about the same size as errors in hydrographic solutions (Ganachaud et al., 1997). However, the time series of the AVISO geostrophic velocities are again band-pass filtered 10-150 d in time and 100-1500 km in space and then the EKE is calculated for the years 2001 (August) to 2004 (Figure 5.3). The equatorial band north of 5°S is suppressed. Enhanced EKE is located between about 5°S to 7°S. EKE increases in the western basin and shows maximum values close to the western boundary. Further to the south along the western boundary patterns of high EKE are apparent as well, in particular in the domain which is covered by the mooring array. But it is also evident that the fluctuating energy decreases towards the south. However, the distribution of EKE in Figure 5.3 shows that high EKE exists in a similar domain as marked with large STD in Figure 5.1.

The EKE distribution derived from four years of FLAME 2 velocity time series at 5 m depth is shown for the southern tropical Atlantic in Figure 5.4. Again the velocity time series are band-pass filtered 10-150 d in time and 100-1500 km in space. As well as in the altimeter observations, high EKE is apparent in a band between about 5°-10°S but confined to the western basin. With decreasing distance from the boundary EKE increases and a domain of maximum values is evident close to the western boundary. Along the boundary further to the south and to the north, the EKE rapidly decreases to values below about 50 cm^2s^{-2}. Important to note is that the magnitude of altimetry-derived EKE is somewhat lower than in the model simulation. A study by Fratantoni (2001) also demonstrates that over most of the Atlantic basin a bias is evident in the EKE field derived from satellite altimetry. A comparison of altimetry-derived EKE to drifter-derived EKE values shows that the drifter values are higher than corresponding values derived from satellite altimetry. The author argues that this is due to the fact that ageostrophic velocity contributions are immeasurable with satellite altimetry. In the equatorial band

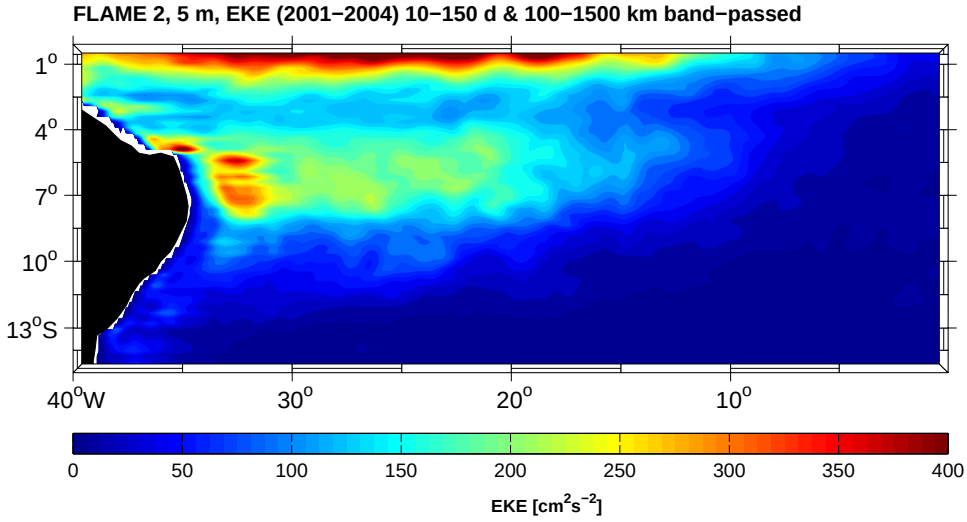

Figure 5.4.: *Eddy kinetic energy (EKE) evaluated from four years (2001 to 2004) of FLAME 2 velocities at 5 m depth. The time series are band-pass filtered 10-150 d in time and 100-1500 km in space.*

EKE becomes strong due to equatorial dynamics which are not discussed further here. Results from the FLAME 1 model simulation reveal a similar EKE distribution (not shown).

5.2.2. Generation of eddy kinetic energy

In this section, the generation mechanisms of enhanced fluctuative energy between 5°-10°S will be studied. To investigate this, energy transfer terms are evaluated in the southern tropical Atlantic, as introduced in section 4.2.1. Thus, averaged values between 5°-10°S of T_2, T_3 and T_4 are evaluated from six years of FLAME 1 model simulation and their distribution from 35°W-0°E are shown in Figure 5.5 (a). The energy transfer terms T_4 (green), T_2 (blue) and T_3 (gray) are averaged for the upper 50 m. However, the distributions of T_2, T_3 and T_4 along the basin indicate that instability mechanisms develop in the central and western basin since the values east of about 10°W drop to zero. West of

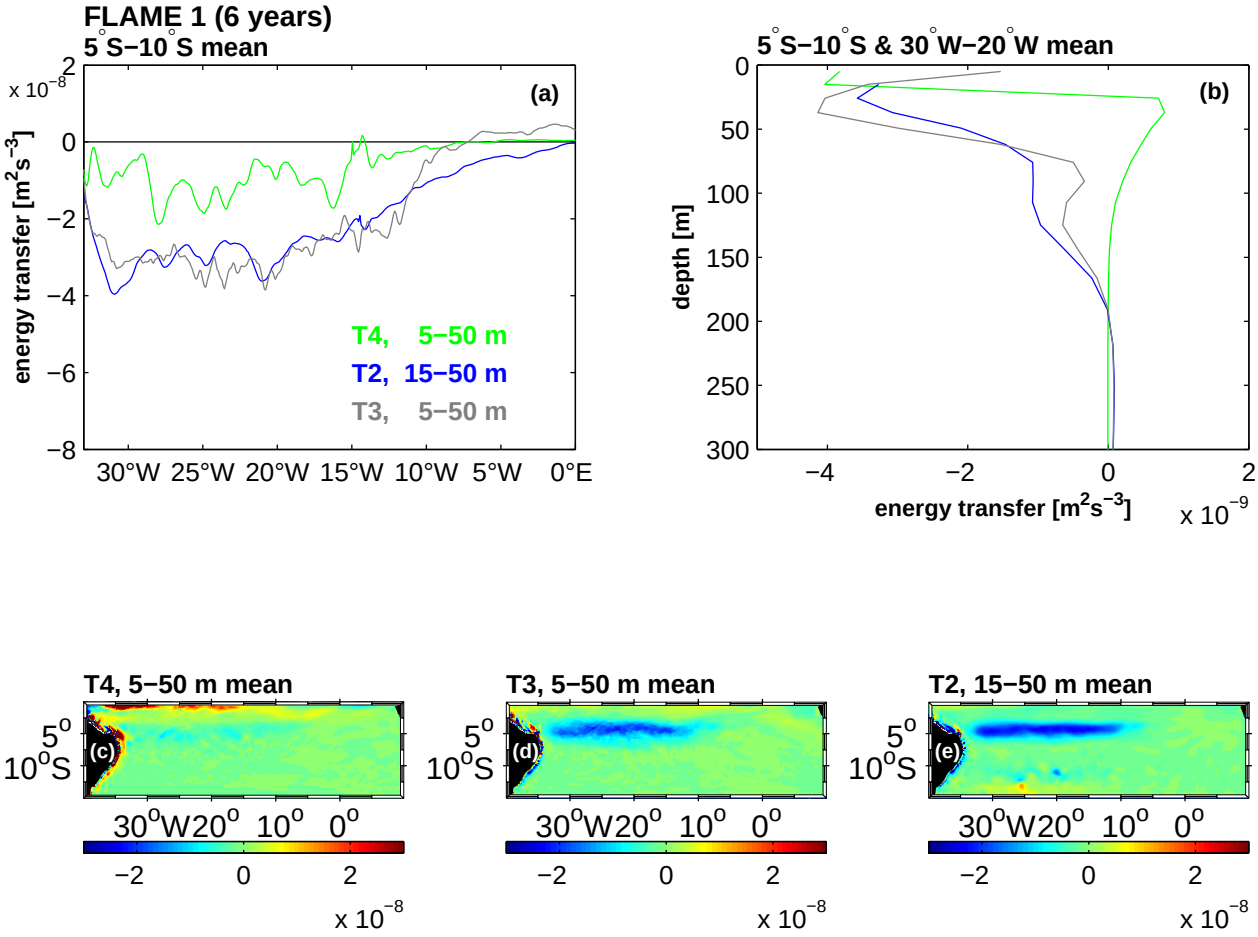

Figure 5.5.: *FLAME 1 6-years mean energy transfer terms (a) as function of longitude averaged between 5°-10° S for the upper 50 m (solid) and (b) as function of depths averaged between 5°-10° S and 30°-20° W. Lower panels: Distribution of (c) T_4, (d) T_3 and (e) T_2 derived from 6 years of FLAME 1 model results, averaged over the upper 50 m. Negative sign of T_4 and T_2 denotes transfer into the fluctuation. Negative sign of T_3 denotes transfer from EPE into EKE.*

10°W energy transfer increases and the values remain large till regions near the western boundary. The energy conversion near the South American coast is high, which is not shown in this context since instability mechanisms near the boundary are discussed in section 4.2.1.

In the upper 50 m T_2 and T_4 are negative, where values of the latter term are weaker. This means that the conversion of energy is directed from the mean field into the fluctuations in this area. But as already mentioned, values of T_2 are generally higher and the amount of EPE generated due to baroclinic instability processes exceeds the signal of EKE generated by horizontal shear instabilities. In this context, the discussion of T_3 plays an important role since it indicates whether EPE is converted into the EKE field or not. Thus, T_3 is shown in Figure 5.5 (a) as well and the distribution of T_3 is very similar to the distribution of T_2. A negative sign of T_3 means that energy is transferred from EPE into the EKE field. Thus, the generation of EKE mainly due to baroclinic instability is established in the central and western basin of the tropical Atlantic between 5°-10°S as it is observed in the EKE distribution derived from the altimeter measurements (Figure 5.3).

To investigate whether the instability processes are confined to the surface or if their signal distribution changes with depth, the averages of T_2, T_3 and T_4 between 5°-10°S and 30°-20°W are shown in Figure 5.5 (b). In the upper 150 m, T_2, T_3 and T_4 are negative. Below 150 m depth all energy transfer terms drop to zero. Thus, the development of instability processes with depth decreases which means that the generation of EKE due to baroclinic and barotropic instabilities is confined to the near surface layer and effects of horizontal and vertical shear instabilities arise from the surface current regime in the southwestern tropical Atlantic. Below 300 m, values of T_2, T_3 and T_4 alter about zero in this domain (not shown).

Maps of T_2, T_3 and T_4 are shown for the southern tropics in order to describe the distribution of the energy conversions more properly since the zonal surface current regime in the tropics appears to be somewhat complex. These maps are shown in the lower panels of Figure 5.5, where the transfer terms of T_2, T_3 and T_4 are averaged in the upper 50 m, respectively. All three distributions show that a sharply bounded pattern is evident, that is a domain of high deviations from zero between about 4°-7°S and west of 10°W. The influence of T_4 is low in that domain, whereas T_3 and T_2 show strong negative values. Close to the western boundary the energy transfer terms change sign and baroclinic instability mechanisms generate turbulent energy fields rather than horizontal shear instability mechanisms. However, this result is restricted to a small domain (about 4°-5°S) and the sign alters close to the western boundary, which indicates that the latter suggestion may not be robust. In the equatorial band T_4 increases again but this pattern will be not discussed in this context and the reader is referred to section 5.4.2.

Attempts to calculate an analysis comparable to Figure 5.5 from measurements has shown that it is difficult to investigate the complete T_2 term (equation 4.2) from the observations since these sources are limited. Only horizontal changes of temperature (SST from TRMM) can be used instead of deviations from density and the following formalism is possible to evaluate from the available basinwide measurements:

$$T_2^{**} = \overline{u'T'}\frac{\partial \bar{T}}{\partial x} + \overline{v'T'}\frac{\partial \bar{T}}{\partial y} \quad , \tag{5.1}$$

where $\overline{u'T'}$, $\overline{v'T'}$ describe the covariance between the velocity field and the temperature, $\bar{T}$ denotes the arithmetic mean of temperature and u' and v' can be calculated from altimetry-derived velocities. Furthermore, T_3 cannot be calculated since basinwide distributions of vertical velocity are not available. On the other hand, the complete T_4 term (equation 4.4) can be calculated from basinwide measurements. The altimetry-derived velocities deliver the variance and covariance terms. To calculate the horizontal derivatives from the mean currents a climatology of near-surface currents at one degree resolution, derived from satellite-tracked surface drifting observations (Lumpkin and Garraffo, 2005) can be used. The horizontal changes in SST (TRMM dataset) as well as the energy conversion term T_4 were evaluated from the datasets but are not shown here since large errors and the rough resolution of the data field are evident. In particular, the distribution of an averaged T_4 term between 5°-10°S is very noisy, and comparisons to the model results as well as interpretations are not possible. Thus, until now it is not possible to deliver a reliable basinwide description of possible instability processes in the measurements and its analysis is confined to model simulations.

The previous analysis has shown that the effect of baroclinic instability processes dominate which implies a vertical geostrophic shear of the mean current and horizontal density gradients. During the growth of the instability processes, available potential energy is released and transferred into the perturbation. In the next step, several sections in the southwestern equatorial Atlantic are investigated, i.e. 23°W, 28°W and 15°W. At first, the sections taken along 23°W and 28°W are shown in Figure 5.6. The shipboard measurements are derived from a Polarstern cruise during June 2005 along 23°W and five cruises during 2000 to 2004 as described in section 4.1 along 28°W. The lower panels show the corresponding mean zonal velocities derived from four years of FLAME 2 model results during 2001 to 2004 and the distribution of EKE.

Between about 3°-7°S a band of westward flow is evident in the upper 100 m in the observations as well as in the model results. This current band is part of the South Equatorial Current (SEC), more precisely the central SEC (cSEC Schott et al., 2004), which exhibits a recirculation branch of the South Equatorial Counter Current (SECC, Stramma and Schott, 1999). Near the equator, an eastward Equatorial Undercurrent (EUC) exists in the upper 200 m. Below the cSEC down to about 400 m depth, the eastward South Equatorial Undercurrent (SEUC) is present. Between about 1°S-3°S and below 300 m depth the eastward South Intermediate Counter Current (SICC) is evident. South of 10°S and below about 100 m an eastward current core exists which is often referred to the SECC (Schott et al., 2005). The comparison of the model results to the observations shows that amplitudes and location of the near surface currents show good agreement. On the other hand, the mean zonal currents below about 100 m depth are weaker in the FLAME 2 results, since the distribution along the section is evaluated from a four year mean. For a detailed overview on the mean flow field in the tropical Atlantic Ocean and its connection to tropical-subtropical and interhemispheric exchange processes the reader is referred to section 1.

Along 23°W, the zonal current regime appears to be more or less similar to the distribution along 28°W. The cSEC is evident between about 3°-7°S and the westward velocities drop to zero below 100 m depth. Differences exist, that is, eastward velocity in

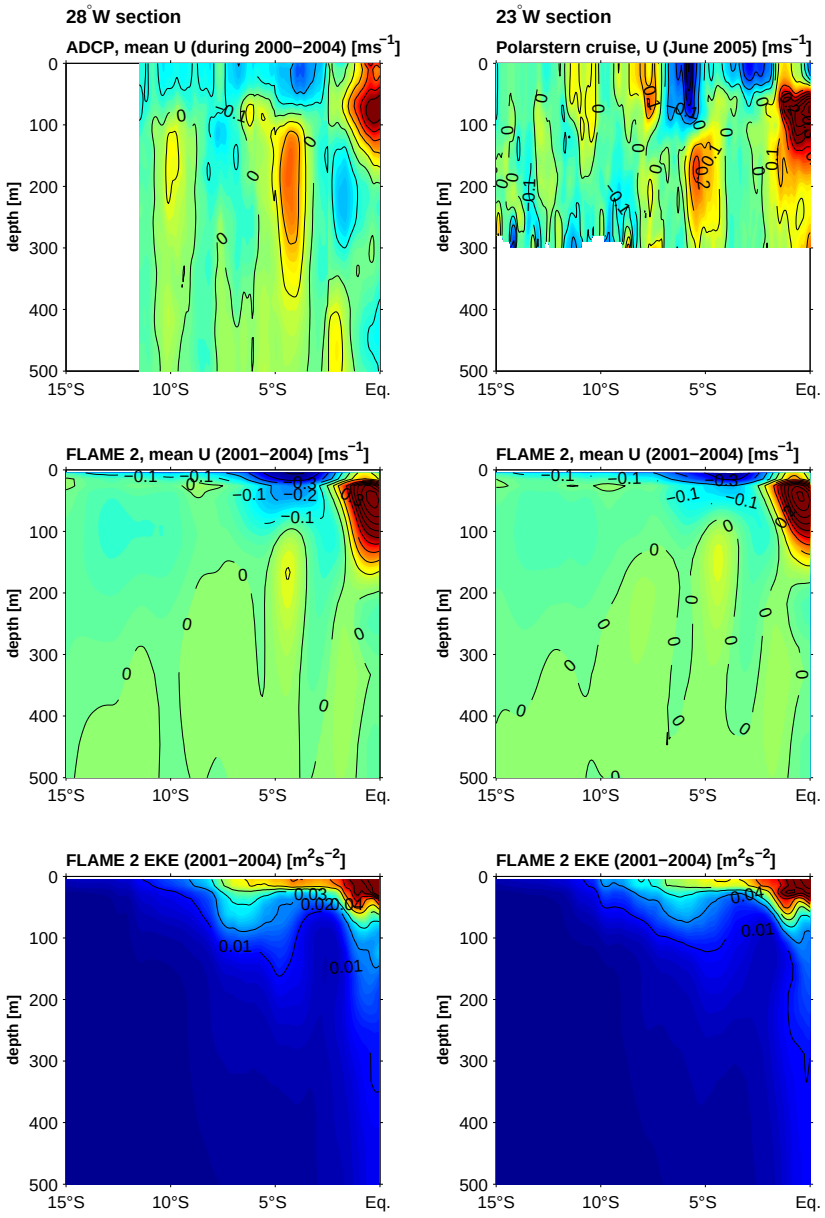

Figure 5.6.: *Left: Mean zonal velocity along 28° W derived from five shipboard ADCP measurements during 2000 to 2004 (modified after Fischer et al. (2006)) and from four years of FLAME 2 results (2001 to 2004) and distribution of EKE with depth derived from the model results for the upper 500 m. Right: Same as left panel, but along 23° W. ADCP velocities are measured during Polarstern cruise in June 2005 (only upper 300 m available).*

the upper 100 m at the southern edge of the cSEC. The mean zonal velocities derived from FLAME 2 show again that amplitudes and location of the mean surface currents are in good agreement, whereas the mean zonal currents below about 100 m depth are weaker.

The analysis of the mean current system in the Southern hemisphere implies that the area of the cSEC covers the region of enhanced ISV and, consequently, vertical but also

horizontal velocity shears of the cSEC favor the growth rate of instability processes. The horizontal map of T_2, for example, has shown that the energy conversion processes dominate between about 4°-5°S (Figure 5.5, lower panel). The 28° and 23°W sections imply that the core of the cSEC is located at similar latitudes (Figure 5.6). Furthermore, the instability processes are clearly confined to the surface and maximum velocities are achieved in the near surface layer, whereas westward flow drops to zero between 3°-7°S and below 100 m depth.

In the lower panels of Figure 5.6 the EKE distribution with depth is shown for the two sections. The EKE shows maximum values in the domain of the EUC along both sections, but, interestingly, with a surface intensified signal, although the core of the EUC has to be subsurface intensified. In the area of interest, i.e. in the domain of the cSEC, EKE again increases. The maximum values are achieved in the near surface layer, and the signal of high EKE decreases with depth. Below the cSEC, i.e. below about 100 m, EKE drops to zero. In contrast to this, near the equator the signal of high EKE is extended vertically, and values above zero exist until about 400 m depth. Thus, the previous results are consistent with the vertical distribution of EKE in the cSEC domain. The horizontal map of EKE in the near surface layer has shown that signals of high EKE are bounded to a band between 5°-10°S in the model results as well as in the altimeter measurements (Figure 5.3 and 5.4). In addition, averaged energy transfer terms in Figure 5.5 (upper panel) show that baroclinic and barotropic instability mechanisms are confined to the surface and thus the generation of EKE decreases with depth, which coincides with the distribution of EKE in Figure 5.6.

In Figure 5.7 (a) mean zonal velocities along 15°W are shown for the southern tropical Atlantic together with an EKE distribution (Figure 5.7 (b)) along the section. The distributions are only derived from the FLAME 2 model simulation during 2001 to 2004 because no measurements are available in the central tropical Atlantic in the southern hemisphere. The westward signal of the cSEC is evident for the upper 50 m, and the EUC exists between 50-200 m at the equator. As expected and as obvious further to the west, intermediate current cores are weak. The mean current core of interest is clearly established between 3°-7°S and compared to the sections further west (Figure 5.6) the westward current is confined to the upper 50 m. At 28°W and 23°W the current expands to depths of about 100 m which indicates that the vertical extension of the westward surface current flattens with increasing distance from the western boundary. This pattern is accompanied by the vertical distribution of EKE in all three sections, since the signal of EKE diminishes in the same area with increasing distance from the western boundary (Figure 5.6 and 5.7 (b)).

Figure 5.7 (c) shows a map of the mean zonal velocity field from the FLAME 2 model simulation during 2001 to 2004 at 5 m depth and Figure 5.7 (d) displays tropical Atlantic near surface currents as well, but derived from a drifter climatology (Lumpkin and Garraffo, 2005, see section 2.1.5). The model simulation as well as the observations show that a band of westward velocity is evident between about 3°-7°S west of 10°W which, as already mentioned, is often referred to as the cSEC (e.g. Stramma and Schott, 1999). The magnitude of westward velocity increases with decreasing distance from the western boundary. Close to the western boundary westward velocity shows maximum values. The

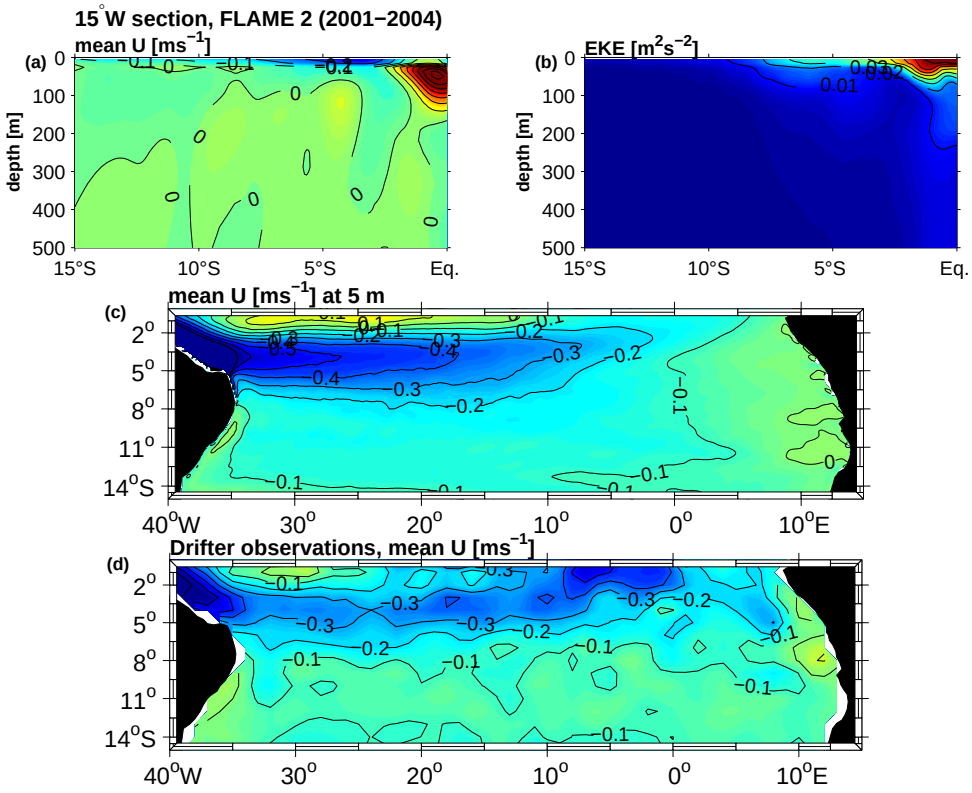

Figure 5.7.: *(a) Mean zonal velocity along 15° W from four years of FLAME 2 results (2001 to 2004) and (b) distribution of EKE with depth for the upper 500 m. (c) Map of mean zonal velocity at 5 m depth, evaluated from four years of FLAME 2 results (2001 to 2004). (d) same as (c), but derived from a drifter-derived climatology of near-surface currents (Lumpkin and Garraffo, 2005, see section 2.1.5).*

cSEC continues equatorwards into the western boundary current. Signal distribution of high energy conversion exists in the same horizontal extension as westward flow becomes strong (Figure 5.5, lower panels). The energy conversion terms T_2, T_3 and T_4 develop and increase as near surface velocity increases within the cSEC. The distribution of EKE at the surface (Figure 5.3 and 5.4) also shows that the signal of high EKE is evident in the domain of the cSEC. EKE increases with decreasing distance from the western boundary and shows maximum values close to the coastline and, against expectation, its maximum is expanded southward along the coast, although the cSEC is expanded equatorward along the boundary (Figure 5.7 (c) and (d)). Thus, the mean near-surface current in the southwestern tropical Atlantic is directed equatorward, whereas the fluctuation pattern is orientated poleward along the western boundary.

In the western tropical Atlantic the thermocline deepens while the northeast and southeast trade winds intensify (May to September) and shoals while the prevailing winds relax (Philander and Pacanowski, 1986). This is interesting in this context since effects of baroclinic instability processes are dominant. Close to the western boundary the tropical thermocline is at its maximum depth and T_2 must increase in that domain since small vertical changes of density are evident in that layer (compare equation 4.2). Further to

the east, thermocline depth shallows and vertical changes of density increase at the same depths as the deviation decreases near the western boundary. Thus, T_2 decreases in the east and possibly reaches values close to zero. In the west, conditions exist which favor the development of baroclinic instabilities. In addition, high horizontal changes of the density field in the near surface layer also influence the growth of baroclinic instability processes (compare equation 4.2). Southern ridges of the western hemisphere warm pool (Wang and Enfield, 2001, their Figure 1) might result in large horizontal changes of density close to the western boundary, and the growth of baroclinic instabilities is favored. At about 10°-15°W a strong salinity gradient must exist due to a diminishing signal of fresh near surface waters from the east which is maintained by African river runoff and enhanced precipitation in this area. In the same domain, baroclinic instability starts to grow (Figure 5.5).

5.3. Summary and discussion of intraseasonal variability in the southern hemisphere

A comparison of the horizontal as well as vertical distributions of hydrography, velocity, fluctuative energy and energy transfer terms between 3°-7°S implies several interrelationships. The thermocline deepens in the western basin due to the prevailing wind system and the surface intensified cSEC shows maximum values in magnitude and vertical extent close to the western boundary. In the same domain (horizontal and vertical expansion), EKE shows maximum values since energy conversion increases due to barotropic and baroclinic instability processes, from which the latter appears to be the leading mechanism generating fluctuative energy in this domain. Further to the east, the mixed layer shallows and westward velocity, fluctuative energy and energy conversion diminish within the latitudinal band of 3°-7°S. Enhanced horizontal gradients of density in the west whithin the near surface layer (e.g. warm pool) favor the growth of baroclinic instability. In the east fresh surface waters let baroclinic instabilities decrease.

The comparison of the different parameters has also shown that high EKE is evident south of the cSEC domain although the mean zonal current turns equatorward in the vicinity of the western boundary rather than poleward. Here, the signal of high variability is evident in the altimeter measurements as well as in the model results (Figure 5.3 and 5.4). Thus, the question arises if the variability pattern south of the cSEC, accompanied by instability processes, exists.

A sequence of snap-shots from the FLAME 1 model simulation in year one is shown in Figure 5.8. The contours indicate the basinwide temperature distribution at 50 m depth at the corresponding time step and the arrows display the current vectors at the same depth. However, at the end of July (t_1) instability processes take place and the surface current between 4°-7°S (cSEC) seems to meander. One month later (August, t_2), instability processes increase and between about 15°-25°W mesoscale patterns are evident south of 7°S. These enclose colder water masses than their surroundings, since the current vectors indicate cyclonic rotation (corresponds to cold core rings in the southern hemisphere). Those features appear to translate to the southwest, as is shown in the November (t_3) snap-shot in Figure 5.8. At this time, the instability processes within the

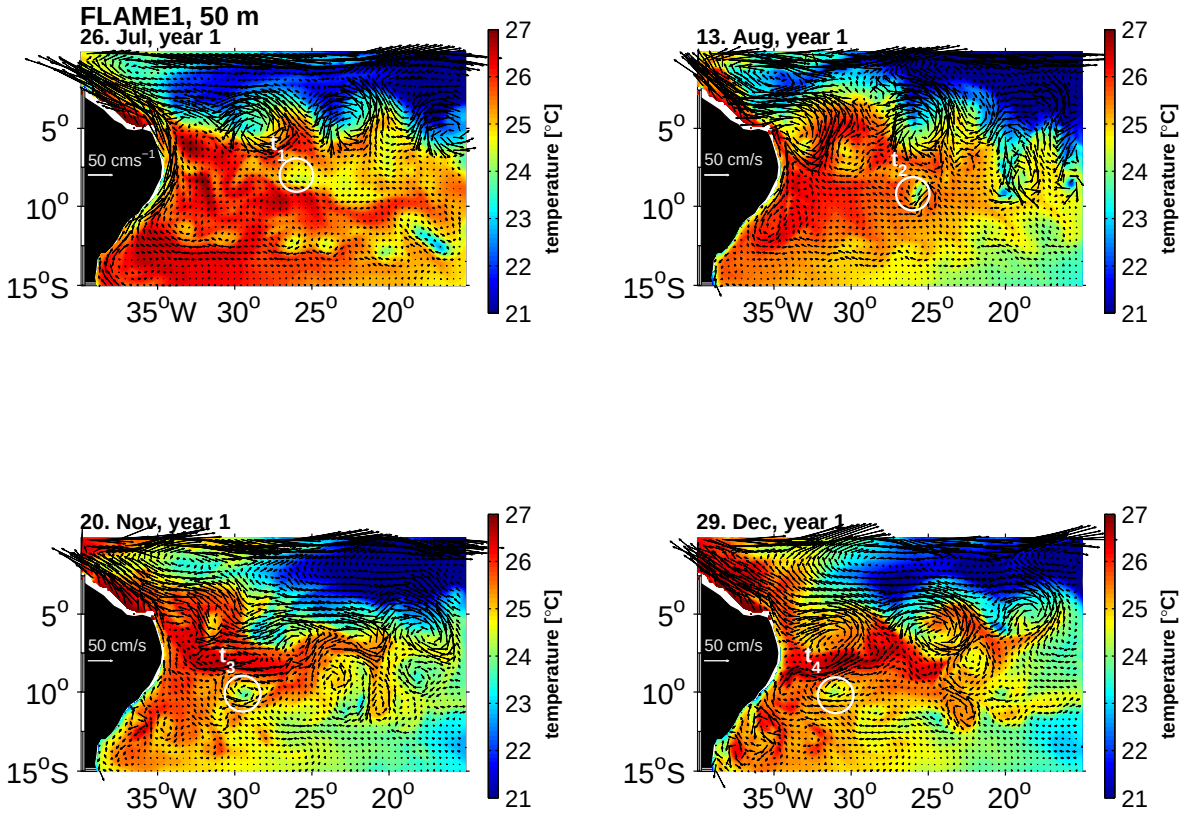

Figure 5.8.: *Sequence of snap-shots during the first year of FLAME 1 model simulation (26. July, 13. August, 20. November and 29. December). Contoured are the temperatures at 50 m depth and the arrows display the current vectors in the same depth level.*

cSEC diminish, and besides the cold core rings, anticyclonic eddies are generated. The cold rings seem to translate southwestward to the western boundary. The variability clearly increases at the western boundary as the rings reach the western boundary, and the instability processes decrease in the interior between 4°-7°S (Figure 5.8, December (t_4) snap-shot). Mesoscale fluctuations are generated mostly due to baroclinic instability processes between 3°-7°S in the domain of the cSEC. Morrow et al. (2004) have shown in a study of gridded satellite altimetry data that cold-core eddies tend to move westward and poleward as shown in theories for vortex propagation on a β-plane (e.g. Gill, 1992). In addition, the translation of cyclonic eddies is smaller than the long wave speed (Nof, 1983). This coincides with the results in section 3.3.2, since phase velocities are evident in the dispersion relation for long waves, which are slower than theoretical values. However, here it is shown that tropical instability processes enhance the ISV at 11°S in the NBUC domain.

5.4. Distribution and generation of tropical instabilities in the near surface layer of the central tropical Atlantic Ocean

In contrast to the southern hemisphere, tropical instabilities in the North Atlantic are frequently described in literature, but their generation mechanisms remain a matter of discus-

sion (see section 1). In the southern hemisphere, tropical instabilities have been discussed in the preceeding section, but the major objective was to explain the ISV signal in the mooring array measurements close to the western boundary. The purpose of this section is to investigate the generation mechanisms of tropical instabilities in the central tropical Atlantic in both hemispheres as simulated by the FLAME numerical model. But before doing this, ISV patterns along the equator are analyzed using current measurements at 23°W and the model results.

5.4.1. Intraseasonal variability along the equator

Current measurements at the equator at 23°W are investigated for the period 2001 to 2006 in order to detect ISV in this area. A basic description of this dataset is given in section 2.1.2. In the upper panel of Figure 5.9 a wavelet transform of meridional velocity is evaluated from the mooring array data covering the depth range from 12 m to 130 m depths in 2001/2002 and from 12 m down to 700 m in 2004 to 2006. In this Figure the distribution of wavelet power at 28 d period with depth is shown. The period of 28 d is chosen since high energy is evident at that period at the equator, especially in the meridional component (Brandt et al., 2006). Gaps are due to missing measurements. As already shown in a study by Brandt et al. (2006) for the measurements in February 2004 to May 2005, the signal of enhanced energy at 28 d period is seasonally modulated with

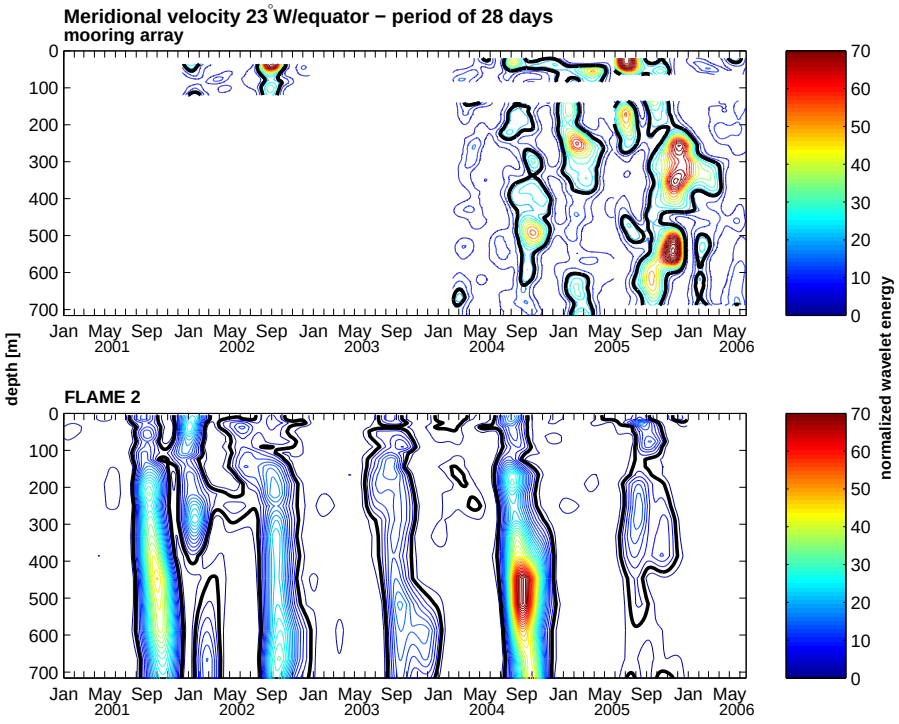

Figure 5.9.: *Normalized wavelet energy distributed with depths at a period of 28 d derived from current measurements from a mooring at 23° W at the equator (upper panel) and derived from 5 years of FLAME 2 model simulations (lower panel). Gaps in the upper panel are due to missing measurements. The 95% significance level is marked with a black line.*

strong maxima in boreal summer (July to August) and sporadic maxima in boreal winter (January to March). The patterns are not confined to mixed layer depths, but rather show maxima between 400-600 m. The strength of the 28 d signal is different in the individual years with large values in boreal summer 2005 and little energy in summer 2004. Especially in the appearance of the winter signal, this interannual modulation is obvious. In boreal winter 2005 a distinctive pattern of 28 d power exists, whereas in winter 2004 the signal is missing. In winter 2006 only little 28 d energy exists.

In the lower panel of Figure 5.9, a wavelet transform is calculated analogous to the analysis of the mooring current measurements. Time series of meridional velocity in the years 2001 to 2005 are used from the FLAME 2 model simulation. As for the observations, enhanced wavelet power at 28 d period is evident and show seasonal modulation, too. Strong signals appear predominantly in boreal summer but also in boreal winter (e.g. winter 2002). However, the maximum values occur at different times in observations and model output. In the year 2005, for example, wavelet power shows enhanced summer maximum in the observations compared to the model results, whereas in 2004 the situation reverses (Figure 5.9, upper panel).

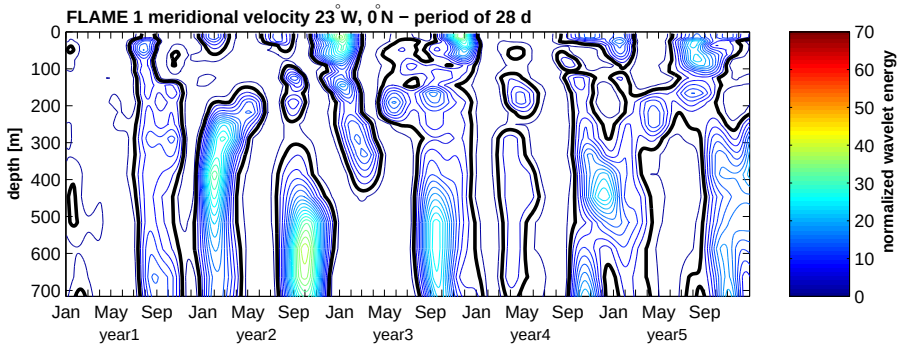

Figure 5.10.: *Normalized wavelet energy distributed with depths at a period of 28 d derived from 6 years of FLAME 1 model simulations. The 95% significance level is marked with a black line.*

The question arises why this discrepancy occurs between model simulation and observations concerning the interannual differences of the 28 d signal. To answer this question, the results from the climatologically forced model (FLAME 1) are discussed. In Figure 5.10 the wavelet transform is evaluated analogous to the calculations in Figure 5.9. The 28 d wavelet power becomes significant in boreal summer and also in boreal winter. As this signal is interannually modulated which hints to the mechanisms accountable for the discrepancy between the current measurements and Flame 2 results. The fact that the climatological forcing (FLAME 1) generates interannual variable conditions points towards a non-deterministic behavior (stochastic variability) and consequently one does not expect agreement between model and observations.

A section of velocities along the equator is derived from the FLAME 2 model output. Since it is interesting to detect the space-time evolution of intraseasonal oscillations of the meridional velocity in the model, it is useful to calculate principle oscillation patterns

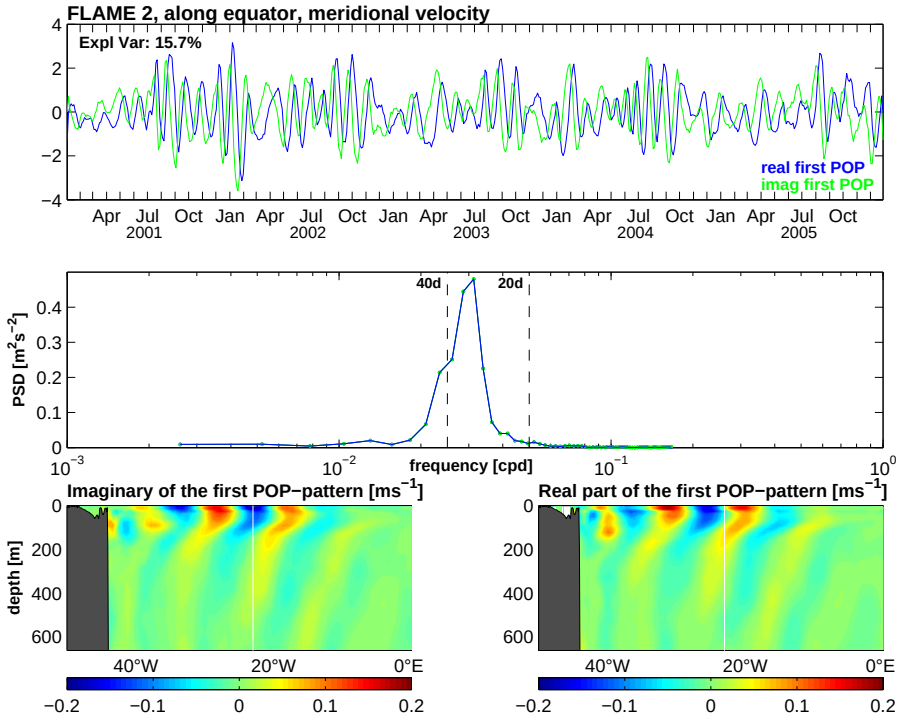

Figure 5.11.: *Non-dimensional coefficients (real part is given by the blue, imaginary by the green line) of the first POP (upper panel) and corresponding spectra of this dominant POP mode (second panel). Time series of FLAME 2 (2001 to 2005) of meridional velocity along the equator are used. Lower left panel: The imaginary part of the POP-pattern in* ms^{-1}*. Lower right panel: The real part of the POP-pattern in* ms^{-1}*. The 23° W longitude is marked with a white line.*

(POPs hereafter, von Storch et al., 1988, 1995). The POP method extracts oscillating patterns from multivariate time series. Figure 5.11 shows the dominant POP of the meridional velocity along the equator. The lower panels show the imaginary (sin) and real (cosine) spatial patterns of the POP, the upper panel the corresponding time-dependent coefficients of the POP and the middle panel its spectral distribution, respectively. The POP coefficients are determined by reconstructing the original time series in terms of POPs (von Storch et al., 1988, 1995). However, the POP coefficients of the real and imaginary part explain 16% of the total variance of the meridional velocity along this section. The phase difference of the imaginary and real part are $-90°$, indicating that the imaginary part leads the real part (Gallagher et al., 1991). The spectra of the dominant POP coefficients have a distinct peak which occurs at periods between 20-40 d. The signal distribution of the time-dependent coefficients are seasonally modulated and amplitudes of the time-dependent coefficients are different between the years, for example, strong winter (boreal) signal 2001/2002, but less intense during other winters.

Together with the spatial distribution of the imaginary (lower left panel) and real (lower right panel) POP pattern in Figure 5.11, the analysis can be explained as follows: In mid of August, for example, the time-dependent coefficients of the imaginary part (green line, upper panel) show maximum values while the real part drops to zero (blue line). This state of the POP corresponds to imaginary spatial pattern of the POP (lower left panel)

and a domain, for example, of positive meridional velocity is evident in the near surface layer directly east of 23°W. As time goes on, at the end of August, one has to look to the real POP pattern (lower right panel), since the phase difference of the imaginary and real part appears to be $-90°$ and the real (cos) POP coefficient is at its maximum, while now the imaginary (sin) part is near zero. This state of the POP corresponds to the real spatial pattern of the POP (lower right panel). The pattern of northward velocity is shifted further west, i.e. closer to the 23°W marker. Roughly estimating, the pattern migrates with a phase velocity of about 0.3 ms^{-1} to the west. The signal of westward shifting is evident from the western boundary until about 0°E, where the signal appears to diminish.

Oscillating patterns are as well extracted from the zonal currents along the equator calculating a POP analysis of FLAME 2 results (Figures 5.12, 5.13). The dominant POP is associated with the annual cycle and explains about 60% of the total variance of the zonal velocity as already investigated in a study by Brandt and Eden (2005). Indeed, the ocean general circulation model (OGCM) used in their study has a coarser horizontal resolution (1/3°) and the POPs are evaluated from monthly mean zonal currents but the results of FLAME 1 and their OGCM are more or less the same. However, the dominant POP shows upward phase propagation of downward propagating equatorial waves. The wave pathways are consistent with equatorial beam solutions of lowest odd meridional mode Rossby waves which are either generated directly by the zonal wind or by the reflection of wind generated

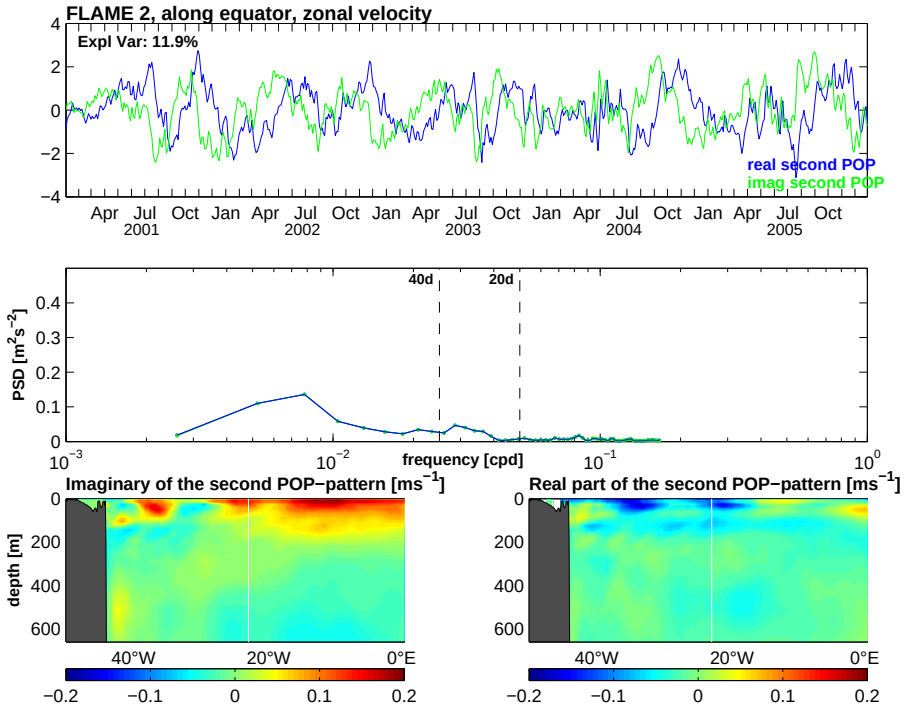

Figure 5.12.: *Non-dimensional coefficients (real part is given by the blue, imaginary by the green line) of the second POP (upper panel) and corresponding spectra of this second POP mode (second panel). Time series of FLAME 2 (2001 to 2005) of zonal velocity along the equator are used. Lower left panel: The imaginary part of the POP-pattern in ms^{-1}. Lower right panel: The real part of the POP-pattern in ms^{-1}. The 23° W longitude is marked with a white line.*

downward propagating equatorial Kelvin waves at the eastern boundary (Brandt and Eden, 2005). In a study by França et al. (2003), planetary equatorial waves in the Atlantic are identified using T/P altimeter data during 1992 to 1999. They showed that predominantly eastward Kelvin and westward first two Rossby modes explain all the variance of the T/P data field along the equator and these variabilities are dominated by the seasonal cycle.

The second POP of zonal velocity along the equator explains about 12% of the variance of the zonal velocity (Figure 5.12). Again, the time-dependent coefficients and their spectral distributions are shown as well as the imaginary and real spatial patterns. Spectra of the second POP coefficients show enhanced variance at periods of the semi-annual cycle and weaker peaks for periods of 20-40 d. The imaginary and real patterns of the second POP indicate that predominantly long waves exist at these periods along the equator.

Although the amplitudes of the zonal and meridional velocity fluctuations associated with the 20-40 d ISV are similar, the third POP of zonal velocity along the equator explains about 7% of the variance of the zonal velocity (Figure 5.13). This shows that zonal velocity is dominated by longer period waves. The spectral density has a peak at 20-40 d corresponding to the peak of the first meridional. The intraseasonal fluctuations are as well seasonally and interannually modulated as evident in the time-dependent coefficients

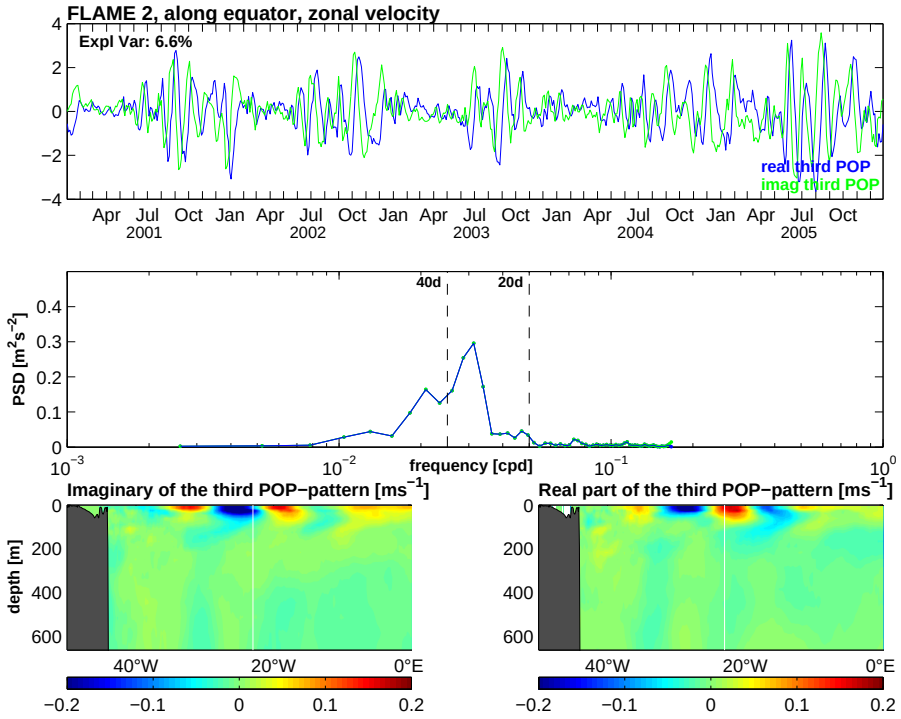

Figure 5.13.: *Non-dimensional coefficients (real part is given by the blue, imaginary by the green line) of the third POP (upper panel) and corresponding spectra of this third POP mode (second panel). Time series of FLAME 2 (2001 to 2005) of zonal velocity along the equator are used. Lower left panel: The imaginary part of the POP-pattern in* ms^{-1}*. Lower right panel: The real part of the POP-pattern in* ms^{-1}*. The 23° W longitude is marked with a white line.*

(Figure 5.13, upper panel) and the westward propagating oscillating patterns are confined to the near surface layer (Figure 5.13, lower panels). In summary, it is evident that the POPs of meridional and zonal velocity describe a westward phase propagation related to ISV at periods of 20-40 d. Interannual modulations of the intraseasonal signal exist which are different for the zonal and meridional component. A similar result could be found in the analysis of the mooring array data (Brandt et al., 2006). In addition, oscillating patterns occur in the zonal velocity at periods of intraseasonal to semiannual cycles which are associated with a signal of long waves.

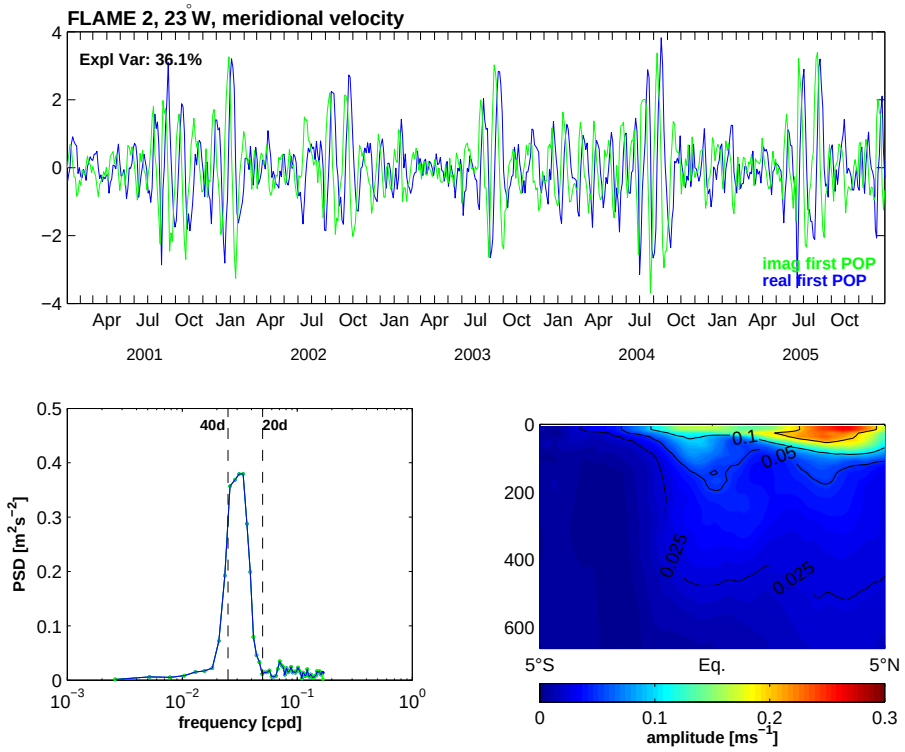

Figure 5.14.: *Non-dimensional coefficients (real part is given by the blue, imaginary by the green line) of the first POP (upper panel) and corresponding spectra of this dominant POP mode (lower left panel). Time series of FLAME 2 (2001 to 2005) of meridional velocity along 23° W between 5° S to 5° N are used. Lower right panel: The square root of the sum of the squares of the imaginary and real patterns of the first POP in* ms^{-1}.

To investigate the meridional extent of the signal a POP of meridional velocity along 23°W between 5° latitude on both sides of the equator is considered (Figure 5.14). The dominant POP of the meridional velocity picks up an intraseasonal oscillation at periods of 20-40 d and which explains about 40% of total variance of meridional velocity. The signals are highly seasonally modulated since the time-dependent coefficients show maximum values predominantly in boreal summer (Figure 5.14, upper panel). The lower right panel of Figure 5.14 shows the square root of the sum of the squares of the sine and cosine spatial patterns of this POP which resembles the amplitude of the oscillation. The dominant structure of the amplitude of the POP is given by a maximum north of the equator in the upper 100 m and the amplitude decreases with

decreasing latitude and increasing depth. This indicates that the signal is confined to the near surface layer and predominantly occurs north of the equator between about 2°-5°N.

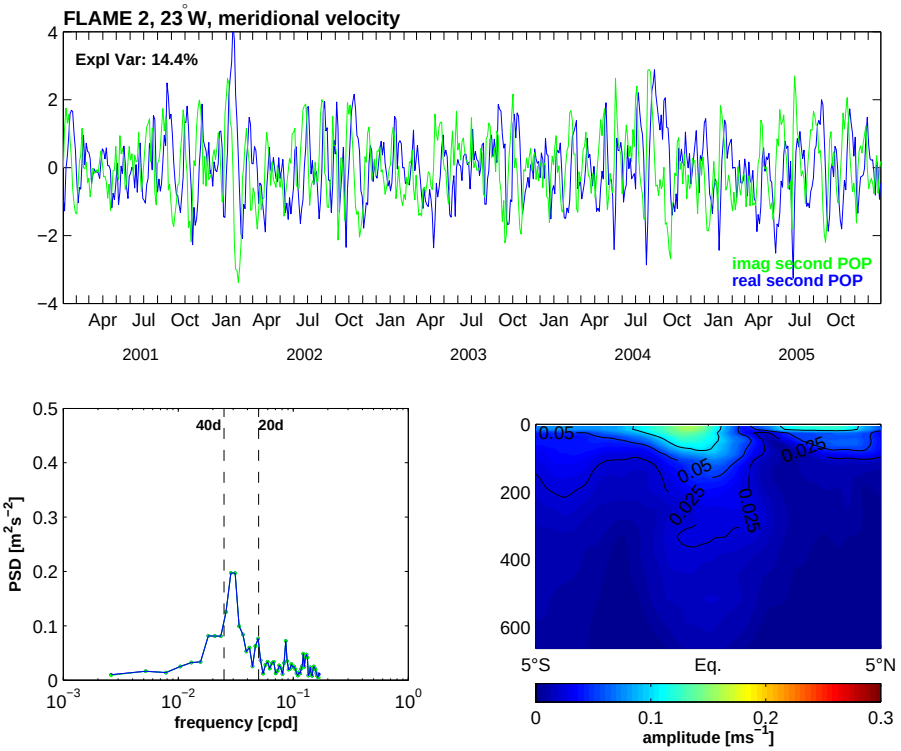

Figure 5.15.: *Non-dimensional coefficients (real part is given by the blue, imaginary by the green line) of the second POP (upper panel) and corresponding spectra of this second POP mode (lower left panel). Time series of FLAME 2 (2001 to 2005) of meridional velocity along 23° W between 5° S to 5° N are used. Lower right panel: The square root of the sum of the squares of the imaginary and real patterns of the second POP in* ms^{-1}.

The second POP of meridional velocity along 23°W is shown in Figure 5.15. The spectral distributions of the time-dependent real and imaginary coefficients peak at periods of 20-40 d, similar to what is obtained for the first POP (Figure 5.14, lower right panel). The explained variance is somewhat lower with 14%. The second oscillating pattern extracted from the FLAME 2 meridional velocity differs from the first in two ways. First, a seasonal modulation of the 20-40 d ISV signal is weak (Figure 5.15, upper panel), whereas the seasonal modulations is one of the striking characteristics of the first POP (Figure 5.14, upper panel). Second, the amplitude in the lower right panel of Figure 5.15 reveals that the second oscillating pattern predominantly occurs close to the equator. Amplitude decreases directly north and south of the equator and the shape of this signal is comparable to a Gaussian distribution, with maximum amplitude slightly shifted to the south. In other words, two oscillating patterns can be extracted by analyzing the meridional velocity along 23°W which both exist in the same period range, i.e. at periods of 20-40 d. The amplitudes of the dominant one show maximum values between 2°-4°N and the patterns are strongly seasonally modulated. The second one, strong as well, occurs predominantly in the equatorial band and a seasonal modulation of the signal is more or less missing.

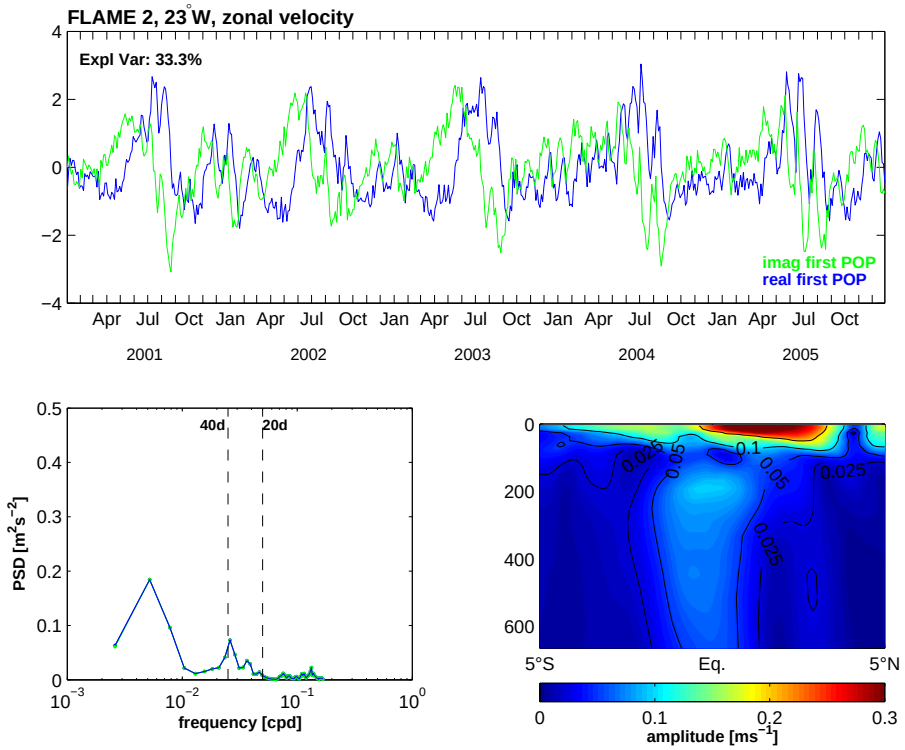

Figure 5.16.: *Non-dimensional coefficients (real part is given by the blue, imaginary by the green line) of the first POP (upper panel) and corresponding spectra of this dominant POP mode (lower left panel). Time series of FLAME 2 (2001 to 2005) of zonal velocity along 23° W between 5° S to 5° N are used. Lower right panel: The square root of the sum of the squares of the imaginary and real patterns of the first POP in* ms^{-1}.

The corresponding POP is evaluated from zonal velocity time series along 23°W and the first POP is shown in Figure 5.16. About 33% of the total variance of the zonal velocity can be explained by this dominant POP which is clearly associated with the annual cycle (Figure 5.16, lower left panel). But beside the annual cycle, enhanced variance is evident on intraseasonal time scales which can be clearly seen in the time-dependent coefficients itself and in its spectral distribution. In boreal summer 2005, for example, about monthly fluctuations are clearly superimposed on the annual cycle, but these fluctuations are present in every year, favorably in May-September (Figure 5.16, upper panel). The amplitudes of the first POP derived from zonal velocity show maximum values between the equator and about 4°S, between the equator and about 4°N and north of 4.5°N in the upper 150 m (Figure 5.16, lower right panel). This distribution of high amplitudes can be associated with the meridional movement of the zonal mean currents in that domain which is associated with the annual cycle of the ITCZ. The first maximum amplitude covers the domain of the westward flowing cSEC, the second that of the westward flowing nSEC and the third is located at the southern flank of the eastward flowing NECC (compare, for example, Figure 5.25). This assumption can be assisted by the fact that the corresponding spatial distributions of the real pattern in the nSEC and NECC domain are out of phase (not shown). In section 5.4.3 this interrelation will be discussed in more detail.

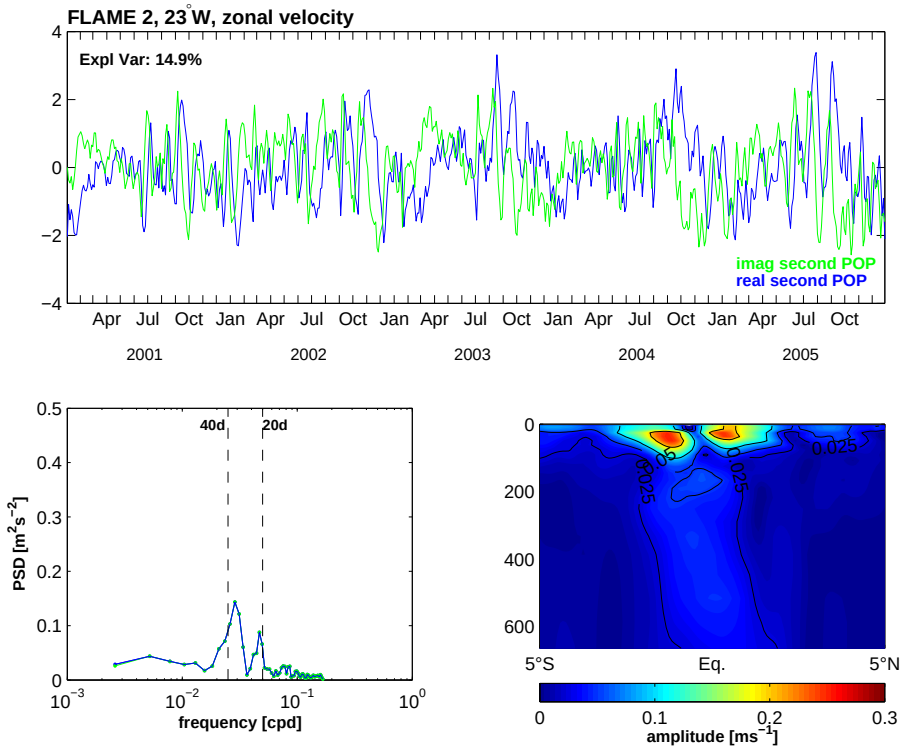

Figure 5.17.: *Non-dimensional coefficients (real part is given by the blue, imaginary by the green line) of the second POP (upper panel) and corresponding spectra of this second POP mode (lower left panel). Time series of FLAME 2 (2001 to 2005) of zonal velocity along 23° W between 5° S to 5° N are used. Lower right panel: The square root of the sum of the squares of the imaginary and real patterns of the second POP in* ms^{-1}.

The second POP of the zonal velocity along 23°W is shown in Figure 5.17. The real and imaginary coefficients of this POP explain about 15% of the zonal velocity. The spectral distribution peaks at 20-40 d periods, but also enhanced variance exists at periods of the annual cycle (Figure 5.17, lower left panel). The monthly fluctuations emerge during the total time domain but a clear seasonal modulation does not occur. The amplitudes of the second POP show maximum values directly north and south of the equator (Figure 5.17, lower right panel). These off-equatorial maxima are subsurface intensified. The amplitudes decrease north and south of these maxima as well as directly on the equator. The spatial distribution of the patterns are out of phase in this domain (not shown). The mechanisms for this characteristic distribution of the amplitudes of the second POP which is associated with a signal of ISV at 20-40 d periods might be either explained by a meandering movement of the EUC or even the result of a Yanai-wave which zonal velocities peak north and south of the equator and drop to zero directly on the equator (Figure 5.18). The fact that the off-equatorial maxima are subsurface intensified poses for the first assumption. But the amplitude of the second POP of the meridional current shows maximum values directly on the equator (Figure 5.15, lower right panel) which even more indicates that the 20-40 d oscillating pattern is associated with a Yanai-wave (compare Figure 5.18).

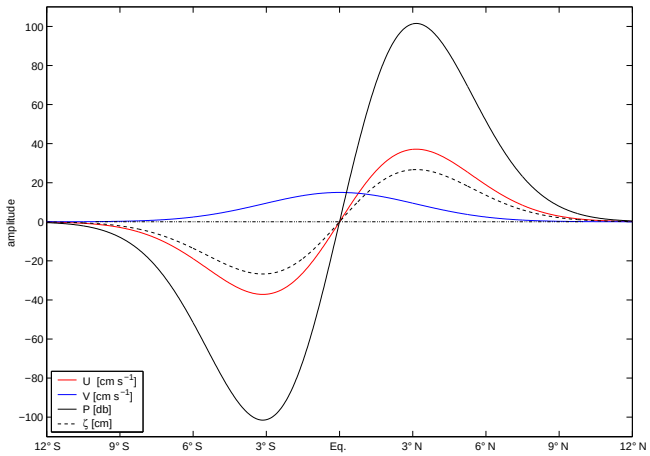

Figure 5.18.: *Theoretical horizontal distribution of a Yanai-wave for zonal velocity U (red), meridional velocity V (blue), pressure P (black) and surface elevation ξ (black dashed).*

In summary, the current measurements of a mooring at the equator reveal that a dominant and seasonally modulated signal of ISV exists at periods of 20-40 d (see also Brandt et al., 2006). Studies using the FLAME 2 model simulations have shown that this signal is associated to a westward propagating pattern with phase speeds of approximately 30 cms^{-1}. Evaluating oscillating patterns along 23°W and between 5° latitude on both sides of the equator in the FLAME 2 simulation indicates that two oscillating patterns can be extracted from the meridional velocity which both exist in the same period range, i.e. at periods of 20-40 d. The amplitudes of the dominant one show maximum values between 2°-4°N and the patterns are strongly seasonally modulated which is probably associated to the annual cycle of the nSEC and the NECC. The second one is located in the equatorial band and a seasonal modulation is more or less missing. The equatorial current measurements at 23°W are affected by the variability at the equator as evident in the POP with maximum amplitude close to the equator. But the signal along the equator seems to be also affected by the 20-40 d ISV with high amplitudes north of the equator since a seasonal modulation of the ISV is evident along the equator.

5.4.2. Spatial distribution of tropical Atlantic variability and EKE generation processes

In the following, the distributions of variability at intraseasonal periods are discussed using altimeter measurements as well as FLAME model simulations. This allows for an identification of different dynamical regimes and thus provides an overview on the various ISV patterns in the tropical Atlantic Ocean. Also, possible relationships of these patterns to tropical instabilities are focused on by means of evaluating energy transfer terms.

The MSLA time series used in this computation span the interval from January 2001 to December 2004. The analysis is restricted to intraseasonal signals since the time series are band-pass filtered 100-150 km in space and 10-150 d in time and the standard deviations

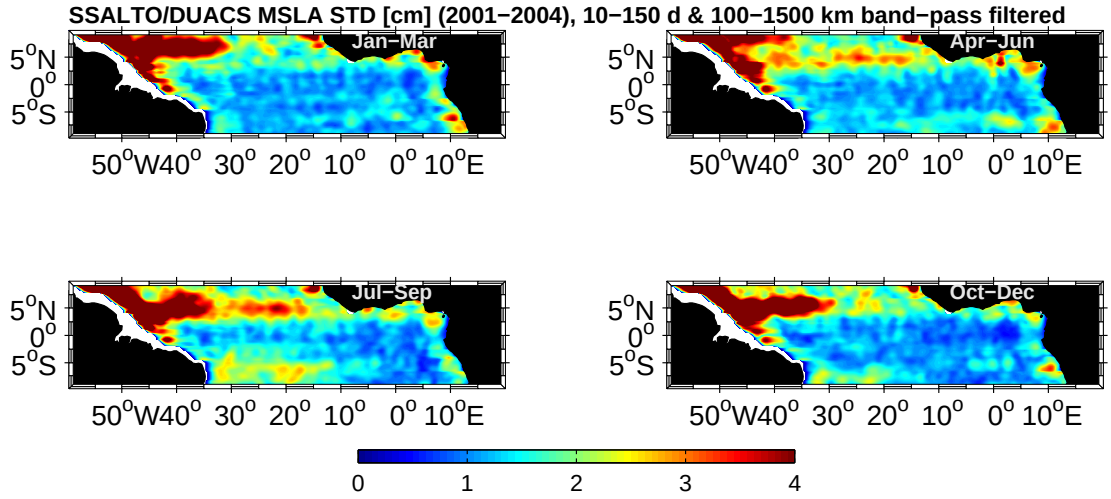

Figure 5.19.: *Seasonal maps of standard deviations, derived from SSALTO/DUACS MSLA during 2001 to 2004. The time series are band pass filtered in both, 10-150 d in time and 100-1500 km in space.*

are then calculated. Especially the dynamics in the northern hemisphere of the tropical Atlantic are characterized by a strong seasonal cycle due to the migration of the ITCZ (e.g. Stramma and Schott, 1999). For this reason, the standard deviations of the MSLA field in Figure 5.19 are calculated for four different seasons since ISV often depends on the background conditions and different intraseasonal signals possibly occur at different times during the year.

In the northern hemisphere along the western boundary, the standard deviations of MSLA show maximum values throughout the year. This signal is most likely linked to the migration of NBC rings along the South American coast into the Caribbean (section 1). Just west of this dynamical regime and north of about 5°N another domain of high values of MSLA standard deviations is present which is possibly related to barotropic instability processes whithin the NECC as described by Jochum and Malanotte-Rizzoli (2003a). Variability in this domain is clearly seasonally modulated. The domain of high standard deviations is extended to the east as the NECC is present in July to January (e.g. Johns et al., 1990) and decreases in boreal spring to summer when the NECC is weak or even reversing (e.g. Richardson and Reverdin, 1987).

Another ISV pattern frequently described in literature is the generation and radiation of TIWs as already discussed in the introduction. One prominent feature that characterizes the signal of TIWs is their low-frequency modulation from season to season. The entire upper equatorial circulation varies seasonally and quickens when the winds are strongest in June to December. The westward cSEC and eastward NECC, for example, are strongest in boreal summer (e.g. Stramma and Schott, 1999). These conditions produce both the strongest meridional shears and sharpest temperature fronts and thus the TIWs occur in May to June and persist through the following season in February to March (e.g. Polito et al., 2001). In Figure 5.19, signals of high standard deviations occur in April to June and in July to September which are located at about 5° latitude north and south of the

equator in the central Atlantic Ocean which are possibly linked to the signal of TIWs. The strength of the signal in the northern hemisphere is more intense compared to the pattern in the southern hemisphere. In a numerical model study by Yu et al. (1995) the asymmetry that TIWs have largest amplitudes north of the equator is investigated. Since the energy sources for the TIWs lead back to instability mechanisms, these dynamics are affected by cross-equatorial asymmetries in the SEC and the equatorial SST fronts. As they could show in their studies, these solutions had slower growth rates and dispersion characteristics compared to those from a symmetric background mean state of the tropical ocean. The existence of the NECC had little or no effect on the symmetry of the solutions.

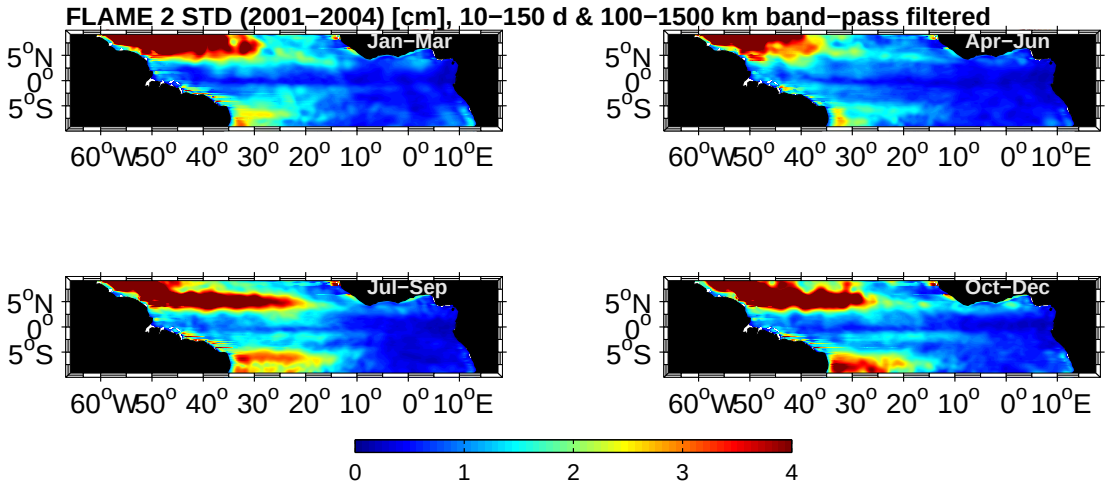

Figure 5.20.: *Seasonal maps of standard deviations, derived from six years of FLAME 1 model results. The time series are band pass filtered in both, 10-150 d in time and 100-1500 km in space.*

In Figure 5.20 the SSH of the FLAME 2 simulation is used to calculate the standard deviation for the different seasons. Four years of model results are band-pass filtered 10-150 d in time and 100-1500 km in space. High values exist as well along the western boundary. But interesting to note here is that NBC-ring variability apparently appears further north compared to the observations in Figure 5.19. Away from the coast further east, NECC instability growths during July to September and October to December. Simultaneously, signals in the central and western tropical Atlantic occur at about 5° latitude on both sides of the equator but which in the northern hemisphere are hard to separate from the signal in the NECC domain. These signals which are linked to TIWs start to develop in April to June in the eastern and central basin, increase in July to September, and persist until early boreal spring. In the southern hemisphere, the development and generation of these signals are discussed in more detail in section 5.1, but in this context it is interesting to note that the standard deviations in the model results are somewhat higher compared to the satellite observations (Figure 5.19) in that domain. Along the equator, enhanced standard deviation is evident, predominantly in late boreal summer to winter.

In Figure 5.21 the distribution of EKE is examined from the FLAME 2 model results between 2001 to 2004 at 50 m depth. The time series are band-pass filtered 10-150 km in

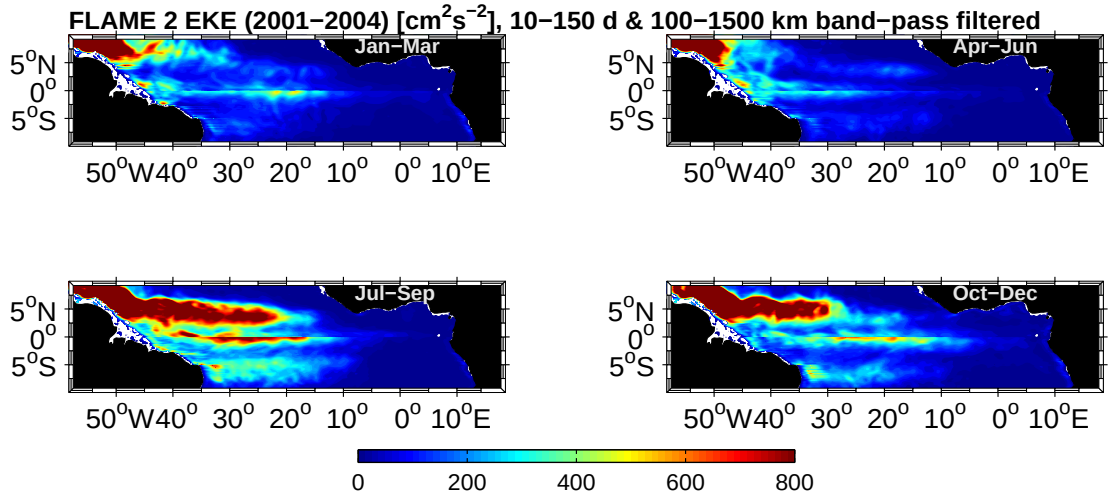

Figure 5.21.: *Seasonal maps of eddy kinetic energy (EKE) at 50 m depth, derived from six years of FLAME 1 model results. The time series are band pass filtered in both, 10-150 d in time and 100-1500 km in space.*

time and 100-1500 km in space and then variances of zonal and meridional velocity are calculated at the different seasons. As expected, the response of strongest EKE signals are located along the pathways of the NBC rings and in the NECC domain when the eastward current is established in the second half of the year. Besides these dominant patterns, EKE starts to be generated in April to June at 5° lat on both sides of the equator and along the equator. These signals show maximum values in July to September, sustain in boreal winter and decrease in January to March. The signal of high EKE along the equator is dominant, although standard deviations are low in the model as well as in the observations due to the effect of intraseasonal equatorial waves.

The distinct concentration of EKE along the shear zone of the tropical currents motivates to analyze in which way these EKE patterns are generated by instabilities of the mean flow field in the central Atlantic ocean. Since the generation of EKE appears to be seasonally modulated energy transfer terms concerning barotropic and baroclinic instability processes are evaluated for the different seasons. For this purpose, six years of FLAME 1 model results are used and seasonal means of zonal and meridional velocity and density have been recognized. The formalism which forms the basis for this analysis have been introduced in section 4.2. If EPE is generated, energy can be converted into the EKE field. In other words, if baroclinic instabilities develop it is possible that large negative values of T_3 can exist. Therefore only T_3 and T_4 are examined for a systematic energy transfer as an indication of barotropic and baroclinic instabilities, respectively. To approve that a discussion of seasonal T_2 in the tropics does not much differ from the distribution of T_3, the reader is referred to Figure B.1 in the appendix.

Figure 5.22 shows seasonal maps of horizontal distribution of T_4, averaged over the top 50 m. The upper ocean is influenced by barotropic instability mostly in the northern hemisphere. Strong instability processes occur along the western boundary and in the NECC domain. In both regions the influence of the annual cycle appears to be strong and

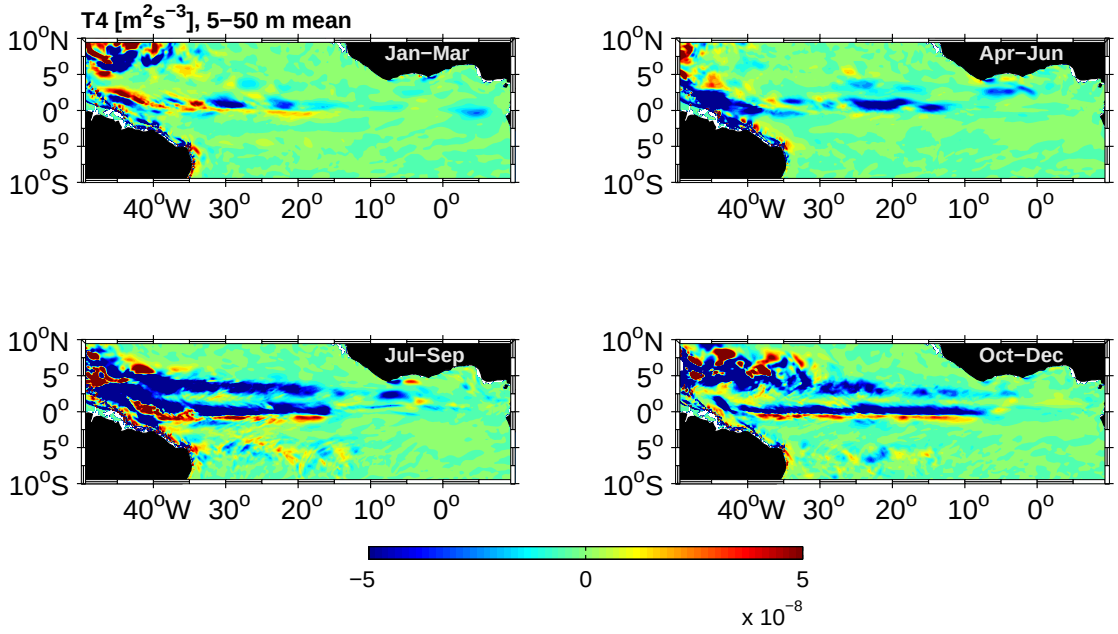

Figure 5.22.: *Seasonal maps of energy conversion term T_4 (equation 4.4), derived from six years of FLAME 1 model results and averaged over the top 50 m. Negative sign denotes transfer into the fluctuation.*

EKE is generated mostly in the second half of the year in the western part of the northern basin. Just north of the equator, values of negative T_4 are evident throughout the year. But the intensity of this signal varies with the seasons and the influence of barotropic instability becomes strong in July to September and in October to December. EKE is generated during that time which is clearly visible in Figure 5.21. Just south and along the equator, values of T_4 are positive which indicates that barotropic instability maintains the structure of the mean front by feeding energy back into the mean flow at the same time when variability is generated (Figure 5.22). A study by Philander (1976) using a two-layer model has shown that the EUC in the Atlantic Ocean is unlikely to become unstable. Thus, the signal of high EKE in the equatorial band is more likely to be generated by horizontal shear instability between the eastward EUC and the westward nSEC which can be assisted by the signal of negative T_4 in that domain.

North of the equator, a band of negative T_4 is evident at about 4°-5°N. This signal predominantly occurs during boreal summer and persists till boreal winter. This result supports of what is already well known in that domain, that is the generation of EKE by horizontal shear instabilities between the westward nSEC and the eastward flowing NECC (e.g. Philander, 1978). Barotropic instability starts to develop in early boreal summer when the NECC is established and becomes maximal when the zonal currents speed up in boreal summer (Figure 5.22). In spring, the NECC is slow or even westward and values of T_4 alter about zero energy conversion. As already recognized in Figure 5.21, the generation of EKE is asymmetrically distributed in the tropical Atlantic since effects of barotropic instability only become important in the northern hemisphere (Figure 5.22).

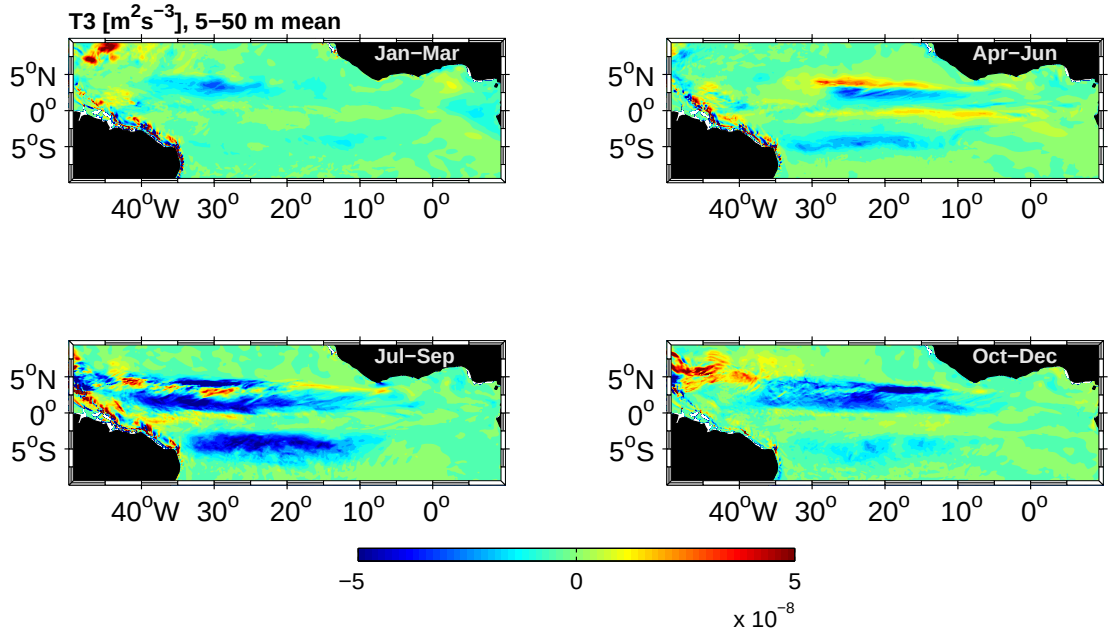

Figure 5.23.: *Seasonal maps of energy conversion term T_3 (equation 4.3), derived from six years of FLAME 1 model results and averaged over the top 50 m. Negative sign denotes transfer from EPE into EKE.*

Figure 5.23 shows seasonal maps of horizontal distribution of T_3, averaged over the top 50 m. Different to the distribution of T_4, energy transfer between EPE and EKE becomes important in both hemispheres. Close to the western boundary and in the NECC domain, positive and negative T_3 exists, indicating that both barotropic and baroclinic instability generate EKE in these two regions. In the central tropical Atlantic, predominantly negative values of T_3 appear between the equator and 5° latitude on both sides of the equator which are strongest in July to September and more or less drop to zero in January to March. These signals are referred to a transfer of energy from the EPE field into the EKE field which also means that baroclinic instability processes must exist in these areas which generate the corresponding amount of EPE (see also Figure B.1 in the appendix). As will be shown later, these areas are covered by the zonal SEC regime which is cutted into an area north of the equator and one south of the equator due to the eastward flowing EUC along the equator. The SEC domain is thought to present conditions favorable to the development of baroclinic instabilities since changes of potential vorticity are strong in this domain (for the northern hemisphere, for example, Beckmann et al., 1994, their Figure 5). Patterns of negative T_3 are more intense in the northern hemisphere reflecting again the asymmetry in the tropics as discussed before.

Besides the influence of baroclinic instabilities, the transfer term T_3 gives also information about the intensity of barotropic instability as discussed in Figure 5.22. Indeed, barotropic instability acts to be strong close to the western boundary north of the equator and in the NECC domain but most of these generated fluctuative energies are advected by migrating rings and waves rather than converted into EPE. Consequently, compared to the generation of EKE less energy remains in these areas as evident in Figure 5.23. In

the central tropical Atlantic, positive values of T_3 exist at about 5°N and just north of the equator predominantly in April to June. In July to September, theses areas covered by positive T_3 decrease and the distribution appears to be scattered. But during the same time, the generation of EKE arrived at its peak level (Figure 5.22). Consequently, fluctuative energy must be dissipated or advected in this domain from which the latter might be established by propagating waves, i.e. TIWs. A similar relationship can be found in the distribution of T_2 (appendix) which suggests that both barotropic as well as baroclinic instabilities generate fluctuative energy predominantly in boreal summer. This energy is advected away from its generation region by propagating waves which occur in late boreal summer and persist until boreal winter (e.g. Polito et al., 2001). Barotropic instability exists close to the equator and at about 5°N whereas baroclinic instability influences the mean flow field in the off-equatorial domain up to 5° latitude in both hemispheres.

5.4.3. Discussion

Various domains of tropical instabilities exist in the Atlantic ocean. The strongest signals are linked to the NECC instabilities and NBC-ring variability close to the western boundary in the northern hemisphere. The analysis of the model output has shown that predominantly barotropic instability mechanisms account for the generation of EKE in this area and effects due to baroclinic instabilities are comparable weak. Jochum and Malanotte-Rizzoli (2003a) have shown in an analysis of a numerical model that barotropic instabilities influence the generation of NBC-rings in that domain. However, the distribution of the conversion terms suggests a more complex behavior of the instability processes leading to NBC-rings since locally confined processes take place as well and the sign of the conversion terms alter from positive to negative sign several times in that domain. The NBC rings are shed at the western boundary where the NBC retroflection occurs (e.g. Fratantoni and Glickson, 2002, see also section 1) and the nature of the ring

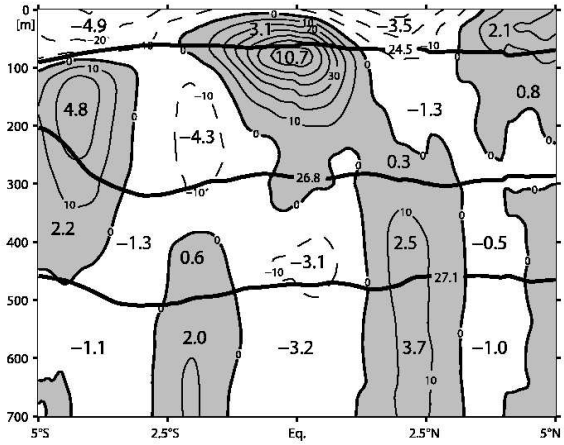

Figure 5.24.: *Mean zonal current distribution from 11 section at 26° W (in cm/s), with layer transports (in Sv = 10^6 m^3s^{-1}) of different current branches overlaid on potential density (thick solid lines). After Brandt et al. (2006).*

formation make the process a highly non-linear one (Jochum and Malanotte-Rizzoli, 2003b).

In the central tropical Atlantic large values of EKE are generated due to barotropic and baroclinic instability. In order to discuss the domain of tropical instabilities with the mean current system in the tropical Atlantic, a distribution of mean zonal current from 11 sections at 26°W is shown in Figure 5.24. As already investigated in section 5.3, the near surface currents in the southern tropics are predominantly characterized by westward flow. This flow can be attributed to the cSEC (e.g. Schott et al., 2004). At the equator, the eastward flowing EUC exists. This equatorial current is subsurface intensified with its mean core depths below the $\sigma_\Theta = 24.5$ kgm^{-3} isopycnal. Between the equator and 4°N, again a core of westward flow is evident and is subscribed to the nSEC (Schott et al., 2004). At the northern edge of this section, the eastward flowing NECC exists. At intermediate depths, several eastward and westward current cores are evident (e.g. Brandt et al., 2006; Schott et al., 2003) that are not important here.

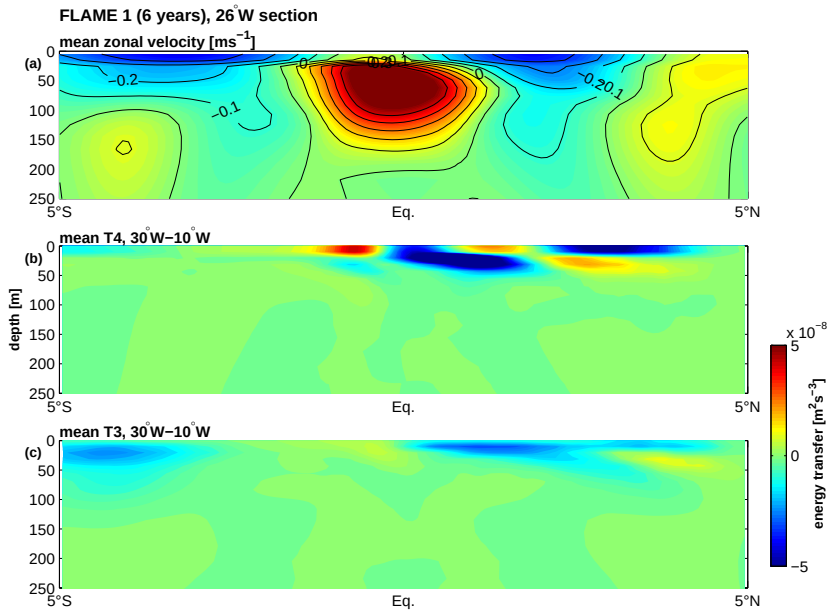

Figure 5.25.: *(a) Mean zonal velocity along 26° W derived from FLAME 2 model results during 2001 to 2004. (b) Mean energy transfer term T_4 between 30° W and 10° W evaluated from six years of FLAME 1 results. Negative sign denotes transfer into the fluctuation. (c) Mean energy transfer term T_3 between 30° W and 10° W evaluated from six years of FLAME 1 results. Negative sign denotes transfer from EPE into EKE.*

In Figure 5.25 (a) the corresponding mean zonal velocity derived from six years of FLAME 1 model results is shown. The model results are in good agreement with the measurements (Figure 5.24). The SEC on both sides of the equator, the EUC as well as the NECC are fully established in the near surface layer. The currents below the thermocline are somewhat weaker in the model. In Figure 5.25 (b) the vertical distribution of mean (30°W-10°W) energy transfer term T_4 is shown. Near the equator, horizontal shear instability occurs in the region of large latitudinal shear between the EUC and the nSEC, where EKE is generated. Further north, again large negative values of T_4 are evident in the latitudinal

shear between the nSEC and the NECC. In both cases, negative T_4 is confined to the near surface layer since below 50 m depth the shear of the zonal currents decreases (Figure 5.25 (a)). Studying oscillating patterns from the FLAME 2 velocity field along 23°W reveals that two oscillating patterns can be extracted from the meridional velocity which both exist in the same period range, i.e. at periods of 20-40 d. The amplitudes of the dominant one show maximum values between 2°-4°N and the patterns are strongly seasonally modulated. This domain of large amplitudes corresponds to the area of strong shear between the nSEC and the NECC as mentioned above. This assumption is confirmed by the fact that the zonal amplitudes of the first POP along 23°W become large in the nSEC and NECC domain. The spectral distributions of the corresponding time-dependent coefficients peaks at the annual cycle which is clearly connected to the annual cycle of the NECC. In addition, seasonal maps of T_4 have shown that barotropic instability generates EKE predominantly at the time where the NECC is established and the shear between the nSEC and the NECC exists.

The second POP of meridional velocity along 23°W (Figure 5.15) indicates enhanced amplitudes at the equator which correspond to the domain of strong horizontal shear between the EUC and the nSEC (Figure 5.25 (a)). The seasonal modulation of the ISV pattern is weak since the annual cycle of the nSEC and EUC is weak compared to the NECC. Nevertheless, barotropic instability increases just north of the equator when the zonal currents speed up in boreal summer. EKE is generated due to horizontal shear instability and is radiated away by propagating waves with westward phase speeds of about 30 cms^{-1} and eastward group velocity at periods of 20-40 d. Results from the model simulation indicate that this oscillating pattern might be associated with an equatorial Yanai-wave.

Not only barotropic instability, but also baroclinic instability generate EKE in the central tropical Atlantic Ocean. In the FLAME model simulation, the signal of baroclinic instability becomes strong in that domain which is covered by the cSEC and nSEC (Figure 5.25 (c)). The generation of fluctuative energies due to baroclinic instability processes intensify simultaneously when the zonal velocities increase in boreal summer. In a study by Jochum et al. (2004) using a 1/4° numerical model for the Atlantic Ocean the generation of TIWs is analyzed. As for the results obtained in this study, they could show that TIWs are generated between May to January. But the results of their analysis of TIW energetics differs from the conclusions drawn here. They demonstrate that barotropic instability of the EUC/nSEC is the main generation mechanism for the Atlantic TIWs. The analysis of the 1/12° FLAME model simulation presented in this study leads to the conclusion that in the southern hemisphere, EKE is generated only by baroclinic instability, whereas in the northern hemisphere also horizontal shear instability of the EUC/nSEC and of the nSEC/NECC contributes to the generation of fluctuative energies in the central tropical Atlantic Ocean, from which the latter barotropic instability process mostly affects the seasonal modulation of the TIWs.

6. Summary and concluding remarks

Measurements from a mooring array, from a morring at the equator and from satellite altimetry as well as results from two numerical model simulations revealed the presence of fluctuations with intraseasonal time scales. Theoretically, intraseasonal fluctuations in the upper-ocean circulation can be excited through several dynamic processes: direct wind forcing, wind forcing in remote areas via waveguide, mean flow instability, and resonance due to coastline geometry. The major objective of this study is to clarify the dynamic processes underlying the observed ISV close to the western boundary in the tropical South Atlantic Ocean from the near surface layer down to intermediate depths and in the near surface layer of the warm water sphere.

The NBUC is the main pathway of AAIW flowing from the southern hemisphere into the northern hemisphere (Suga and Talley, 1995). This salinity poor water then spreads into the equatorial band (Schott et al., 1998). The results of this study have shown that the direct pathway of the oxygen and nutrient rich water mass along the western boundary is intermitted at about 4°-5°S since there barotropic instability influences the NBUC and a recirculation cell is developed. This water mass then recirculates between 5°-14°S and is accompanied by a signal of large EKE values which is generated by horizontal shear instabilities. But nevertheless, fractures of AAIW reach the equator and spread into the equatorial zonal current system. Time-latitude plots along the South American coast have shown that the salinity minimum reaches the equator at sporadic intervals, rather than by a continuous flow. Maybe this is the reason why the question how AAIW crosses the equator is still under consideration since it is easier to capture a continuous flow by measurements rather than a sporadic supply of AAIW from the south.

In the near surface layer of the central tropical Atlantic Ocean barotropic as well as baroclinic instabilities generate EKE in the northern hemisphere which is then advected by the existence of wave dynamics. In the southern hemisphere, only baroclinic instabilities develop in the model simulation. This explains the often mentioned asymmetry between the intensity of TIWs in the northern and southern hemisphere since in the northern hemisphere, two mechanisms exist which generate EKE whereas in the southern hemisphere EKE is only produced by baroclinic instability processes. However, in the southern hemisphere the generation of EKE is discussed in more detail with focus on enhanced ISV at 11°S in the mooring array data close to the western boundary. It could be shown that tropical instability processes in the cSEC domain are linked to the signal of ISV at 11° near the coast. In boreal summer, baroclinic instability increases in the eastern part of the cSEC and simultaneously mesoscale patterns in the central basin are evident south of 7°S. These enclose colder water masses than its surroundings since current vectors indicate cyclonic circulation. As these patterns reach the western boundary, variability clearly increases. Examining Lagrangian drifter trajectories indicates that especially between 10° to 15°S a strong tendency for drifter exists to exhibit cyclonic loops (R. Lumpkin, personal

communication, 2006).

Current measurements of a mooring array at 23°W and results from the FLAME model simulations at the equator have shown with consistency that their dominant oscillating pattern is associated with ISV at periods of 20-40 d. In addition, the model studies show that these patterns can be described as westward propagating waves at phase speeds of 0.2-0.3 ms^{-1} which show characteristics similar to a Yanai-wave. Examining the generating mechanisms reveals that horizontal shear instability between the EUC and the nSEC are the main source for these propagating disturbances. But barotropic instability processes further north in the shear region between the nSEC and the NECC also influence the generation of equatorial waves at intraseasonal time scales. Oscillating patterns generated in this area are characterized by a strong seasonal cycle which is associated with the pronounced annual signal of the NECC. In addition, effects of baroclinic instabilities exist in the domain in between, i.e. in the area covered by the nSEC.

Since it is very difficult to diagnose energetics from sparse ocean observations, most of this work concerning ocean energetics here based on the FLAME model simulations. But nevertheless, several attempts have been made to evaluate energy transfer terms with the help of the existing observations. For the first attempt the current measurements along 11°S close to western boundary have been used. Concerning barotropic instability, only a fraction of energy transfer term T_4 can be calculated from the mooring array data because derivations of velocity in meridional direction are missing. However, variances and covariances of zonal velocity could be evaluated and compared to the corresponding model solutions. But estimating the baroclinic energy transfer term is somewhat difficult and several presumptions need to be done. In particular, the salinity must be estimated from CTD casts to evaluate the potential density since only temperature measurements are obtained from the mooring array. Besides the covariance of zonal velocity and potential density, horizontal and vertical gradients need to be estimated which means that the results are highly sensitive to possible noise ratios and errors. In addition, a basinwide discussion of energy transfer terms in the western tropical south Atlantic indicates that energy transfer terms along a section at 11°S appear not to be robust, even if the model simulation itself is used for computations. Thus, one can conclude that it is important to discuss energy transfer terms averaged over a domain which is large enough that the influence of altering signs due to local effects disappears.

In the near surface layer several measurements exist which cover the entire tropical Atlantic and an attempt is made to estimate energy transfer terms from these observations. For the baroclinic instability term only horizontal changes of temperature can be evaluated by using measurements from the microwave sensor. To calculate the horizontal derivatives from the mean currents a climatology of near-surface currents derived from satellite-tracked surface drifting observations (Lumpkin and Garraffo, 2005) is used. But the resolution is too sparse to sufficiently resolve the driving ocean internal dynamics. As discussed above, especially in the central tropical Atlantic as well as in the equatorial band the generation of ocean energetics is somewhat complex. In addition, the FLAME model results have shown that barotropic and baroclinic instability are located close to each other and interactions are to be expected. The distribution of an averaged T_4 and T_2 term between 5°-10°S is very noisy and comparisons to the model results as well as interpretations are not possible.

The comparison of the model results to the observations has shown, that most of the ISV signals detected in the observations are simulated by FLAME. But discrepancies also exist. In particular, the comparison of variance and EKE derived from simulated velocities shows that these values are generally lower compared to corresponding observations, especially at intraseasonal and shorter time scales. Part of this discrepancy could be explained by transport errors made by using a sparser resolution concerning the observations, but a significant difference remains. On the other hand, the comparison of simulated sea surface elevation to altimeter measurements reveals another result. Derived variance from the simulations is systematically higher in regions where the influence of the annual and semiannual cycle is low, for example, in the domain of the cSEC and further south. This discrepancy could be explained as follows. The spectral distributions along 11°S from the western to the eastern boundary has shown, that variance is also strong below about 20 d in the model results whereas the variance of the observations is predominantly banded between 50-100 d. The time interval of the merged MSLA product is 7 days and consequently periods below 14 d are not acquired. The model output is given every third day and periods below 20 d are resolved.

The results of this thesis contribute to the observation of ISV in the tropical Atlantic Ocean. Analyzing both, observations and models, it could be shown that the use of numerical model simulations fundamentally helps to diagnose dynamics which generate signals of large energies in the observations. But the findings obtained from the observations also support the model design so that those simulations are possible to approach to what is real in ocean dynamics.

A. Mooring array at 11°S

Station	Lat/Lon/bottom	depth [m]	Record length [d]	mean temperature [°]
K1	10°16.0'S; 35°51.7'W	408	171	9.3
		622	466	6.6
K2	10°22.8'S; 35°40.8'W	292	456	11.3
		499	1139	6.4
		909	1320	3.9
		1407	1594	4.3
		1899	1605	3.6
K3	10°36.7'S; 35°23.4'W	506	1151	6.3
		888	685	3.8
		1400	1151	4.3
		2438	1013	3.0
		2936	1518	2.6
K4	10°56.5'S; 34°59.5'W	123	1602	24.2
		310	463	10.7
		515	1602	6.0
		919	464	3.7
		1416	1602	4.0
		1913	1602	3.5
		2410	1602	3.0
		3402	1035	2.4

Table A.1.: *Mooring position and temperature profiling instrumentation for the 11° S array between March 2000 and August 2004.*

B. Distribution of baroclinic instability in the tropical Atlantic

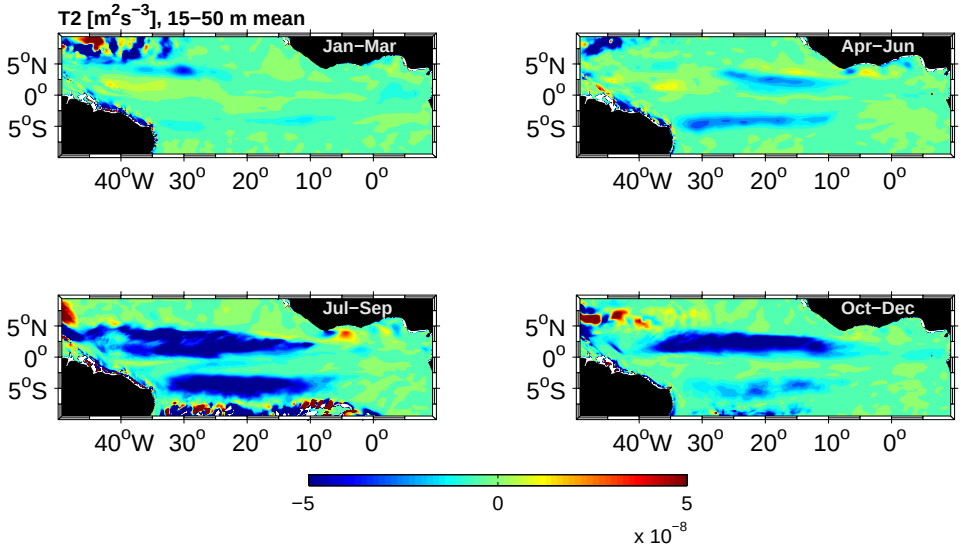

Figure B.1.: *Seasonal maps of energy conversion term T_2 (equation 4.2), derived from six years of FLAME 1 model results and averaged over the top 50 m. Negative sign denotes transfer into the fluctuation.*

Bibliography

Aanderaa, 1981: Operating Manual RCM 4+5. *Aanderaa Instruments, Fanaveien 13, 5051 Bergen, Norwegen, Technical Description N°119*.

Aanderaa, 1993: Operating Manual RCM 7+8. *Aanderaa Instruments, Fanaveien 13, 5051 Bergen, Norwegen, Technical Description N°159*.

Arhan, M., H. Mercier, B. Bourles, and Y. Gouriou, 1998: Two hydrographic sections across the Atlantic at 7°30N and 4°30S. *Deep-Sea Research*, **45**, 829–872.

Arkawa, A. and V. Lamb, 1977: Computational design of basic dynamical processes of the UCLA General Circulation Model. *Methods in Computational Physics*, pp. 173–265.

AVISO, 2004: SSALTO/DUACS User Handbook: (M)SLA and (M)ADT Near-Real Time and Delayed Time Products. *Nomenclature: SALP-MU-P-EA-21065-CLS*, **Version: 1rev3**.

Barnier, B., L. Siefridt, and P. Marchesiello, 1995: Thermal forcing for a global ocean circulation model using a three-year climatology of ECMWF analyses. *Journal of Marine Systems*, **6(4)**, 363–380.

Beckmann, A., C. Böning, B. Brügge, and D. Stammer, 1994: On the generation and role of eddy variability in the central North Atlantic Ocean. *Journal of Geophysical Research*, **99(C10)**, 20,381–20,391.

Bernstein, L. and W. White, 1981: Stationary and traveling mesoscale perturbations in the Kuroshio Extension Current. *Journal of Physical Oceanography*, **11**, 692–704.

Bleck, R., C. Rooth, D. Hu, and L. Smith, 1992: Salinity-driven thermohaline transients in a wind- and thermohaline-forced isopycnic coordinate model of the North Atlantic. *Journal of Physical Oceanography*, **22**, 1486–1505.

Boebel, O., R. Davis, M. Ollitrault, R. Peterson, P. Richardson, C. Schmid, and W. Zenk, 1999a: The intermediate depth circulation of the western South Atlantic. *Geophysical Research Letters*, **26(21)**, 3329–3332.

Boebel, O., C. Schmid, and W. Zenk, 1999b: Kinematic elements of Antarctic Intermediate Water in the western South Atlantic. *Deep-Sea Research II*, **46**, 355–392.

Boyer, T. and S. Levitus, 1997: *Objective Analysis of temperature and salinity for the world ocean on a 1/4° grid*. Technical Report, NOAA Atlas NESDIS 11, U.S. Gov. Printing Office, Washington D.C.

Brandt, P., M. Dengler, A. Rubino, D. Quadfasel, and F. Schott, 2003: Intraseasonal variability in the southwestern Arabian Sea and its relation to the seasonal circulation. *Deep-Sea Research II*, **50**, 2129–2141.

Brandt, P. and C. Eden, 2005: Annual cycle and interannual variability of the mid-depth tropical Atlantic Ocean. *Deep-Sea Research I*, **52**, 199–219.

Brandt, P., F. Schott, C. Provost, A. Kartavtseff, V. Hormann, B. Bourlés, and J. Fischer, 2006: Circulation in the central equatorial Atlantic: Mean and intraseasonal to seasonal variability. *Geophysical Research Letters*, **33**, doi:10.1029/2005GL025498.

Bretherton, C., M. Widman, V. Dymnikov, J. Wallace, and I. Bladé, 1999: The effective number of spatial degrees freedom of a time-varying field. *Journal of Climate*, **12**, 1990–2009.

Bretherton, F., R. Davis, and C. Fandry, 1976: A technique for objective analysis and design of oceanic experiments. *Deep-Sea Research*, **23**, 559–582.

Broecker, W., T.-H. Peng, J. Jouzel, and G. Russel, 1990: The magnitude of global freshwater transports of importance to ocean circulation. *Climate Dynamics*, **4**, 73–79.

Brooks, R., D. Lockwood, and D. H. III, 1990: Effects of islands in the Geosat footprint. *Journal of Geophysical Research*, **95(C3)**, 2849–2855.

Caltabiano, A., I. Robinson, and L. Pezzi, 2005: Multi-year satellite observations of instability waves in the Tropical Atlantic Ocean. *Ocean Science Discussions*, **2**, 1–35.

Chelton, D., R. de Szoeke, and M. Schlax, 1998a: *Global atlas of the first-baroclinic Rossby radius of deformation and gravity-wave phase speed*. College of Oceanic and Atmospheric Sciences Oregon State University. http://www.oce.orst.edu/research/po/research/chelton/index.html.

Chelton, D., R. de Szoeke, M. Schlax, K. E. Naggar, and N. Siwertz, 1998b: Geographical variability of the first-baroclinic Rossby radius of deformation. *Journal of Physical Oceanography*, **28**, 433–460.

Chelton, D., S. Esbesen, M. Schlax, N. Thum, M. Freilich, F. Wentz, C. Gentemann, M. McPhaden, and P. Schopf, 2001: Geographical variability of the first-baroclinic Rossby radius of deformation. *Journal of Climate*, **14**, 1479–1498.

Chelton, D. and M. Schlax, 1996: Global observations of oceanic Rossby waves. *Science*, **272**, 234–238.

Conkright, M., J. Antonov, O. Baranova, T. Boyer, H. Garcia, R. Gelfeld, D. Johnson, R. Locanini, P. Murphy, T. O'Brien, I. Smolyar, and C. Stephens, 2002: World Ocean Database 2001. Vol. 1: Introduction. *NOAA Atlas NESDID 42, U.S. Gov. Printing Office, Washington D.C.*, p. 159.

Csanady, G., 2001: *Air-sea interactions: Laws and mechanisms*. Camebridge University Press, New York.

da Silveira, I., L. de Miranda, and W. Brown, 1994: On the origins of the North Brazil Current. *Journal of Geophysical Research*, **99**, 22,501–22,512.

Dengler, M., F. Schott, C. Eden, P. Brandt, J. Fischer, and R. Zantopp, 2004: Break-up of the Atlantic deep western boundary current into eddies at 8°S. *Nature*, **432**, 1018–1020.

Deser, C., S. Wahl, and J. Bates, 1993: The influence of sea surface temperature gradients on stratiform cloudiness along the equatorial front in the Pacific Ocean. *Journal of Climate*, **6**, 1172–1180.

Didden, S. and F. Schott, 1992: Seasonal variations in the western tropical Atlantic: Surface circulation from Geosat altimetry and WOCE model results. *Journal of Geophysical Research*, **97**, 3529–3541.

Didden, S. and F. Schott, 1993: Eddies in the North Brazil Current retroflection region as observed by GEOSAT altimetry. *Journal of Geophysical Research*, **98**, 20121–20131.

Diggs, S., J. Kappa, D. Kinkade, and J. Swift, 2002: WOCE Hydrographic Program Office, Scripps Institution of Oceanography. *University of California, San Diego, La Jolla, CA 92093*.

Ducet, N. and P. L. Traon, 2000: Global high-resolution mapping of ocean circulation from TOPEX/Poseidon and ERS-1 and -2. *Journal of Geophysical Research*, **105(C8)**, 19,477–19,498.

Eden, C. and T. Jung, 2006: Wind-driven eddies and plankton blooms in the North Atlantic Ocean. *Internal Report ECMWF, Technical Memorandum*, **490**, 1–13.

Edwards, C. and J. Pedlosky, 1998: Dynamics of nonlinear cross-equatorial flow. Part I: potential vorticity transformation. *Journal of Physical Oceanography*, **28**, 2382–2406.

Emery, W. and R. Thomson, 2001: *Data analysis methods in physical oceanography*. Elsevier Science B.V. Second and revised edition.

ETOPO5, 1988: *Data relief of the surface of the earth*. 88-mg-02, National Geophysical Data Center, Boulder Colorado.

Fischer, J., P. Brandt, M. Dengler, M. Müller, and D. Symonds, 2003: Surveying the upper ocean with the ocean surveyor: A new phased array Doppler current profiler. *Journal of Atmospheric and Oceanic Technology*, **20**, 742–751.

Fischer, J., V. Hormann, P. Brandt, F. Schott, B. Rabe, and A. Funk, 2006: The South Equatorial Undercurrent in the tropical Atlantic deduced from floats and shipboard current measurements. *Geophysical Research letters, submitted*.

Foltz, G. and J. Carton, 2004: Tropical instability vortices in the Atlantic Ocean. *Journal of Geophysical Research*, **109**, doi:10.1029/2003JC001942.

Foltz, G. and M. McPhaden, 2004: The 30-70 day oscillations in the tropical Atlantic. *Journal of Geophysical Research*, **31**, doi:10.1029/2004GL020023.

França, C., I. Wainer, A. de Mesquita, and G. Goni, 2003: Planetary equatorial trapped waves in the Atlantic ocean from TOPEX/POSEIDON altimetry. *in Interhemispheric Water Exchange in the Atlantic Ocean, Elsevier Oceanographic Series*, **68**, 213–232.

Fratantoni, D., 2001: North Atlantic surface circulation during the 1990's observed with satellite-tracked drifters. *Journal of Geophysical Research*, **106(C10)**, 22,067–22,093.

Fratantoni, D. and D. Glickson, 2002: North Brazil Current ring generation and evolution observed with SeaWiFS. *Journal of Physical Oceanography*, **32**, 1058–1074.

Fratantoni, D., W. Johns, T. Townsend, and H. Hurlburt, 2000: Low-Latitude circulation and mass transport pathways in a model of the tropical Atlantic ocean. *Journal of Physical Oceanography*, **30**, 1944–1966.

Fratantoni, D. and P. Richardson, 2006: The evolution and demise of North Brazil Current Rings. *Journal of Physical Oceanography*, **36**, 1241–1264.

Fu, L.-L. and D. Chelton, 2001: Large-Scale Ocean Circulation. In: Satellite Altimetry and Earth Sciences. A Handbook of Techniques and Applications. *edited by L.-L. Fu and A. Cazenave, International Geophysics Series, Academic Press*, **69**, 133–169.

Gallagher, F., H. von Storch, R. Schnur, and G. Hannoschoeck, 1991: The POP manual. *Technical Report, Deutsches Klimarechenzentrum, Hamburg, Germany*, **1**, 66.

Ganachaud, A. and C. Wunsch, 2003: Large-Scale Ocean Heat and Freshwater Transports during the World Ocean Circulation Experiment. *Journal of Climate*, **16**, 696–705.

Ganachaud, A., C. Wunsch, M. Kim, and B. Tapley, 1997: Combination of TOPEX/POSEIDON data with a hydrographic inversion for determination of the oceanic general circulation and its relation to geoid accuracy. *Geophysical Journal International*, **128**, 708–722.

Garraffo, Z., W. Johns, E. Chassignet, and G. Goni, 2003: North Brazil Current rings and transport of southern waters in a high resolution numerical simulation of the North Atlantic. *in: Interhemispheric Water Exchange in the Atlantic Ocean, G. Goni and P. Malanotte-Rizzoli (Ed), Elsevier Press*, pp. 375–403.

Garzoli, S. and E. Katz, 1993: The forced annual reversal of the North Atlantic Equatorial Countercurrent. *Journal of Physical Oceanography*, **13**, 2082–2090.

Gerdes, R. and C. Wübber, 1991: Seasonal variability of the North Atlantic Ocean - a model intercomparison. *Journal of Physical Oceanography*, **21**, 1300–1322.

Giarolla, E., P. Nobre, M. Malagutti, and L. Pezzi, 2005: The Atlantic Equatorial Undercurrent: PIRATA observations and simulations with GFDL Modular Ocean Model at CPTEC. *Geophysical Research Letters*, **32**, doi:10.1029/2004GL022206.

Gill, A., 1992: *Atmosphere-ocean dynamics*. Academic Press. Volume 30 in International Geophysics Series.

Goni, G. and W. Johns, 2001: A census of North Brazil Current rings observed from TOPEX/Poseidon Altimetry: 1992-1998. *Geophysical Research Letters*, **28(1)**, 1–4.

Gordon, A., 1986: Interocean exchange of thermocline water. *Journal of Geophysical Research*, **91**, 5037–5046.

Gouretski, V. and K. Jancke, 1999: A description and Quality Assessment of the Historical Hydrographic Data for the South Pacific Ocean. *Journal of Atmospheric and Ocean Technology*, **16(1)**, 1791–1815.

Gouretski, V. and K. Koltermann, 2004: WOCE Global Hydrographic Climatology. A Technical Report. *Berichte des Bundesamtes für Seeschiffahrt und Hydrographie*, **35**, 5–51.

Grodsky, S., J. Carton, C. Provost, J. Servain, J. Lorenzzetti, and M. McPhaden, 2005: Tropical instability waves at 0°N, 23°W in the Atlantic: A case study using Pilot Research Moored Array in the Tropical Atlantic (PIRATA) mooring data. *Journal of Geophysical Research*, **110**, doi:10.1029/2005JC002941.

Haney, L., 1971: Surface thermal boundary conditions for ocean circulation models. *Journal of Physical Oceanography*, **1**, 241–248.

Hansen, D. and C. Paul, 1984: Genesis and effects of long waves in the equatorial Pacific. *Journal of Geophysical Research*, **89**, 10431–10440.

Hastenrath, S. and A. Greischar, 1993: Circulation mechanisms related to Northeast Brazil rainfall anomalies. *Journal of Geophysical Research*, **98**, 5093–5102.

Hazeleger, W. and P. de Vries, 2003: Fate of the Equatorial Undercurrent in the Atlantic. *in Interhemispheric Water Exchange in the Atlantic Ocean, Elsevier Oceanographic Series*, **68**, 175–191.

Hazeleger, W., P. de Vries, and Y. Friocourt, 2003: Sources of the Equatorial Undercurrent in the Atlantic in a high-resolution ocean model. *Journal of Physical Oceanography*, **33(4)**, 677–693.

Hendon, H., B. Liebmann, and J. Glick, 1998: Oceanic Kelvin Waves and the Madden-Julian Oscillation. *Journal of Atmospheric Science*, **55**, 88–101.

Isachsen, P., J. LaCasce, and J. Pedlosky, 2005: Rossby wave instability and apparent phase speeds in large ocean basins. *Journal of Physical Oceanography (submitted)*.

Jochum, M. and P. Malanotte-Rizzoli, 2003a: On the generation of North Brazil Current rings. *Journal of Marine Research*, **61**, 147–173.

Jochum, M. and P. Malanotte-Rizzoli, 2003b: The flow of AAIW along the equator. *in Interhemispheric Water Exchange in the Atlantic Ocean, Elsevier Oceanographic Series*, **68**, 193–212.

Jochum, M., P. Malanotte-Rizzoli, and A. Busalacchi, 2004: Tropical instability waves in the Atlantic Ocean. *Ocean Modelling*, **7**, 145–163.

Johns, W., T. Lee, F. Schott, R. Zantopp, and R. Evans, 1990: The North Brazil Current retroflection: Seasonal structure and eddy variability. *Journal of Geophysical Research*, **95**, 22,103–22,120.

Johns, W., T. N. Lee, R. C. Beardsley, J. Candela, R. Limeburner, and B. Castro, 1998: Annual cycle and variability of the North Brazil Current. *Journal of Physical Oceanography*, **28(1)**, 103–128.

Johns, W., R. Zantopp, and G. Goni, 2003: Cross-gyre transport by North Brazil Current rings. *in Interhemispheric Water Exchange in the Atlantic Ocean, Elsevier Oceanographic Series*, **68**, 411–441.

Jones, C., D. Waliser, and C. Gautier, 1998: The Influence of the Madden-Julian Oscillation on Ocean Surface Heat Fluxes and Sea Surface Temperature. *Journal of Climate*, **11**, 1057–1072.

Katz, E., 1995: Dynamics of the equatorial Atlantic from altimetry. *Journal of Geophysical Research*, **100**, 25,61–25,67.

Katz, E., 1997: Waves along the Equator in the Atlantic. *Journal of Physical Oceanography*, **27**, 2536–2544.

Kelly, B., S. Meyers, and J. O'Brien, 1995: On a generating mechanism for Yanai waves and the 25-day oscillation. *Journal of Geophysical Research*, **100**, 10.589–10,612.

Kessler, W., 1990: Observations of long Rossby waves in the northern tropical Pacific. *Journal of Geophysical Research*, **95**, 5183–5217.

Killworth, P., D. Chelton, and R. D. Szoeke, 1997: The speed of observed and theoretical long extratropical planetary waves. *Journal of Physical Oceanography*, **27**, 1946–1966.

Kuragano, T. and M. Kamachi, 2000: Global statistical space-time scales of oceanic variability estimated from the TOPEX/POSEIDON altimeter data. *Journal of Geophysical Research*, **105**, 955–974.

LaCasce, J. and J. Pedlosky, 2004: The instability of Rossby basin modes and the oceanic eddy field. *Journal of Physical Oceanography*, **34**, 2027–2041.

Lau, K.-M. and H. Weng, 1995: Climate signal detection using wavelet transform: How to make a time series sing. *Bulletin of the American Meteorological Society*, **76(12)**, 2391–2402.

Legeckis, R., 1977: Long waves in the eastern equatorial Pacific ocean: A view from a geostationary satellite. *Science*, **197**, 1179–1181.

Legeckis, R. and G. Reverdin, 1987: Long waves in the equatorial Atlantic Ocean during 1983. *Journal of Geophysical Research*, **92**, 2835–2842.

Levitus, S., 1982: Climatological Atlas of the World Ocean. *U.S. Gov. Printing Office, Washington, D.C.*, p. 173.

Levitus, S., R. Bargett, and T. Boyer, 1994: World Ocean Atlas 1994. Vol. 3: Salinity. *NOAA Atlas NESDID 3, U.S. Gov. Printing Office, Washington D.C.*, p. 99.

Levitus, S. and T. Boyer, 1994a: World Ocean Atlas 1994. Vol. 2: Oxygen. *NOAA Atlas NESDID 2, U.S. Gov. Printing Office, Washington D.C.*, p. 186.

Levitus, S. and T. Boyer, 1994b: World Ocean Atlas 1994. Vol. 4: Temperature. *NOAA Atlas NESDID 4, U.S. Gov. Printing Office, Washington D.C.*, p. 117.

Levitus, S., T. Boyer, M. Conkright, T. O'Brian, J. Antonov, C. Stevens, L. Stathopolos, D. Johnson, and R. Gelfeld, 1998: World Ocean Database 1998. Vol. 1: Introduction. *NOAA Atlas NESDID 18, U.S. Gov. Printing Office, Washington D.C.*, p. 346.

Lorenz, E., 1955: Available potential energy and the maintenance of the general circulation. *Tellus*, **2**, 157–167.

Lumpkin, R., 2003: Decomposition of surface drifter observations in the Atlantic Ocean. *Geophysical Research Letters*, **30(14)**, 1753(10.1029/2003GL017519.

Lumpkin, R. and Z. Garraffo, 2005: Evaluating the decomposition of tropical Atlantic drifter observations. *Journal of Atmospheric Oceanic Technology I*, **22**, 1403–1415.

Lumpkin, R. and S. Garzoli, 2005: Near-surface circulation in the Tropical Atlantic Ocean. *Deep-Sea Research I*, **52**, 495–518.

Madden, R. and P. Julian, 1971: Description of a 40-50 day oscillation in the zonal wind in the tropical Pacific. *Journal of Atmospheric Science*, **28**, 702–708.

Malanotte-Rizzoli, P., K. Hedstrom, H. Arango, and D. Haidvogel, 2000: Water mass pathways between the subtropical and tropical ocean in a climatological simulation of the North Atlantic ocean circulation. *Dynamics of Atmospheres and Oceans*, **32(3)**, 331–371.

McCreary, J. and Z. Yu, 1992: Equatorial dynamics in a 21/2-layer model. *Progress in Oceanography*, **29**, 61–132.

McPhaden, M., X. Zhang, H. Hendon, and M. Wheeler, 2006: Large scale dynamics and mjo forcing of enso variability. *Geophysical Research Letters*, **33**, doi:10.1029/2006GL026786.

Menkes, C., S. Kennan, and P. F. et al., 2002: A whirling ecosystem in the equatorial Atlantic. *Geophysical Research Letters*, **29(11)**, doi:10.1029/2001GL014576.

Metcalf, W. and M. Stalcup, 1967: Origin of the Atlantic Equatorial Undercurrent. *Journal of Geophysical Research*, **72**, 4959–4974.

Meyers, G., 1979: On the annual Rossby wave in the tropical North Pacific Ocean. *Journal of Physical Oceanography*, **9**, 663–674.

Molinari, R., 1982: Observations of eastward currents in the tropical South Atlantic Ocean: 1978-1980. *Journal of Geophysical Research*, **87**, 9707–9714.

Morrow, R., F. Birol, D. Griffin, and J. Sudre, 2004: Divergent pathways of cyclonic and anti-cyclonic ocean eddies. *Geophysical Research Letters*, **31**, doi:10.1029/2004GL020974.

Müller, P. and J. Willebrandt, 1989: Equations for oceanic motions. *In: Landoldt Börnstein, Group V, Oceanography, Volume 3b, J. Sündermann, Ed., Springer Verlag Berlin*, pp. 1–14.

Niiler, P., 2001: The world ocean surface circulation. *In: G. Siedler, J. Church, J. Gould (Eds.), Ocean Circulation and Climate, International Geophysics Series*, **77**, 193–204.

Nof, D., 1981: On the β-induced movement of isolated baroclinic eddies. *Journal of Physical Oceanography*, **11**, 1662–1672.

Nof, D., 1983: On the migration of isolated eddies with application to Gulf stream rings. *Journal of Marine Research*, **41**, 399–425.

Nof, D. and T. Pichevin, 1996: The retroflexion paradox. *Journal of Physical Oceanography*, **26**, 2344–2358.

Ollitrault, M., M. Lankhorst, D. Fratantoni, P. Richardson, and W. Zenk, 2006: Zonal intermediate currents in the atlantic ocean. *Geophysical Research Letters*, **33**, doi:10.1029/2005GL025368.

Oort, A., S. Ascher, S. Levitus, and J. Peixóto, 1989: New estimates of the available potential energy in the world ocean. *Journal of Geophysical Research*, **94(C3)**, 3187–3200.

Pacanowski, R., 1995: *MOM 2 documentation, User's guide and reference manual*. Technical Report 3, GFDL Ocean Group.

Pedlosky, J., 1987: *Geophysical fluid dynamics*. Springer-Verlag, New York. 2nd ed.

Peterson, R. and L. Stramma, 1991: Upper-level circulation in the South Atlantic Ocean. *Progress in Oceanography*, **26**, 1–73.

Philander, S., 1976: Instabilities of zonal equatorial currents. *Journal of Geophysical Research*, **81**, 3725–3735.

Philander, S., 1978: Instabilities of zonal equatorial currents, 2. *Journal of Geophysical Research*, **83**, 3679–3682.

Philander, S., W. Hurlin, and R. Pacanowski, 1986: Properties of Long Equatorial Waves in Models of the Seasonal Cycle in the Tropical Atlantic and Pacific Oceans. *Journal of Geophysical Research*, **91(C12)**, 14,207–14,211.

Philander, S. and R. Pacanowski, 1986: A model of seasonal cycle in the tropical Atlantic ocean. *Journal of Geophysical Research*, **91(C12)**, 14,192–14,206.

Picaut, J. and A. Busalacchi, 2001: Tropical ocean variability. *In: Satellite Altimetry and Earth Sciences. A Handbook of Techniques and Applications edited by L.-L. Fu and A. Cazenave, International Geophysics Series, Academic Press*, **69**, 217–236.

Picaut, J., M. McPhaden, and S. Hayes, 1989: On the use of the geostrophic approximation to estimate time-varying zonal currents at the equator. *Journal of Geophysical Research*, **94**, 3228–3236.

Polito, P., J. Ryan, W. Liu, and F. Chavez, 2001: Oceanic and atmospheric anomalies of tropical instability waves. *Geophysical Research Letters*, **28(11)**, 2233–2236.

Rahmstorf, S., 2006: Thermohaline Ocean Circulation. *In: Encyclopedia of Quaternary Science, Edited by S.A. Elias. Elsevier, Amsterdam.*

RD Instruments, 1989: *Acoustic Doppler Current Profilers, Principles of operation: A practical primer*. RD Instruments, 9855 Businesspark Avenue, San Diego, California, 92131.

Redler, R., K. Ketelsen, J. Dengg, and C. Böning, 1998: A high-resolution numerical model for the circulation of the Atlantic ocean. *In: Proceedings of the fourth European SGI/GRAY MPP workshop, H. Lederer and F. Hertweck, Hg. Max-Planck-Institute für Plasmaphysik*, pp. 95–108.

Reid, J., 1989: On the total geostrophic circulation of the South Atlantic Ocean: Flow patterns, tracers and transports. *Progress in Oceanography*, **23**, 149–244.

Rhein, M. and U. Send, 1995: The Atlantic Deep Western Boundary Current: Water masses and transports near the equator. *Journal of Geophysical Research*, **100(C2)**, 2441–2457.

Richardson, P. and G. Reverdin, 1987: Seasonal Cycle of Velocity in the Atlantic North Equatorial Countercurrent as Measured by Surface Drifters, Current Meters, and Ship Drifts. *Journal of Geophysical Research*, **92(C4)**, 3691–3708.

Richardson, P. and W. Schmitz, 1993: Deep cross-equatorial flow in the Atlantic measured with SOFAR floats. *Journal of Geophysical Research*, **98**, 8371–8387.

Schmid, C., Z. Garraffo, E. Johns, and S. Garzoli, 2003: Pathways and variability at intermediate depths in the tropical Atlantic. *in Interhemispheric Water Exchange in the Atlantic Ocean, Elsevier Oceanographic Series*, **68**, 233–268.

Schmid, C., G. Siedler, and W. Zenk, 2000: Dynamics of intermediate water circulation in the subtropical South Atlantic. *Journal of Physical Oceanography*, **30(12)**, 3191–3211.

Schott, F., P. Brandt, M. Hamann, J. Fischer, and L. Stramma, 2002: On the boundary flow off Brazil at 5-10°S and its connection to the interior tropical Atlantic. *Geophysical Research Letters*, **29(17)**, doi:10.1029/2002GL014786.

Schott, F., M. Dengler, P. Brandt, K. Affler, J. Fischer, B. Bourlés, Y. Gouriou, R. Molinari, and M. Rhein, 2003: The zonal currents and transports at 35°W in the tropical Atlantic. *Geophysical Research Letters*, **30(7)**, 1349–1352.

Schott, F., M. Dengler, R. Zantopp, L. Stramma, J. Fischer, and P. Brandt, 2005: The shallow and deep western boundary circulation of the Southern Atlantic at 5-11°S. *Journal of Physical Oceanography*, **35**, 2031–2053.

Schott, F., J. McCreary, and G. Johnson, 2004: Shallow overturning circulations of the tropical-subtropical oceans. *Geophysical Monograph Series*, **147**, 261–304.

Schott, F., L. Stramma, and J. Fischer, 1998: Transports and pathways of the upper-layer circulation in the western tropical Atlantic. *Journal of Physical Oceanography*, **28**, 1904–1928.

Schott, F. A. and C. W. Böning, 1991: The WOCE model in the western equatorial Atlantic: Upper layer circulation. *Journal of Geophysical Research*, **96(C4)**, 6993–7004.

Schott, F. A., L. Stramma, and J. Fischer, 1995: The warm water inflow into the western tropical Atlantic boundary regime, spring 1994. *Journal of Geophysical Research*, **100**, 24,745–24,760.

Schouten, M., R. Matano, and T. Strub, 2005: A description of the seasonal cycle of the equatorial Atlantic from altimeter data. *Deep-Sea Research I*, **52**, 477–493.

Seo, H., M. Jochum, R. Murtugudde, and A. Miller, 2006: Effect of ocean mesoscale variability on the mean state of tropical Atlantic climate. *Geophysical Research Letters*, **33**, doi:10.1029/2005GL025651.

Servain, J., A. Busalacchi, M. McPhaden, A. Moura, G. Reverdin, M. Vianna, and S. Zebiak, 1998: A Pilot Research Moored Array in the Tropical Atlantic (PIRATA). *Bulletin of American Meteorological Society*, **79**, 2019–2031.

Siedler, G., T. Müller, R. Onken, M. Arhan, H. Mercier, B. King, and P. Saunders, 1996: *The zonal WOCE sections in the South Atlantic: Present and past circulation*. Springer-Verlag, New York. Edited by G. Wefer et al.

Snowden, D. and R. Molinari, 2003: Subtropical cells in the Atlantic ocean: An observational summary. *in Interhemispheric Water Exchange in the Atlantic Ocean, Elsevier Oceanographic Series*, **68**, 287–312.

Storch, H. and F. Zwiers, 1999: *Statistical analysis in climate research*. Cambridge University Press, United Kingdom.

Stramma, L. and M. England, 1999: On the water masses and mean circulation of the South Atlantic Ocean. *Journal of Geophysical Research*, **104(C9)**, 20,863–20,883.

Stramma, L., J. Fischer, and J. Reppin, 1995: The North Brazil Undercurrent. *Deep-Sea Research*, **42**, 773–795.

Stramma, L. and R. Peterson, 1990: The South Atlantic Current. *Journal of Physical Oceanography*, **20**, 846–859.

Stramma, L. and F. Schott, 1999: The mean flow field of the tropical Atlantic Ocean. *Deep-Sea Research II*, **46**, 279–303.

Suga, T. and L. Talley, 1995: Antarctic Intermediate Water circulation in the tropical and subtropical Atlantic. *Journal of Geophysical Research*, **100**, 13441–13453.

Talley, L., 1996: Antarctic Intermediate Water in the South Atlantic. *In: the South Atlantic: Present and Past Circulation. G. Wefer and G. Siedler and D.J. Webb (Ed), Springer Verlag, Berlin*, pp. 219–238.

Thierry, V., A.-M. Treguier, and H. Mercier, 2004: Numerical study of the annual and semi-annual fluctuations in the deep equatorial Atlantic Ocean. *Ocean Modelling*, **6**, 1–30.

Tomczak, M. and J. Godfrey, 1994: *Regional oceanography: An introduction*. Elsevier, New York.

Torrence, C. and G. Compo, 1998: A practical guide to wavelet analysis. *Bulletin of the American Meteorological Society*, **79(1)**, 61–78.

Traon, R. L., F. Nadal, and N. Ducet, 1998: An improved Mapping Method of Multisatellite Altimeter Data. *Journal of Atmospheric and Oceanic Technology*, **15**, 522–534.

Traon, R. L. and F. Ogor, 1999: ERS-1/2 orbit improvement using TOPEX/POSEIDON: the 2 cm challenge. *Journal of Geophysical Research*, **103**, 8045–8058.

Tsuchiya, M., 1986: Thermostats and circulation in the upper layer of the Atlantic Ocean. *Progress in Oceanography*, **16**, 235–267.

Visbeck, M., 2002: Deep velocity profiling using lowered acoustic Doppler current profilers: Bottom track and inverse solutions. *Journal of Atmospheric and Oceanic Technology*, **19**, 794–807.

Visbeck, M. and J. Fischer, 1995: Sea surface conditions remotly sensed by upward-looking ADCPs. *Journal of Atmospheric and Oceanic Technology*, **12**, 141–149.

von Storch, H., T. Bruns, I. Fischer-Bruns, and K. Hasselmann, 1988: Principal oscillation pattern analysis of the 30- to 60-day oscillation in general circulation model equatorial troposphere. *Journal of Geophysical Research*, **93**, 11,022–11,036.

von Storch, H., G. Bürger, R. Schnur, and J. von Storch, 1995: Principal oscillation patterns: a review. *Journal of Climate*, **8**, 377–400.

Wang, C. and D. Enfield, 2001: The tropical western hemisphere warm pool. *Geophysical Research Letters*, **28(8)**, 1635–1638.

Weisberg, R. and T. Weingartner, 1988: Instability waves in the equatorial Atlantic ocean. *Journal of Physical Oceanography*, **18**, 1641–1657.

White, W., 1977: Annual forcing of baroclinic long waves in the tropical North Pacific Ocean. *Journal of Physical Oceanography*, **7**, 50–61.

Wilson, W. and W. Johns, 1997: Velocity structure and transport in the Windward Island Passages. *Deep-Sea Research I*, **44**, 487–520.

Wunsch, C. and A. E. Gill, 1976: Observations of equatorially trapped waves in Pacific sea level variations. *Deep-Sea Research*, **23**, 371–390.

Yu, Z., J. McCreary, and J. Proehl, 1995: On the meridional asymmetry and energetics of tropical instability waves. *Journal of Physical Oceanography*, **25**, 1680–1686.

Zhang, D., M. McPhaden, and W. Johns, 2003: Observational evidence for flow between the subtropical and tropical Atlantic: The Atlantic subtropical cells. *Journal of Physical Oceanography*, **33**, 1783–1797.

Danksagung

Ich danke Herrn Priv.-Doz. Dr. P. Brandt und Herrn Prof. Dr. F. Schott für die Unterstützung bei der Erstellung dieser Arbeit. Beide hatten immer Zeit und Interesse für Diskussionen und trugen durch hilfreiche Kommentare und Anregungen zum Gelingen dieser Arbeit bei.
Besonders möchte ich mich bei Priv.-Doz. Dr. C. Eden für die intensive Hilfestellung bedanken, vor allem im Zusammenhang mit der Bearbeitung der Modelldaten. Ihm und Dr. T. Jung danke ich für die Bereitstellung der Modelldaten. Für die vielen Anregungen und die engagierte Unterstützung danke ich Prof. Dr. M. Visbeck. Mein Dank gilt auch R. Schönefeldt, J. Karstensen, M. Dengler, A. Funk, B. Rabe, J. Möller und allen Mitarbeitern der Abteilung Ozeanzirkulation und Klimadynamik.

Besonders danken möchte ich Jelto und Papaopi.

Erklärung

Hiermit bestätige ich, dass ich die vorliegende Dissertation selbstständig verfasst und keine anderen als die angegebenen Quellen und Hilfsmittel verwendet habe.
Ich versichere, dass diese Arbeit noch nicht zur Erlangung eines Doktorgrades an anderer Stelle vorgelegen hat.
Ich erkläre, dass die vorliegende Arbeit gemäß der Grundsätze zur Sicherung guter wissenschaftlicher Praxis der Deutschen Forschungsgemeinschaft erstellt wurde.

Kiel, September 2006

(Karina von Schuckmann)